A CONSTITUTIVE LAW FOR TRABECULAR BONE

THÈSE N^{O} 1252 (1994)

PRÉSENTÉE AU DÉPARTEMENT DE GÉNIE MÉCANIQUE

ÉCOLE POLYTECHNIQUE FÉDÉRALE DE LAUSANNE

POUR L'OBTENTION DU GRADE DE DOCTEUR ÈS SCIENCES

PAR

PHILIPPE ZYSSET
Ingénieur physicien diplômé EPFL
originaire de Troinex (GE)

acceptée sur proposition du jury:

Dr A. Curnier, rapporteur
Prof. W.C. Hayes, corapporteur
Dr P.-F. Leyvraz, corapporteur
Prof. Ch. Stuart, corapporteur
Dr H. Taaks, corapporteur

Lausanne, EPFL
1994

Chacun des grains de cette pierre, chaque éclat minéral de cette montagne pleine de nuit, à lui seul forme un monde. La lutte elle-même vers les sommets suffit à remplir un cœur d'homme.

Le mythe de Sisyphe, Albert Camus

à mes parents,
à Nicole,
ainsi qu'à Anne

Acknowledgements

I wish to express my deepest gratitude to Dr Alain Curnier who directed this thesis and shared his outstanding scientific expertise and enthusiasm, as well as his sincere friendship with a boundless generosity.

I am most grateful to Prof. W.C. Hayes who introduced me in the world of biomechanics at Harvard University in 1989 and tought me the rigor of scientific writing.

My sincere thanks go to Dr Q.-C. He and Dr P.J. Rubin for the fruitful discussions we had together on the theoretical, respectively numerical aspects of this work.

I would like to express my special thanks to Prof. E.R. Weibel (Fondation Maurice E. Müller, Bern), Dr H. Taaks (Protek AG, Bern), Prof. M. Del Pedro (Laboratoire de Mécanique Appliquée, Lausanne), Dr P.-F. Leyvraz (Hôpital Orthopédique de la Suisse Romande, Lausanne) and the Swiss National Fund for their trust and support for the realization of this thesis.

I owe many thanks to all members of the jury for their careful reading and relevant review of this manuscript.

The major experimental part of this thesis relied on collaborations with the Maurice E. Müller Institut für Biomechanik in Bern on the one hand and the Laboratoire de Technologie des Composites et Polymères in Lausanne on the other hand. I gratefully acknowledge Prof. E. Hunziker, Prof. A. Manson, Dr L.-P. Nolte and Dr P. Witschger for their spontaneous welcome and help.

My further thanks go to M. Angst, F. Bonjour, P. Brunner, I. Couillard, G. Crivellari, Prof. R. Krstić, Dr K. Lippuner, Dr M.C. Michel and S. Pruvot for their valuable assistance.

I also wish to acknowledge all members of the Orthopaedic Biomechanics Laboratory, of the Laboratoire de Mécanique Appliquée and of the Maurice E. Müller Institut für Biomechanik for their friendship and encouragements.

Last, but not least my warmest thanks go to my wife Anne, who shared the joys and dispairs of this privileged adventure.

Abstract

Motivated by applications in orthopaedic surgery, new constitutive laws for trabecular (or spongious) bone are developed in the framework of continuum mechanics, implemented in a mechanical analysis computer program, validated by a number of *in vitro* experiments and illustrated by the simulation of a femoral total hip component.

Current knowledge about the morphological and mechanical properties of trabecular bone is reviewed for setting the background and clarifying the contributions of the thesis.

Comprehensive 1D and 3D theoretical models based on the approach of standard generalized materials are developed with a specific attention towards irreversible phenomena. The 1D model includes linear elasticity and rate-independent as well as rate-dependent plastic strain flow with damage. Based on a second order fabric tensor, the 3D model includes inhomogeneous, orthotropic linear elasticity and rate-independent plasticity with damage.

In order to solve boundary value problems involving complex bone or bone-implant structures, implicit projection algorithms are developed for integrating the plastic flow rules with damage and implemented in the computer program TACT combining the finite element method, the linear iteration method and the finite difference method. The resulting numerical models are illustrated by the means of traction, bending and torsion benchmark tests.

A number of pilot *in vitro* experiments are undertaken on human and bovine trabecular bone specimens in order to validate the theoretical models and identify the material constants. Quasistatic uniaxial and torsion experiments are performed with a method avoiding artefacts due to the inhomogeneous boundary conditions associated with porosity. Anisotropic elasticity, plasticity and damage of trabecular bone prove to be successfully described by the models in terms of structural density and morphology.

Finally, the 3D constitutive law is applied to the biomechanical problem of primary stability of a cementless femoral total hip component in order to illustrate its potential.

Résumé

Motivées par des applications en chirurgie orthopédique, de nouvelles lois constitutives pour l'os trabéculaire (ou spongieux) sont développées dans le cadre de la mécanique des milieux continus, intégrées à un programme informatique d'analyse mécanique, validées au moyens d'expériences *in vitro* et illustrées par la simulation du composant fémoral d'une arthroplastie totale de hanche.

Les connaissances actuelles sur les propriétés morphologiques et biomécaniques de l'os trabéculaire sont passées en revue afin d'exposer le contexte et de clarifier les contributions de cette thèse.

Des modèles 1D et 3D basés sur l'approche des matériaux standards généralisés sont développés en mettant l'accent sur les phénomènes irréversibles. Le modèle 1D comprend l'élasticité linéaire ainsi que l'écoulement quasistatique ou visqueux de la déformation plastique et de l'endommagement. Fondé sur un tenseur de fabrique, le modèle 3D inclut l'élasticité inhomogène et orthotrope ainsi que la plasticité quasistatique avec endommagement.

Afin de résoudre des problèmes aux limites pour des structures complexes d'os ou d'os-implant, des algorithmes de projection implicite sont développés pour l'intégration des lois d'écoulement plastique et endommagée puis joints au programme TACT qui combine la méthode des éléments finis, la méthode des itérations linéaires et la méthode des différences finies. Les modèles numériques résultants sont testés à l'aide d'expériences de traction, de flexion et de torsion.

Un certain nombre d'expériences pilotes *in vitro* sont entreprises avec des échantillons d'os trabéculaire humain et bovin afin d'éprouver le modèle et d'identifier les constantes du matériau. Des expériences d'endommagement quasistatiques sont effectuées à l'aide d'une méthode évitant les artefacts dûs aux conditions de bord inhomogènes associés à la porosité. L'élasticité anisotrope, la plasticité et l'endommagement de l'os trabéculaire sont décrits avec succès par les modèles proposés en termes de la densité structurale et de la morphologie.

La loi constitutive 3D est finalement appliquée au problème biomécanique de la stabilité primaire du composant fémoral d'une arthroplastie totale de hanche non-cimentée afin d'illustrer son potentiel.

Contents

Chapter 1

Introduction

1.1 What is trabecular bone ?

Bone is the essential structural element of the human and other mammal's body. It provides stiffness and strength to resist the forces of gravity and protects vital internal organs. Bone is also a metabolic tissue, serving as a calcium repository and playing an important role in the production of blood-forming marrow. While the external shell of each skeletal part is constituted of compact or cortical bone, the core is often filled with a porous or spongious cellular tissue designated as cancellous or trabecular bone (Fig. 1.1b). In fact, cancellous bone forms an interconnected three-dimensional meshwork of thin rods and plates of bone called trabeculae. The spaces are filled with red marrow that insures the nutritional supply of the bone tissue (Fig. 1.1c).

Cancellous bone plays an important role in the mechanical behaviour and functionality of the skeleton wherever it is located and in particular (Fig. 1.1a):

- At the ends of long bones, under synovial joints.
- In the core of short bones.
- In the core of flat bones.
- Under protuberances to which tendons are attached.

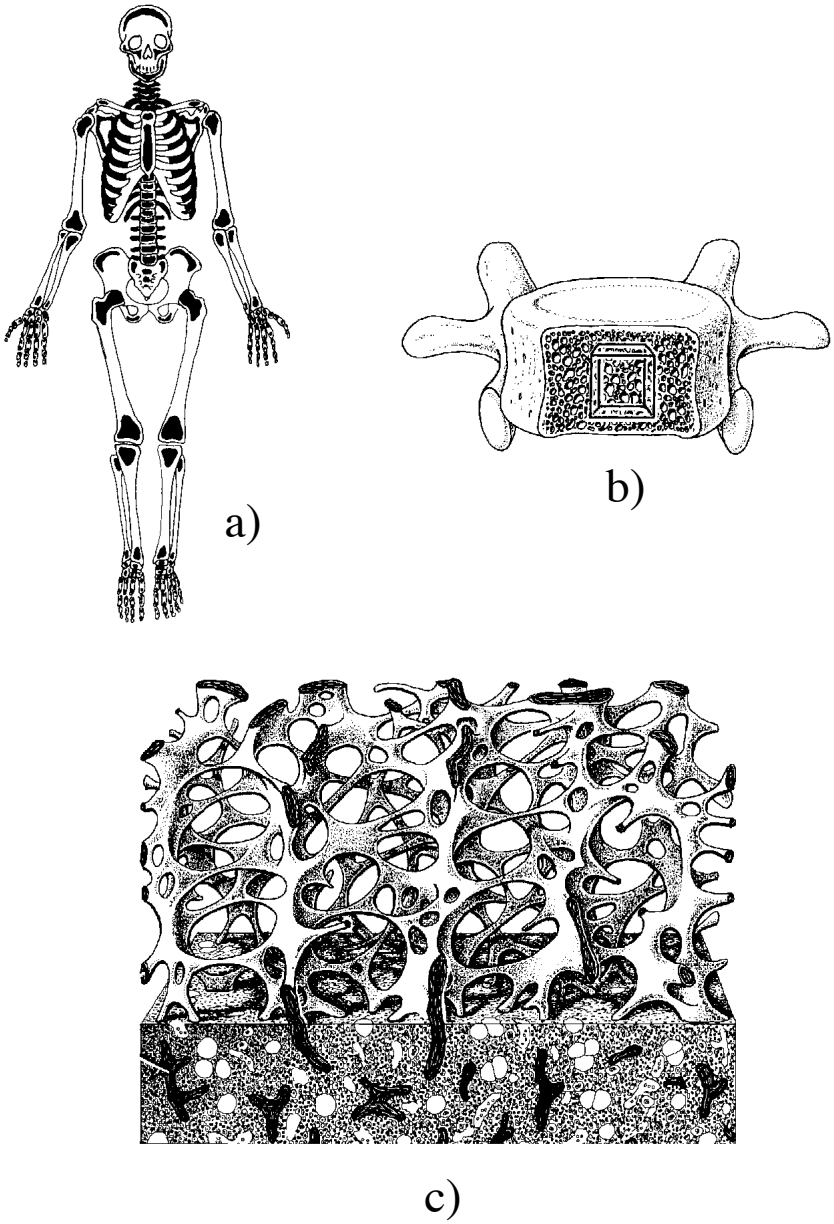

Figure 1.1: a) Distribution of trabecular bone in the human skeleton. b) Vertebra with trabecular bone core. c) Three-dimensional meshwork of trabecular bone and its marrow. From Krstić [85].

At the ends of long bones, trabecular bone transmits and gradually concentrates the large compressive loads from the cartilaginous joint surfaces into the compact bone of the shaft [65].

In short bones, the presence of trabecular bone with reduced thickness of the cortical shell optimizes the weight of the whole structure with respect to stiffness when compared to a thick but hollow cortical shell alone.

In the core of flat bones, trabecular bone constitutes a lightweighted filling material that keeps the bending or buckling walls of compact bone apart and improves the shock absorbing properties like in a sandwich structure.

Under protuberances, as for instance the human tibial tuberosity to which the patellar tendon attaches, trabecular bone progressively concentrates the high tensile forces of the knee extensor apparatus into compact bone.
In all anatomical locations, morphology of the trabecular structure seems closely related to the physiological load intensity and direction to which it is apparently subjected [39].

1.2 Brief historical review

The application of the concepts and laws of mechanics to biological systems such as bone, can be traced back to the very foundation of physical science. Galileo already commented on Nature's skill in structural design and illustrated the principles of bending with living examples such as the quill of a bird's feather or the hollow shaft of the reed. However, the period extending from the 17th to the middle of the 19th century was strongly influenced by Descartes' mechanistic view as well as Lamarck's evolution theory and bone mechanics was essentially subsumed to the notion of adaptation. Most efforts were invested in understanding the shape and structure of bones with respect to their apparent function and environmental context. These primary biomechanical ideas were later extensively discussed by D'Arcy Thompson, who wrote a fascinating book on the intrinsic relationship between growth and form in the natural world [126]. Questionning the teleological aspects of Nature's design, he provided numerous and enlightening examples of mechanical adaptations of bones from the albatross's wing to the

spine of prehistoric reptiles.

The first description of trabecular architecture seems to be due to Bourgery in 1832, who insisted on the apparent weight optimization of bone structures. However, the initial attempt to give a mathematical interpretation of the structural properties of bones must be attributed to the anatomist Meyer [100] and the mathematician Culmann, who noticed that the architecture of trabecular bone in the human proximal femur corresponded to the directions of principal stresses deduced from graphic statics (Fig. 1.2). This original observation lead to the

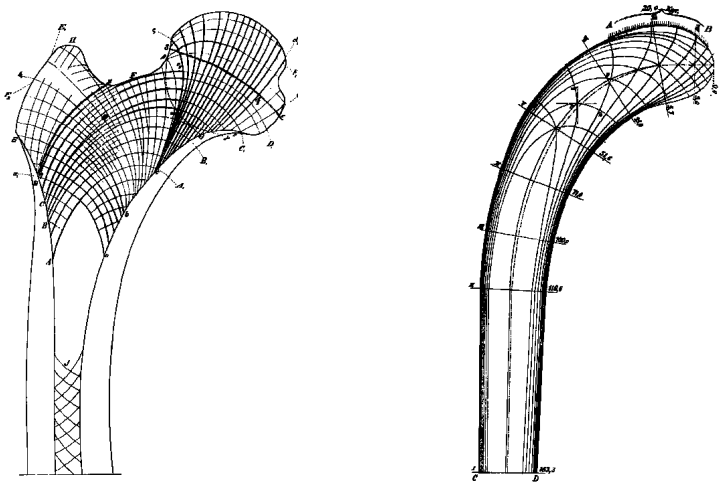

Figure 1.2: Comparison between the architecture of cancellous bone in the proximal femur and the principal stress lines of Culmann's crane. From Wolff [138].

famous law of bone remodelling published by Wolff in 1892, which was later confusingly involved with Roux's principle of functional adaptation and remains now as an unresolved hypothesis [138].

The investigation of the material properties of bone started in 1876 with the work of Rauber, who designed his own equipment and performed uniaxial, shear and torsion tests for both cortical and cancellous specimens. He observed the influence of humidity, temperature and anatomical locations on bone's stiffness and strength. A few years later, Messerer analysed the failure behaviour of whole bones using hydraulic equipment [113]. Motivated by clinical practice, a large amount of mechanical data has been collected for bovine and human bone since 1955 with testing methods conventionally used for engineering materials

[40, 111, 21, 24]. Comprehensive reports were published on both cortical and trabecular bone material properties such as the elastic modulus or the yield stress while the notions of anisotropy and inhomogeneity progressively appeared in the literature. Ultrasonic measurements allowed the assessment of the anisotropic elastic constants of both cortical and trabecular bone [3], but further properties such as viscoelasticity, plasticity, creep and fatigue were first investigated for cortical bone [7, 17, 18]. Fracture mechanics was later successfully applied to cortical bone and accumulation of irreversible damage investigated [11, 44].

After the introduction of artificial orthopaedic devices, the complex problem of bone-implant interaction emerged and recalled the importance of the interrelations between biological and mechanical properties. Hence, the theoretical understanding of bone remodelling was improved after 1960 by the models of Pauwels [105], Frost and Gjelsvik and remains today as a very active issue of biomechanical research [34, 22, 135].

Numerical techniques such as the finite element method were introduced in the early seventies and opened the decisive era of computer modelling and simulation of bone or bone-implant structures. Size and complexity of the solved problems followed the evolution of computer technology and application software [71]. In the same period, use of scanning electron microscopy provided three-dimensional images of bone's microstructure [136].

The need for informations on the relationship between the microscopic structure of bone and its mechanical properties was emphasized by Evans in 1973 and inspired a large number of composite models for cortical bone as well as structural models for trabecular bone [75, 57]. Apparition of homogeneization techniques in the eighties brought promising perspectives in this attempt to deduce macroscopic mechanical properties from geometrical and constituent properties [35].

At the macroscopic scale, quantitative stereology has proven to be an interesting tool for characterization of trabecular morphology [61], while continuum mechanics extended its application field to accumulation of damage preceeding failure of materials [82].

Finally, development of non-invasive bone assessment techniques such as quantitative computed assisted tomography (QCT), magnetic resonnance imaging

(MRI) or dual energy X-ray absorptiometry (DEXA) initiated a major breakthrough in both clinical practice and biomechanical research of the past decades [29]. Geometric properties of whole bones were obtained with good accuracy and material properties of trabecular bone estimated from mineral density [19].

1.3 Social and economical aspects

1.3.1 Hip and vertebral fractures

In aging populations, hip and vertebral fractures are becoming issues of major concern. For instance in the United States, about 500'000 vertebral fractures and 250'000 hip fractures occur annually. About one out of three women and one out of six men will experience a hip fracture if she or he lives to age 90. Beside the significant mortality due to postoperative complications, the resulting rehabilitation costs supported by the public health care are disturbing. There is growing evidence that hip and vertebral fracture incidence is related to both reduced mechanical properties of bone associated with osteoporosis and increased propensity for accidental trauma [63].

1.3.2 Total joint replacement

Total joint replacement is currently the procedure of choice for treatment of late stage osteoarthritis of the hip or the knee. In 1987, more than 450'000 total hip and 187'000 total knee arthroplasties were performed worldwide [46]. While contemporary total joint replacement is generally a successful procedure with a significant improvement of the patients quality of life, aseptic loosening of the prosthesis seems to be the rule after 10 to 20 years of function. Prosthetic failure implies demanding revision surgery and thus new potential complications and rehabilitation costs. Aseptic loosening of a prosthesis is often characterized by bone resorption and growth of a fibrous membrane around the artificial implant and involves coupled biological and mechanical interactions between implant, bone cement when used and trabecular bone [70].

1.4 Objectives

The existence of major public health problems associated with trabecular bone failure calls for a better understanding of the nucleation and accumulation of damage. From a biomechanical point of view, analysis of the mechanisms preceeding failure of trabecular bone requires a specific attention towards the postyield behaviour including plastic deformation and damage i.e. progressive degradation of elastic properties. In this respect, continuum damage mechanics (CDM) represents an appropriate framework for modelling and quantifying these postyield mechanisms [81].

On the other hand, improvement of non-invasive techniques for the assessment of trabecular morphology suggests a growing interest for quantification of mechanical properties from morphologic data. Non-invasive failure prediction of trabecular bone may be substantially improved by the development of an efficient model relating morphologic data to the decisive mechanical parameters governing the apparition and accumulation of damage.

In orthopaedic biomechanics, failure prediction in bones or bone-implant structures with complex geometries relies essentially on numerical techniques, in particular the finite element method (FEM). Credible application of the finite element method requires accurate constitutive laws of the involved materials. For this purpose, inhomogeneous, anisotropic and nonlinear material behaviour of trabecular bone needs to be refined and appropriate algorithms assembled for resolution of the clinically relevant boundary value problems.

> *In this context, the present thesis proposes a new constitutive law for trabecular bone based on morphologic data with an emphasis on irreversible damage behaviour. The thesis includes the theoretical formulation of the law, its numerical implementation, its experimental identification and a biomechanical illustration.*

More specifically, the four innovative parts of the thesis can be summarized as follows:

Firstly, 1D and 3D theoretical models are developed for the simultaneous flow of plasticity and damage in the framework of continuum mechanics and thermodynamics of irreversible processes. Secondly, the corresponding numerical models based on the implicit projection algorithm are conceived and integrated in our experimental finite element package TACT. Thirdly, the constitutive laws are identified and validated by a number of mechanical tests. Finally, in order to demonstrate the potential of the achieved work, the overall model is applied to the classical problem of primary stability of a total hip prosthesis.

1.5 Outline

According to these objectives, the thesis is organized as follows:

- Chapter 2 begins with a brief anatomical and physiological description of trabecular bone tissue followed by a progressive and detailed review of both morphological and biomechanical properties. The limitations of classical assessment methods are emphasized and the principal approaches relating morphology to mechanics are exposed.

- Chapter 3 consists in the elaboration of the 1D and 3D theoretical models. The hypotheses and balance equations of continuum mechanics are summarized and the framework of standard generalized materials presented. The different elements of the 1D and 3D constitutive laws, such as elasticity, viscoelasticity, rate-independent or rate-dependent plasticity with damage are progressively introduced and assembled in terms of porosity and anisotropic morphology.

- Chapter 4 describes the numerical methods traditionally employed in solid mechanics, in particular the finite element method (FEM), the iterative linearization method (ILM) and the finite difference method (FDM). The algorithms of implicit projection and implicit integration developed for numerical simulation of the constitutive laws are then exposed and applied to the 1D and 3D models. The resulting schemes are then illustrated by a number of benchmark tests.

- Chapter 5 presents the methods, results and discussions of a number of pilot *in vitro* mechanical tests that were undertaken on bovine and human bone for identification of the material constants and thus validation of the 1D and 3D constitutive laws. The original findings obtained with a method avoiding artefacts associated with inhomogeneous boundary conditions are outlined.

- Chapter 6 is devoted to the application of the developed 3D constitutive law to a comprehensive bone-prosthesis finite element model of the human hip. The geometrical and material characteristics as well as the boundary conditions of the model are described and the simulation of a physiological stair climbing load analysed with an emphasis on damage accumulation.

- Chapter 7 provides a critical discussion of the developed 1D and 3D constitutive laws and concludes on their potential in future orthopaedic biomechanics.

Chapter 2

Morphology and biomechanical behaviour

In this chapter, a brief anatomical and physiological description of trabecular bone tissue is made followed by a more detailed review of both morphological and biomechanical properties. In the last section the existing bridges between morphology and biomechanics are presented.

2.1 Anatomy and physiology

Bone belongs to the connective and supporting tissue group that differentiates from the mesenchyme in the first weeks of the mammal's embrio development. Bone formation involves the conjugate activity of osteoblasts and osteoclasts, which respectively produce and destroy the organic matrix of bone called osteoid. Calcification of the osteoid traps the osteoblasts that become osteocytes (bone-maintaining cells) and produce a primary, poorly organized and randomly oriented tissue designated as woven bone. After initial deposition, bone is subjected to secondary reconstruction, whereby a highly organized and regularly oriented lamellar tissue is laid down. In cortical bone, the resulting structure is composed of concentric lamellar rings called osteons, while in trabecular bone the lamellae are deposed along the rods and plates of the meshwork (Fig. 2.1). Unlike cortical tissue, trabecular tissue does not include blood vessels, and the

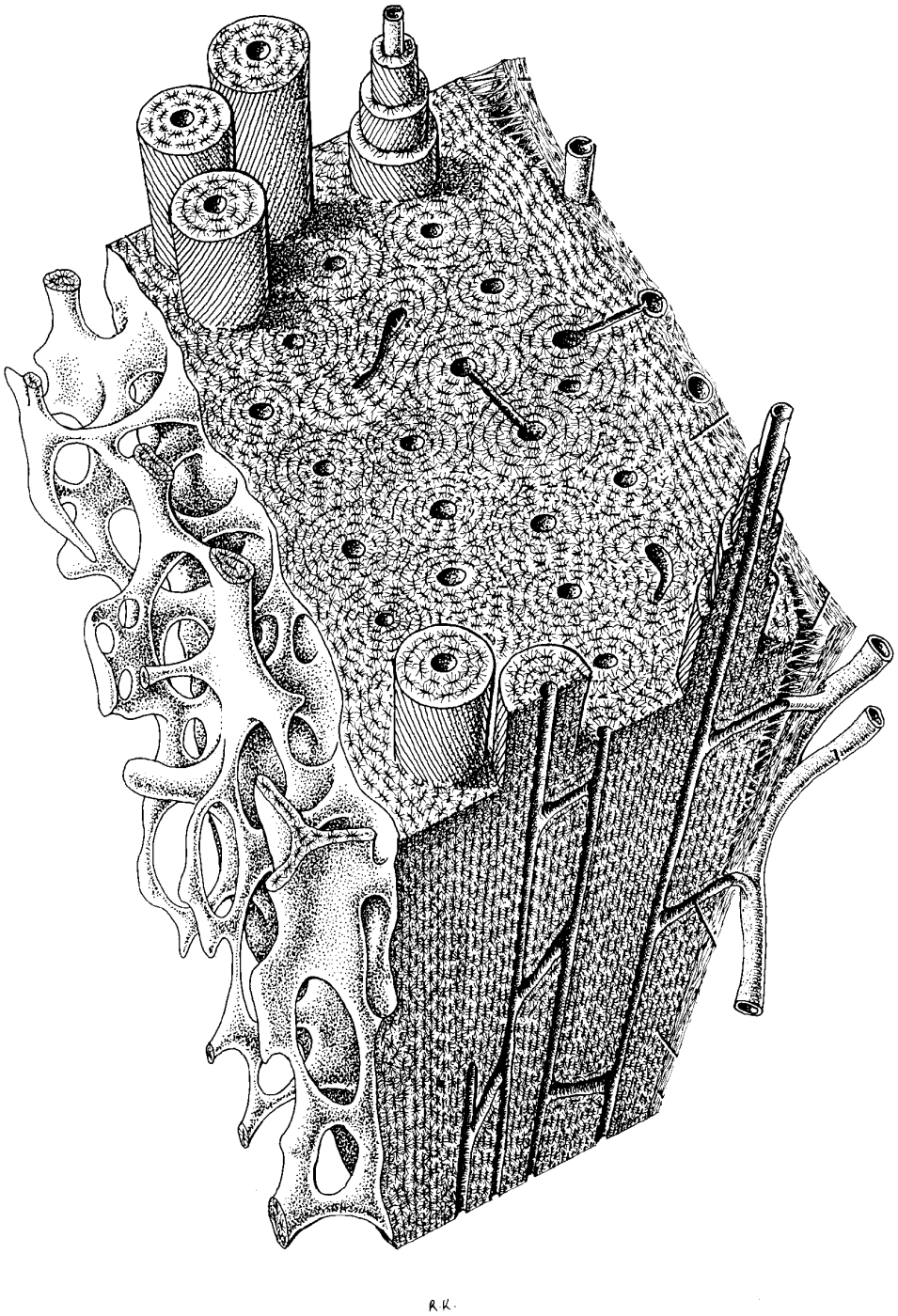

Figure 2.1: Lamellar structure of trabecular and cortical bone including osteocytes. From Krstić [84].

nutritional supply is insured through the red marrow and the extensive network of canaliculae allowing the osteocytes processes to contact each other.

Remodelling Bone tissue is characterized by a continuous remodelling activity, whereby osteoclasts create resorption cavities that are filled with new bone by osteoblasts. This turnover activity is essentially controlled by the parathyroid hormone and calcitonin. Vitamin D affects bone tissue through its ability to regulate the body's absorption of calcium and phosphate, while estrogens seem to influence the global skeletal mineral content in females. Trabecular bone exhibits a higher remodelling rate than cortical bone and demonstrates an impressive adaptation potential with respect to external loading conditions. Pathological loading associated with space flight, heavy exercise, surgical treatments or osteoarthritis has proven to induce significant changes in morphological and mechanical properties of trabecular bone.

Composition The organic matrix of bone contains 90% collagen and 10% ground substance, essentially glycoproteins and glycosaminoglycans. The mineral phase comprises hydroxyapatite crystals of 5 to 10 nanometers long and amorphous calcium phosphate. Mineralization of human bone increases from birth to

	Water $[mg/cm^3]$	Organic $[mg/cm^3]$	Ash $[mg/cm^3]$	Total $[mg/cm^3]$
Human	270	497	1076	1924
Dog	292	507	1049	1911
Monkey	271	514	1011	1878
Bovine	281	514	1067	1930

Table 2.1: Density of the main constituents of trabecular bone in human and other mammals. From Gong et al. [56].

the sixth or seventh decade and declines afterwards, while water content follows the inverse path. The organic fraction remains approximately constant throughout life [101]. A pathological reduction in bone tissue mineralization is designated

by osteomalacia. Trabecular bone shows a similar composition as cortical bone, but appears to be a few percent less mineralized [56].

Porosity Trabecular bone is often considered as a two-phase porous structure: a bone and a marrow phase. Porosity is the volume proportion of the marrow phase and the value of 0.3 is sometimes used as an objective criterion to distinguish cortical from trabecular tissue. Relative or structural density ρ_s is the volume proportion of the bone phase and constitutes the complementary notion of porosity. The useful concept of apparent density ρ_a is defined as the weight of the bone phase divided by total volume, while apparent ash density is the weight of ash divided by the same total volume. Osteoporosis is characterized by a reduction in apparent density and not by an alteration of tissue composition [132]. The X-ray absorption properties of the mineral phase allow non-invasive

	Apparent density $[mg/cm^3]$	Authors
Vertebra	131 - 424	Galante et al. [47]
Tibia	90 - 600	Hvid et al. [72]
Femur	160 - 950	Lotz et al. [95]
Ilium	109 - 959	Dalstra et al. [41]

Table 2.2: Range of apparent density for trabecular bone in a few locations of the human skeleton.

and accurate evaluation of apparent ash density in trabecular bone by quantitative computed tomography (QCT) or dual energy X-ray absorptiometry (DEXA) [48, 63]. Structural and apparent density can thus be estimated *in vivo* under the assumption of normal and homogeneous tissue composition.

2.2 Morphology

2.2.1 Description

Light and scanning electron microscopy reveal striking variations in the trabecular meshwork and emphasize the anisotropic and inhomogeneous nature of cancellous bone (Fig. 2.2). The finest classification of trabecular morphology was elaborated

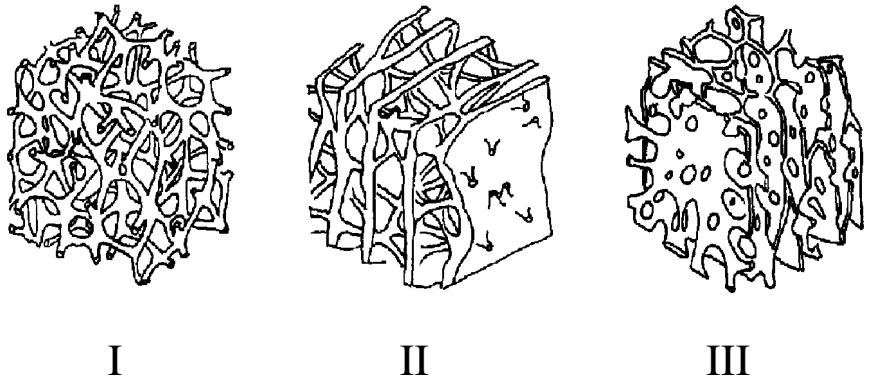

Figure 2.2: Morphological types of trabecular bone. From Singh [120].

by Singh, who distinguished three main types of structure [120]:

- Type I constituted exclusively of fine straight or curved rods $0.08-0.14mm$ in diameter and about $1mm$ in length. The rods become thicker towards the ends, where they connect to form a meshwork with low structural density and without preferred orientation. This type of morphology is found in long bones at the margins of the medullary cavity.

- Type II made up of plates arranged parallel to each other and connected by numerous rods. The plates are $0.16-0.3mm$ thick, a few milimeters long and are separated by a gap of $0.4-0.8mm$. They give the meshwork a well marked orientation. This type of architecture with varying structural density is found next to some articular surfaces such as the distal end of the femur.

- Type III formed entirely of irregular plates $0.12 - 0.24mm$ thick with numerous fenestration. The plates enclose more or less tubular spaces of $0.7 - 2.0mm$ in diameter, which give again a well marked orientation to the meshwork. This type of morphology exhibits varying structural density and is typically found in vertebrae.

Refined analysis reveals a range of intermediary morphologies, but does not suggest the existence of other structural elements.

On the macroscopic scale of whole bones, the preferred orientations of the trabecular meshwork produce a clear pattern of intersecting trajectories (Fig. 2.3) that were drawn for a large number of anatomical locations [105, 125, 64].

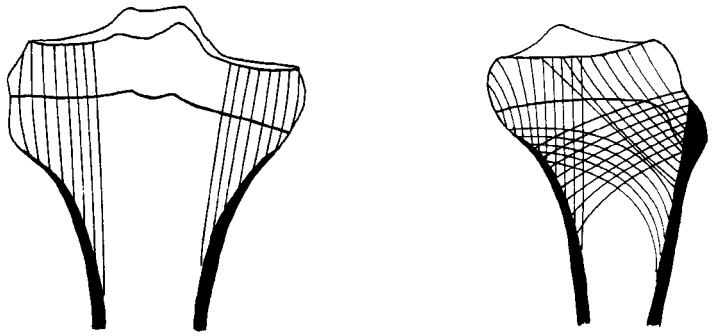

Figure 2.3: Epiphyseal line and trabecular trajectories in the human proximal tibia, coronal (left) and sagittal (right) views.

2.2.2 Cellular models

The histologic sections and scanning electron microscopy (SEM) images of trabecular bone do not support the hypothesis of material periodicity. However, this simplifying assumption brings some qualitative insights in both morphology and biomechanical behaviour. Thus, a number of elementary cells were proposed in the literature, which can be classified according to their symmetry group and the morphological types described by Singh (Fig. 2.4).

Each of these elementary cells fills the three-dimensional space and represents an idealized periodic model of the trabecular meshwork:

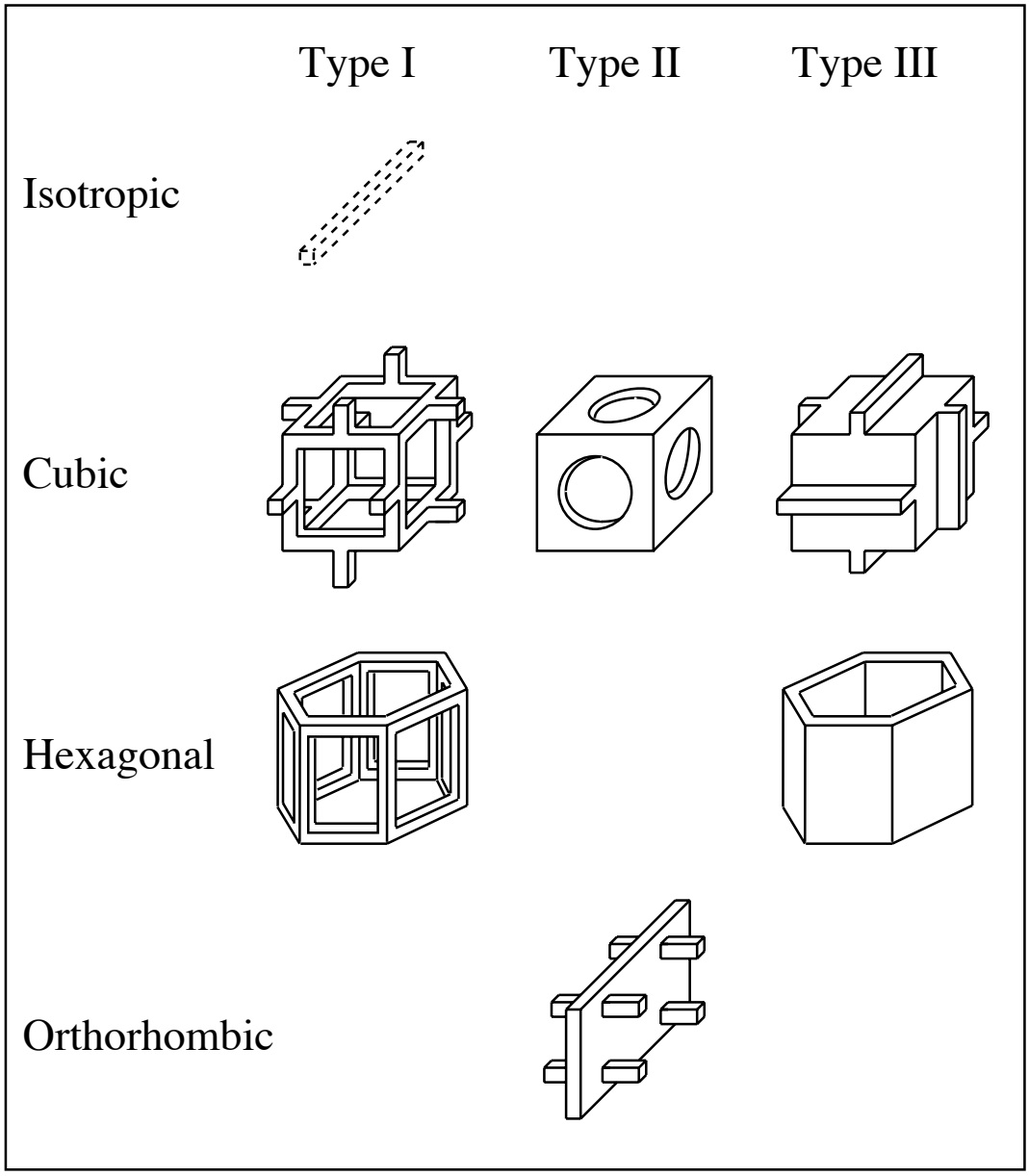

Figure 2.4: Elementary cells of a periodic model for trabecular bone.

- The isotropic model proposed by Christensen is based on a spatial distribution of rods with random orientation and corresponds fairly well to trabecular morphology of type I.
- The orthorhombic model developed by Klever is made of plates with interconnecting rods and is specifically designed for type II morphology [79].
- The closed hexagonal model is a natural generalization of the two-dimensional honeycomb structure studied by Gibson and Ashby and involves the morphologic features of type III [51].

Gibson also proposed cubic, hexagonal and orthorhombic models that may be associated with the rod-rod (type I), respectively the plate-plate (type III) structures [50]. Another interesting model suggested by Beaupré and Hayes is composed of a cubic element containing a spherical cavity [8]. Depending on the size of the cavity, the cell's structural elements can be considered as rods or plates. The three models that belong to the cubic symmetry class can directly be extended to the orthorhombic class by changing the characteristic lengths of the cell.

Structural density of the resulting periodic structures can be easily calculated with respect to cell parameters such as rod or plate thickness t_b and length l_b (Table 2.3).

	Type	Density
Isotropic	I	$\rho_s \div (\frac{t_b}{l_b})^2$
Cubic	I	$\rho_s \div (\frac{t_b}{l_b})^2$
	III	$\rho_s \div (\frac{t_b}{l_b})$
Hexagonal	I	$\rho_s \div (\frac{t_b}{l_b})^2$
	III	$\rho_s \div (\frac{t_b}{l_b})$
Orthorhombic	II	$\rho_s \div (\frac{t_b}{l_b})$

Table 2.3: Summary of the relationships between aspect ratio of the cellular rod or plate element t_b/l_b and structural density ρ_s for several morphologic models. These relations are exact in the limit of small aspect ratios.

2.2.3 Stereology

Since properties of trabecular bone volumes containing a large number of trabeculae are also of interest, morphological analysis should be extended to the macroscopic scale. For a non-periodic structure such as real trabecular bone, a continuum assumption needs to be done and averaged or "homogeneized" properties defined on a statistical basis. Using a one-dimensional probabilistic approach, Harrigan et al. showed that the continuum assumption for trabecular bone is valid from a representative length of three to five intertrabecular spaces i.e. ($\simeq 2.4 - 4mm$) [60].

Surface and structural density Beside structural density sometimes written V_b, surface density S_V is another macroscopic parameter defined as the surface area of the interface between bone and bone marrow per unit total volume. Surface density corresponds to the potential area for osteoblast and osteoclast activity per unit total volume and constitutes an important parameter for bone remodelling [99].

Stereology represents a group of mathematical methods for estimating such three-dimensional morphological parameters from two-dimensional measurements performed on histological sections [133]. According to the principles of Delesse and Buffon, structural and surface density can be estimated from analogous two-dimensional definitions:

$$V_b \simeq A_b \tag{2.1}$$

$$S_V \simeq \frac{4}{\pi} B_A \tag{2.2}$$

where A_b is the relative area of the bone phase and B_A the boundary length of the interface per unit area in the section.

The stereological data shown in Fig. 2.5 confirm the geometrical fact that the surface per unit bone volume decreases with structural density and suggest the higher sensitivity of highly porous bone with respect to remodelling activity. Furthermore, the data demonstrate the broad distribution of stereological parameters in the trabecular structure and emphasize the statistical difficulty to detect subtle morphological changes.

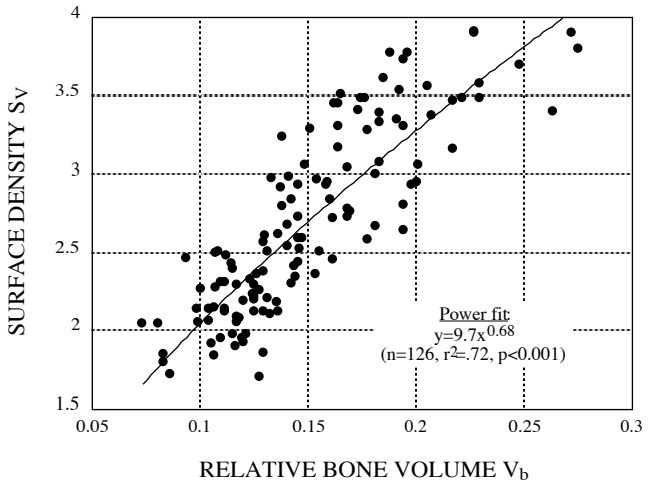

Figure 2.5: Surface versus structural density of trabecular bone from the human proximal tibia. From Zysset et al. [141].

For the elementary cells described in Fig. 2.4, it can be shown that rod or plate thickness t_b is proportional to the ratio of structural versus surface density in the limit of low aspect ratios:

$$t_b \div \frac{V_b}{S_V} \qquad \text{when} \qquad \frac{t_b}{l_b} \to 0 \tag{2.3}$$

where l_b is the characteristic rod or plate length.

Method of directed secants Among other stereological tools, the method of directed secants is a suitable procedure to characterize structural anisotropy. This method consists in projecting an array of equidistant parallel test lines on the two-dimensional sections of the trabecular structure and counting the intersections of the test line with the boundaries between the bone and marrow phases (Fig. 2.6). Mean intercept length in bone is the average length of the test line path inside the bone phase. Since the projection is repeated for different orientations of the structure and the analysis may be repeated in three mutually orthogonal sections, mean intercept length is a function of a unit vector $\boldsymbol{n} \in \mathcal{R}^3$:

$$L_b(\boldsymbol{n}) = 2\frac{A_b}{I_L(\boldsymbol{n})} \tag{2.4}$$

where A_b is the relative area of the bone phase in the considered section and $I_L(\boldsymbol{n})$ is the number of intersections between the test grid and the boundary interface along the direction of $\boldsymbol{n}$.

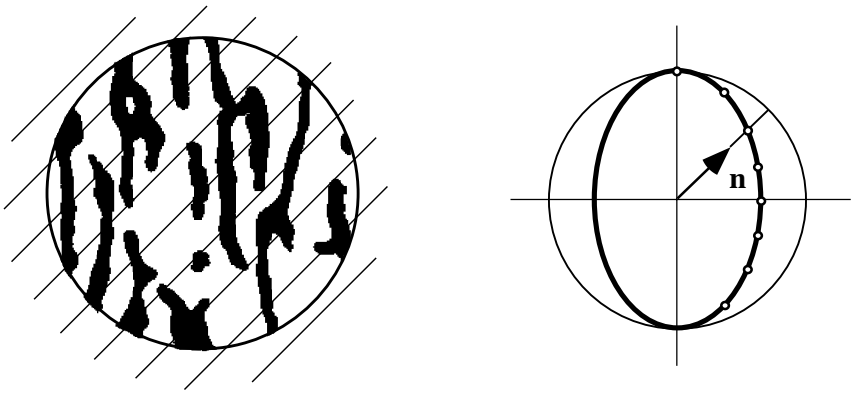

Figure 2.6: Method of directed secants producing a polar plot of mean intercept length.

Since mean intercept length verifies:

$$L_b(\boldsymbol{n}) = L_b(-\boldsymbol{n}) \tag{2.5}$$

the function $L_b(\boldsymbol{n})$ can be replaced by a function $\hat{L}_b(\boldsymbol{N})$ of the second order tensor $\boldsymbol{N} = \boldsymbol{n} \otimes \boldsymbol{n}$ [66].

Isotropy For isotropic structures, mean intercept length is an isotropic function of $\boldsymbol{N}$:

$$\hat{L}_b(\boldsymbol{N}) = \hat{L}_b(\boldsymbol{Q}^T \boldsymbol{N} \boldsymbol{Q}) = c \qquad \forall \boldsymbol{Q} \in \mathcal{O} \tag{2.6}$$

where $\mathcal{O}$ is the orthogonal tensor group and c a constant.

Anisotropy For anisotropic structures, the mean intercept length function becomes anisotropic and can be expanded in a generalized spherical Fourier series [103]:

$$\hat{L}_b(\boldsymbol{N}) = c \cdot 1 + \boldsymbol{C} : \boldsymbol{F}_b(\boldsymbol{N}) + \mathbb{C} :: \mathbb{F}_b(\boldsymbol{N}) + \ldots \tag{2.7}$$

where 1, $\boldsymbol{F}_b(\boldsymbol{N})$ and $\mathbb{F}_b(\boldsymbol{N})$ represent the even ranked tensorial basis and c, $\boldsymbol{C}$ and $\mathbb{C}$ the corresponding even ranked tensorial coefficients.

The first order of this development can be identified with the positive constant c that characterizes isotropy, while the second order is associated with a traceless tensor of rank two $\boldsymbol{C}$, accounting for five constants. Hence, the most general function that can be represented by the first and second orders is ellipsoidal and belongs to the orthorhombic or orthotropic symmetry group. Representation of a function exhibiting cubic symmetry requires terms of higher orders, namely a tensor of rank four.

There is a large experimental evidence that the polar plot of trabecular mean intercept length approximately fits an ellipsoid, and can thus be described by a fabric tensor of rank two [61, 121, 136]. To our knowledge, identification of terms with order higher than two was not reported.

Optical Fourier analysis (ODA) is another method for assessment of trabecular morphology. The method consists in projecting a laser source on a two-dimensional radiograph and perform a double Fourier transform on the resulting picture [104]. A recent ODA study suggests that a more general symmetry group than orthotropy may be found in vertebral bone [104]. This finding corroborates previous observations according to which orthogonal intersections of trabecular trajectories and thus orthotropic symmetry is not always the rule [120, 136].

2.3 Biomechanical behaviour

Due to clinical motivations oriented towards *in vivo* environments, fresh or fresh frozen human bone was presumed to be most suitable for mechanical testing, but fresh or fresh frozen bovine bone was found to be a reasonable model for qualitative investigations. All the results presented in this section deal with fresh or fresh frozen bone tested in wet conditions.

The principal experiments identifying the mechanical behaviour of trabecular bone were often limited to unconfined one-dimensional compressive or tensile tests (Fig. 2.7). The one-dimensional mechanical behaviour is characterized by a relationship between applied stress, the force divided by the area of the undeformed section, and strain, the relative displacement measured on the specimen.

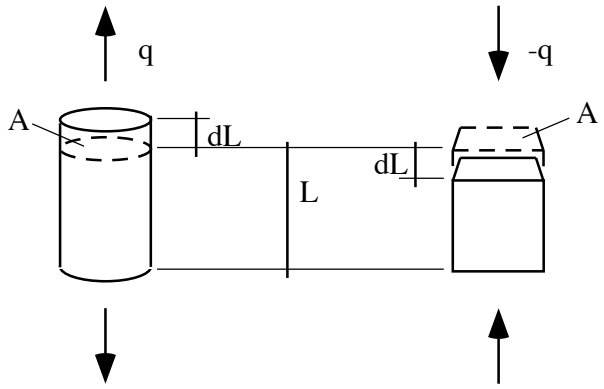

Figure 2.7: Uniaxial tensile and compressive testing of cubic or cylindrical bone specimens.

2.3.1 One-dimensional mechanics

Quasistatic behaviour The one-dimensional quasistatic stress-strain curve shown in Fig. 2.8 is rather different in tension and compression. In tension, the response is approximately linear elastic up to rupture which is characteristic of a brittle material. In compression the response involves an approximately linear part ended by a yield point followed by an nonlinear part that reaches a maximum in stress magnitude and decreases to an almost constant value. At large strains, the compressive stress magnitude increases again due to contacting of crushed trabeculae and this phenomenon is designated as densification. Such a behaviour is characteristic of an elastic-plastic material with nonlinear hardening and locking effect.

The linear relationship between stress and strain provides Young's elastic modulus ϵ, while maximum tensile and compressive stresses born by the specimen are defined as tensile σ_{u+} and compressive σ_{u-} strengths. A Poisson's ratio characterizes the relative lateral contraction or dilatation of the specimen for tensile, respectively compressive tests.

Despite substantial artefacts, one-dimensional compression tests have been the object of considerable refinements as non-destructive procedures [90, 89]. Cyclic loading in the linear part of the stress-strain curve leads to a steady state after a number of conditioning cycles and the elastic modulus as well as elastic energy were measured with a fair reproducibility [94, 92].

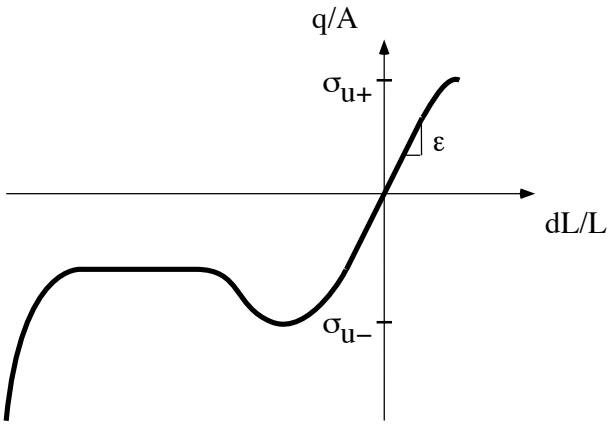

Figure 2.8: One-dimensional quasistatic stress-strain curve for trabecular bone.

In destructive tests, proportionality was systematically found between Young's modulus and strength [112].

According to Brear et al. the influence of increasing temperature from 21^0C to 37^0C reached reductions of 7% for Young's modulus and 13% for strength [14].

Artefacts Such one-dimensional identifications of trabecular bone properties rely implicitely on the assumption of material, strain and stress homogeneity made in continuum mechanics. At the microscopic level, trabecular bone is not homogeneous and the application of a continuum theory deserves caution.

The displacements and forces applied to the specimen constrain a finite number of trabeculae and the boundary conditions are thus highly inhomogeneous. According to Saint-Venant's principle the effect of irregular boundary conditions on the strain and stress field is negligible at a sufficient distance from the boundary (Fig. 2.9). Therefore, both specimen length L and width W should be much larger (at least an order of magnitude) than the representative trabecular length δ:

$$L \gg \delta \qquad W \gg \delta \tag{2.8}$$

In fact, boundary effects associated with strain and stress inhomogeneity are due to material inhomogeneity and experiments should be done on specimen with smallest dimension much larger than the representative length of the trabeculae

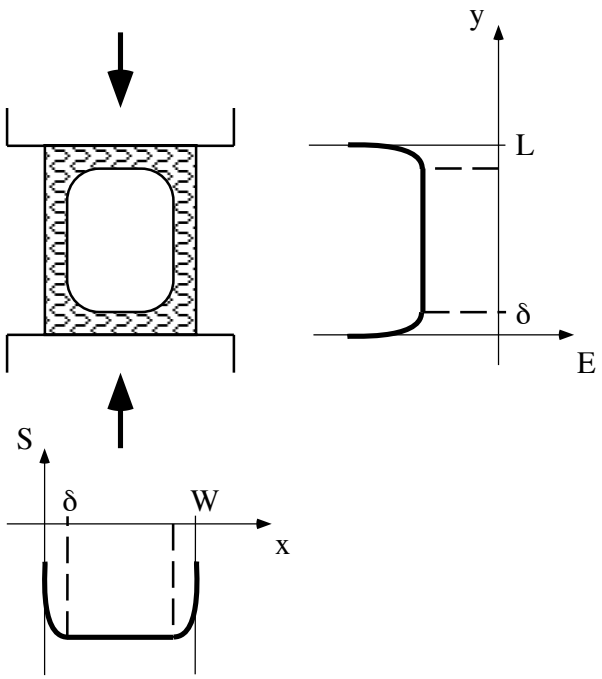

Figure 2.9: Compressive experiments of a trabecular bone specimen with the boundary effects associated with strain and stress inhomogeneity.

for the continuum assumption to hold (c.f. Section 2.2):

$$min(L, W) \gg \delta \tag{2.9}$$

However, this theoretical restriction is difficult to respect in practice, since trabecular bone exhibits varying structural density and does not extend more than a few centimeters in the human or bovine skeleton. Therefore, most investigators tested specimens with dimensions ranging between 5 and $20mm$ and neglected the often important effects of material inhomogeneity.

There is clear experimental evidence, that strain inhomogeneities occur at the specimen ends and that material constants such as Young's modulus and strength measured in these conditions are significantly influenced by the specimen size [6, 77, 91, 102]. In addition, disturbing friction effects between bone and testing plattens were noticed. A standard cylindrical geometry with an aspect ratio of 2:1 and a diameter of 5mm was recently proposed by Keaveny to minimize these artefacts and standardize future mechanical tests [77]. It should be noted

that the same recommendation was already made by Schoenfeld in 1974 [116]. Nevertheless, strain inhomogeneities due to both boundary effects and friction can be avoided by excluding the critical zone from the strain measurement zone like in standard material testing procedures.

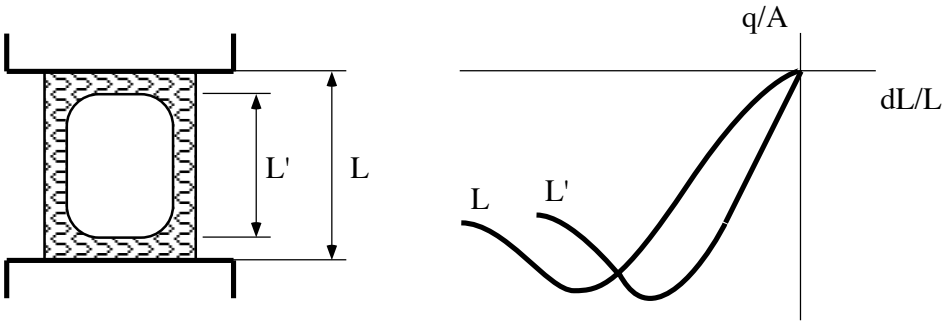

Figure 2.10: Stress-strain curves of one-dimensional quasistatic tests including (L) and not including (L') the specimen's ends. From Zysset et al., unpublished data.

To our knowledge, stress inhomogeneities were not investigated yet, but we suspect a boundary layer of the specimen section to be subjected to a lower stress than the central part (Fig. 2.9). This effect would lead to an underestimation of the applied stress and thus of both elastic modulus and strength. A simple correction of this effect would consist of assuming the existence of a boundary layer that does not contribute to the internal forces acting in the specimen and calculate an effective section for the assessment of stress.

To conclude, one-dimensional tests should not include the specimen ends for strain measurement and take into account stress inhomogeneities for precise identification of material constants.

Distribution of mechanical properties As shown in Table 2.4, distribution of Young's modulus and strength according to anatomical location is extremely broad and corresponds to some extent to an amplified distribution of apparent density [9, 15, 55, 54, 96].

Relation to apparent density In fact, both elastic modulus and strength are found to follow a power function of apparent or structural density [47, 21, 5].

	Modulus $[MPa]$	Strength $[MPa]$	Authors
Vertebra	10 - 428	0.06 - 15	Struhl et al. [123]
Tibia	4 - 430	1 - 13	Goldstein et al. [55]
Femur	7.6 - 800	0.56 - 18.6	Ciarelli et al. [28]
Ilium	5 - 282	0.12 - 8.2	Struhl et al. [123]

Table 2.4: Range of mechanical properties for trabecular bone in a few locations of the human skeleton.

Depending on specimens size, aspect ratio, anatomical location, orientation, and testing procedure the exponent of this power relationship ranges from 1 to 3, while the squared coefficient of determination reaches sometimes 0.9. The remaining variability of mechanical properties can be attributed to tissue mineralization or microstructural features [112].

A statistical review of these results suggests that both elastic modulus and strength vary as the square of structural density and that the constants of the model are somewhat different in human and bovine bone [112].

$$\epsilon = \epsilon_c \rho_s^2 \tag{2.10}$$

$$\sigma_u = \sigma_{u_c} \rho_s^2 \tag{2.11}$$

A direct consequence of these power relationships, which is essential for clinicians, is the dramatic decrease of strength in osteoporotic trabecular bone. As another important consequence, elastic modulus and strength of trabecular bone can be directly estimated *in vivo* by non-invasive methods such as QCT or DEXA [95, 63, 72].

Tissue modulus The natural question emerges whether extrapolation of these power functions provides the correct modulus and strength for cortical bone, in other words if cortical bone can be considered mechanically as dense trabecular bone. The answer appears to be negative, the mechanical properties of cortical bone being seriously underestimated by such an extrapolation [112]. Attempts to measure the elastic modulus of single trabeculae furnished results ranging

between 0.76 to 12.7 GPa (Table 2.5), thus substantially lower than cortical bone ($6 - 28$ GPa) [111]. The broad distribution of the data may be attributed to

	Bone	Modulus $[GPa]$	Authors
Ultrasonic	human	12.7 ± 2.0	Ashman et al. [4]
	bovine	10.9 ± 1.6	Ashman et al. [4]
Mechanical	human	11.38	Townsend et al. [128]
		5.3 ± 2.6	Mente and Lewis [98]
		3.17 ± 1.5	Kuhn et al. [86]
	bovine	0.76 ± 0.39	Ryan and Williams [115]

Table 2.5: Elastic modulus for individual trabeculae.

surface imperfections of the specimens as well as experimental and theoretical limitations of mechanical testing at this scale.

Postyield behaviour Mechanical behaviour under large strains was studied by Hayes and Carter, who performed confined compressive tests of bovine specimens up to 75% strain. They showed that the mechanism for energy absorption was primarily buckling and fracture of trabeculae and emphasized the importance of the energy absorption capacity of trabecular bone in this regime [62].

Another study conducted by Carter et al. demonstrated that strength of trabecular bone was comparable in tension and compression, but that energy absorption was much lower in tension than in compression [23]. However, Kaplan et al. found that tensile strength was 40% lower than compressive strength in bovine trabecular bone [74]. The problem of symmetry between tensile and compressive strength seems not to be definitively settled.

Surprisingly, no information is available about the reversible and irreversible aspects of the one-dimensional stress-strain curve. The definition of the yield stress σ remains vague, the nature of the nonlinear stress-strain relationship was not identified and the unloading curve following a monotonic loading beyond the yield point was not characterized. Permanent plastic deformations and damage,

i.e. progressive reduction of the elastic modulus due to accumulation of microdefects, were hardly mentioned (Fig. 2.11).

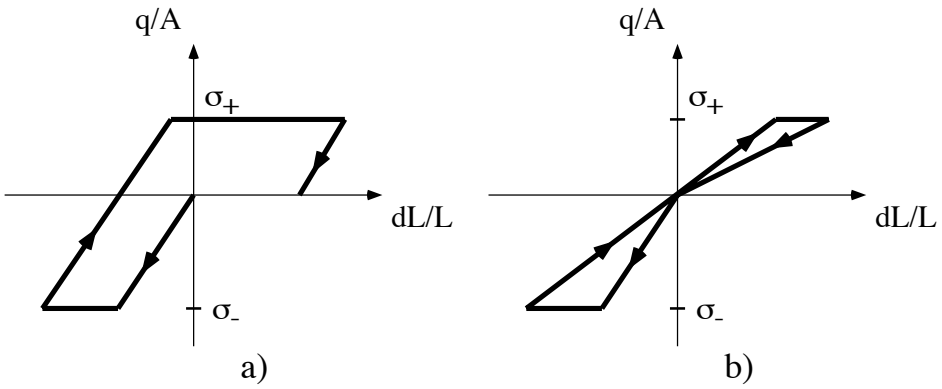

Figure 2.11: a) Perfect plastic behaviour for a strain-driven loading cycle. b) Perfect damage behaviour for a strain-driven loading cycle.

Viscoelasticity Beside quasistatic properties, interest grew also in the viscous or rate-dependent mechanical properties. Galante et al. reported a decrease of 24% in the regression slope relating compressive strength to apparent density for one-dimensional tests at strain rate $0.017s^{-1}$ when compared to tests at strain rate $0.00017s^{-1}$ [47]. Using a viscoelastometer, Pugh et al. measured the time-dependent properties of human specimens by one-dimensional sinusoidal loading and concluded that trabecular bone behaves purely elastically for strain rates between 0.001 and $0.03s^{-1}$ [107]. Hence, they rejected the hypothesis that bone marrow plays a hydraulic strengthening role (Fig. 2.12).

A few years later, Carter and Hayes performed confined compressive tests with strain rates ranging from 0.001 to $10s^{-1}$ and reported that both modulus ϵ and strength σ_u were proportional to a weak power law of strain rate $\dot{E}$ [20]:

$$\epsilon = \epsilon_c \dot{E}^{0.06} \tag{2.12}$$

$$\sigma_u = \sigma_{u_c} \dot{E}^{0.06} \tag{2.13}$$

where ϵ_c and σ_{u_c} are material constants.

This result was recently confirmed by Linde et al. for strain rates ranging between 0.0001 and $10s^{-1}$. They obtained exponents of 0.05 for elastic modulus

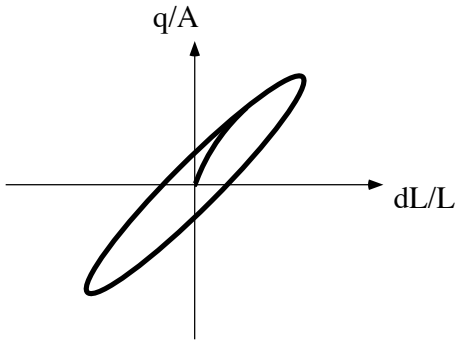

Figure 2.12: Stress-strain curve of a linear viscoelastic material subjected to sinusoidal loading cycles.

and 0.07 for strength, but pointed out that linear models were statistically better and more realistic in the extrapolation to infinite low strain rate [93].

$$\epsilon = \epsilon_{c_1} + \epsilon_{c_2}\dot{E} \tag{2.14}$$

$$\sigma_u = \sigma_{u_{c1}} + \sigma_{u_{c2}}\dot{E} \tag{2.15}$$

where ϵ_{c_1} and $\sigma_{u_{c1}}$ are the quasistatic modulus and strength.

Linde et al. concluded that for strain rates applied in conventional testing i.e. $0.001 - 0.01s^{-1}$, viscosity had little influence on stiffness and strength when compared to other factors. A nonlinear viscous model of trabecular bone as for instance the Ramberg-Osgood equation used for cortical bone seems not to have been proposed yet [67].

It should be noted that for a solid, the observed dependence of the elastic modulus upon strain rate is in contradiction with the second axiom of thermodynamics [12]. This paradox is most probably due to an inappropriate formulation of the rate-dependent aspect of the constitutive law and the resulting experimental definition of the elastic modulus.

Due to the absence of marrow constriction in unconfined one-dimensional tests, some investigators believe that substantial hydraulic strengthening of bones occur *in vivo* at high strain rates, for instance at impact loading, but experimental data supporting this hypothesis are sparse [73].

Creep An investigation of creep was attemped by Zilch et al., who restricted their interest to viscoelasticity and did not apply sufficient load to observe plastic or damage phenomena [140].

Further compression experiments done by Bowman et al. [13] exhibited the classical three stages of creep associated with viscoplasticity and revealed a relationship between time of failure T_f and initial normalized stress level S according to the law of Norton (Fig. 2.13a):

$$T_f = T_c(\frac{S}{\epsilon})^k \tag{2.16}$$

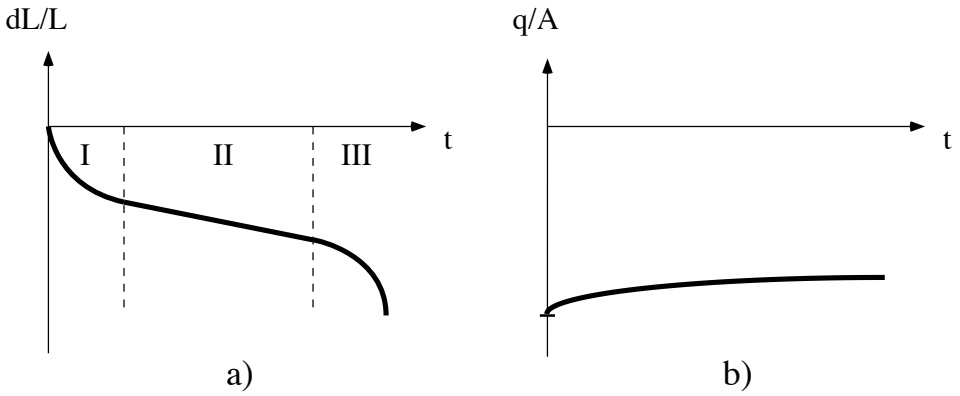

Figure 2.13: a) Compressive creep behaviour including the primary, secondary and tertiary stage. b) Compressive stress relaxation behaviour.

Stress relaxation Schoenfeld et al. performed compressive stress relaxation tests at 37^0C and obtained approximately 15% decay of stress in a period of $100s$ for any initial stress (Fig. 2.13b). The corresponding strains were not reported, but the viscous nature of trabecular bone confirmed [116].

Fatigue Fatigue or cycle-dependent behaviour has been thoroughly examined by Guo [58]. Aware of the problems associated with boundary artefacts, he performed a precise identification of the S-N curve for one-dimensional compressive loading of waisted bovine specimens and obtained a similar curve as Caler and

Carter [18] for cortical bone (Fig. 2.14):

$$N_f = N_c(\frac{S}{\epsilon})^l \tag{2.17}$$

where N_f is the number of cycles to failure and S the maximum applied stress.

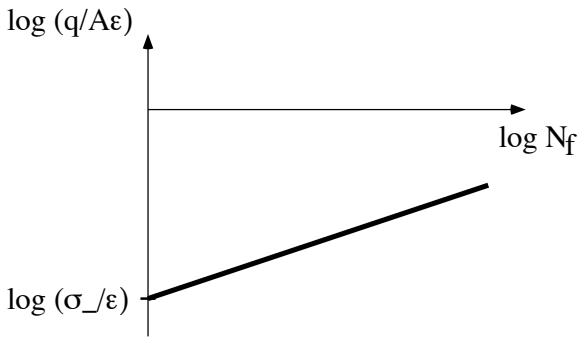

Figure 2.14: Compressive normalized stress versus number of cycles to failure (S-N curve) obtained in fatigue testing of trabecular bone.

2.3.2 Three-dimensional mechanics

Despite a number of open questions and the lack of a unified theoretical model, the one-dimensional behaviour of trabecular bone becomes fairly well understood. However, the strain and stress states encountered in real bone structures are obviously not one-dimensional and a three-dimensional theory is required to describe and quantify the true mechanical behaviour.

Remark 2.1 *The theoretical foundations of three-dimensional continuum mechanics will be exposed in Chapter 3 and this subsection is limited to the principal experimental results.*

Anisotropy of mechanical properties was already observed by pioneering investigators [47] and motivated the carrying of one-dimensional tests in three orthogonal anatomical directions. As shown in Table 2.6, the elastic moduli measured along the dominant direction of the trabeculae are substantially higher than in the other two directions.

Method	Axial $[MPa]$	Coronal $[MPa]$	Sagittal $[MPa]$	Authors
Mechanical	45 - 476	9 - 84	8 - 130	Williams et al. [137]
Ultrasonic	340 - 3350	110 - 1230	140 - 1750	Ashman et al. [5]

Table 2.6: Ranges of elastic moduli measured along the three anatomical directions for specimens retrieved from the human proximal tibia.

Elasticity The description of the three-dimensional linear elastic behaviour of a solid requires a tensor of rank four which involves in general 21 distinct material constants. The hypothesis of orthotropic symmetry supported by quantitative stereology reduces the number of constants to 9.

Development of ultrasonic techniques allowed considerable progress in the identification of the elastic behaviour of trabecular bone, since up to six constants can be consistently measured on a single specimen [5, 131]. The remaining constants can be estimated with lower and upper bounds imposed by thermodynamic restrictions or eventually by Fourier harmonic analysis [66].

Yahia et al. subjected vertebral specimens to hydrostatic pressure and one-dimensional tests in order to identify six elastic constants. Their results were in fair agreement with the previous ultrasonic measurements [139].

An original method to assess the nine elastic constants was explored by Snyder et al., who repeated orthogonal one-dimensional tests on a small cubic specimen extracted from a larger one [121].

Remark 2.2 *As for mechanical tests, inhomogeneity of trabecular bone at the microscale puts a limit on the continuum assumption underlying the calculation of elastic moduli from ultrasonic wave propagation and raise doubts about the accuracy of such a measurement technique. However, little information is available about these potential problems.*

Postyield behaviour The yield point encountered in one-dimensional mechanics becomes a six-dimensional yield surface in three-dimensional modelling.

Stone et al. conducted multiaxial testing of butterfly shaped specimens and

measured shear strengths they attempted to fit on Hoffmann's isotropic yield criterion [122].

An objective anisotropic elastoplastic constitutive law of trabecular bone was developed by Rakotomanana [110]. The model, involving a Hill criterion for perfect plastic flow, was used for several finite element studies [114].

Nevertheless, no experimental program was undertaken to identify this yield surface [33].

Time and cycle dependent properties Rate and fatigue dependent properties were apparently not investigated on a three-dimensional basis.

2.4 Morphology versus biomechanics

2.4.1 Structural models

A first approach to the relationship between morphological and biomechanical properties consists in neglecting the role of the marrow phase and focussing one's attention on microstructural models of the bone phase.

Remark 2.3 *Use of local or cellular models for calculation of global mechanical properties of a microstructure involves a choice of boundary conditions. The correct mathematical formulation of the problem, as done in homogeneization techniques, consists of prescribing periodicity for strain and aperiodicity for stress at the cell boundary. Application of homogeneous displacements, or forces, do not necessarily verify the exact boundary conditions and lead to an overestimation, respectively an underestimation, of the structure's stiffness.*

The early finite element model of Pugh et al. modelling the first trabecular layer beneath a subchondral plate suggested that bending and buckling were major components of the elastic deformation of the structure [109]. They stated also that due to the inhomogeneous load distribution, fatigue failure may necessarily occur in specific trabeculae.

Williams et al. developed another two-dimensional finite element model representing the exact morphology of a cubic trabecular specimen [137]. They obtained an approximate correspondance between the experimental orthogonal elastic moduli of the specimen and the values predicted by the model.

A three-dimensional finite element model by Beaupré and Hayes representing a cubic elementary cell with a spherical void lead also to an overestimation of the elastic modulus, partly due to the uniaxial deformation mode of the trabeculae associated with vertical alignment of the cells [8].

Using a low-density isotropic model corresponding to trabecular bone morphology of type I, Christensen assumed axial deformation of randomly oriented rods and calculated the elastic modulus, Poisson ratio and hydrostatic strength with respect to structural density. He claimed that best mechanical performance, i.e. highest stiffness and strength of a low-density structure is achieved by axial compression instead of bending of the rods [27].

Klever conceived a comprehensive analytical and numerical model of an orthorhombic cell of morphologic type II [79]. Including perfect plasticity of the beams in a two-dimensional finite element model of the cell, he obtained stress-strain curves for monotonic uniaxial and shear loading. He found that rods were more likely to fail by plastic yielding rather than by buckling.

Motivated by the mechanics of foams, Gibson and Ashby proposed a number of cellular models belonging to morphologic type I to III, often distinguished by open or closed interfaces [50]. Applying classical beam and plate theory they analysed the elastic deformation modes of these elementary cells and calculated the apparent elastic modulus in terms of structural density. They investigated also collapse of the cells and mentioned elastic buckling, plastic yielding and brittle fracture as the main mechanisms underlying the macroscopic postyield behaviour. Recently, they proposed a three-dimensional yield criterion based on these respective mechanisms for a cubic cell [52].

The theoretical relationships between structural density and mechanical properties are summarized in Table 2.7. In particular, the predictions of elastic modulus and strength involve power functions with exponent ranging between 1 and 3 and coincide thus with the spectrum of experimental results mentioned in Section

2.3. No theoretical bounds are mentioned for these exponents.

Using a two-dimensional finite element model of a honeycomb structure, Guo demonstrated the qualitative strain localization process preceeding fatigue failure of trabecular bone [58]. Crack propagation in single trabeculae and progressive number of brittle trabecular fractures help explain the accumulation of damage and the reduction in elastic modulus of the structure.

2.4.2 Homogeneization

Another approach of the relationship between morphological and biomechanical properties consists in solving the exact local boundary value problem for an elementary cell in a periodic lattice and deduce the macroscopic materials constants from the resulting average or apparent stress-strain fields. This procedure developed by mathematicians is called homogeneization [35].

The first attempt to apply homogeneization theory to trabecular bone is due to Hollister et al. [69]. They used finite element modelling to solve the boundary value problem for three elementary cubic cells (Fig. 2.15). First, they confirmed

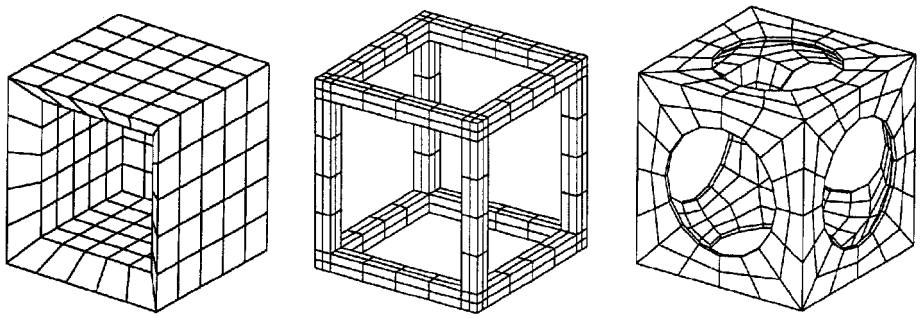

Figure 2.15: Finite element models of three elementary cells used for homogeneization calculation of trabecular bone. From Hollister et al. [69]

that the power law fit between structural density and apparent elastic moduli was strongly dependent on morphological type. In fact, connectivity or alignment of the elementary cells promotes either bending or uniaxial stress and influences the power law relationships according to the previously described structural models (Table 2.7). Second, they showed that fluctuation of local strain energy density

Model	Type	Direction	Mode	Relation	Authors
Isotropic	I		uniaxial	$\epsilon \div \rho_s$	Christensen [27]
				$\nu = const.$	
Cubic	I		buckling	$\sigma \div \rho_s^2$	Gibson [51]
			bending	$\epsilon \div \rho_s^2$	
				$\nu = const.$	
			buckling	$\sigma \div \rho_s$	
			plastic	$\sigma \div \rho_s^{3/2}$	
			brittle	$\sigma \div \rho_s^{3/2}$	
	III		bending	$\epsilon \div \rho_s^3$	Gibson [51]
			buckling	$\sigma \div \rho_s^3$	
			plastic	$\sigma \div \rho_s^2$	
Hexagonal	I	axial	uniaxial	$\epsilon \div \rho_s$	Gibson [51]
			buckling	$\sigma \div \rho_s^2$	
			plastic	$\sigma \div \rho_s$	
		transverse	bending	$\epsilon \div \rho_s^2$	
			plastic	$\sigma \div \rho_s^2$	
	III	axial	uniaxial	$\epsilon \div \rho_s$	Gibson [51]
			buckling	$\sigma \div \rho_s^3$	
			plastic	$\sigma \div \rho_s$	
		transverse	bending	$\epsilon \div \rho_s^3$	
			plastic	$\sigma \div \rho_s^3$	
Orthorhombic	II	axial	uniaxial	$\epsilon \div \rho_s$	Gibson [51]
		coronal	bending	$\epsilon \div \rho_s^3$	
		sagittal	bending	$\epsilon \div \rho_s^3$	

Table 2.7: Summary of theoretical relations between mechanical properties and structural density according to morphologic type, loading direction and mode of deformation. ρ_s is structural density, ϵ the elastic modulus, ν Poisson's ratio and σ the yield stress.

(SED) around the apparent value was also dependent on microstructure and increased with porosity. The limitation of SED prediction in highly porous bone using a continuum model was thus pointed out. Finally, the authors cited the growing need for microstructural analysis and extension of homogeneization theory to quasiperiodic materials in order to improve its applicability to trabecular bone.

Homogeneization appears as a promising tool to evaluate the interaction between remodelling processes occurring at the microscopic level and the apparent stress-strain fields determining the global mechanical behaviour of bone or bone-implant structures.

2.4.3 Continuum mechanics

A third approach to the relationship between morphology and biomechanical behaviour of trabecular bone considers all properties at the continuum level and suggests models relating macroscopic parameters.

One-dimensional model The similar power fit relations obtained for elastic modulus and strength with respect to structural density suggests that one-dimensional trabecular bone mechanics may be formulated in terms of normalized stress:

$$\hat{S} = \frac{S}{\epsilon} \tag{2.18}$$

This adimensional variable allows expression of strength and other stress parameters used in plasticity, creep or fatigue modelling independently from structural density [13, 58]. In the case of linear elasticity $\hat{S}$ represents elastic strain and yield strain associated with yield stress turns out to be constant:

$$\hat{\sigma} = \frac{\sigma}{\epsilon} = \delta_\sigma \tag{2.19}$$

Nevertheless, the constants obtained with this normalization hold only for a specific microstructure and anatomical direction.

While relationships between one-dimensional mechanical properties and structural density remain somewhat simplistic and fragmentary, the formulation of

three-dimensional mechanics with respect to anisotropic morphology offers a complex but wide modelling field.

Three-dimensional model Cowin et al. chose the mean intercept length function as an average measure of morphology and retained a fabric tensor of rank two $\boldsymbol{M}$ on the basis of previous experimental results [31].

$$\boldsymbol{M} = \boldsymbol{K}^{-\frac{1}{2}} \tag{2.20}$$

where $\boldsymbol{K}$ is defined by mean intercept length through:

$$\frac{1}{L_b^2(\boldsymbol{N})} = \boldsymbol{N} : \boldsymbol{K} \tag{2.21}$$

and $\boldsymbol{N} = \boldsymbol{n} \otimes \boldsymbol{n}$ is the second order tensor defined in Subsection 2.2.3.

Assuming that anisotropy of trabecular bone was entirely contained in the fabric, they proposed general forms for the stress-strain law $\boldsymbol{S}$ and the Tsai-Wu yield surface function y:

$$\boldsymbol{S} = \boldsymbol{S}(\rho_s, \boldsymbol{E}, \boldsymbol{M}) \tag{2.22}$$

$$y = y(\rho_s, \boldsymbol{E}, \boldsymbol{M}) = 1 \tag{2.23}$$

by the requirement that $\boldsymbol{S}$ and y are isotropic functions of ρ_s, $\boldsymbol{E}$ and $\boldsymbol{M}$:

$$\boldsymbol{Q}^T \boldsymbol{S}(\rho_s, \boldsymbol{E}, \boldsymbol{M}) \boldsymbol{Q} = \boldsymbol{S}(\rho_s, \boldsymbol{Q}^T \boldsymbol{E} \boldsymbol{Q}, \boldsymbol{Q}^T \boldsymbol{M} \boldsymbol{Q}) \qquad \forall \boldsymbol{Q} \in \mathcal{O} \tag{2.24}$$

$$y(\rho_s, \boldsymbol{E}, \boldsymbol{M}) = y(\rho_s, \boldsymbol{Q}^T \boldsymbol{E} \boldsymbol{Q}, \boldsymbol{Q}^T \boldsymbol{M} \boldsymbol{Q}) = 1 \qquad \forall \boldsymbol{Q} \in \mathcal{O} \tag{2.25}$$

where $\mathcal{O}$ is the orthogonal tensor group.

They calculated the approximate nine orthotropic elastic constants and the twelve constants characterizing the orthotropic yield surface as polynomial functions of structural density and eigenvalues m_i of the fabric tensor.
For elasticity:

$$\epsilon_i = c_1 + c_2 \rho_s^2 + (c_3 + c_4 \rho_s^2) m_i + (c_5 + c_6 \rho_s^2) m_i^2 \tag{2.26}$$

$$\mu_{ij} = c_7 + c_8 \rho_s^2 + (c_9 + c_{10} \rho_s^2)(m_i + m_j) + (c_{11} + c_{12} \rho_s^2)(m_i^2 + m_j^2) \tag{2.27}$$

where ϵ_i is Young's modulus in the direction i and μ_{ij} the shear modulus in the plane defined by directions i and j. As expected, the direction of maximum stiffness corresponds to the direction of maximum mean intercept length.
As shown by Snyder et al. and Turner et al., this model provided reasonable predictions of three-dimensional elastic properties in both bovine and human trabecular bone [121, 131]. The proposed yield criterion could not be validated since no experimental data was available.

Chapter 3

Theoretical models

In this chapter, the framework of continuum mechanics and thermodynamics of irreversible processes is summarized and original constitutive laws for trabecular bone are formulated in one- and three-dimensional spaces.

3.1 Continuum mechanics background

Continuum mechanics aims at describing motion of continuous deformable bodies by means of the force, moment and energy balance principles as well as constitutive laws relating the kinematic to the dynamic aspects. The hypothesis of continuity presumes that the dimensions of the bodies are sufficiently large with respect to their microscopic structure.

3.1.1 Definitions

Kinematics In the material or Lagrangian description chosen for our purposes, each particle of a body $\mathcal{B}$ is labelled by its reference position $\boldsymbol{x}$ at $t = 0$. The present deformed position $\boldsymbol{y}$ at time t of each particle is defined by a map of the reference position $\boldsymbol{x}$:

$$\boldsymbol{y} = \boldsymbol{y}(\boldsymbol{x}, t) \qquad with \qquad \boldsymbol{y}(\boldsymbol{x}, 0) = \boldsymbol{x} \tag{3.1}$$

The map $\boldsymbol{y}(\boldsymbol{x}, t)$ transforming the reference configuration Ω_0 of the body $\mathcal{B}$ into the present configuration Ω is called motion or deformation.

The associated displacement is defined as:

$$\boldsymbol{u} = \boldsymbol{u}(\boldsymbol{x}, t) := \boldsymbol{y}(\boldsymbol{x}, t) - \boldsymbol{x} \tag{3.2}$$

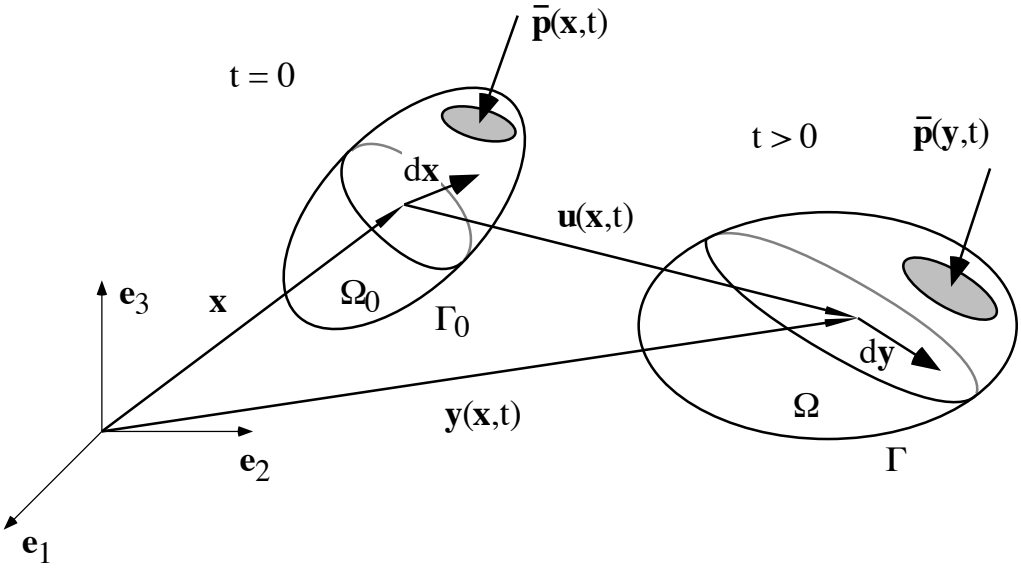

Figure 3.1: Reference and present configurations used in the Lagrangian description.

The deformation of an infinitesimal material fiber $d\boldsymbol{x}$ is given by:

$$d\boldsymbol{y} = \boldsymbol{F} d\boldsymbol{x}$$

where $\boldsymbol{F}$ is the asymmetric deformation gradient:

$$\boldsymbol{F} = \boldsymbol{F}(\boldsymbol{x}, t) := \nabla \boldsymbol{y} = \frac{\partial \boldsymbol{y}}{\partial \boldsymbol{x}}(\boldsymbol{x}, t) \tag{3.3}$$

The displacement gradient $\boldsymbol{H}$ is defined as:

$$\boldsymbol{H} = \boldsymbol{H}(\boldsymbol{x}, t) := \nabla \boldsymbol{u} = \boldsymbol{F} - \boldsymbol{I}$$

The rates of the deformation and displacement gradients are equal:

$$\dot{\boldsymbol{F}} = \nabla \dot{\boldsymbol{y}} = \frac{\partial^2 \boldsymbol{y}}{\partial \boldsymbol{x} \partial t}(\boldsymbol{x}, t) = \dot{\boldsymbol{H}} \tag{3.4}$$

An objective (indifferent to a rigid body motion) measure of deformation is given by the symmetric Green-Lagrange material strain tensor:

$$\boldsymbol{E} = \boldsymbol{E}(\boldsymbol{x}, t) := \frac{1}{2}(\boldsymbol{F}^T\boldsymbol{F} - \boldsymbol{I}) = \frac{1}{2}(\boldsymbol{H} + \boldsymbol{H}^T + \boldsymbol{H}^T\boldsymbol{H}) \tag{3.5}$$

For small deformations ($\|\boldsymbol{E}\| \ll 1$):

$$\boldsymbol{E} \simeq \frac{1}{2}(\boldsymbol{H} + \boldsymbol{H}^T)$$
$$\dot{\boldsymbol{E}} \simeq \frac{1}{2}(\dot{\boldsymbol{H}} + \dot{\boldsymbol{H}}^T)$$

Dynamics The external forces supposed to act on the solid are divided into body and contact forces. They are assumed to be continuously distributed over Ω_0 and Γ_0^p respectively. The present body and inertia force densities are defined per unit volume of the reference configuration:

$$\begin{aligned} \boldsymbol{b} &= \boldsymbol{b}(\boldsymbol{x}, t) \\ \rho\ddot{\boldsymbol{y}} &= \rho(\boldsymbol{x}, t)\ddot{\boldsymbol{y}}(\boldsymbol{x}, t) \end{aligned}$$

where $\rho(\boldsymbol{x}, t)$ is the material density defined in the reference configuration Ω_0. The present contact forces are characterized by a nominal stress vector defined per unit reference area:

$$\boldsymbol{p} = \boldsymbol{p}(\boldsymbol{x}, t)$$

The set of external forces is then assumed to produce internal contact forces $d\boldsymbol{q}$ on the surface $\partial\omega_0$ of any part $\omega_0 \subseteq \Omega_0$ again represented by a nominal stress vector $\boldsymbol{p}$ defined per unit area of the reference configuration, which depends only on the surface orientation:

$$d\boldsymbol{q} = \boldsymbol{p}(\boldsymbol{x}, t, \boldsymbol{n}(\boldsymbol{x}))dA$$

where $\boldsymbol{n}(\boldsymbol{x})$ refers to the outward unit normal to the surface $\partial\omega_0$ and dA to its area element. Applying the balance principle of force to an infinitesimal tetrahedron, Cauchy's theorem states that the nominal stress vector $\boldsymbol{p}$ depends linearly on $\boldsymbol{n}$ and thus demonstrates the existence of an asymmetric nominal (Piola-Kirchhoff-1) stress tensor $\boldsymbol{P}$ such that:

$$\boldsymbol{p}(\boldsymbol{x}, t, \boldsymbol{n}(\boldsymbol{x})) = \boldsymbol{P}(\boldsymbol{x}, t)\boldsymbol{n}(\boldsymbol{x}) \tag{3.6}$$

An objective measure of internal forces per unit area is given by the symmetric material (Piola-Kirchhoff-2) stress tensor:

$$\boldsymbol{S} = \boldsymbol{S}(\boldsymbol{x}, t) = \boldsymbol{F}^{-1}(\boldsymbol{x}, t)\boldsymbol{P}(\boldsymbol{x}, t) \tag{3.7}$$

Under the assumption of small deformations ($\|\boldsymbol{E}\| \ll 1$):

$$\boldsymbol{S}(\boldsymbol{x}, t) \simeq \boldsymbol{P}(\boldsymbol{x}, t)$$

3.1.2 Balance equations

Assuming sufficient smoothness of the functions $\boldsymbol{y}(\boldsymbol{x}, t)$, $\boldsymbol{b}(\boldsymbol{x}, t)$ and $\boldsymbol{p}(\boldsymbol{x}, t)$ introduced in the previous subsection, the local material versions of the balance equations can be derived.

Remark 3.1 *Description of plastic localization bands for instance involves a piecewise continuous deformation field and balance equations should then be written in a weak form compatible with the appropriate functional spaces.*

Balance of mass The body $\mathcal{B}$ is assumed to be endowed with the scalar property of material mass density ρ defined per unit volume of the reference configuration. The conservation of the body's mass is implicitely expressed by a rate independent material density:

$$\rho(\boldsymbol{x}, t) = \rho(\boldsymbol{x}) \qquad or \qquad \dot{\rho}(\boldsymbol{x}, t) = 0 \tag{3.8}$$

Balance of linear momentum According to Newton's law, inertia forces are balanced by the body and contact forces, which in a continuum take the Euler-Cauchy form:

$$\rho\ddot{\boldsymbol{y}} = Div\boldsymbol{P} + \boldsymbol{b} \tag{3.9}$$

Balance of angular momentum Equilibrium of angular momentum is realized if the following relation holds:

$$\boldsymbol{P}\boldsymbol{F}^T = \boldsymbol{F}\boldsymbol{P}^T \tag{3.10}$$

Balance of energy For isothermal processes, the change of total energy is expressed as contributions of the power of the contact and body forces:

$$\dot{\overline{\rho(\varepsilon + \frac{1}{2}\dot{\boldsymbol{y}}^2)}} = \boldsymbol{P} : \dot{\boldsymbol{F}} + \dot{\boldsymbol{y}} \cdot Div\boldsymbol{P} + \dot{\boldsymbol{y}} \cdot \boldsymbol{b} \tag{3.11}$$

where $\varepsilon(\boldsymbol{x}, t)$ is the internal energy density and the nominal heat flux vector as well as heat supply density are assumed to be zero. This equality represents a local form of the first axiom of thermodynamics.
The reduced form of the balance of energy is given by:

$$\rho\dot{\varepsilon} = \boldsymbol{P} : \dot{\boldsymbol{F}} \tag{3.12}$$

Entropy inequality The body $\mathcal{B}$ is further assumed to be endowed with the scalar property of temperature $\theta(\boldsymbol{x}, t)$ and entropy density $\eta(\boldsymbol{x}, t)$, but the corresponding nominal entropy flux vector and entropy supply density are assumed to be zero.

Under this assumption, the second axiom of thermodynamics states that the total variation of entropy is larger or equal to zero:

$$\rho\dot{\eta} \geq 0 \tag{3.13}$$

Using Eq. 3.12 and the free energy density:

$$\psi := \rho(\varepsilon - \eta\theta) \tag{3.14}$$

the local form of the second axiom is known as the Clausius-Duhem inequality:

$$\Phi = \rho\dot{\overline{\eta\theta}} = -\dot{\psi} + \boldsymbol{P} : \dot{\boldsymbol{F}} \geq 0 \tag{3.15}$$

where Φ is the dissipated power.

3.1.3 Constitutive laws

Kinematics of the body $\mathcal{B}$ is determined by the map $\boldsymbol{y}(\boldsymbol{x}, t)$. Balance of linear and angular momentum involves the unknown stress field $\boldsymbol{P}(\boldsymbol{x}, t)$. Balance of energy involves in addition the internal energy density $\varepsilon(\boldsymbol{x}, t)$. Finally, the

Clausius-Duhem inequality involves the new function $\psi(\boldsymbol{x}, t)$. In order to determine these four functions, a number of constitutive laws must be constructed that are consistent with the balance equations and the second axiom of thermodynamics. If this consistency is achieved, the set of constitutive laws is said to be a thermodynamically admissible process.

Remark 3.2 *In the above list of unknown functions, the internal energy* $\varepsilon(\boldsymbol{x}, t)$ *can be replaced by the unknown dissipated power* $\Phi(\boldsymbol{x}, t)$.

The theory of constitutive laws in continuum mechanics is based on a number of hypotheses, which we intend to follow here point by point.

- **Mechanical state**. The mechanical state of the body $\mathcal{B}$ is defined by the set:

$$\{\boldsymbol{x}, t; \boldsymbol{y}\}$$

  where the observable θ is not mandatory for isothermal processes.

- **Causality**. A constitutive function Σ defined at each particle $\boldsymbol{x}$ at time t depends on the previous mechanical states of the whole body $\mathcal{B}$:

$$\begin{aligned}\Sigma = \Sigma(\boldsymbol{x}, t; \quad & \boldsymbol{y}, \nabla\boldsymbol{y}, \nabla^2\boldsymbol{y}... \\ & \dot{\boldsymbol{y}}, \nabla\dot{\boldsymbol{y}}, \nabla^2\dot{\boldsymbol{y}}... \\ & \ddot{\boldsymbol{y}}, \nabla\ddot{\boldsymbol{y}}, \nabla^2\ddot{\boldsymbol{y}}... \\ & ..., ..., ..., ...)\end{aligned}$$

- **Equipresence**. If one constitutive function depends on a variable z, then all constitutive equations depend on this variable z unless this fact enters in contradiction with the balance equations or the second axiom of thermodynamics.

- **Localization**. A constitutive function depends only on the first gradients in space:

$$\Sigma = \Sigma(\boldsymbol{x}, t; \quad \boldsymbol{y}, \nabla\boldsymbol{y},$$

$$\dot{\boldsymbol{y}}, \nabla\dot{\boldsymbol{y}},$$
$$\ddot{\boldsymbol{y}}, \nabla\ddot{\boldsymbol{y}},$$
$$..., ...)$$

The mechanical state of a particle $\boldsymbol{x}$ at time t is thus completely defined by the state variable at $\boldsymbol{x}$. Evolution of the body $\mathcal{B}$ is considered as a succession of equilibrium states, whereby all balance equations and the Clausius-Duhem inequality are satisfied.

- **Instantaneization**. The dependency of a constitutive law with respect to the mechanical history of body $\mathcal{B}$ is restricted to the first derivative in time of the state variable.

$$\Sigma = \Sigma(\boldsymbol{x}, t; \boldsymbol{y}, \nabla\boldsymbol{y}, \dot{\boldsymbol{y}}, \nabla\dot{\boldsymbol{y}})$$

- **Internal variables**. In specific irreversible phenomena such as plasticity or damage, additional internal variables $\boldsymbol{\xi}_i = \boldsymbol{\xi}_i(\boldsymbol{x}, t)$ with $i = 1, 2, ..., n$ need to be defined for characterization of the microstructural state that cannot be directly measured.

$$\Sigma = \Sigma(\boldsymbol{x}, t; \boldsymbol{y}, \nabla\boldsymbol{y}, \dot{\boldsymbol{y}}, \nabla\dot{\boldsymbol{y}}, \boldsymbol{\xi}_i, \dot{\boldsymbol{\xi}}_i) \qquad i = 1, 2, ..., n$$

where $i = 1, 2, ..., n$ will often be omitted in the subsequent work. Internal variables allow one to account for the material's memory without giving up the axiom of instantaneization.

- **Objectivity or material frame indifference**. The response of the material characterized by the constitutive functions has to be independent of the frame of reference. Considering a translation τ of the reference time, a translation $\boldsymbol{c}$ and a rotation $\boldsymbol{R}$ of the frame of reference, the state variable becomes:

$$\tilde{\boldsymbol{y}}(\boldsymbol{x}, t) = \boldsymbol{R}\boldsymbol{y}(\boldsymbol{x}, t + \tau) + \boldsymbol{c}$$

Accordingly, a constitutive function cannot depend explicitely on t and $\boldsymbol{y}$, and the gradients of $\boldsymbol{y}$ as well as the internal variables have to be replaced

by objective measures:

$$\Sigma = \Sigma(\boldsymbol{x}; \boldsymbol{E}, \dot{\boldsymbol{E}}, \boldsymbol{\Xi}_i, \dot{\boldsymbol{\Xi}}_i)$$

where

$$\begin{aligned} \tilde{\boldsymbol{E}} &= \boldsymbol{E} \\ \tilde{\boldsymbol{\Xi}}_i &= \boldsymbol{\Xi}_i \\ \dot{\tilde{\boldsymbol{E}}} &= \dot{\boldsymbol{E}} \\ \dot{\tilde{\boldsymbol{\Xi}}}_i &= \dot{\boldsymbol{\Xi}}_i \end{aligned}$$

- **Material symmetry**. The constitutive laws have to be invariant relative to the symmetry group of the material. In the case where Σ is a scalar function and $\boldsymbol{\Xi}_i$ are second order tensors, this requirement is formulated by:

$$\begin{aligned} \Sigma(\boldsymbol{x}, \boldsymbol{E}, \dot{\boldsymbol{E}}, \boldsymbol{\Xi}_i, \dot{\boldsymbol{\Xi}}_i) &= \Sigma(\boldsymbol{x}, \boldsymbol{Q}^T\boldsymbol{E}\boldsymbol{Q}, \boldsymbol{Q}^T\dot{\boldsymbol{E}}\boldsymbol{Q}, \boldsymbol{Q}^T\boldsymbol{\Xi}_i\boldsymbol{Q}, \boldsymbol{Q}^T\dot{\boldsymbol{\Xi}}_i\boldsymbol{Q}) \\ \forall \boldsymbol{Q} &\in \mathcal{G} \end{aligned}$$

  where $\mathcal{G}$ is the symmetry group of the material (e.g. the orthogonal group $\mathcal{O}$ for isotropic materials).

- **Existence and uniqueness**. The boundary value problems formulated with the constitutive equations should be well posed (at least for small deformations), that is a unique solution of the problem exists for appropriate initial and boundary conditions. The boundary value problem for the displacement function $\boldsymbol{u}(\boldsymbol{x}, t)$ can be stated as follows:

  Assuming

$$\Omega_0 \subset \mathcal{R}^3, \qquad \partial\Omega_0 = \Gamma_0^u \cup \Gamma_0^p$$
$$\rho(\boldsymbol{x}), \boldsymbol{P}(\boldsymbol{x}, \nabla\boldsymbol{u}, \nabla\dot{\boldsymbol{u}}, \boldsymbol{\xi}_i), \boldsymbol{b}(\boldsymbol{x}, t), \boldsymbol{v}_0(\boldsymbol{x}), \bar{\boldsymbol{u}}(\boldsymbol{x}, t), \bar{\boldsymbol{p}}(\boldsymbol{x}, t)$$
$$\bar{\boldsymbol{u}}(\boldsymbol{x}, 0) = 0 \qquad \dot{\bar{\boldsymbol{u}}}(\boldsymbol{x}, 0) = \boldsymbol{v}_0(\boldsymbol{x}) \qquad \forall \boldsymbol{x} \in \Gamma_0^u$$

  Find $\boldsymbol{u}(\boldsymbol{x}, t)$ such that

$$\rho\ddot{\boldsymbol{u}} - div\,\boldsymbol{P} - \boldsymbol{b} = 0 \qquad \forall \boldsymbol{x} \in \Omega_0, \qquad \forall t > 0 \tag{3.16}$$

$$\boldsymbol{u}(\boldsymbol{x},0) = 0, \forall \boldsymbol{x} \in \Omega_0 \qquad \boldsymbol{u}(\boldsymbol{x},t) = \bar{\boldsymbol{u}}(\boldsymbol{x},t), \forall \boldsymbol{x} \in \Gamma_0^u$$
$$\dot{\boldsymbol{u}}(\boldsymbol{x},0) = \boldsymbol{v}_0(\boldsymbol{x}), \forall \boldsymbol{x} \in \Omega_0 \qquad \boldsymbol{P}(\boldsymbol{x},t)\boldsymbol{n}(\boldsymbol{x}) = \bar{\boldsymbol{p}}(\boldsymbol{x},t), \forall \boldsymbol{x} \in \Gamma_0^p$$

Unfortunately, there are no general mathematical theorems insuring existence and uniqueness of such a solution even for small deformations, except for specific cases such as linear elasticity [59, 80]. However, the formalism of standard generalized materials allows the formulation of an incremental problem, whereby the equilibrium of the body $\mathcal{B}$ is required after an infinitesimal deformation or loading increment. The existence and sometimes uniqueness of the incremental boundary value problem was demonstrated in a few cases such as rate-independent plasticity with hardening or viscoplasticity [68, 118].

Standard generalized materials A classical and efficient approach for construction of an admissible thermodynamic process consists of choosing a free energy potential $\psi = \psi(\boldsymbol{x}, \boldsymbol{E}, \boldsymbol{\Xi}_i)$ and postulating the existence of a dissipation potential $\phi = \phi(\boldsymbol{x}, \dot{\boldsymbol{E}}, \dot{\boldsymbol{\Xi}}_i, \boldsymbol{E}, \boldsymbol{\Xi}_i)$. The free energy potential function ψ is assumed to be twice continuously differentiable and convex with respect to $\boldsymbol{E}$ and $\boldsymbol{\Xi}_i$. The dissipation potential ϕ is assumed to be continuous, non-negative, zero at the origin and convex with respect to $\dot{\boldsymbol{E}}$ and $\dot{\boldsymbol{\Xi}}_i$.
The constitutive laws of the material are then derived from these two potentials:

$$\boldsymbol{S} - \frac{\partial \psi}{\partial \boldsymbol{E}} \in \partial_{\dot{\boldsymbol{E}}} \phi \tag{3.17}$$
$$-\frac{\partial \psi}{\partial \boldsymbol{\Xi}_i} \in \partial_{\dot{\boldsymbol{\Xi}}} \phi \qquad i = 1, 2, ..., n \tag{3.18}$$

where ∂ designates the subdifferential [43].

Remark 3.3 *If the potential ϕ is differentiable everywhere, the subdifferential contains a single element, which is identified with the classical gradient.*

Remark 3.4 *The distinct arguments appearing in the free energy potential and the dissipation potential that seem to violate the principle of equipresence are in fact justified by consistency with the second axiom of thermodynamics [12].*

If the dissipation function Φ (Eq. 3.15) is continuous, convex with respect to all flow variables, quasi-homogeneous [49] and verifies the conditions:

$$\begin{aligned} \Phi &\geq 0 \\ \Phi(\boldsymbol{x}, 0, 0, \boldsymbol{E}, \boldsymbol{\Xi}_i) &= 0 \end{aligned}$$

the potential ϕ can be constructed by:

$$\phi(\boldsymbol{x}, \dot{\boldsymbol{E}}, \dot{\boldsymbol{\Xi}}, \boldsymbol{E}, \boldsymbol{\Xi}_i) = \int_0^1 \frac{\Phi(\boldsymbol{x}, s\dot{\boldsymbol{E}}, s\dot{\boldsymbol{\Xi}}_i, \boldsymbol{E}, \boldsymbol{\Xi}_i)}{s} ds \tag{3.19}$$

Structural density At this point arises the question of the role of structural density in the presented framework. If large time effects such as osteoporosis or bone remodelling are considered, balance of mass is apparently violated and evolution of $\rho(\boldsymbol{x}, t)$ requires an additional constitutive equation (open system). These considerations extend beyond the scope of this work and structural density is kept constant in time. In agreement with well-established experimental findings [112], the influence of trabecular bone density on the stress variable can be taken into account by defining a normalized stress such that:

$$\hat{\boldsymbol{S}} := \frac{\boldsymbol{S}}{{\rho_s}^{2l}} \tag{3.20}$$

where l is a positive real number ranging in practice between $\frac{1}{2}$ and $\frac{3}{2}$.
Similar definitions for normalized potentials seem appropriate:

$$\hat{\psi}(\boldsymbol{x}, \boldsymbol{E}, \boldsymbol{\Xi}_i) = \frac{\psi(\boldsymbol{x}, \boldsymbol{E}, \boldsymbol{\Xi}_i)}{\rho_s^{2l}(\boldsymbol{x})} \tag{3.21}$$

$$\hat{\phi}(\boldsymbol{x}, \dot{\boldsymbol{E}}, \dot{\boldsymbol{\Xi}}_i, \boldsymbol{E}, \boldsymbol{\Xi}_i) = \frac{\phi(\boldsymbol{x}, \dot{\boldsymbol{E}}, \dot{\boldsymbol{\Xi}}_i, \boldsymbol{E}, \boldsymbol{\Xi}_i)}{\rho_s^{2l}(\boldsymbol{x})} \tag{3.22}$$

Using the same scaling for the potentials as for the stress variable is equivalent to a change of physical unit and obviously does not affect the constitutive laws. The approach becomes transparent to the influence of trabecular bone density.

Remark 3.5 *In order to simplify the notations, we will omit in the future the variable $\boldsymbol{x}$ in the potential ψ and the variables $\boldsymbol{x}, \boldsymbol{E}, \boldsymbol{\Xi}_i$ in ϕ.*

3.2 One-dimensional model

The one-dimensional model aims at describing the quasistatic and rate-dependent mechanical behaviour observed in uniaxial loading of trabecular bone. Beside the properties reviewed in Chapter 2, preliminary one-dimensional experiments demonstrated that simultaneous plastic and damage flow occur in trabecular bone beyond a relatively low elastic limit. Consequently, elasticity, viscoelasticity, plasticity and damage will be successively formulated in the framework of standard generalized materials and synthesized in a new model to account for the major aspects of the mechanical response of trabecular bone, excepted fatigue, bone remodelling as well as strain or damage localization.

3.2.1 Elasticity

An elastic material exhibits an infinite memory of one reference configuration and its mechanical state is fully characterized by the strain $\boldsymbol{E}$. No internal variable is required. In elasticity, no dissipation takes place. The free energy potential ψ is thus assumed to be a twice continuously differentiable and convex function of the single observable variable E and the dissipation function Φ is zero.

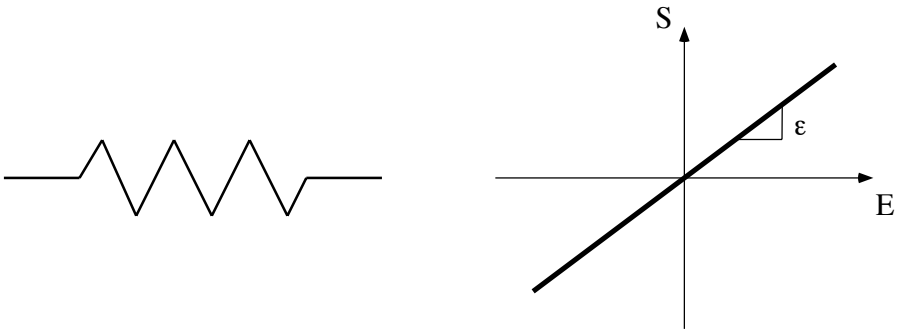

Figure 3.2: Rheological model and constitutive law of a linear elastic material.

For linear elasticity, the free energy is quadratic:

$$\psi = \psi(E) = \frac{1}{2}\epsilon E^2 \tag{3.23}$$

where $\epsilon > 0$ is Young's modulus.

The dissipation potential ϕ is zero:

$$\phi = \phi(\dot{E}) \equiv 0 \tag{3.24}$$

The single constitutive equation provides the material stress:

$$S = S^E := \frac{\partial \psi}{\partial E} = \epsilon E \tag{3.25}$$

3.2.2 Bimodular elasticity

A different behaviour in tension and compression may be considered by dividing the strain space into the subdomains $\mathcal{R}^-$ and $\mathcal{R}^+$.

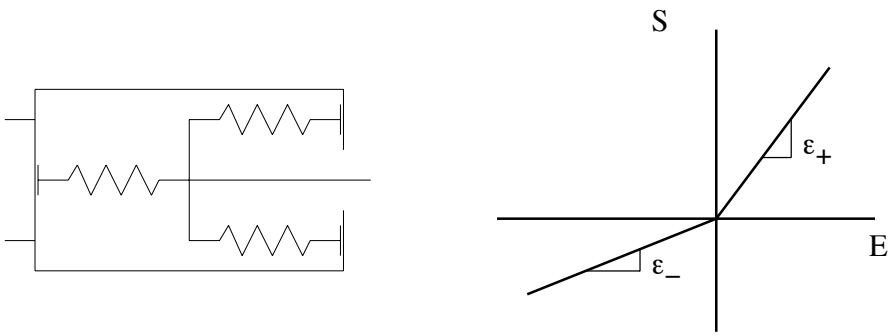

Figure 3.3: Rheological model and constitutive law of a bimodular linear elastic material.

The free energy potential remains convex, but is allowed to be only piecewise twice continuously differentiable:

$$\psi(E) = \begin{cases} \frac{1}{2}\epsilon_- E^2 & \text{if } E < 0 \\ \frac{1}{2}\epsilon_+ E^2 & \text{if } E \geq 0 \end{cases} \tag{3.26}$$

where $\epsilon_- > 0$ and $\epsilon_+ > 0$ are the compressive, respectively tensile elastic moduli. The resulting stress is then piecewise continuously differentiable:

$$S = \begin{cases} \epsilon_- E & \text{if } E < 0 \\ \epsilon_+ E & \text{if } E \geq 0 \end{cases} \tag{3.27}$$

3.2.3 Viscoelasticity

A viscoelastic material of the Kelvin-Voigt type has an evanescent memory in the sense that its mechanical behaviour depends on the present rate of deformation. An internal variable is sometimes used but in this case not mandatory.

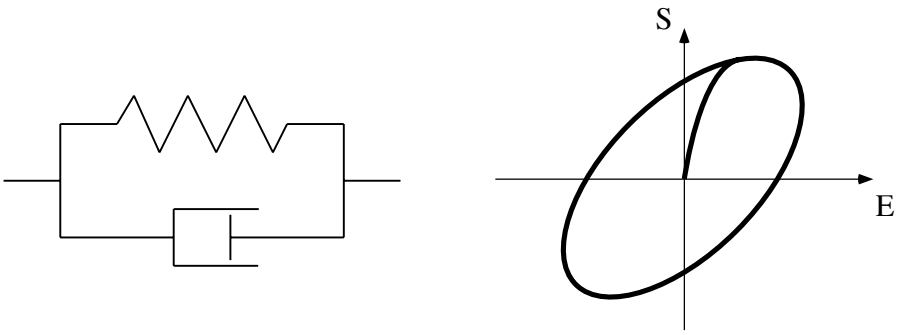

Figure 3.4: Rheological model and stress-strain curve for a viscoelastic bar submitted to a harmonic displacement.

The same free energy potential as in elasticity is chosen and the following dissipation potential is postulated:

$$\phi = \phi(\dot{E}) = \frac{n}{n+1} v |\dot{E}|^{\frac{n+1}{n}} \tag{3.28}$$

where $v \geq 0$ is the viscosity coefficient and $n > 0$ an integer.
The resulting constitutive equation is:

$$S = S(E, \dot{E}) = S^E + S^{\dot{E}} := \frac{\partial \psi}{\partial E} + \frac{\partial \phi}{\partial \dot{E}} = \epsilon E + v |\dot{E}|^{\frac{1}{n}} \frac{\dot{E}}{|\dot{E}|} \tag{3.29}$$

The inverse relation can be obtained through the Legendre transform of the potential ϕ:

$$\phi^* = \phi^*(S^{\dot{E}}) = S^{\dot{E}} \dot{E} - \phi(\dot{E}) = \frac{v}{(n+1)} \left(\frac{|S^{\dot{E}}|}{v} \right)^{n+1}$$

$$\dot{E} = \frac{\partial \phi^*}{\partial S^{\dot{E}}} = \left(\frac{|S^{\dot{E}}|}{v} \right)^n \frac{S^{\dot{E}}}{|S^{\dot{E}}|} \tag{3.30}$$

3.2.4 Rate-independent plasticity

A plastic material exhibits a memory in the form of a permanent strain and requires the introduction of an internal variable E^p. In general, this permanent strain occurs beyond a certain elastic limit or yield stress. Following a standard hypothesis [37], material strain is divided into an elastic and a plastic part:

$$E = E^e + E^p \tag{3.31}$$

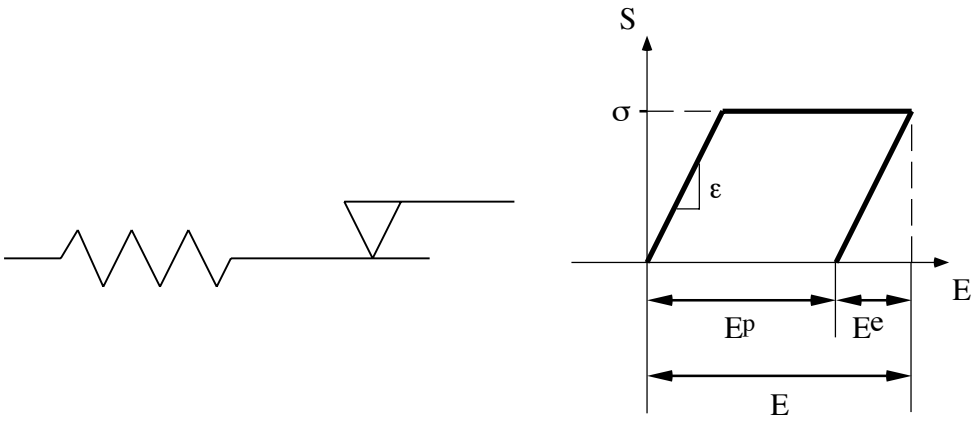

Figure 3.5: Rheological model and constitutive law of an elastic, perfectly plastic material.

The free energy potential involves only the elastic deformation:

$$\psi = \psi(E, E^p) = \frac{1}{2}\epsilon(E - E^p)^2 \tag{3.32}$$

The dissipation potential is a function of the single flow variable $\dot{E}^p$:

$$\phi = \phi(\dot{E}^p) = \sigma|\dot{E}^p| \tag{3.33}$$

where $\sigma > 0$ is the yield stress and ϕ is not differentiable at $\dot{E}^p = 0$.

Remark 3.6 *For rate-independent processes, the dissipation function* Φ *is positively homogenous of degree one:*

$$\Phi(t\dot{E}^p) = t\Phi(\dot{E}^p) \qquad \forall t \geq 0$$

Hence, the dissipation function Φ *and the potential* ϕ *are identical:*

$$\phi(\dot{E}^p) = \int_0^1 \frac{\Phi(s\dot{E}^p)}{s} ds \equiv \Phi(\dot{E}^p)$$

The conjugate variables of E and E^p with respect to ψ are given by:

$$\begin{aligned} S^E &:= \frac{\partial \psi}{\partial E} = \epsilon(E - E^p) \\ S^{E^p} &:= -\frac{\partial \psi}{\partial E^p} = \epsilon(E - E^p) \end{aligned}$$

Using this notation, the constitutive Eq. 3.17 and 3.18 reduces to:

$$S = S^E \tag{3.34}$$

$$S^{E^p} \in \partial_{\dot{E}^p}\phi = \begin{cases} -\sigma & \text{if } \dot{E}^p < 0 \\ [-\sigma; +\sigma] & \text{if } \dot{E}^p = 0 \\ +\sigma & \text{if } \dot{E}^p > 0 \end{cases} \tag{3.35}$$

Inversion of the second constitutive relation requires the construction of the dual function of ϕ by the means of a Legendre-Fenchel transform:

$$\phi^* = \phi^*(S^{E^p}) := Sup_{\dot{E}^p}[S^{E^p}\dot{E}^p - \phi(\dot{E}^p)]$$

Direct calculation or inspection of the graph of ϕ suggests that ϕ^* is the indicator function of the convex domain $[-\sigma, \sigma]$:

$$\phi^*(S^{E^p}) = I_{[-\sigma,+\sigma]} = \begin{cases} 0 & \text{if } S^{E^p} \in [-\sigma; +\sigma] \\ +\infty & \text{otherwise} \end{cases}$$

The flow rule for the plastic deformation is finally given by:

$$\dot{E}^p \in \partial_{S^{E^p}}\phi^* = \begin{cases} \emptyset & \text{if } S^{E^p} < -\sigma \\ ]-\infty; 0] & \text{if } S^{E^p} = -\sigma \\ 0 & \text{if } S^{E^p} \in]-\sigma; +\sigma[\\ [0; +\infty[& \text{if } S^{E^p} = +\sigma \\ \emptyset & \text{if } S^{E^p} > +\sigma \end{cases} \tag{3.36}$$

The domain of the conjugate variable S^{E^p} whereby no plastic deformation occurs is thus deduced from the dual dissipation potential, but can also be expressed with the classical yield function y:

$$y = y(S^{E^p}) = |S^{E^p}| - \sigma < 0$$

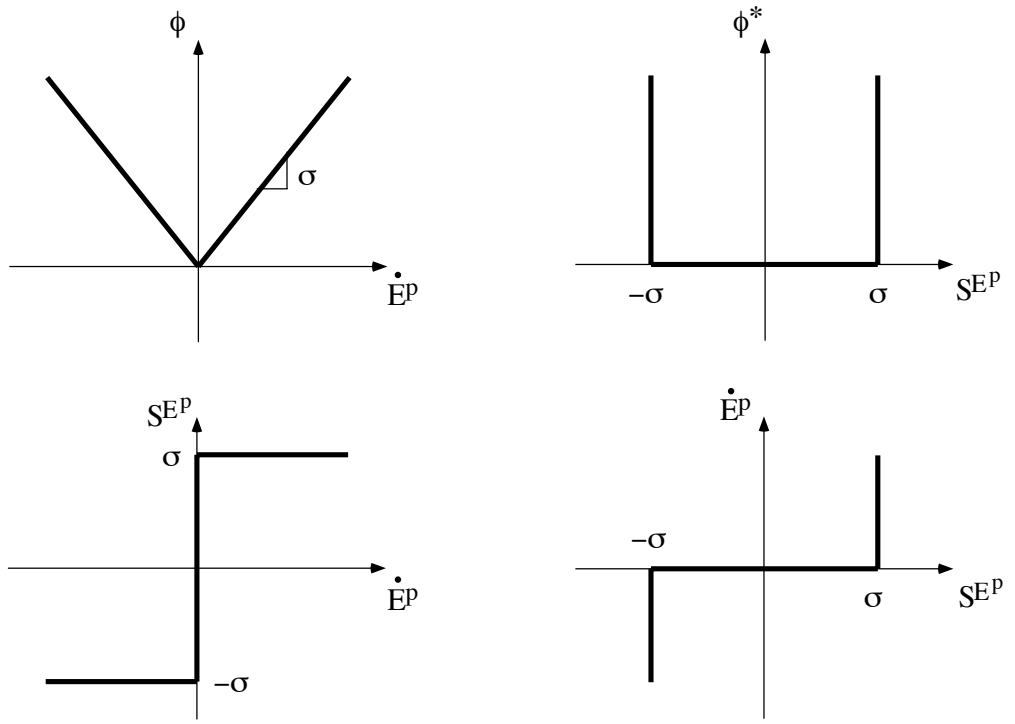

Figure 3.6: Legendre-Fenchel transform of the plastic dissipation potential.

The flow rule is then given in the Kuhn-Tucker form:

$$\dot{E}^p = \dot{\lambda}_L \frac{dy}{dS^{E^p}} = \dot{\lambda}_L \frac{S^{E^p}}{|S^{E^p}|}$$

$$\dot{\lambda}_L \geq 0 \qquad y \leq 0 \qquad \dot{\lambda}_L y = 0$$

In standard generalized materials, the normality rule holds, that is the plastic strain is normal to the yield criterion $y(S^{E^p})$ and the plasticity model is said to be associated.

A different yield stress in tension and in compression can be obtained by dividing the strain flow space in two parts $\mathcal{R}^-$ and $\mathcal{R}^+$ and choosing the appropriate dissipation potential:

$$\phi(\dot{E}^p) = \begin{cases} -\sigma_- \dot{E}^p & \text{if } \dot{E}^p < 0 \\ +\sigma_+ \dot{E}^p & \text{if } \dot{E}^p \geq 0 \end{cases} \tag{3.37}$$

where $\sigma_- > 0$ and $\sigma_+ > 0$ are the compressive and tensile yield stresses.

3.2.5 Rate-independent damage

A damaged material exhibits a memory in the form of a reduction in the elastic constant ϵ and also requires an internal variable. The classical choice consists of a dimensionless variable D characterizing the relative area occupied by microvoids or microcracks in a damaged solid. The progressive reduction in resisting area during the damage process leads to the concept of effective stress:

$$\tilde{S} = \frac{S}{1-D}$$

The principle of equivalent strain states that the constitutive laws of a damaged material may be obtained by replacing the stress S by $\tilde{S}$ in the constitutive laws of the undamaged material [88]. Problems encountered in the generalization of this approach suggested a principle of equivalent energy, whereby S is replaced by $\tilde{S}$ directly in the free energy potential and the yield criterion [30]. We suspect that such methods can produce constitutive laws that are not compatible with the hypotheses of a standard generalized material.

Therefore, we prefer to rely on a phenomenological approach that conforms strictly to the definition of a standard generalized material. In these circumstances and in order to follow parallel tracks in plasticity and damage, we postulate a cumulated strain variable α. This variable represents the residual strain cumulated during the damage process and is non-negative (Fig. 3.7).

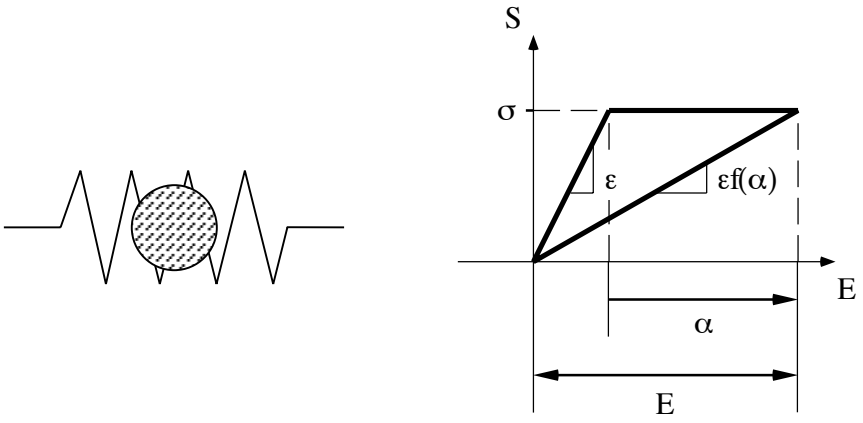

Figure 3.7: Rheologic model and constitutive law of a damaged elastic material.

The free energy potential is a function of E and α:

$$\psi = \psi(E, \alpha) = \frac{1}{2}\epsilon f(\alpha) E^2 \tag{3.38}$$

where f is a positive, monotone, twice continuously differentiable function of α such that $f'(\alpha) < 0$ and $f(0) = 1$. These conditions insure that no repair process is admitted and that the undamaged elastic modulus is $\epsilon > 0$.
The dissipation potential is a function of the single flow variable $\dot{\alpha}$:

$$\phi = \phi(\dot{\alpha}) = h(\alpha)\dot{\alpha} + I_{[0;+\infty]}(\dot{\alpha}) \tag{3.39}$$

where $I_{[0;+\infty]}$ is the indicatrix function of the interval $[0; +\infty]$ and the yield function $h(\alpha)$ is given by:

$$h(\alpha) = -\sigma^2 \frac{f'(\alpha)}{2\epsilon f^2(\alpha)}$$

with $\sigma > 0$, the associated yield stress.
The dissipation potential ϕ is not differentiable for $\dot{\alpha} \in [-\infty; 0]$.
The conjugate variables are given by:

$$\begin{aligned} S^E &:= \frac{\partial \psi}{\partial E} = \epsilon f(\alpha) E \\ S^\alpha &:= -\frac{\partial \psi}{\partial \alpha} = \frac{1}{2}\epsilon f'(\alpha) E^2 \end{aligned}$$

The constitutive equations become:

$$S = S^E \tag{3.40}$$

$$S^\alpha \in \partial_{\dot{\alpha}}\phi = \begin{cases} \emptyset & \text{if } \dot{\alpha} < 0 \\ [-\infty; h(\alpha)[& \text{if } \dot{\alpha} = 0 \\ h(\alpha) & \text{if } \dot{\alpha} > 0 \end{cases} \tag{3.41}$$

Using the Fenchel-Legendre transform the following dual dissipation potential is obtained:

$$\phi^*(S^\alpha) = \begin{cases} 0 & \text{if } S^\alpha \in [-\infty; h(\alpha)] \\ +\infty & \text{otherwise} \end{cases}$$

The resulting flow rule is:

$$\dot{\alpha} \in \partial_{S^\alpha}\phi^* = \begin{cases} 0 & \text{if } S^\alpha \in [-\infty; h(\alpha)[\\ [0; +\infty] & \text{if } S^\alpha = h(\alpha) \\ \emptyset & \text{if } S^\alpha > h(\alpha) \end{cases} \tag{3.42}$$

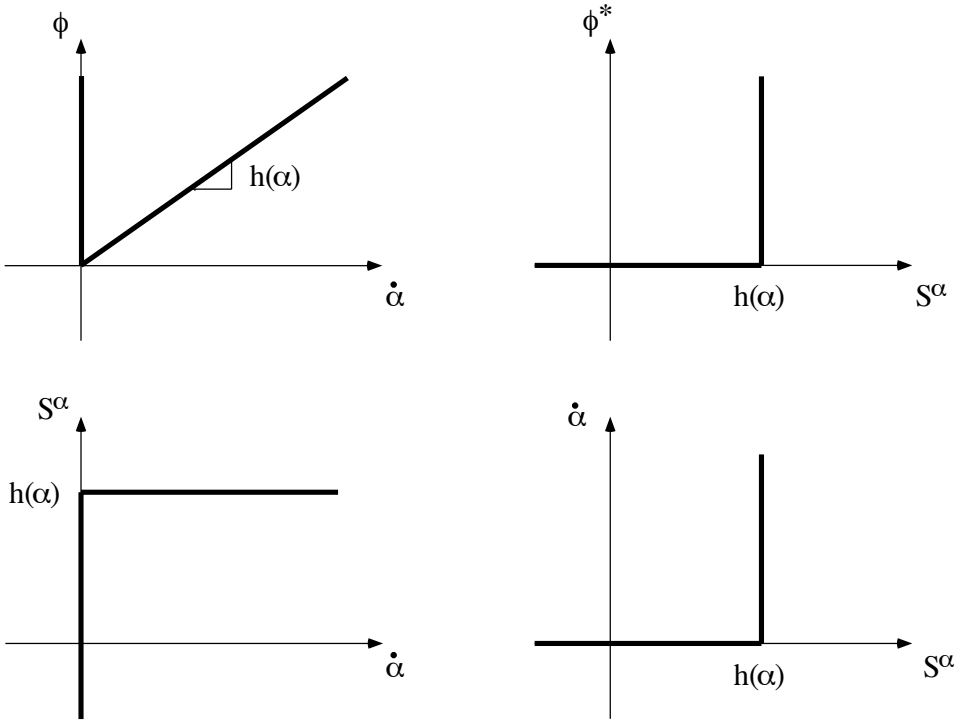

Figure 3.8: Legendre-Fenchel transform of the damage dissipation potential.

The domain of the conjugate variable S^α where no damage occurs is a convex set of which the dual dissipation potential ϕ^* is the indicatrix function. This set can also be characterized by the classical yield criterion:

$$y = y(S^\alpha) = S^\alpha - h(\alpha) < 0$$

In the Kuhn-Tucker form, the flow rule is then expressed by:

$$\dot{\alpha} = \dot{\lambda}_L \frac{dy}{dS^\alpha} = \dot{\lambda}_L$$

$$\dot{\lambda}_L \geq 0 \qquad y \leq 0 \qquad \dot{\lambda}_L y = 0$$

Since the cumulated damage variable is not sensitive to the sign of strain, distinct stress limits for the flow of damage in tension and compression would require definition of an additional internal variable.

3.2.6 Synthesis

Trabecular bone is known to exhibit a viscoelastic behaviour and we discovered that simultaneous plastic and damage flow occurs beyond a certain yield limit up to densification of the strain-stress curve in compression or up to brittle failure in tension. In addition, rate-dependency of plastic and damage flow was demonstrated by creep experiments.

We attempt now to assemble the previously described models in a consistent manner in order to provide a global rheological model and constitutive law for trabecular bone, which is an original feature of this thesis. Simultaneous flow of plasticity and damage implies the use of both internal variables E^p and α and the existence of a common yield criterion.

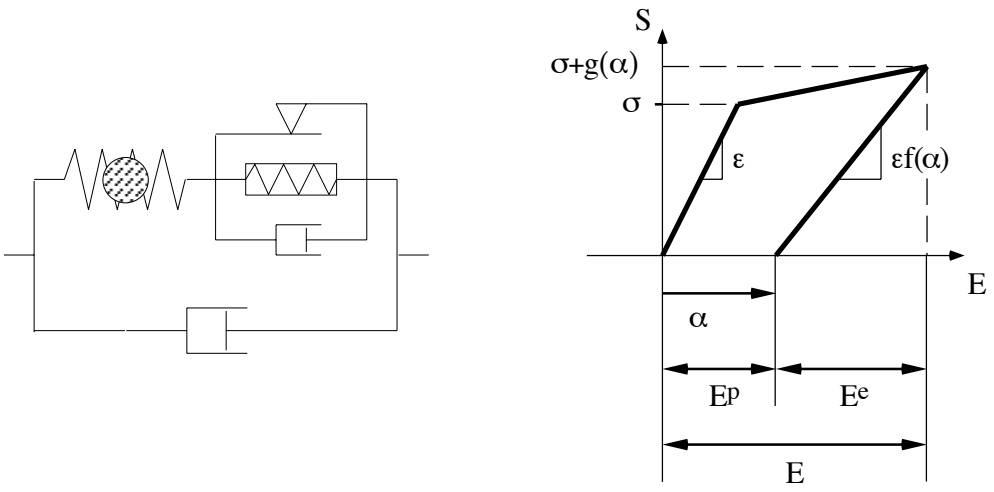

Figure 3.9: Rheological model and rate-independent part of the 1D constitutive law.

For this purpose, we redefine the damage variable α as the cumulated plastic deformation:

$$\alpha(t) := \int_0^t |\dot{E}^p| d\tau \tag{3.43}$$

As a consequence, the rates of the two internal variables are related by:

$$\dot{\alpha} = |\dot{E}^p|$$

while α and E^p are independent.

The previous plastic and damage models suggest the free energy potential:

$$\psi(E, E^p, \alpha) = \frac{1}{2}\epsilon f(\alpha)(E - E^p)^2 + \tilde{\psi}(\alpha) \tag{3.44}$$

where $f(\alpha)$ remains a twice continuously differentiable, positive and monotone function with $f'(\alpha) < 0$ and $f(0) = 1$. The material constant $\epsilon > 0$ is the elastic modulus and $\tilde{\psi}(\alpha)$ is a twice continuously differentiable convex function with $\tilde{\psi}(0) = 0$. This function $\tilde{\psi}$ is an additional hardening potential associated with the increase of stress during plastic and damage flow. From a physical point of view, $\tilde{\psi}$ represents the elastic energy stored in the secondary spring (Fig. 3.9).
The conjugate variables with respect to ψ are given by:

$$\begin{aligned} S^E &= \epsilon f(\alpha)(E - E^p) \\ S^{E^p} &= \epsilon f(\alpha)(E - E^p) \\ S^\alpha &= -\frac{1}{2}\epsilon f'(\alpha)(E - E^p)^2 - \tilde{\psi}'(\alpha) \end{aligned}$$

The dissipation potential is assumed to be divided into three parts:

$$\phi(\dot{E}, \dot{E}^p, \dot{\alpha}) = \phi_1(\dot{E}) + \phi_2(\dot{E}^p) + \phi_3(\dot{\alpha})$$

with

$$\phi_1 = \frac{n}{n+1}\upsilon|\dot{E}|^{\frac{n+1}{n}} \tag{3.45}$$

$$\phi_2 = (\sigma + g)|\dot{E}^p| + \frac{m}{m+1}\zeta|\dot{E}^p|^{\frac{m+1}{m}} \tag{3.46}$$

$$\phi_3 = (h - g)\dot{\alpha} + \tilde{\phi}_3(\dot{\alpha}) + I_{[0;+\infty]}(\dot{\alpha}) \tag{3.47}$$

$$\tilde{\phi}_3(\dot{\alpha}) = \frac{-f'}{2\epsilon f^2}\left(2(\sigma + g)\zeta\frac{m}{m+1}\dot{\alpha}^{\frac{m+1}{m}} + \zeta^2\frac{m}{m+2}\dot{\alpha}^{\frac{m+2}{m}}\right) \tag{3.48}$$

and

$$h = h(\alpha) = -\sigma^2\frac{f'(\alpha)}{2\epsilon f^2(\alpha)}$$

where $g = g(\alpha)$ is a continuously differentiable and positive function such that $g'(\alpha) > 0$ and $g(0) = 0$. The coefficients $\upsilon > 0$, $\zeta > 0$ are viscosity constants, $\sigma > 0$ is the symmetric yield stress limit and $m > 0$, $n > 0$ are integers.
The function $g(\alpha)$ represents the increase of stress beyond the yield limit and $h(\alpha)$ is the yield function of the damage process.

It should be noticed that the potential ϕ_2 is not differentiable at $\dot{E}^p = 0$, while the potential ϕ_3 is not differentiable for $\dot{\alpha} \in [-\infty; 0]$.

Remark 3.7 *The hardening potential is related to the previous functions by:*

$$\tilde{\psi}(\alpha) = \int_0^\alpha g(s) - h(s) - \frac{f'(s)((\sigma + g(s))^2}{2\epsilon f^2(s)} ds$$

The conjugate variable of $\dot{E}$ with respect to ϕ is:

$$S^{\dot{E}} = \upsilon |\dot{E}|^{\frac{1}{n}} \frac{\dot{E}}{|\dot{E}|}$$

The resulting constitutive equations are:

$$S^E = S - S^{\dot{E}} \tag{3.49}$$

$$S^{E^p} \in \partial_{\dot{E}^p} \phi_2 = \begin{cases} -(\sigma + g) - \zeta |\dot{E}^p|^{\frac{1}{m}} & \text{if } \dot{E}^p < 0 \\ [-\sigma - g; +\sigma + g] & \text{if } \dot{E}^p = 0 \\ (\sigma + g) + \zeta |\dot{E}^p|^{\frac{1}{m}} & \text{if } \dot{E}^p > 0 \end{cases} \tag{3.50}$$

$$S^\alpha \in \partial_{\dot{\alpha}} \phi_3 = \begin{cases} \emptyset & \text{if } \dot{\alpha} < 0 \\ [-\infty; h - g] & \text{if } \dot{\alpha} = 0 \\ h - g + \frac{-f'}{2\epsilon f^2} \left(2(\sigma + g)\zeta \dot{\alpha}^{\frac{1}{m}} + \zeta^2 \dot{\alpha}^{\frac{2}{m}} \right) & \text{if } \dot{\alpha} > 0 \end{cases} \tag{3.51}$$

In the rate-independent case, ($\upsilon = 0$ and $\zeta = 0$), the dual potentials are:

$$\phi_1{}^* = 0$$

$$\phi_2{}^* = \begin{cases} 0 & \text{if } S^{E^p} \in [-\sigma - g; +\sigma + g] \\ +\infty & \text{otherwise} \end{cases}$$

$$\phi_3{}^* = \begin{cases} 0 & \text{if } S^\alpha \in [0; h - g] \\ +\infty & \text{otherwise} \end{cases}$$

The resulting flow rules are then:

$$\dot{E} = 0 \tag{3.52}$$

$$\dot{E}^p \in \begin{cases} \emptyset & \text{if } S^{E^p} < -\sigma - g \\ ]-\infty; 0] & \text{if } S^{E^p} = -\sigma - g \\ 0 & \text{if } S^{E^p} \in]-\sigma - g; +\sigma + g[\\ [0; +\infty[& \text{if } S^{E^p} = +\sigma + g \\ \emptyset & \text{if } S^{E^p} > +\sigma + g \end{cases} \tag{3.53}$$

$$\dot{\alpha} \in \begin{cases} 0 & \text{if } S^{\alpha} \in [-\infty; h-g[\\ [0; +\infty] & \text{if } S^{\alpha} = h-g \\ \emptyset & \text{if } S^{\alpha} > h-g \end{cases} \tag{3.54}$$

Formally, plasticity and damage can be described as two independent dissipation processes. However, the coupling of plasticity and damage in the free energy potential introduces a coupling between S^{E^p} and S^{α} that involves an interdependency of $S^{\dot{E}^p}$ and $S^{\dot{\alpha}}$ in the case of simultaneous dissipation. The resulting relationship between $\dot{E}^p$ and $\dot{\alpha}$ must then be consistent with their initial definition. In the rate-independent case, a normality rule including both internal variables can be reformulated in the space of the conjugate variables (Fig. 3.10). The rate-independent flow rules can also be derived in the Kuhn-Tucker form:

$$y = y(S^{E^p}, S^{\alpha}) = |S^{E^p}| + S^{\alpha} - h(\alpha) - \sigma \leq 0$$

$$\begin{aligned} \dot{E}^p &= \dot{\lambda}_L \frac{dy}{dS^{E^p}} = \dot{\lambda}_L \frac{S^{E^p}}{|S^{E^p}|} \\ \dot{\alpha} &= \dot{\lambda}_L \frac{dy}{dS^{\alpha}} = \dot{\lambda}_L \end{aligned}$$

$$\dot{\lambda}_L \geq 0 \qquad y \leq 0 \qquad \dot{\lambda}_L y = 0$$

In the rate-dependent case, the dual dissipation potential become:

$$\begin{aligned} {\phi_1}^* &= \frac{v}{(n+1)} \left(\frac{|S^{\dot{E}}|}{v} \right)^{n+1} \\ {\phi_2}^* &= \begin{cases} 0 & \text{if } S^{E^p} \in [-\sigma - g; +\sigma + g] \\ \frac{\zeta}{m+1} \left(\frac{|S^{E^p}| - g - \sigma}{\zeta} \right)^{m+1} & \text{otherwise} \end{cases} \\ {\phi_3}^* &= \begin{cases} 0 & \text{if } S^{\alpha} \in [-\infty; h-g] \\ (S^{\alpha} - (h-g)) z^m - \tilde{\phi_3}^*(z) & \text{otherwise} \end{cases} \end{aligned}$$

$$\tilde{\phi_3}^*(z) = \frac{-f'}{2\epsilon f^2} \left(2(\sigma+g)\zeta \frac{m}{m+1} z^{m+1} + \zeta^2 \frac{m}{m+2} z^{m+2} \right)$$

with

$$z = z(S^{\alpha}) = \frac{\sqrt{\frac{-2\epsilon f^2}{f'}(S^{\alpha} - (h-g)) + (\sigma+g)^2} - g - \sigma}{\zeta}$$

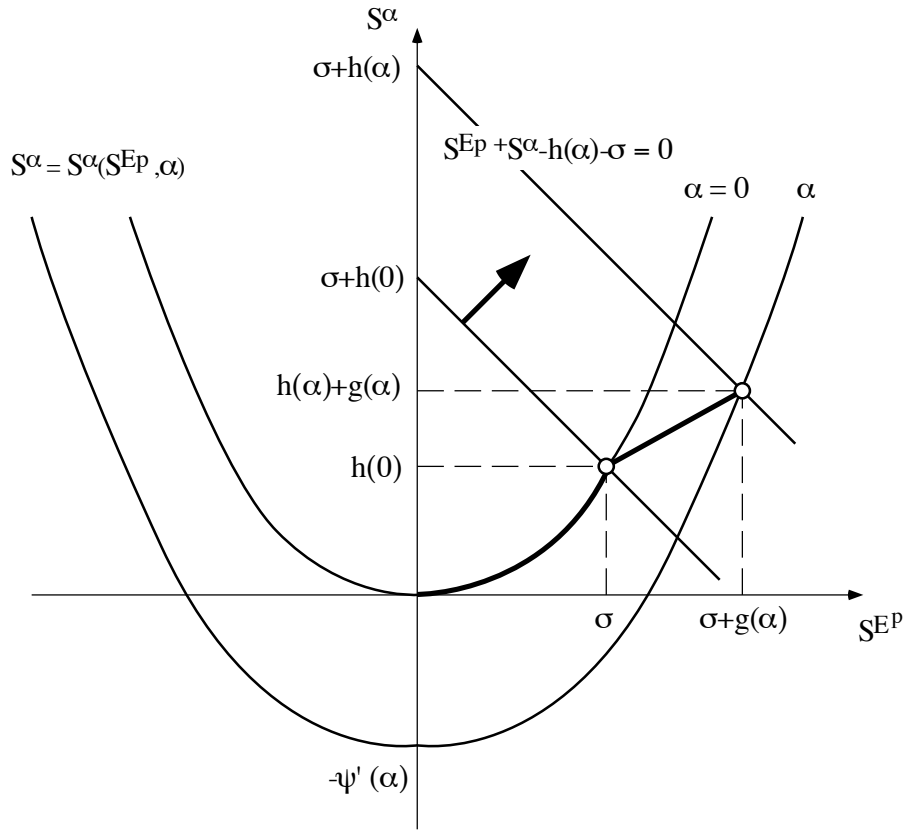

Figure 3.10: Rate-independent normality rule of the simultaneous flow of plasticity and damage.

The associated rate-dependent flow rules are:

$$\dot{E} = \frac{\partial {\phi_1}^*}{\partial S^{\dot{E}}} = \left(\frac{|S^{\dot{E}}|}{\upsilon}\right)^n \frac{S^{\dot{E}}}{|S^{\dot{E}}|} \tag{3.55}$$

$$\dot{E}^p \in \partial_{S^{Ep}} {\phi_2}^* = \begin{cases} 0 & \text{if } S^{Ep} \in [-\sigma - g; +\sigma + g] \\ \left(\frac{|S^{Ep}| - g - \sigma}{\zeta}\right)^m \frac{S^{Ep}}{|S^{Ep}|} & \text{otherwise} \end{cases} \tag{3.56}$$

$$\dot{\alpha} \in \partial_{S^{\alpha}} {\phi_3}^* = \begin{cases} 0 & \text{if } S^{\alpha} \in [-\infty; h - g] \\ \left(\frac{\sqrt{\frac{-2\epsilon f^2}{f'}(S^{\alpha} - (h-g)) + (\sigma+g)^2} - g - \sigma}{\zeta}\right)^m & \text{otherwise} \end{cases} \tag{3.57}$$

with

$$|S^{Ep}| \equiv \sqrt{\frac{-2\epsilon f^2}{f'}(S^{\alpha} - (h-g)) + (\sigma+g)^2}$$

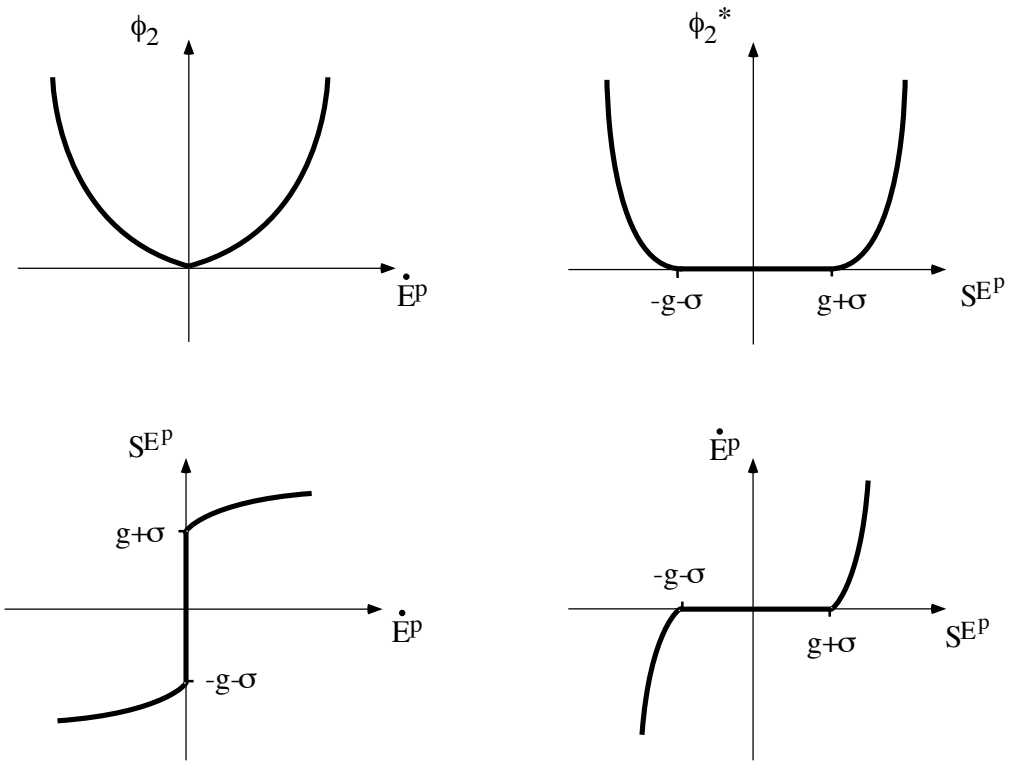

Figure 3.11: Legendre-Fenchel transform of the second rate-dependent part of the dissipation potential.

Remark 3.8 *Like in the rate-independent case, the criterions of the plasticity and damage processes are superimposed when simultaneous dissipation occurs and the flow rules remain compatible with the definition of the internal variables.*

In summary, the one-dimensional mechanical behaviour of trabecular bone is completely determined by the four constants ϵ, υ, ζ, σ, the two exponents n, m and the two functions $f(\alpha)$ and $g(\alpha)$.

Remark 3.9 *The present definition of the internal variable α as the cumulated plastic strain breaks down in the formulation of damage without plasticity. In fact, the most appropriate definition for α appears to be the one chosen in Subsection 3.2.5 for the pure damage model. This original variable degenerates into the*

cumulated plastic strain for plasticity without damage and remains thus always well defined. The relationship between this variable and the cumulated plastic strain would allow us to modify the dissipation potential and obtain the adequate flow rules. Nevertheless, we keep the present definition for its convenience with respect to the numerical applications and the future experimental identification.

The dissipation function is defined by:

$$\begin{aligned}\Phi = \Phi(\dot{E}, \dot{E}^p, \dot{\alpha}) &= S\dot{E} - \dot{\psi}(E, E^p, \alpha) \\ &= (S - S^E)\dot{E} + S^{E^p}\dot{E}^p + S^{\alpha}\dot{\alpha}\end{aligned}$$

where the conjugate internal variables of the dissipation potential are identified with the conjugate variables of the free energy potential.
Using the constitutive Eq. 3.49-3.51, the dissipated power becomes:

$$\Phi = \upsilon|\dot{E}|^{\frac{n+1}{n}} + \sigma|\dot{E}^p| + \zeta|\dot{E}^p|^{\frac{m+1}{m}} + h\dot{\alpha} + \frac{-f'}{2\epsilon f^2}\left(2(\sigma + g)\zeta\dot{\alpha}^{\frac{m+1}{m}} + \zeta^2\dot{\alpha}^{\frac{m+2}{m}}\right)$$

In the rate-independent case the dissipation reduces to:

$$\Phi = \sigma|\dot{E}^p| + h\dot{\alpha}$$

The second axiom of thermodynamics:

$$\Phi(\dot{E}, \dot{E}^p, \dot{\alpha}) \geq 0$$

is thus clearly verified with the previous assumptions for both rate-dependent and rate-independent processes.
The stored or blocked energy as well as the respective contributions of plasticity and damage of the rate-independent part of the dissipated power are illustrated in Fig. 3.12.

Remark 3.10 *Distinct yield limits σ_+ in tension and σ_- in compression can be included in the model by dividing the internal variable α into two variables:*

$$\alpha_+(t) := \int_0^t | < \dot{E}^p >_+ |d\tau$$
$$\alpha_-(t) := \int_0^t | < \dot{E}^p >_- |d\tau$$

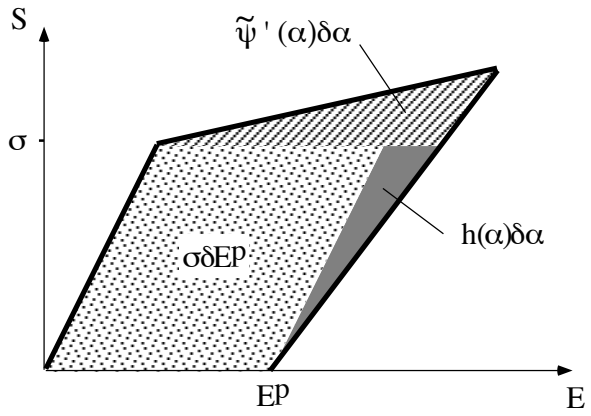

Figure 3.12: Dissipated and stored energy for the rate-independent part of the constitutive law.

where

$$< x >_- = \begin{cases} x & if\, x < 0 \\ 0 & if\, x \geq 0 \end{cases}$$

$$< x >_+ = \begin{cases} 0 & if\, x < 0 \\ x & if\, x \geq 0 \end{cases}$$

and

$$\alpha_+ + \alpha_- = \alpha$$

The variable α_- is thus the plastic strain cumulated in the negative strain direction, while α_+ is the strain cumulated in the positive strain direction.
In particular:

$$E^p = \alpha_+ - \alpha_-$$

The functions $\tilde{\psi}(\alpha)$ and $h(\alpha)$ would have to be redefined accordingly in two parts, each of them being a function of α_+ or α_-.

Remark 3.11 *To add the feature of linear kinematic hardening, the free energy potential ψ needs to be completed by the term:*

$$\frac{1}{2}\iota E^{p2}$$

where $\iota \geq 0$ is the kinematic hardening slope.

3.3 Three-dimensional model

The purpose of this section is to extend the preceeding one-dimensional model to the more difficult three-dimensional case. A new model of elasticity based on mean intercept length is first proposed that satisfies the hyperelastic assumption a priori. The model of coupled plastic and damage flow is then generalized to the three-dimensional case without viscosity in order to come out with a quasistatic constitutive law. Finally, an original anisotropic model for trabecular bone including elasticity and rate-independent plasticity with damage is suggested.

Notations The strain and stress vector spaces are denoted $\mathcal{E}$ and $\mathcal{S}$ respectively. A tensor product of two second order tensors $\boldsymbol{A}$ and $\boldsymbol{B}$ is defined by:

$$(\boldsymbol{A} \otimes \boldsymbol{B})\boldsymbol{X} = (\boldsymbol{B} : \boldsymbol{X})\boldsymbol{A} \qquad \forall \boldsymbol{X} \in \mathcal{E}$$

Three other useful products are defined by:

$$\begin{aligned}
(\boldsymbol{A}\underline{\otimes}\boldsymbol{B})\boldsymbol{X} &= \boldsymbol{A}\boldsymbol{X}\boldsymbol{B}^T \qquad \forall \boldsymbol{X} \in \mathcal{E} \\
(\boldsymbol{A}\overline{\otimes}\boldsymbol{B})\boldsymbol{X} &= \boldsymbol{A}\boldsymbol{X}^T\boldsymbol{B}^T \qquad \forall \boldsymbol{X} \in \mathcal{E} \\
(\boldsymbol{A}\underline{\overline{\otimes}}\boldsymbol{B})\boldsymbol{X} &= \frac{1}{2}(\boldsymbol{A}\boldsymbol{X}\boldsymbol{B}^T + \boldsymbol{A}\boldsymbol{X}^T\boldsymbol{B}^T) \qquad \forall \boldsymbol{X} \in \mathcal{E}
\end{aligned}$$

The intrinsic notation will be used throughout.

3.3.1 Elasticity

The free energy potential ψ is a function of the strain tensor $\boldsymbol{E}$, while the dissipation potential is zero. For linear elasticity, the potential is quadratic:

$$\psi = \psi(\boldsymbol{E}) = \frac{1}{2}\boldsymbol{E} : \mathbb{S}\boldsymbol{E} \tag{3.58}$$

where $\mathbb{S}$ is the fourth-order elasticity tensor with two minor symmetries resulting from those of $\boldsymbol{E}$ and $\boldsymbol{S}$ and a major one due to the existence of ψ:

$$\begin{aligned}
\mathbb{S} &= \mathbb{S}(\boldsymbol{I}\overline{\otimes}\boldsymbol{I}) \\
\mathbb{S} &= (\boldsymbol{I}\overline{\otimes}\boldsymbol{I})\mathbb{S} \\
\boldsymbol{H} : \mathbb{S}\boldsymbol{G} &= \boldsymbol{G} : \mathbb{S}\boldsymbol{H} \qquad \forall \boldsymbol{G}, \boldsymbol{H} \in \mathcal{E}
\end{aligned}$$

Convexity of ψ is insured by requiring that the elasticity tensor $\mathbb{S}$ is positive definite:

$$\boldsymbol{E} : \mathbb{S}\boldsymbol{E} > 0 \qquad \forall \boldsymbol{E}(\neq \mathbf{o}) \in \mathcal{E}$$

The constitutive equation is:

$$\boldsymbol{S} = \boldsymbol{S}(\boldsymbol{E}) = \boldsymbol{S}^E := \nabla_E \psi(\boldsymbol{E}) = \mathbb{S}\boldsymbol{E} \tag{3.59}$$

The inverse constitutive relation is obtained by the Legendre transform of ψ:

$$\psi^* = \psi^*(\boldsymbol{S}) = \boldsymbol{S} : \boldsymbol{E} - \psi$$

$$\boldsymbol{E} = \boldsymbol{E}(\boldsymbol{S}) = \nabla_S \psi^*(\boldsymbol{S}) = \mathbb{E}\boldsymbol{S} = \mathbb{S}^{-1}\boldsymbol{S} \tag{3.60}$$

where $\mathbb{E}$ is called the compliance tensor. In general anisotropy, the elasticity and compliance tensors involve 21 material constants.

3.3.2 Conewise linear elasticity

Conewise linear elasticity is the proper generalization of one-dimensional bimodular elasticity and consists in dividing the strain space into convex cones [38]. In practice, the division into two half-spaces is the most rational to account for a different behaviour in tension and in compression. Considering a hyperplane characterized by its unit normal $\boldsymbol{N}_E$ separating two half-spaces $\mathcal{E}_-$ and $\mathcal{E}_+$, the free energy potential is defined as:

$$\psi(\boldsymbol{E}) = \begin{cases} \frac{1}{2}\boldsymbol{E} : \mathbb{S}_-\boldsymbol{E} & \text{if } \boldsymbol{N}_E : \boldsymbol{E} < 0 \\ \frac{1}{2}\boldsymbol{E} : \mathbb{S}_+\boldsymbol{E} & \text{if } \boldsymbol{N}_E : \boldsymbol{E} \geq 0 \end{cases} \tag{3.61}$$

where $\mathbb{S}_-$ and $\mathbb{S}_+$ are two distinct elasticity tensors with the above symmetries and satisfying the condition:

$$\mathbb{S}_+ - \mathbb{S}_- = s\boldsymbol{N}_E \otimes \boldsymbol{N}_E \tag{3.62}$$

This latter condition ensures that the resulting constitutive law remains continuous:

$$\boldsymbol{S}(\boldsymbol{E}) = \begin{cases} \mathbb{S}_-\boldsymbol{E} & \text{if } \boldsymbol{N}_E : \boldsymbol{E} < 0 \\ \mathbb{S}_+\boldsymbol{E} & \text{if } \boldsymbol{N}_E : \boldsymbol{E} \geq 0 \end{cases} \tag{3.63}$$

Convexity of ψ is obtained if both elasticity tensors $\mathbb{S}_-$ and $\mathbb{S}_+$ are positive definite.
In stress space, a similar division into two half-spaces is obtained with a hyperplane defined by the normal $\boldsymbol{N}_S$:

$$\boldsymbol{N}_S = \mathbb{S}_-^{-1}\boldsymbol{N}_E = \mathbb{E}_-\boldsymbol{N}_E = \mathbb{E}_+\boldsymbol{N}_E$$

The Legendre transform of the free energy potential is the following:

$$\psi^*(\boldsymbol{S}) = \begin{cases} \frac{1}{2}\boldsymbol{S} : \mathbb{E}_-\boldsymbol{S} & \text{if } \boldsymbol{N}_S : \boldsymbol{S} < 0 \\ \frac{1}{2}\boldsymbol{S} : \mathbb{E}_+\boldsymbol{S} & \text{if } \boldsymbol{N}_S : \boldsymbol{S} \geq 0 \end{cases}$$

The inverse relations are then given by:

$$\boldsymbol{E}(\boldsymbol{S}) = \begin{cases} \mathbb{E}_-\boldsymbol{S} & \text{if } \boldsymbol{N}_S : \boldsymbol{S} < 0 \\ \mathbb{E}_+\boldsymbol{S} & \text{if } \boldsymbol{N}_S : \boldsymbol{S} \geq 0 \end{cases} \tag{3.64}$$

with

$$\mathbb{E}_+ - \mathbb{E}_- = e\boldsymbol{N}_S \otimes \boldsymbol{N}_S \tag{3.65}$$

and

$$e = -\frac{s}{1 + s\boldsymbol{N}_S : \boldsymbol{N}_E}$$

Remark 3.12 *The choice of the hyperplane characterized by $\boldsymbol{N}_E$ is a matter of experimental identification, but may be restricted by a condition on the material symmetry. For an isotropic material, the only admissible choice is given by:*

$$\boldsymbol{N}_E = \frac{1}{\sqrt{3}}\boldsymbol{I}$$

Remark 3.13 *Modelling distinct elastic properties in tension and compression is of particular interest in the case of unilateral damage, whereby the tensors $\mathbb{S}_-$ and $\mathbb{S}_+$ undergo different evolutions. However, this feature was not retained for the 3D constitutive law of trabecular bone in order to limit complexity of the model.*

3.3.3 Elasticity based on morphology

We emphasized in Subsection 2.2.3 that trabecular morphology can be described by a mean intercept length function, which seems to be reasonably approximated by the means of a positive definite second order tensor $\boldsymbol{M}$:

$$L_b(\boldsymbol{x}, \boldsymbol{N}) = \boldsymbol{N} : \boldsymbol{M}(\boldsymbol{x}) \tag{3.66}$$

where the argument $\boldsymbol{x}$ recalls that privileged directions and degree of anisotropy are allowed to be inhomogeneous, but will be omitted in the subsequent development to simplify the notation. The eigenvalues of $\boldsymbol{M}$ are thus the mean intercept lengths along the three orthogonal principal directions of the tensor.
In a first step, we admit that material symmetry of trabecular bone is completely described by morphology and that the symmetry group $\mathcal{G}$ associated with trabecular bone material is characterized by the tensor $\boldsymbol{M}$:

$$\boldsymbol{Q} \in \mathcal{G} \Longleftrightarrow \boldsymbol{Q}^T \boldsymbol{M} \boldsymbol{Q} = \boldsymbol{M} \tag{3.67}$$

A tensor valued function $f(\boldsymbol{E})$ invariant with respect to the elements of the symmetry group $\mathcal{G}$ can be identified to an isotropic function $\tilde{f}(\boldsymbol{E}, \boldsymbol{M})$ of the same argument and the corresponding structural tensor $\boldsymbol{M}$:

$$\begin{aligned} f(\boldsymbol{E}) &= f(\boldsymbol{Q}^T \boldsymbol{E} \boldsymbol{Q}) \qquad \forall \boldsymbol{Q} \in \mathcal{G} \\ \tilde{f}(\boldsymbol{E}, \boldsymbol{M}) &= \tilde{f}(\boldsymbol{Q}^T \boldsymbol{E} \boldsymbol{Q}, \boldsymbol{Q}^T \boldsymbol{M} \boldsymbol{Q}) \qquad \forall \boldsymbol{Q} \in \mathcal{O} \end{aligned} \tag{3.68}$$

Representation theorems provide then the most general form of an isotropic tensor valued function $\tilde{f}(\boldsymbol{E}, \boldsymbol{M})$ in terms of invariants of the arguments [10].
For two second order tensor arguments, a set of irreducible invariants is given by:

$$\begin{gathered} Tr(\boldsymbol{E}), Tr(\boldsymbol{E}^2), Tr(\boldsymbol{E}^3) \\ Tr(\boldsymbol{M}), Tr(\boldsymbol{M}^2), Tr(\boldsymbol{M}^3) \\ Tr(\boldsymbol{E}\boldsymbol{M}), Tr(\boldsymbol{E}^2\boldsymbol{M}), Tr(\boldsymbol{E}\boldsymbol{M}^2), Tr((\boldsymbol{E}\boldsymbol{M})^2) \end{gathered}$$

Remark 3.14 *In this list we use the product* $Tr((\boldsymbol{E}\boldsymbol{M})^2)$ *instead of the more usual* $Tr(\boldsymbol{E}^2\boldsymbol{M}^2)$.

Retaining only quadratic terms in $\boldsymbol{E}$ to obtain linear elasticity, the general form of the free energy potential becomes:

$$\begin{aligned}\psi = \psi(\boldsymbol{E},\boldsymbol{M}) &= \frac{c_1}{2}Tr^2(\boldsymbol{E}) + \frac{c_2}{2}Tr(\boldsymbol{E}^2) + \frac{c_3}{2}Tr^2(\boldsymbol{EM}) \\ &+ c_4 Tr(\boldsymbol{E}^2\boldsymbol{M}) + \frac{c_5}{2}Tr^2(\boldsymbol{EM}^2) + \frac{c_6}{2}Tr((\boldsymbol{EM})^2) \\ &+ c_7 Tr(\boldsymbol{E})Tr(\boldsymbol{EM}) + c_8 Tr(\boldsymbol{EM})Tr(\boldsymbol{EM}^2) \\ &+ c_9 Tr(\boldsymbol{E})Tr(\boldsymbol{EM}^2) \end{aligned} \tag{3.69}$$

where the c_i are functions of the three invariants of $\boldsymbol{M}$.
The constitutive equation is then given by:

$$\begin{aligned}\boldsymbol{S} &= c_1 Tr(\boldsymbol{E})\boldsymbol{I} + c_2\boldsymbol{E} + c_3 Tr(\boldsymbol{EM})\boldsymbol{M} \\ &+ c_4(\boldsymbol{EM}+\boldsymbol{ME}) + c_5 Tr(\boldsymbol{EM}^2)\boldsymbol{M}^2 + c_6(\boldsymbol{MEM}) \\ &+ c_7(Tr(\boldsymbol{EM})\boldsymbol{I} + Tr(\boldsymbol{E})\boldsymbol{M}) + c_8(Tr(\boldsymbol{EM}^2)\boldsymbol{M} + Tr(\boldsymbol{EM})\boldsymbol{M}^2) \\ &+ c_9(Tr(\boldsymbol{EM}^2)\boldsymbol{I} + Tr(\boldsymbol{E})\boldsymbol{M}^2) \end{aligned} \tag{3.70}$$

The elasticity tensor becomes:

$$\begin{aligned}\mathbb{S} &= c_1\boldsymbol{I}\otimes\boldsymbol{I} + c_2\boldsymbol{I}\underline{\otimes}\boldsymbol{I} + c_3\boldsymbol{M}\otimes\boldsymbol{M} \\ &+ c_4(\boldsymbol{M}\underline{\otimes}\boldsymbol{I} + \boldsymbol{I}\underline{\otimes}\boldsymbol{M}) + c_5\boldsymbol{M}^2\otimes\boldsymbol{M}^2 + c_6\boldsymbol{M}\underline{\otimes}\boldsymbol{M} \\ &+ c_7(\boldsymbol{I}\otimes\boldsymbol{M} + \boldsymbol{M}\otimes\boldsymbol{I}) + c_8(\boldsymbol{M}\otimes\boldsymbol{M}^2 + \boldsymbol{M}^2\otimes\boldsymbol{M}) \\ &+ c_9(\boldsymbol{I}\otimes\boldsymbol{M}^2 + \boldsymbol{M}^2\otimes\boldsymbol{I}) \end{aligned} \tag{3.71}$$

We consider now the spectral decomposition of $\boldsymbol{M}$:

$$\boldsymbol{M} = m_i\boldsymbol{M}_i \qquad \boldsymbol{M}_i = \boldsymbol{m}_i\otimes\boldsymbol{m}_i \tag{3.72}$$

where the $\boldsymbol{m}_i$ are the unit orthogonal eigenvectors and m_i the eigenvalues of $\boldsymbol{M}$.

The above constitutive equations correspond to different symmetry groups according to the eigenvalues m_i of the structural tensor $\boldsymbol{M}$. If the three eigenvalues are distinct, the symmetry group is orthotropy. If two eigenvalues are degenerated, the symmetry group is transverse isotropy and if all three eigenvalues are degenerated, the symmetry group is isotropy.

Remark 3.15 *Despite the number of coefficients appearing in the elasticity tensor, the present approach based on a single second order structural tensor can not describe general orthotropy. As a matter of proof it is sufficient to realize that cubic symmetry, which is a particular case of general orthotropy, can not be characterized.*

At this stage, the model is extremely general and additionnal assumptions are necessary to guide the choice of the nine functions c_i. For this purpose, we imagine the structural tensor as a deformation of material frame:

$$\boldsymbol{m}_i = \sqrt{\boldsymbol{M}}\boldsymbol{e}_i \qquad i = 1,2,3 \tag{3.73}$$

This deformation of material frame substitutes the identity tensor $\boldsymbol{I}$ mapping the original into the new material space by $\boldsymbol{M}$ and an isotropic elasticity tensor:

$$\mathbb{S} = \hat{\lambda}_c \boldsymbol{I} \otimes \boldsymbol{I} + 2\hat{\mu}_c \boldsymbol{I} \underline{\overline{\otimes}} \boldsymbol{I}$$

is transformed into:

$$\mathbb{S} = \hat{\lambda}_c \boldsymbol{M} \otimes \boldsymbol{M} + 2\hat{\mu}_c \boldsymbol{M} \underline{\overline{\otimes}} \boldsymbol{M} \tag{3.74}$$

where $\hat{\lambda}_c$ and $\hat{\mu}_c$ are Lamé like constants.
In the principal reference frame of $\boldsymbol{M}$:

$$\begin{aligned}\mathbb{S} = &\frac{\hat{\lambda}_c}{2} m_i m_j (\boldsymbol{M}_i \otimes \boldsymbol{M}_j + \boldsymbol{M}_j \otimes \boldsymbol{M}_i) \\ &+ \hat{\mu}_c m_i m_j (\boldsymbol{M}_i \underline{\overline{\otimes}} \boldsymbol{M}_j + \boldsymbol{M}_j \underline{\overline{\otimes}} \boldsymbol{M}_i)\end{aligned}$$

which turns out to be a particular form of the previous model, where:

$$c_3 = \hat{\lambda}_c \tag{3.75}$$

$$c_6 = 2\hat{\mu}_c \tag{3.76}$$

and

$$c_1 = c_2 = c_4 = c_5 = c_7 = c_8 = c_9 = 0 \tag{3.77}$$

This geometrical approximation provides the most simple orthotropic model (2 constants) that degenerates in transverse isotropy and isotropy if two, respectively three, eigenvalues of $\boldsymbol{M}$ are identical.

In order to work with dimensionless variables, we choose the following normalization of the tensor $\boldsymbol{M}$:

$$Tr^2(\boldsymbol{M}) = (\sum_{i=1}^{3} m_i)^2 = 1 \tag{3.78}$$

The same transformation as Eq. 3.73 can be considered for an arbitrary positive power k of $\boldsymbol{M}$ and provides the following engineering constants:

$$\epsilon_i = \hat{\epsilon}_c m_i^{2k} \tag{3.79}$$

$$\nu_{ij} = \hat{\nu}_c \frac{m_j^k}{m_i^k} \tag{3.80}$$

$$\mu_{ij} = \hat{\mu}_c m_i^k m_j^k \tag{3.81}$$

with

$$\hat{\mu}_c = \frac{\hat{\epsilon}_c}{2(1+\hat{\nu}_c)} \tag{3.82}$$

The elasticity tensor $\mathbb{S}$ is positive definite under the conditions:

$$\hat{\epsilon}_c > 0 \qquad \frac{1}{2} > \hat{\nu}_c > -1 \tag{3.83}$$

or

$$3\hat{\lambda}_c + 2\hat{\mu}_c > 0 \qquad \hat{\mu}_c > 0 \tag{3.84}$$

whereby these results hold for any positive definite tensor $\boldsymbol{M}$ and exponent k.

Remark 3.16 *A similar approach has already been explored by Cowin [32], but the choice of* $Tr((\boldsymbol{EM})^2)$ *instead of* $Tr(\boldsymbol{E}^2\boldsymbol{M}^2)$ *and the assumption 3.74 allows to construct a different model that provides invertible constitutive equations and ensures convexity of the free energy potential under trivial conditions.*

Unfortunately, our experimental data seem to show that the relation 3.82 does not always hold and shows that mechanical anisotropy of trabecular bone does not automatically degenerate into isotropy when the eigenvalues of $\boldsymbol{M}$ degenerate (Table 5.4). This finding suggests that mechanical anisotropy of trabecular bone derives not only from the second order stereological tensor $\boldsymbol{M}$ and that a generalization of the previous model is required.

3.3.4 Elasticity of trabecular bone

For general orthotropy, the symmetry group $\mathcal{G}$ is the following:

$$\mathcal{G} = \{+\mathcal{I}, -\mathcal{I}, \mathcal{M}_1, \mathcal{M}_2, \mathcal{M}_3\} \tag{3.85}$$

where $\mathcal{M}_1$, $\mathcal{M}_2$, $\mathcal{M}_3$ are the reflexions with respect to the orthogonal planes $(\boldsymbol{m}_2, \boldsymbol{m}_3)$, $(\boldsymbol{m}_3, \boldsymbol{m}_1)$ and $(\boldsymbol{m}_1, \boldsymbol{m}_2)$. We assume that these planes of symmetry are defined by trabecular morphology and thus correspond to the planes defined by the 3 orthogonal eigenvectors of the stereological tensor $\boldsymbol{M}$.
The structural tensors associated with $\mathcal{G}$ are given by:

$$\boldsymbol{M}_1 = \boldsymbol{m}_1 \otimes \boldsymbol{m}_1 \qquad \boldsymbol{M}_2 = \boldsymbol{m}_2 \otimes \boldsymbol{m}_2 \qquad \boldsymbol{M}_3 = \boldsymbol{m}_3 \otimes \boldsymbol{m}_3 \tag{3.86}$$

with $\boldsymbol{M}_1 + \boldsymbol{M}_2 + \boldsymbol{M}_3 = \boldsymbol{I}$.
These structural tensors have the property:

$$\boldsymbol{Q} \in \mathcal{G} \Longleftrightarrow \boldsymbol{Q}^T \boldsymbol{M}_i \boldsymbol{Q} = \boldsymbol{M}_i \qquad i = 1, 2, 3 \tag{3.87}$$

Representation theorems provide again the general form of a scalar function in terms of basic invariants of its tensorial arguments under the symmetry group $\mathcal{G}$. Retaining the quadratic terms in $\boldsymbol{E}$ to remain in linear elasticity and introducing the normalized eigenvalues of $\boldsymbol{M}$ to account for trabecular morphology, the free energy potential exhibits the following general form:

$$\psi = \psi(\boldsymbol{E}, \boldsymbol{M}_i) = \frac{1}{2}\lambda_{ij} Tr(\boldsymbol{M}_i \boldsymbol{E}) Tr(\boldsymbol{M}_j \boldsymbol{E}) + \mu_{ij} Tr(\boldsymbol{M}_i \boldsymbol{E} \boldsymbol{M}_j \boldsymbol{E}) \tag{3.88}$$

where the 9 independent functions λ_{ij} and $\mu_{ij, i \neq j}$ depend on the three eigenvalues m_i of $\boldsymbol{M}$ and the three structural tensors $\boldsymbol{M}_i$ correspond to the orthogonal principal directions of the tensor $\boldsymbol{M}$.

Remark 3.17 *Unlike the previous model based on a single structural tensor, this formulation allows the description of all types of orthotropy and involves 9 independent constants and three orthogonal directions. In particular, cubic symmetry can be characterized.*

Following a similar approach as in the previous case, we postulate an orthotropic free energy potential that degenerates into cubic symmetry when the eigenvalues of the fabric tensor $\boldsymbol{M}$ are identical:

$$\begin{aligned}\psi &= \sum_{i=1}^{3}(\hat{\lambda}_c + 2\hat{\mu}_c)m_i^{2k}Tr^2(\boldsymbol{M}_i\boldsymbol{E}) \\ &+ \sum_{i,j=1,i<j}^{3}\hat{\lambda}_c^* m_i^k m_j^k Tr(\boldsymbol{M}_i\boldsymbol{E})Tr(\boldsymbol{M}_j\boldsymbol{E}) \\ &+ \sum_{i,j=1,i<j}^{3}\hat{\mu}_c m_i^k m_j^k Tr(\boldsymbol{M}_i\boldsymbol{E}\boldsymbol{M}_j\boldsymbol{E}) \end{aligned} \tag{3.89}$$

The associated constitutive law is given by:

$$\begin{aligned}\boldsymbol{S} &= \sum_{i=1}^{3}(\hat{\lambda}_c + 2\hat{\mu}_c)m_i^{2k}Tr(\boldsymbol{M}_i\boldsymbol{E})\boldsymbol{M}_i \\ &+ \sum_{i,j=1,i<j}^{3}\frac{1}{2}\hat{\lambda}_c^* m_i^k m_j^k(Tr(\boldsymbol{M}_i\boldsymbol{E})\boldsymbol{M}_j + Tr(\boldsymbol{M}_j\boldsymbol{E})\boldsymbol{M}_i) \\ &+ \sum_{i,j=1,i<j}^{3}\hat{\mu}_c m_i^k m_j^k(\boldsymbol{M}_i\boldsymbol{E}\boldsymbol{M}_j + \boldsymbol{M}_j\boldsymbol{E}\boldsymbol{M}_i) \end{aligned} \tag{3.90}$$

The elasticity tensor becomes:

$$\begin{aligned}\mathbb{S} &= \sum_{i=1}^{3}\hat{\lambda}_c m_i^{2k}\boldsymbol{M}_i \otimes \boldsymbol{M}_i \\ &+ \sum_{i,j=1,i<j}^{3}\frac{1}{2}\hat{\lambda}_c^* m_i^k m_j^k(\boldsymbol{M}_i \otimes \boldsymbol{M}_j + \boldsymbol{M}_j \otimes \boldsymbol{M}_i) \\ &+ \sum_{i,j=1,i\leq j}^{3}\hat{\mu}_c m_i^k m_j^k(\boldsymbol{M}_i\underline{\overline{\otimes}}\boldsymbol{M}_j + \boldsymbol{M}_j\underline{\overline{\otimes}}\boldsymbol{M}_i) \end{aligned} \tag{3.91}$$

The inverse compliance tensor:

$$\begin{aligned}\mathbb{E} &= \sum_{i=1}^{3}\frac{1}{\hat{\epsilon}_c}\frac{1}{m_i^{2k}}\boldsymbol{M}_i \otimes \boldsymbol{M}_i \\ &+ \sum_{i,j=1,i<j}^{3}\frac{1}{2}\frac{\hat{\nu}_c}{\hat{\epsilon}_c}\frac{1}{m_i^k m_j^k}(\boldsymbol{M}_i \otimes \boldsymbol{M}_j + \boldsymbol{M}_j \otimes \boldsymbol{M}_i) \\ &+ \sum_{i,j=1,i\leq j}^{3}\frac{1}{\hat{\mu}_c}\frac{1}{m_i^k m_j^k}(\boldsymbol{M}_i\underline{\overline{\otimes}}\boldsymbol{M}_j + \boldsymbol{M}_j\underline{\overline{\otimes}}\boldsymbol{M}_i) \end{aligned} \tag{3.92}$$

The usual engineering constants are given by:

$$\epsilon_i = \hat{\epsilon}_c m_i^{2k} \tag{3.93}$$

$$\nu_{ij} = \hat{\nu}_c \frac{m_j^k}{m_i^k} \tag{3.94}$$

$$\mu_{ij} = \hat{\mu}_c m_i^k m_j^k \tag{3.95}$$

where

$$\begin{aligned} \hat{\epsilon}_c &= \frac{(\hat{\lambda}_c + 2\hat{\mu}_c - \hat{\lambda}_c^*)(\hat{\lambda}_c + 2\hat{\mu}_c + 2\hat{\lambda}_c^*)}{(\hat{\lambda}_c + 2\hat{\mu}_c + \hat{\lambda}_c^*)} \\ \hat{\nu}_c &= \frac{\hat{\lambda}_c^*}{(\hat{\lambda}_c + 2\hat{\mu}_c + \hat{\lambda}_c^*)} \\ \hat{\mu}_c &= \hat{\mu}_c \end{aligned}$$

or conversely:

$$\begin{aligned} \hat{\lambda}_c &= \frac{\hat{\epsilon}_c(1-\hat{\nu}_c)}{(1+\hat{\nu}_c)(1-2\hat{\nu}_c)} - 2\hat{\mu}_c \\ \hat{\lambda}_c^* &= \frac{\hat{\epsilon}_c \hat{\nu}_c}{(1+\hat{\nu}_c)(1-2\hat{\nu}_c)} \\ \hat{\mu}_c &= \hat{\mu}_c \end{aligned}$$

The compliance and elasticity tensors are positive definite under the following conditions:

$$\hat{\epsilon}_c > 0 \qquad \frac{1}{2} > \hat{\nu}_c > -1 \qquad \hat{\mu}_c > 0 \tag{3.96}$$

or

$$\hat{\lambda}_c + 2\hat{\mu}_c > 0 \qquad \hat{\lambda}_c + 2\hat{\mu}_c > \hat{\lambda}^* > -\frac{1}{2}(\hat{\lambda}_c + 2\hat{\mu}_c) \qquad \hat{\mu}_c > 0$$

whereby this result holds for any set of positive eigenvalues m_i and thus for any mean intercept length tensor $\boldsymbol{M}$.

Remark 3.18 *Recalling the normalization of the model with respect to structural density, the previous engineering constants represent in fact:*

$$\begin{aligned} \hat{\epsilon}_c &= \epsilon_c \rho^{2l} \\ \hat{\nu}_c &= \nu_c \\ \hat{\mu}_c &= \mu_c \rho^{2l} \end{aligned}$$

where ϵ_c,ν_c and μ_c are true constants.

The elastic behaviour of trabecular bone is thus completely defined by the three constants ϵ_c, μ_c, ν_c, the two exponents k, l and the normalized eigenvalues m_i.

Remark 3.19 *The essential difference between the second model and the first one lies in the choice of the structural tensors. By considering three independent structural tensors, the full class of orthotropy is obtained, in particular cubic symmetry is included.*

3.3.5 Plasticity and damage

For plasticity, the internal variable remains the irreversible deformation tensor $\boldsymbol{E}^p$ and a similar decomposition of the total deformation is assumed as in the one-dimensional model:

$$\boldsymbol{E} = \boldsymbol{E}^e + \boldsymbol{E}^p \tag{3.97}$$

For damage, the choice is more difficult. There is no general agreement whether damage should be represented by a zero, first, second, fourth or even eighth order tensor [81]. In fact, a natural generalization of the one-dimensional damage model would consist of attaching a damage variable to each of the 21 constants of the elasticity tensor. The complexity of such a model is prohibitive. In particular, the break of material symmetry induced by real damage constitutes an extreme theoretical and experimental difficulty. In this perspective, description of damage is often restricted to single monotonic loading experiments. The most simple approach assumes that the distribution and thus mechanical effect of damage remains isotropic and requires a single scalar variable [88].
Following this track and attempting to build a standard generalized model, we assume a decomposition of the elasticity and compliance tensor spaces in orthogonal direct sums:

$$\boldsymbol{\mathcal{S}} = \overline{\boldsymbol{\mathcal{S}}} \oplus \boldsymbol{\mathcal{S}}' \qquad \boldsymbol{\mathcal{E}} = \overline{\boldsymbol{\mathcal{E}}} \oplus \boldsymbol{\mathcal{E}}' \tag{3.98}$$

The elasticity and compliance tensors can thus be divided in two contributions,

$$\mathbb{S} = \overline{\mathbb{S}} + \mathbb{S}' \qquad \mathbb{E} = \overline{\mathbb{E}} + \mathbb{E}' \tag{3.99}$$

such that:

$$\overline{\mathbb{S}}\mathbb{S}' \equiv 0 \qquad \overline{\mathbb{E}}\mathbb{E}' \equiv 0$$

The strain and stress spaces $\mathcal{E}$ and $\mathcal{S}$ are divided accordingly:

$$\mathcal{E} = \overline{\mathcal{E}} \oplus \mathcal{E}' \qquad \mathcal{S} = \overline{\mathcal{S}} \oplus \mathcal{S}' \tag{3.100}$$

The elastic constitutive law can be split:

$$\overline{\boldsymbol{S}} = \overline{\mathbb{S}}\boldsymbol{E} \qquad \boldsymbol{S}' = \mathbb{S}'\boldsymbol{E} \tag{3.101}$$

Remark 3.20 *The existence and uniqueness of such a decomposition, excepted the trivial case where $\overline{\mathbb{S}} = 0$ or $\mathbb{S}' = 0$, is verified for isotropic tensors, but uniqueness seems not to hold for anisotropic tensors [124]. The spectral decomposition of symmetric fourth-order tensors involves up to six eigenspaces and the division into two subspaces appears not to be unique.*

Assuming that only one part of the elasticity tensor is damaged, the following free energy potential is then postulated:

$$\begin{aligned} \psi(\boldsymbol{E}, \boldsymbol{E}^p, \alpha) &= \frac{1}{2}(\boldsymbol{E} - \boldsymbol{E}^p) : \overline{\mathbb{S}}(\boldsymbol{E} - \boldsymbol{E}^p) \\ &+ \frac{1}{2} f(\alpha)(\boldsymbol{E} - \boldsymbol{E}^p) : \mathbb{S}'(\boldsymbol{E} - \boldsymbol{E}^p) + \tilde{\psi}(\alpha) \end{aligned} \tag{3.102}$$

where f and $\tilde{\psi}$ satisfy the same conditions as in the one-dimensional model.
The conjugate variables are:

$$\begin{aligned} \boldsymbol{S}^E &:= \overline{\mathbb{S}}(\boldsymbol{E} - \boldsymbol{E}^p) + f(\alpha)\mathbb{S}'(\boldsymbol{E} - \boldsymbol{E}^p) \\ \boldsymbol{S}^{Ep} &:= \overline{\mathbb{S}}(\boldsymbol{E} - \boldsymbol{E}^p) + f(\alpha)\mathbb{S}'(\boldsymbol{E} - \boldsymbol{E}^p) \\ S^\alpha &:= -\frac{1}{2} f'(\alpha)(\boldsymbol{E} - \boldsymbol{E}^p)\mathbb{S}'(\boldsymbol{E} - \boldsymbol{E}^p) - \tilde{\psi}'(\alpha) \end{aligned}$$

The dissipation potential is divided in two parts:

$$\phi(\dot{\boldsymbol{E}}^p, \dot{\alpha}) = \phi_1(\dot{\boldsymbol{E}}^p) + \phi_2(\dot{\alpha})$$

with

$$\phi_1(\dot{\boldsymbol{E}}^p) = (y_\sigma + g)\sqrt{\dot{\boldsymbol{E}}^p : \mathbb{S}'\dot{\boldsymbol{E}}^p} \tag{3.103}$$

$$\phi_2(\dot{\alpha}) = (h - g)\dot{\alpha} + I_{[0;+\infty]}(\dot{\alpha}) \tag{3.104}$$

where $y_\sigma > 0$ is the yield limit, $g = g(\alpha)$ satisfies the same conditions as in the one-dimensional model and

$$h = h(\alpha) = -y_\sigma^2 \frac{f'(\alpha)}{2f^2(\alpha)}$$

The function $g(\alpha)$ represents the increase of elastic energy density beyond the yield limit and $h(\alpha)$ is the conjugate quantity responsible for the dissipation of damage.

The resulting constitutive equations are:

$$\boldsymbol{S}^{E^p} \in \partial_{\dot{E}^p}\phi_1 = \begin{cases} \left\{\boldsymbol{S} | \sqrt{\boldsymbol{S} : \mathbb{E}'\boldsymbol{S}} < y_\sigma + g\right\} & \text{if } \dot{\boldsymbol{E}}^p = \mathbf{o} \\ (y_\sigma + g)\dfrac{\mathbb{S}'\dot{\boldsymbol{E}}^p}{\sqrt{\dot{\boldsymbol{E}}^p : \mathbb{S}'\dot{\boldsymbol{E}}^p}} & \text{if } \dot{\boldsymbol{E}}^p \neq \mathbf{o} \end{cases} \tag{3.105}$$

$$S^\alpha \in \partial_{\dot{\alpha}}\phi_2 = \begin{cases} \emptyset & \text{if } \dot{\alpha} < 0 \\ [-\infty; h - g] & \text{if } \dot{\alpha} = 0 \\ h - g & \text{if } \dot{\alpha} > 0 \end{cases} \tag{3.106}$$

The Fenchel-Legendre transform provides the dual dissipation functions:

$$\phi_1^*(\boldsymbol{S}^{E^p}) = \begin{cases} 0 & \text{if } \sqrt{\boldsymbol{S}^{E^p} : \mathbb{E}'\boldsymbol{S}^{E^p}} \in [0; y_\sigma + g] \\ +\infty & \text{otherwise} \end{cases}$$

$$\phi_2^*(S^\alpha) = \begin{cases} 0 & \text{if } S^\alpha \in [-\infty; h - g] \\ +\infty & \text{otherwise} \end{cases}$$

The flow rules for the internal state variables become:

$$\dot{\boldsymbol{E}}^p \in \partial_{S^{E^p}}\phi_1^* = \begin{cases} 0 & \text{if } \sqrt{\boldsymbol{S}^{E^p} : \mathbb{E}'\boldsymbol{S}^{E^p}} \in [0; y_\sigma + g[\\ \dot{\lambda}_L \dfrac{\mathbb{E}'\boldsymbol{S}^{E^p}}{\sqrt{\boldsymbol{S}^{E^p} : \mathbb{E}'\boldsymbol{S}^{E^p}}} & \text{if } \sqrt{\boldsymbol{S}^{E^p} : \mathbb{E}'\boldsymbol{S}^{E^p}} = y_\sigma + g \\ \emptyset & \text{if } \sqrt{\boldsymbol{S}^{E^p} : \mathbb{E}'\boldsymbol{S}^{E^p}} > y_\sigma + g \end{cases} \tag{3.107}$$

$$\dot{\alpha} \in \partial_{S^\alpha}\phi_2^* = \begin{cases} 0 & \text{if } S^\alpha \in [-\infty; h - g[\\ \dot{\lambda}_L & \text{if } S^\alpha = h - g \\ \emptyset & \text{if } S^\alpha > h - g \end{cases} \tag{3.108}$$

where $\dot{\lambda}_L \in [0, +\infty]$. In this formulation, α remains a measure of the cumulated plastic strain, but with respect to the metric $\mathbb{S}'$:

$$\alpha(t) = \int_0^t \sqrt{\dot{\boldsymbol{E}}^p : \mathbb{S}'\dot{\boldsymbol{E}}^p} d\tau \tag{3.109}$$

The variable α as well as the quantities S^α, y_σ, g and h have thus the physical dimension of the square root of an energy density.
In the Kuhn-Tucker form, the simultaneous flow rules can be derived from:

$$\begin{aligned} y(\boldsymbol{S}^{E^p}, S^\alpha) &= \sqrt{\boldsymbol{S}^{E^p} : \mathbb{E}' \boldsymbol{S}^{E^p}} + S^\alpha - h - y_\sigma \\ \dot{\boldsymbol{E}}^p &= \dot{\lambda}_L \frac{\mathbb{E}' \boldsymbol{S}^{E^p}}{\sqrt{\boldsymbol{S}^{E^p} : \mathbb{E}' \boldsymbol{S}^{E^p}}} \\ \dot{\alpha} &= \dot{\lambda}_L \\ \dot{\lambda}_L \geq 0 \qquad y &\leq 0 \qquad \dot{\lambda}_L y = 0 \end{aligned}$$

Isotropic symmetry In the case of isotropic symmetry, there is a unique orthogonal decomposition of $\mathbb{S}$ in hydrostatic and deviatoric parts:

$$\mathbb{S} = \lambda(\boldsymbol{I} \otimes \boldsymbol{I}) + 2\mu(\boldsymbol{I} \underline{\overline{\otimes}} \boldsymbol{I}) \tag{3.110}$$

$$\overline{\mathbb{S}} = \kappa(\boldsymbol{I} \otimes \boldsymbol{I}) \tag{3.111}$$

$$\mathbb{S}' = 2\mu(\boldsymbol{I} \underline{\overline{\otimes}} \boldsymbol{I} - \frac{1}{3}\boldsymbol{I} \otimes \boldsymbol{I}) \tag{3.112}$$

where κ is the compressibility modulus:

$$\kappa = \frac{3\lambda + 2\mu}{3}$$

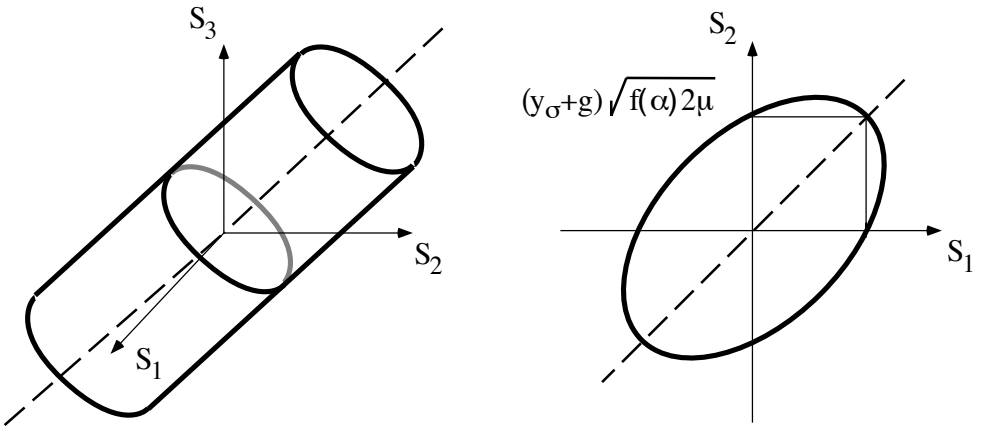

Figure 3.13: Von Mises yield surface in a three- and two-dimensional stress space.

For this decomposition, the model corresponds to the classical Von Mises criterion with associated flow rules:

$$\begin{aligned} y(\boldsymbol{S}, S^\alpha) &= \frac{\|\boldsymbol{S}'\|}{\sqrt{2\mu}} + S^\alpha - h - y_\sigma \\ \dot{\boldsymbol{E}}^p &= \frac{\dot{\lambda}_L}{\sqrt{2\mu}} \frac{\boldsymbol{S}'}{\|\boldsymbol{S}'\|} \\ \dot{\alpha} &= \dot{\lambda}_L \\ \dot{\lambda}_L \geq 0 \qquad y &\leq 0 \qquad \dot{\lambda}_L y = 0 \end{aligned}$$

The damage of the deviatoric part of the elasticity tensors can be identified through the shear coefficient:

$$\kappa = \kappa_0 \tag{3.113}$$

$$\mu = \mu_0 f(\alpha) \tag{3.114}$$

where κ_0 and μ_0 are the undamaged material constants.

Orthotropic symmetry In orthotropic symmetry, the spectral decomposition of a fourth-order tensor involves six one-dimensional invariant subspaces and decomposition of this tensor into two subspaces is apparently not unique. The choice of a specific decomposition seems somewhat arbitrary and generalization of the previous damage formulation would require extensive experimental support. Therefore, we restrict ourselves to the most simple model of damage for an orthotropic elasticity tensor by choosing:

$$\overline{\mathbb{S}} \equiv 0 \qquad \mathbb{S}' \equiv \mathbb{S} \tag{3.115}$$

The free energy potential reduces to:

$$\psi(\boldsymbol{E}, \boldsymbol{E}^p, \alpha) = \frac{1}{2} f(\alpha)(\boldsymbol{E} - \boldsymbol{E}^p) : \mathbb{S}(\boldsymbol{E} - \boldsymbol{E}^p) + \tilde{\psi}(\alpha) \tag{3.116}$$

The assumed dissipation potential is:

$$\phi(\dot{\boldsymbol{E}}^p, \dot{\alpha}) = (y_\sigma + g)\sqrt{\dot{\boldsymbol{E}}^p : \mathbb{S}\dot{\boldsymbol{E}}^p} + (h - g)\dot{\alpha} + I_{[0;+\infty]}(\dot{\alpha}) \tag{3.117}$$

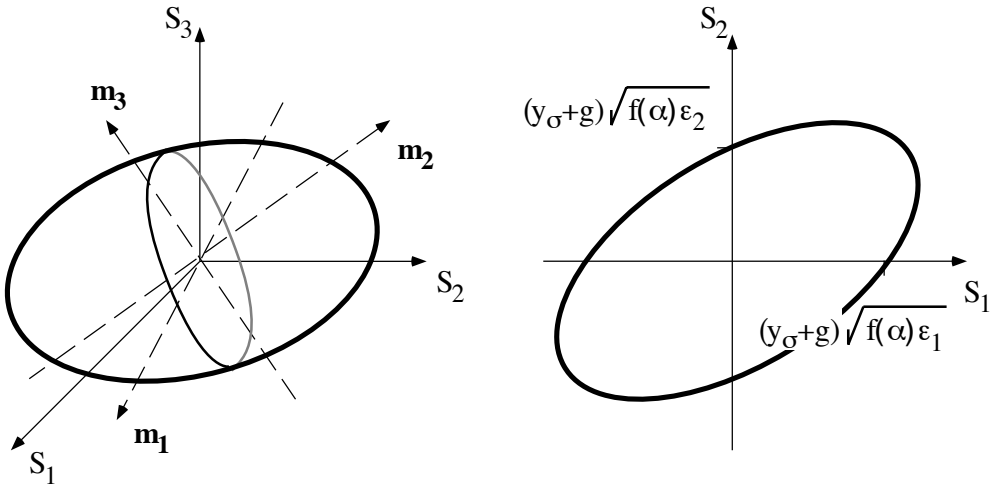

Figure 3.14: Yield surface in a three- and two-dimensional principal stress space for the orthotropic model.

In this case, the yield function includes the elastic energy:

$$y(\boldsymbol{S}, S^\alpha) = \sqrt{\boldsymbol{S} : \mathbb{E}\boldsymbol{S}} + S^\alpha - h - y_\sigma$$

The flow rule for the plastic deformation becomes radial:

$$\begin{aligned} \dot{\boldsymbol{E}}^p &= \dot{\lambda}_L \sqrt{\frac{f(\alpha)}{\boldsymbol{S} : \mathbb{E}\boldsymbol{S}}} (\boldsymbol{E} - \boldsymbol{E}^p) \\ \dot{\alpha} &= \dot{\lambda}_L \\ \dot{\lambda}_L \geq 0 \qquad y &\leq 0 \qquad \dot{\lambda}_L y = 0 \end{aligned}$$

The damaged material coefficients are:

$$\epsilon_i = f(\alpha)\epsilon_{i_0} \tag{3.118}$$

$$\nu_{ij} \equiv \nu_{ij_0} \tag{3.119}$$

$$\mu_{ij} = f(\alpha)\mu_{ij_0} \tag{3.120}$$

To conclude, using the orthotropic elasticity model based on three structural tensors, the latter simplified model for plasticity and damage flow and leaving aside the conewise definition of elasticity, the three-dimensional rate-independent mechanical behaviour of trabecular bone is completely defined by the four coefficients ϵ_c, ν_c, μ_c, y_σ, the two exponents k, l, the mean intercept tensor $\boldsymbol{M}$ and the two functions $f(\alpha)$ and $g(\alpha)$.

Remark 3.21 *We are aware of the rather artificial bearance of assumption 3.115, but the usual approach of Hill of assuming an incompressible yield criterion in stress space which does not correspond to an "isovolumic" plastic strain in strain space for anisotropic materials seems at least as artificial [68]. Another author [129] suggested recently the use of an "isovolumic" yield criterion for trabecular bone, but this choice was in clear contradiction with our experimental findings.*

Chapter 4

Numerical models

In this chapter, the classical numerical methods employed in solid mechanics are reviewed together with the implicit projection algorithm used for rate-independent plasticity. The incremental algorithms we developed for the resolution of boundary value problems involving our 1D and 3D constitutive laws for elastoplasticity with damage are then described.

4.1 Numerical methods in solid mechanics

In general, the resolution of boundary value problems in continuum mechanics implies integrating a set of coupled nonlinear partial differential equations. In biomechanical applications, these boundary value problems often involve complex geometries, highly nonlinear material behaviours and sophisticated boundary conditions [71]. For such problems, analytical solutions remain exceptional and numerical schemes are necessary for their resolution.

A synthetic approach for solving complex boundary value problems consists of applying successively the finite element method for space discretization, the iteration method for the resolution of the geometric and material nonlinearities and the finite difference method for discretization in time [37]. Along these procedures, the set of nonlinear partial differential equations is progressively transformed into a set of algebraic equations that can be solved by a computer.

4.1.1 The principle of virtual work

A more general and more useful formulation of the boundary value problem exposed in Subsection 3.1.3 is the principle of virtual work, i.e. the work developped by all the forces through an arbitrary virtual diplacement $\boldsymbol{w}$, which is kinematically admissible but does not satisfy the dynamic equilibrium of the solid.
Given

$$\Omega_0 \subset \mathcal{R}^3, \qquad \partial\Omega_0 = \Gamma_0^u \cup \Gamma_0^p$$
$$\rho(\boldsymbol{x}), \boldsymbol{P}(\boldsymbol{x}, \nabla\boldsymbol{u}, \nabla\dot{\boldsymbol{u}}, \boldsymbol{\xi}_i), \boldsymbol{b}(\boldsymbol{x}, t), \boldsymbol{u}_0(\boldsymbol{x}), \boldsymbol{v}_0(\boldsymbol{x}), \bar{\boldsymbol{u}}(\boldsymbol{x}, t), \bar{\boldsymbol{p}}(\boldsymbol{x}, t)$$

Find $\boldsymbol{u}(\boldsymbol{x}, t)$ such that

$$\begin{aligned}\boldsymbol{w} \cdot \boldsymbol{r}(\boldsymbol{u}) = &\int_\Omega \boldsymbol{w} \cdot \rho\ddot{\boldsymbol{u}} dV + \int_\Omega \nabla\boldsymbol{w} : \boldsymbol{P} dV \\ &- \int_\Omega \boldsymbol{w} \cdot \boldsymbol{b} dV - \int_{\Gamma^p} \boldsymbol{w} \cdot \bar{\boldsymbol{p}} dA = 0 \qquad \forall \boldsymbol{w}(\boldsymbol{x}, t) \qquad \forall t > 0 \end{aligned} \tag{4.1}$$

$$\boldsymbol{u}(\boldsymbol{x}, 0) = \boldsymbol{u}_0(\boldsymbol{x}), \forall \boldsymbol{x} \in \Omega_0 \qquad \boldsymbol{u}(\boldsymbol{x}, t) = \bar{\boldsymbol{u}}(\boldsymbol{x}, t), \forall \boldsymbol{x} \in \Gamma_0^u$$
$$\dot{\boldsymbol{u}}(\boldsymbol{x}, 0) = \boldsymbol{v}_0(\boldsymbol{x}), \forall \boldsymbol{x} \in \Omega_0 \qquad \boldsymbol{w}(\boldsymbol{x}, t) = 0, \forall \boldsymbol{x} \in \Gamma_0^u$$

The principle of virtual work (PVW) 4.1 is also known as the weak form of the differential Eq. 3.16 and is equivalent to it if the problem data and the virtual displacement are sufficiently smooth.

4.1.2 The finite element method

The finite element method is a general numerical strategy for calculating approximate solutions to boundary value problems. The method consists in dividing a solid in simple geometric elements connected by a finite number of nodes and approximating the solution and virtual displacement by a series of nodal basis functions:

$$\boldsymbol{u}_h(\boldsymbol{x}, t) = b^n(\boldsymbol{x})\boldsymbol{u}^n(t) = B(\boldsymbol{x})u(t)$$
$$\boldsymbol{w}_h(\boldsymbol{x}, t) = b^n(\boldsymbol{x})\boldsymbol{w}^n(t) = B(\boldsymbol{x})w(t)$$

where the summation convention is applied on the repeated indices, u is a global vector representing the displacements of the nodes, b^n are the nodal basis function and B the corresponding global matrix:

$$\begin{aligned} u &= (\boldsymbol{u}^1, \boldsymbol{u}^2, \ldots, \boldsymbol{u}^N)^T \\ B &= (b^1\boldsymbol{I}, b^2\boldsymbol{I}, \ldots, b^N\boldsymbol{I}) \end{aligned}$$

with N the number of nodes.

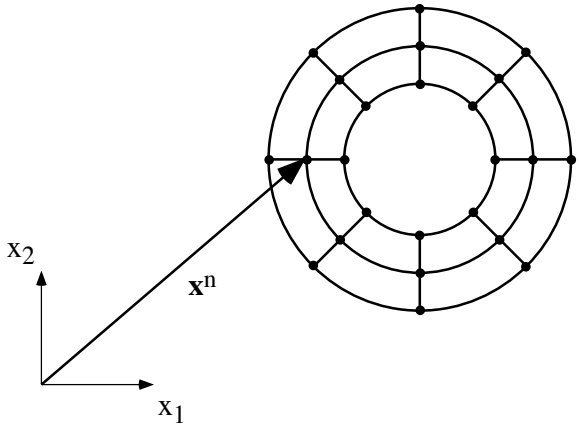

Figure 4.1: Discretization of a two-dimensional torus in elements and nodes.

Using the previous series approximation, a discrete model can be built that leads to the following discrete weak form of the principle of virtual work:

$$w \cdot r(u) \equiv w^T[h(\ddot{u}) + f(u, \dot{u}, \xi_i) - b - q] = 0 \qquad \forall w \tag{4.2}$$

where

$$\begin{aligned} h(\ddot{u}) &= \int_{\Omega_0} B^T \rho B \ddot{u} dV \\ f(u, \dot{u}, \xi_i) &= \int_{\Omega_0} B'^T \boldsymbol{P}_h(x, B'u, B'\dot{u}, \xi_i) dV \\ b &= \int_{\Omega_0} B^T \boldsymbol{b} dV \\ q &= \int_{\Gamma_0^p} B^T \bar{\boldsymbol{p}} dA \end{aligned}$$

with h, f, b and q representing discrete inertia, internal, body and contact forces respectively.

Remark 4.1 *The nodal basis functions are required to belong to the functional space* $\mathcal{H}^1$ *and to satisfy:*

$$b^m(\boldsymbol{x}^n) = \delta^{mn}$$

In practice, these functions are piecewise polynomials and are thus continuous and piecewise differentiable in Ω_0.

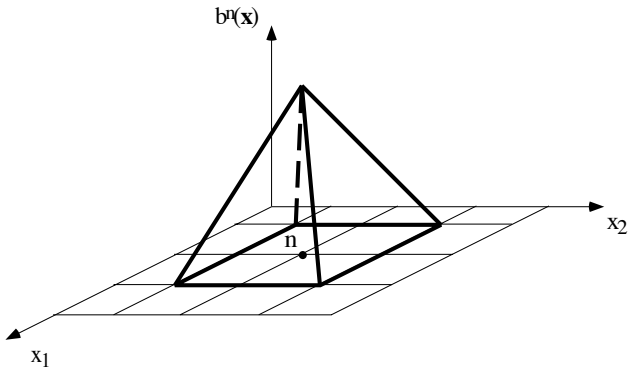

Figure 4.2: Linear nodal basis function.

The discrete form of Eq. 4.2 is:

$$r(u) \equiv h(\ddot{u}) + f(u, \dot{u}, \xi_i) - b - q = 0 \tag{4.3}$$

If the nodal basis functions are redefined on elementary domains, the solution and the virtual displacement can be localized accordingly:

$$^e\boldsymbol{u}_h(\boldsymbol{x}, t) = {}^eb^k(\boldsymbol{x})\,{}^e\boldsymbol{u}^k(t) = {}^eB(\boldsymbol{x})\,{}^eu(t)$$
$$^e\boldsymbol{w}_h(\boldsymbol{x}, t) = {}^eb^k(\boldsymbol{x})\,{}^e\boldsymbol{w}^k(t) = {}^eB(\boldsymbol{x})\,{}^ew(t)$$

where ${}^eu$ is a local vector containing the displacements of the nodes associated with an element e, ${}^eb^k$ are the localized basis function and ${}^eB$ the corresponding local matrix:

$$\begin{aligned} {}^eu &= ({}^e\boldsymbol{u}^1, {}^e\boldsymbol{u}^2, \ldots, {}^e\boldsymbol{u}^K)^T \\ {}^eB &= ({}^eb^1\boldsymbol{I}, {}^eb^1\boldsymbol{I}, \ldots, {}^eb^K\boldsymbol{I}) \end{aligned}$$

with K, the number of nodes associated with a single element. In fact, global and local vectors are related by a localization matrix:

$$^e x = {}^e L x$$

The division of the solid in elements allows to calculate the forces involved in the discrete form 4.3 as the assembly of elementary contributions:

$$\begin{aligned} h(\ddot{u}) &= \sum_{e=1}^{E} {}^e L^T \int_{^e\Omega_0} {}^e B^T \rho {}^e B {}^e \ddot{u} dV \\ f(u, \dot{u}, \xi_i) &= \sum_{e=1}^{E} {}^e L^T \int_{^e\Omega_0} {}^e B'^T \boldsymbol{P}_h({}^e x, {}^e B' {}^e u, {}^e B' {}^e \dot{u}, {}^e \xi_i) dV \\ b &= \sum_{e=1}^{E} {}^e L^T \int_{^e\Omega_0} {}^e B^T \boldsymbol{b} dV \\ q &= \sum_{e=1}^{E} {}^e L^T \int_{^e\Gamma_0^p} {}^e B^T \bar{\boldsymbol{p}} dA \end{aligned}$$

where E is the number of elements and ${}^e L^T$, the transposed forms of the localization matrix, are assembling matrix mapping the appropriate elementary contributions of the local force vectors onto the global force vector.
In order to standardize the calculation of the local force vectors, each element of the mesh is looked as the transformation of a unit cube through:

$$\boldsymbol{x}(\boldsymbol{\zeta}) = b^k(\boldsymbol{\zeta}) \boldsymbol{x}^k \qquad k = 1, 2, \ldots, K$$

where b^k are natural basis functions in terms of natural coordinates $\boldsymbol{\zeta}$ of the cube. Using this transformation, the local displacement vector can be expressed by:

$${}^e \boldsymbol{u}_h(\boldsymbol{x}, t) = {}^e \hat{\boldsymbol{u}}_h(\boldsymbol{\zeta}, t) = {}^e b^k(\boldsymbol{\zeta}) {}^e \boldsymbol{u}^k(t)$$

thus the name isoparametric attributed to such elements.
Numerical integration of the elementary forces is then performed in the natural coordinates with the Gauss formula:

$$\begin{aligned} \int_{^e\Omega} f(x) dV &= \int_{-1}^{+1} \int_{-1}^{+1} \int_{-1}^{+1} \hat{f}(\zeta_1, \zeta_2, \zeta_3) j(\zeta_1, \zeta_2, \zeta_3) d\hat{V} \\ &= \sum_{i=1}^{I} \sum_{j=1}^{J} \sum_{k=1}^{K} \hat{f}(\zeta_1^i, \zeta_2^j, \zeta_3^k) j(\zeta_1^i, \zeta_2^j, \zeta_3^k) \omega_1^i \omega_2^j \omega_3^k d\hat{V} \end{aligned}$$

where j is the determinant of the jacobian matrix of the transformation and ω_n^m is the weight associated with the integration point ζ_n^m.

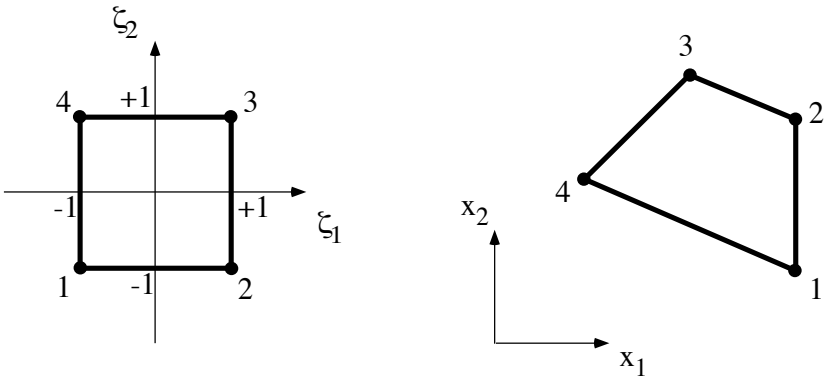

Figure 4.3: Two-dimensional isoparametric element.

4.1.3 The linear iteration method

After discretization by the finite element method, the boundary value problem still involves a set of nonlinear ordinary differential equations. In solid mechanics, the nonlinearities originate from the kinematics of the deformed body (geometric) on the one hand and from the constitutive law of the material (material) on the other hand. The generalized Newton method or linear iteration method (LIM) is an iterative procedure replacing a nonlinear equation by a sequence of linear equations.

Considering the nonlinear scalar equation:

$$r(u) = 0$$

the principle of the linear iteration method uses the approximate linearization:

$$r(u^{i+1}) \simeq r(u^i) + S^i(u^{i+1} - u^i) = 0$$

where S^i is an approximation of $\frac{dr}{du}$ at u^i, for generating the recurrence formula:

$$u^{i+1} = u^i - \frac{r(u^i)}{S^i}$$

This general method includes among others the modified Newton, the gradient and the full Newton method, distinguished by different choices for S^i.

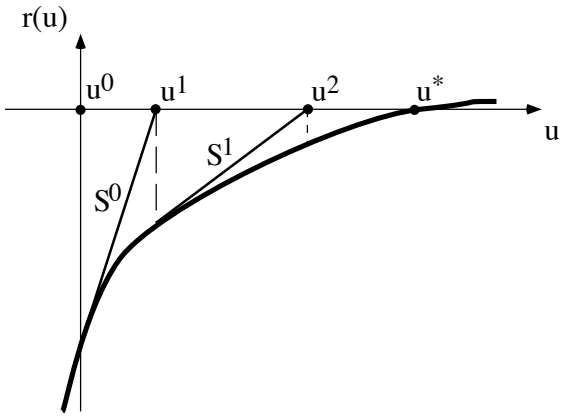

Figure 4.4: The full Newton method.

Resolution of the nonlinear Eq. 4.3 by the full Newton method requires the linearization of the operator $r(u)$ in the direction w:

$$\begin{aligned}\tilde{r}(w,\dot{w},\ddot{w}) \equiv\ & h(\ddot{u}) + f(u,\dot{u},\xi_i) - b - q \\ & + \frac{dh}{d\ddot{u}}(\ddot{u})\ddot{w} + \frac{\partial f}{\partial \dot{u}}(u,\dot{u},\xi_i)\dot{w} + \frac{\partial f}{\partial u}(u,\dot{u},\xi_i)w\end{aligned}$$

The linearized equation becomes:

$$C\ddot{w} + D\dot{w} + Ew = b + q - h(\ddot{u}) - f(u,\dot{u},\xi_i) \tag{4.4}$$

where

$$\begin{aligned}C &:= \frac{dh}{d\ddot{u}} = \int_{\Omega_0} B^T \rho \boldsymbol{I} B dV \\ D &:= \frac{\partial f}{\partial \dot{u}} = \int_{\Omega_0} B'^T \frac{\partial \boldsymbol{P}_h}{\partial \dot{u}} dV = \int_{\Omega_0} B'^T P_h^{\dot{u}} B dV \\ E &:= \frac{\partial f}{\partial u} = \int_{\Omega_0} B'^T \frac{\partial \boldsymbol{P}_h}{\partial u} dV = \int_{\Omega_0} B'^T P_h^{u} B dV\end{aligned}$$

In the above equations, C is the mass, D the damping and E the stiffness matrix and B' the basis function derivative matrix. Following the finite element method, these matrix are calculated by assembling elementary matrices:

$$C = \sum_{e=1}^{E} {}^eL^T \int_{{}^e\Omega_0} {}^eB^T {}^eI {}^eB dV {}^eL$$

$$
\begin{aligned}
D &= \sum_{e=1}^{E} {}^{e}L^{T} \int_{{}^{e}\Omega_0} {}^{e}B'^{T} {}^{e}P_h^{\dot{u}} {}^{e}B' dV \, {}^{e}L \\
E &= \sum_{e=1}^{E} {}^{e}L^{T} \int_{{}^{e}\Omega_0} {}^{e}B'^{T} {}^{e}P_h^{u} {}^{e}B' dV \, {}^{e}L
\end{aligned}
$$

where ${}^{e}P_h^{\dot{u}}$ and ${}^{e}P_h^{u}$ are the elementary nominal tangent matrices.

Convergence of the linear iteration method is controlled by stability and consistency. Roughly speaking, stability controls the ability of the algorithm to initiate convergence from an arbitrary initial guess u^0 whereas consistency controls its ability to achieve it [37].

4.1.4 The finite difference method

After space discretization and linearization, the boundary value problem we aim to solve still involves a set of linear ordinary differential equations. The finite difference method is precisely a general numerical technique for step-by-step integration of differential equations in time. The method consists of replacing the derivatives of a function by suitable finite differences quotients and thus approximating the trajectory by a piecewise linear function.
For a scalar first order differential equation with initial condition:

$$
\begin{aligned}
u(0) &= u_0 \\
\dot{u} &= f(u)
\end{aligned}
$$

The generalized Euler finite difference method provides the following coupled equations:

$$
\begin{aligned}
\frac{u_{n+1} - u_n}{t_{n+1} - t_n} &= \alpha_c v_{n+1} + (1 - \alpha_c) v_n \\
v_{n+1} &= f(u_{n+1})
\end{aligned}
$$

where $\alpha_c \in [0, 1]$ is a parameter controlling the degree of implicitness of the algorithm and it also characterizes its stability.
Integration of Eq. 4.3 can be achieved with the help of two additional finite difference equations. The resulting set of equations is known as the generalized

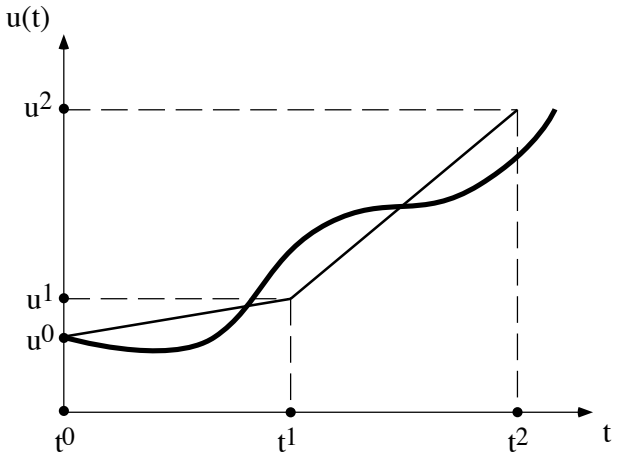

Figure 4.5: The finite difference method.

trapezoidal rule or Newmark scheme:

$$\begin{aligned} h(a_{n+1}) &+ f(u_{n+1}, v_{n+1}, \xi_{in+1}) - b_{n+1} - q_{n+1} = 0 \\ u_{n+1} &= u_n + (1-\alpha_c)\tau v_n + \alpha_c \tau v_{n+1} + (\frac{1}{2} - \alpha_c)\tau^2 a_n \\ v_{n+1} &= v_n + (1-\beta_c)\tau a_n + \beta_c \tau a_{n+1} \end{aligned}$$

where u_n, v_n, a_n, b_n, q_n are approximations of $u(t_n)$, $\dot{u}(t_n)$, $\ddot{u}(t_n)$, $b(t_n)$ and $q(t_n)$ respectively. The parameter $\alpha_c \in [0, \frac{2}{3}]$ controls implicitness and $\beta_c \in [\frac{1}{2}, \frac{3}{2}]$ governs dissipation of the algorithm. For $\alpha_c = 0$ the algorithm is explicit and for $\beta_c = \frac{1}{2}$ the algorithm is conservative.

Convergence of the generalized trapezoidal rule results also from the conjugate properties of stability and consistency [37].

An efficient procedure to put the generalized trapezoidal rule into practice consists of making an initial prediction corresponding to the centered difference scheme:

$$\begin{aligned} u^0_{n+1} &= u_n + \tau v_n + \frac{\tau^2}{2} a_n \\ v^0_{n+1} &= v_n + \tau a_n \\ a^0_{n+1} &= a_n \end{aligned}$$

and solve the resulting linear equation,

$$\left(\frac{C_{n+1}^{i+1}}{\alpha_c\beta_c\tau^2}+\frac{D_{n+1}^{i+1}}{\alpha_c\tau}+E_{n+1}^{i+1}\right)w=b_{n+1}+q_{n+1}-h_{n+1}-f_{n+1} \qquad (4.5)$$

followed by a correction

$$\begin{aligned} u_{n+1}^{i+1} &= u_{n+1}^{i}+w \\ v_{n+1}^{i+1} &= v_{n+1}^{i}+\frac{w}{\alpha_c\tau} \\ a_{n+1}^{i+1} &= a_{n+1}^{i}+\frac{w}{\alpha_c\beta_c\tau^2} \end{aligned}$$

where the displacement formulation is chosen.

4.1.5 Synthesis

At this point, the nonlinear continuous initial boundary value problem involving a set of three nonlinear partial differential equations has been transformed into a double time and iterative sequence of linear discrete problems, each one of them being a large system of linear algebraic equations. The global algorithm combining the finite element method, the linear iteration method and the finite difference method is presented in Table 4.1.
To conclude this section, the numerical resolution of the boundary value problem requires:

- The constitutive law of the involved material

$$\begin{aligned} \boldsymbol{P} &= \boldsymbol{P}(\boldsymbol{x},\boldsymbol{F},\dot{\boldsymbol{F}},\boldsymbol{\xi}_i)=\boldsymbol{F}\boldsymbol{S} \\ \boldsymbol{S} &= \boldsymbol{S}(\boldsymbol{x},\boldsymbol{E},\dot{\boldsymbol{E}},\boldsymbol{\Xi}_i) \end{aligned}$$

- The associated tangent operators

$$\begin{aligned} \mathbb{P}^{u} &= \nabla_F\boldsymbol{P}=\boldsymbol{I}\underline{\otimes}\boldsymbol{S}+(\boldsymbol{F}\underline{\otimes}\boldsymbol{I})\mathbb{S}^{u}(\boldsymbol{F}\underline{\otimes}\boldsymbol{I})^T \\ \mathbb{P}^{\dot{u}} &= \nabla_{\dot{F}}\boldsymbol{P}=(\boldsymbol{F}\underline{\otimes}\boldsymbol{I})\mathbb{S}^{\dot{u}}(\boldsymbol{F}\underline{\otimes}\boldsymbol{I})^T \\ \mathbb{S}^{u} &= \nabla_E\boldsymbol{S} \\ \mathbb{S}^{\dot{u}} &= \nabla_{\dot{E}}\boldsymbol{S} \end{aligned}$$

Initialize	$u_0,\ v_0,\ a_0;\ n=0,\ \tau>0,\ M\tau=T,\ t_0=0;\ \alpha_c, \beta_c$	
	$i=0,\ t_{n+1}=t_n+\tau$	
Predict	$u^0_{n+1}=u_n+\tau v_n+\frac{\tau^2}{2}a_n$	$\bar{u}^0_{n+1}=\bar{u}(t_{n+1})$
prescribe	$v^0_{n+1}=v_n+\tau a_n$	$\bar{v}^0_{n+1}=\dot{\bar{u}}(t_{n+1})$
	$a^0_{n+1}=a_n$	$\bar{a}^0_{n+1}=\ddot{\bar{u}}(t_{n+1})$
	$e=0$	
specify	$r^i_{n+1}=-q(t_{n+1})$	$\mathbb{S}^i_{n+1}=0$
Form	$e=e+1$	
localize	${}^e u={}^e L u^i_{n+1}$ ${}^e v={}^e L v^i_{n+1}$	${}^e a={}^e L a^i_{n+1}$
interpolate	$\boldsymbol{u}'\approx {}^e B'^e u$ $\boldsymbol{v}'\approx {}^e B'^e v$	$\boldsymbol{a}\approx {}^e B\,{}^e a$
integrate	${}^e f=\int_e B'^T \boldsymbol{P}^u dV$	${}^e E=\int_e B'^T P^u B' dV$
and	${}^e g=\int_e B'^T \boldsymbol{P}^{\dot{u}} dV$	${}^e D=\int_e B'^T P^{\dot{u}} B' dV$
linearize	${}^e h=\int_e B^T \rho \boldsymbol{a} dV$	${}^e C=\int_e B^T \rho B dV$
assemble	$r^i_{n+1}\leftarrow r^i_{n+1}+{}^e L^T({}^e h+{}^e g+{}^e f-{}^e b)$	
	$\mathbb{S}^i_{n+1}\leftarrow \mathbb{S}^i_{n+1}+{}^e L^T(\frac{1}{\alpha_c\beta_c\tau^2}{}^e C+\frac{1}{\alpha_c\tau}{}^e D+{}^e E)^e L$	
	$e>E$?	
Solve	$\mathbb{S}^i_{n+1}\delta u=-r^i_{n+1}$	
Correct	$u^{i+1}_{n+1}=u^i_{n+1}+\delta u$	$\bar{u}^{i+1}_{n+1}=\bar{u}^i_{n+1}$
	$v^{i+1}_{n+1}=v^i_{n+1}+\frac{1}{\alpha_c\tau}\delta u$	$\bar{v}^{i+1}_{n+1}=\bar{v}^i_{n+1}$
	$a^{i+1}_{n+1}=a^i_{n+1}+\frac{1}{\alpha_c\beta_c\tau^2}\delta u$	$\bar{a}^{i+1}_{n+1}=\bar{a}^i_{n+1}$
Test	$\|r^{i+1}_{n+1}\|<\epsilon_r$?	
	$i=i+1$	
	$n>M$?	
	$n=n+1$	

Table 4.1: Combination of the finite element, linear iteration and finite difference algorithms. From Curnier [37].

4.1.6 Implicit projection algorithm

In spite of the generality of the numerical methods described in the previous subsections, their application to irreversible processes such as plasticity or damage requires additional work and deserves some caution. In particular, the flow rules for the internal state variables have to be integrated to calculate the elementary forces and the tangent operators. In addition, the constitutive equations for materials exhibiting yield surfaces may be only piecewise differentiable and the linear iteration method cannot be applied blindly. For this latter reason, the usual boundary value problem needs to be replaced by an incremental problem, that we present now for both rate-dependent and rate-independent constitutive laws.

Rate-independent process In the rate-independent case, the incremental problem can be formulated as follows:
Assume an initial state:

$$\{\boldsymbol{E}_0, \boldsymbol{\Xi}_{i0}\}$$

with the corresponding conjugate variables:

$$\begin{aligned} \boldsymbol{S}_0^E &= \boldsymbol{S}^E(\boldsymbol{E}_0, \boldsymbol{\Xi}_{i_0}) \\ \boldsymbol{S}_0^{\Xi_i} &= \boldsymbol{S}^{\Xi_i}(\boldsymbol{E}_0, \boldsymbol{\Xi}_{i_0}) \end{aligned}$$

satisfying the yield criterion:

$$y(\boldsymbol{S}_0^{\Xi_i}) \leq 0$$

Consider a new strain $\boldsymbol{E}$ and find a final state:

$$\{\boldsymbol{E}, \boldsymbol{\Xi}_i\}$$

with final conjugate variables:

$$\begin{aligned} \boldsymbol{S}^E &= \boldsymbol{S}^E(\boldsymbol{E}, \boldsymbol{\Xi}_i) \\ \boldsymbol{S}^{\Xi_i} &= \boldsymbol{S}^{\Xi_i}(\boldsymbol{E}, \boldsymbol{\Xi}_i) \end{aligned}$$

satisfying the yield criterion:

$$y(\boldsymbol{S}^{\Xi_i}) \leq 0$$

For this purpose, consider a trial state based on the new strain and the initial internal variables, that is not necessarily admissible:

$$\{\boldsymbol{E}, \boldsymbol{\Xi}_{i_0}\}$$

with the corresponding trial conjugate variables:

$$\begin{aligned} \boldsymbol{S}_T^E &= \boldsymbol{S}^E(\boldsymbol{E}, \boldsymbol{\Xi}_{i0}) \\ \boldsymbol{S}_T^{\Xi_i} &= \boldsymbol{S}^{\Xi_i}(\boldsymbol{E}, \boldsymbol{\Xi}_{i0}) \end{aligned}$$

that may violate the yield criterion:

$$y(\boldsymbol{S}_T^{\Xi_i}) > 0$$

The final state is obtained by projecting the trial state on the yield criterion. Among several proposed algorithms to perform this projection, the implicit projection algorithm or catching up algorithm , enforces the flow rules to hold at the final state as shown in Fig. 4.6. In particular, the algorithm satisfies the consistency condition exactly:

$$y(\boldsymbol{S}^{\Xi_i}) = 0$$

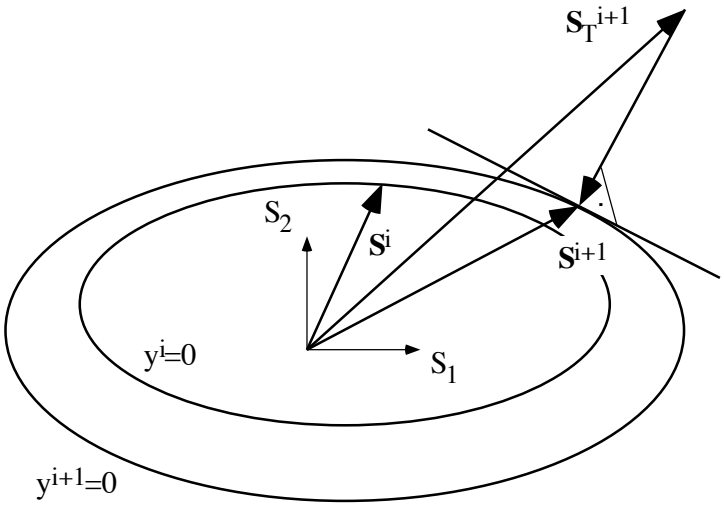

Figure 4.6: The implicit projection algorithm.

The incremental algorithm with implicit projection can be summarized as follows:

- Calculate the trial conjugate variables and evaluate the yield criterion:

$$y(\boldsymbol{S}_T^{\Xi_i})$$

- If the yield criterion is satisfied ($y \leq 0$), the trial state is the final state:

$$\{\boldsymbol{E}, \boldsymbol{\Xi}_i\} = \{\boldsymbol{E}, \boldsymbol{\Xi}_{i0}\}$$

- If the yield criterion is violated ($y > 0$), the implicit projection is done by solving:

$$\begin{aligned} \boldsymbol{\Xi}_i &= \boldsymbol{\Xi}_{i0} + \lambda_{\Xi_i} \nabla_{S^{\Xi_i}} y(S^{\Xi_i}) \\ \boldsymbol{S}^{\Xi_i} &= \boldsymbol{S}^{\Xi_i}(\boldsymbol{E}, \boldsymbol{\Xi}_i) \\ y(\boldsymbol{S}^{\Xi_i}) &= 0 \end{aligned}$$

Convergence of the implicit projection algorithm has been established for an elastic, perfectly plastic model in the case of small strains [83].

Rate-dependent process For rate-dependent processes, the incremental problem is only slightly different:
Assume an initial state at $t = t_0$:

$$\{\boldsymbol{E}_0, \boldsymbol{\Xi}_{i0}\}$$

with the corresponding conjugate variables:

$$\begin{aligned} \boldsymbol{S}_0^E &= \boldsymbol{S}^E(\boldsymbol{E}_0, \boldsymbol{\Xi}_{i0}) \\ \boldsymbol{S}_0^{\Xi_i} &= \boldsymbol{S}^{\Xi_i}(\boldsymbol{E}_0, \boldsymbol{\Xi}_{i0}) \end{aligned}$$

Consider a new time $t = t_0 + \tau$ with the new strain $\boldsymbol{E}$ and find the final state:

$$\{\boldsymbol{E}, \boldsymbol{\Xi}_i\}$$

with final conjugate variables:

$$\begin{aligned} \boldsymbol{S}^E &= \boldsymbol{S}^E(\boldsymbol{E}, \boldsymbol{\Xi}_i) \\ \boldsymbol{S}^{\Xi_i} &= \boldsymbol{S}^{\Xi_i}(\boldsymbol{E}, \boldsymbol{\Xi}_i) \end{aligned}$$

satisfying a flow rule of the type:

$$\dot{\boldsymbol{\Xi}}_i = \dot{\boldsymbol{\Xi}}_i(\boldsymbol{S}^{\Xi_i})$$

For this purpose, consider a trial state based on the new strain and the initial internal variables, that is not necessarily admissible:

$$\{\boldsymbol{E}, \boldsymbol{\Xi}_{i0}\}$$

with the corresponding trial conjugate variables:

$$\begin{aligned} \boldsymbol{S}_T^E &= \boldsymbol{S}^E(\boldsymbol{E}, \boldsymbol{\Xi}_{i0}) \\ \boldsymbol{S}_T^{\Xi_i} &= \boldsymbol{S}^{\Xi_i}(\boldsymbol{E}, \boldsymbol{\Xi}_{i0}) \end{aligned}$$

that may violate the flow rule:

$$\dot{\boldsymbol{\Xi}}_i \neq \dot{\boldsymbol{\Xi}}_i(\boldsymbol{S}^{\Xi_i})$$

The final state is obtained by integrating the flow rules for the internal variables. This integration can be done by the means of an implicit Euler scheme, that enforces the flow rules to hold exactly at the final state (Fig. 4.7).
The incremental algorithm with implicit integration can be summarized as follows:

- Calculate the trial conjugate variables and evaluate the yield criterion:

$$y(\boldsymbol{S}_T^{\Xi_i})$$

- If the yield criterion is satisfied ($y \leq 0$), the trial state is the final state:

$$\{\boldsymbol{E}, \boldsymbol{\Xi}_i\} = \{\boldsymbol{E}, \boldsymbol{\Xi}_{i0}\}$$

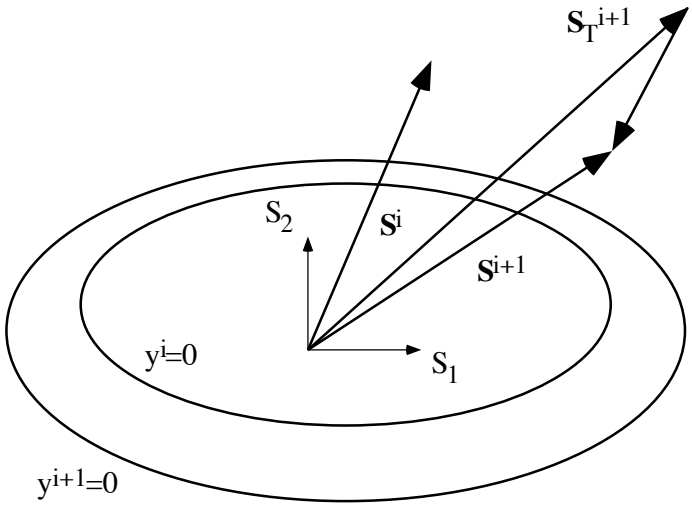

Figure 4.7: The implicit integration method.

- If the yield criterion is violated ($y > 0$), the implicit integration is done by solving:

$$\begin{aligned} \boldsymbol{\Xi}_i &= \boldsymbol{\Xi}_{i0} + \tau \dot{\boldsymbol{\Xi}}_i \\ \boldsymbol{S}^{\Xi_i} &= \boldsymbol{S}^{\Xi_i}(\boldsymbol{E}, \boldsymbol{\Xi}_i) \\ \dot{\boldsymbol{\Xi}}_i &= \dot{\boldsymbol{\Xi}}_i(\boldsymbol{S}^{\Xi_i}) \end{aligned}$$

The previous rate-independent and rate-dependent incremental algorithms need now to be applied in the particular cases of our one- and three-dimensional constitutive laws and tangent operators have to be calculated for use of the linear iteration method when flow of the internal variables occurs.

4.2 One-dimensional model

In this section the algorithms adapted for the general one-dimensional constitutive law are presented and a number of validation experiments reviewed.

4.2.1 Formulation

The incremental algorithm developed for the one-dimensional elastoplastic law with damage and isotropic hardening can be described as follows:
Assume an initial kinematic state E_0, E_0^p, α_0, to which corresponds a dynamic state:

$$\begin{aligned} S_0^{E^p} &= \epsilon f(\alpha_0)(E_0 - E_0^p) \\ S_0^{\alpha} &= -\frac{1}{2}\epsilon f'(\alpha_0)(E_0 - E_0^p)^2 - \tilde{\psi}'(\alpha_0) \end{aligned}$$

which satisfies the yield criterion:

$$y(S_0^{E^p}, S_0^{\alpha}) \leq 0$$

Given a new total strain E, define a trial kinematic state E, E_0^p, α_0 and calculate the corresponding trial stresses:

$$\begin{aligned} S_T^{E^p} &= \epsilon f(\alpha_0)(E - E_0^p) \\ S_T^{\alpha} &= -\frac{1}{2}\epsilon f'(\alpha_0)(E - E_0^p)^2 - \tilde{\psi}'(\alpha_0) \end{aligned}$$

If the resulting yield function $y(S_T^{E^p}, S_T^{\alpha})$ verifies the criterion $y \leq 0$ then:

$$\begin{aligned} \{E^p, \alpha\} &= \{E_0^p, \alpha_0\} \\ S^{E^p} &= S_T^{E^p} \\ S^{\alpha} &= S_T^{\alpha} \end{aligned}$$

Remark 4.2 *The conjugate variable of E has the property:*

$$S^E \equiv S^{E^p}$$

and is thus not repeated in the algorithms.

According to Eq. 3.49, the total material stress is given by:

$$S = S^E + S^{\dot{E}} = \epsilon f(\alpha_0)(E - E_0^p) + v|\dot{E}|^{\frac{1}{n}}\frac{\dot{E}}{|\dot{E}|} \tag{4.6}$$

The tangent operators are the elastic and viscous ones:

$$\frac{dS^E}{dE} = \epsilon f(\alpha_0) \tag{4.7}$$

$$\frac{dS^{\dot{E}}}{d\dot{E}} = \upsilon \frac{1}{n} |\dot{E}|^{\frac{1-n}{n}} \tag{4.8}$$

If the yield criterion is not satisfied, that is $y > 0$, distinction has to be made between the rate-independent and the rate-dependent cases.

Rate-independent plastic and damage flow For rate-independent flow rules ($\zeta = 0$), the implicit projection consists of solving a set of five equations:

$$\begin{aligned} S^{E^p} &= \epsilon f(\alpha)(E - E^p) \\ S^{\alpha} &= -\frac{1}{2}\epsilon f'(\alpha)(E - E^p)^2 - \tilde{\psi}'(\alpha) \\ E^p - E_0^p &= \lambda_\alpha \frac{S^E}{|S^E|} \equiv \lambda_\alpha N \\ \alpha - \alpha_0 &= \lambda_\alpha \\ y(S^{E^p}, S^{\alpha}) &= 0 \end{aligned}$$

This set of equations can be directly reduced to a single nonlinear equation:

$$F(\lambda_\alpha) = |\epsilon f(\alpha_0 + \lambda_\alpha)(E - E_0^p - \lambda_\alpha N_T)| - g(\alpha_0 + \lambda_\alpha) - \sigma = 0$$

where λ_α is the unknown plastic strain and damage magnitude.
This equation is solved by a Newton method using the linearization:

$$\begin{aligned} F^{i+1} &= F^i + F^i{}_{,\lambda_\alpha^i}(\lambda_\alpha^{i+1} - \lambda_\alpha^i) \\ \lambda_\alpha^{i+1} &= \lambda_\alpha^i - \frac{F^i}{F^i{}_{,\lambda_\alpha^i}} \end{aligned} \tag{4.9}$$

where

$$F^i{}_{,\lambda_\alpha^i} = \epsilon f'(\alpha_0 + \lambda_\alpha^i)(E - E_0^p - \lambda_\alpha^i N_T)N_T - \epsilon f(\alpha_0 + \lambda_\alpha^i) - g'(\alpha_0 + \lambda_\alpha^i)$$

The projected state is then given by:

$$\begin{aligned} E^p &= E_0^p + \lambda_\alpha N_T \\ \alpha &= \alpha_0 + \lambda_\alpha \end{aligned}$$

where λ_α is the converged solution.

The total material stress becomes:

$$S = S^E + S^{\dot{E}} = \epsilon f(\alpha)(E - E^p) + v|\dot{E}|^{\frac{1}{n}} \frac{\dot{E}}{|\dot{E}|} \tag{4.10}$$

The tangent operator with respect to E is obtained by enforcing the consistency condition $\dot{y}(S^{E^p}, S^\alpha) = 0$, which provides:

$$\frac{dS^E}{dE} = \epsilon f(\alpha) - \frac{\epsilon f(\alpha)(\epsilon f(\alpha) - \epsilon f'(\alpha)|E - E^p|)}{(\epsilon f(\alpha) - \epsilon f'(\alpha)|E - E^p|) + g'(\alpha)} \tag{4.11}$$

$$\frac{dS^{\dot{E}}}{d\dot{E}} = v\frac{1}{n}|\dot{E}|^{\frac{1-n}{n}} \tag{4.12}$$

Remark 4.3 *The model of rate-independent elastoplasticity with linear hardening is retrieved from the present model by setting $f(\alpha) \equiv 1$ and $g(\alpha) = \gamma\alpha$. In this case, the tangent operator 4.11 reduces to the classical result:*

$$\frac{dS^E}{dE} = \frac{\epsilon\gamma}{\epsilon + \gamma}$$

where γ is the linear hardening coefficient.

Rate-dependent plastic and damage flow In the rate-dependent case, that is $\zeta > 0$, the flow rules have to be integrated without projection. The implicit finite difference scheme provides the following set of equations:

$$\begin{aligned}
S^{E^p} &= \epsilon f(\alpha)(E - E^p) \\
S^\alpha &= -\frac{1}{2}\epsilon f'(\alpha)(E - E^p)^2 - \tilde{\psi}'(\alpha) \\
\dot{E}^p &= \begin{cases} -\left(\frac{|S^{E^p}| - g - \sigma}{\zeta}\right)^m & \text{if } S^{E^p} \le -\sigma - g \\ +\left(\frac{|S^{E^p}| - g - \sigma}{\zeta}\right)^m & \text{if } S^{E^p} \ge +\sigma + g \end{cases} \\
\dot{\alpha} &= \left(\frac{\sqrt{\frac{-2\epsilon f^2}{f'}(S^\alpha - (h - g)) + (\sigma + g)^2} - g - \sigma}{\zeta}\right)^m \qquad \text{if } S^\alpha \ge h - g \\
E^p &= E_0^p + \tau\dot{E}^p \\
\alpha &= \alpha_0 + \tau\dot{\alpha}
\end{aligned}$$

where τ is the time step of the main finite difference algorithm.

This set of equations can again be reduced to a single nonlinear equation,

$$G(\lambda_\alpha) = \lambda_\alpha - \tau \left(\frac{|\epsilon f(\alpha_0 + \lambda_\alpha)(E - E_0^p - \lambda_\alpha N_T)| - g(\alpha_0 + \lambda_\alpha) - \sigma}{\zeta} \right)^m = 0$$

which can be simplified by the means of the previous function $F(\lambda_\alpha)$:

$$G(\lambda_\alpha) = \lambda_\alpha - \tau (\frac{F(\lambda_\alpha)}{\zeta})^m$$

This equation is solved by a standard Newton method using the linearization:

$$\begin{aligned} G^{i+1} &= G^i + G^i{}_{,\lambda_\alpha^i}(\lambda_\alpha^{i+1} - \lambda_\alpha^i) \\ \lambda_\alpha^{i+1} &= \lambda_\alpha^i - \frac{G^i}{G^i{}_{,\lambda_\alpha^i}} \end{aligned} \tag{4.13}$$

where

$$G^i{}_{,\lambda_\alpha^i} = 1 - \frac{\tau}{\zeta} m (\frac{F^i}{\zeta})^{m-1} F^i{}_{,\lambda_\alpha^i}$$

The final state is given by:

$$\begin{aligned} E^p &= E_0^p + \lambda_\alpha N_T \\ \alpha &= \alpha_0 + \lambda_\alpha \end{aligned}$$

where λ_α is the converged solution.

The total material stress becomes again:

$$S = S^E + S^{\dot{E}} = \epsilon f(\alpha)(E - E^p) + v|\dot{E}|^{\frac{1}{n}} \frac{\dot{E}}{|\dot{E}|} \tag{4.14}$$

The tangent operator is obtained by differentiating Eq. 4.13 with respect to E:

$$\begin{aligned} \frac{dS^E}{dE} &= \epsilon f(\alpha) \\ &+ \frac{\frac{\tau}{\zeta} m z^{m-1} \epsilon f(\alpha)(\epsilon f(\alpha) - \epsilon f'(\alpha)|E - E^p|)}{1 - \frac{\tau}{\zeta} m z^{m-1}(\epsilon f(\alpha) - \epsilon f'(\alpha)|E - E^p| + g'(\alpha))} \end{aligned} \tag{4.15}$$

$$\frac{dS^{\dot{E}}}{d\dot{E}} = \frac{dS_0^{\dot{E}}}{d\dot{E}} = v \frac{1}{n} |\dot{E}|^{\frac{1-n}{n}} \tag{4.16}$$

with

$$z = \left(\frac{|S^{E^p}| - g - \sigma}{\zeta} \right) = \left(\frac{\sqrt{\frac{-2\epsilon f^2}{f'}(S^\alpha - (h - g)) + (\sigma + g)^2} - g - \sigma}{\zeta} \right)$$

Remark 4.4 *It should be noticed that the time-dependent tangent operator is a function of the ratio $\frac{\tau}{\zeta}$, where τ is the time step of the numerical algorithm and ζ the viscosity coefficient of the irreversible process. Two asymptotic tangent operators can be drawn from this ratio.*

If the viscous effects are negligible with respect to the time step:

$$\tau \gg \zeta \qquad \frac{\tau}{\zeta} \longrightarrow +\infty$$

The tangent operator tends toward the rate-independent tangent operator:

$$\frac{dS^E}{dE} \longrightarrow \epsilon f(\alpha) - \frac{\epsilon f(\alpha)(\epsilon f(\alpha) - \epsilon f'(\alpha)|E - E^p|)}{(\epsilon f(\alpha) - \epsilon f'(\alpha)|E - E^p|) + g'(\alpha)}$$

If the viscous effects are important with respect to the time step:

$$\tau \ll \zeta \qquad \frac{\tau}{\zeta} \longrightarrow 0$$

The tangent operator tends toward the purely elastic tangent operator:

$$\frac{dS^E}{dE} \longrightarrow \epsilon f(\alpha)$$

Remark 4.5 *During flow of the internal variables the free energy potential ψ from which material stress derives is replaced by the incremental pseudopotential $\psi + \tau\phi$, where τ is a real or virtual time increment, depending if the flow rule is rate-dependent or rate-independent. Resolution of the incremental problem during flow of the internal variables is thus similar to the resolution of a classical elasticity problem with a different potential and associated tangent operator. In particular, an incremental problem without viscoelasticity remains hyperbolic if the tangent operator is strictly positive.*

For the rate-dependent damage law, the parameter $\frac{\tau}{\zeta}$ plays an important role in the applicability of the algorithm. In fact, a sufficiently small time step will always provide a positive tangent operator and thus warrant that the incremental problem remains hyperbolic.

4.2.2 Validation

The above described one-dimensional model has been coded in a FORTRAN subroutine E1GBAR, which has been implemented in the one-dimensional finite element software ONED developed at the Laboratory of Applied Mechanics for research and teaching purposes. The subroutine E1GBAR has been the object of extensive validation experiments, whereby the behaviour of each rheologic part of the numerical model has been compared to the analytical solution and all combinations of these parts have been successfully tested for convergence. In this Subsection, we will expose briefly some basic validation experiments and provide a synthetic example to demonstrate the potential of the numerical model.

All validation tests were performed with a homogeneous bar including ten elements and attached at one end. In a first test series, the other end was subjected to a displacement schedule reproducing a single sine wave period. In a second test series a force was applied following a similar schedule. For examination of viscoplasticity, a relaxation test was done, where the other end of the bar was subjected to a constant displacement.

The schedule of the first test series was:

$$\bar{u}(t) = \bar{u}_0 sin(\omega_s t) \tag{4.17}$$

$$\dot{\bar{u}}(t) = \omega_s \bar{u}_0 cos(\omega_s t) \tag{4.18}$$

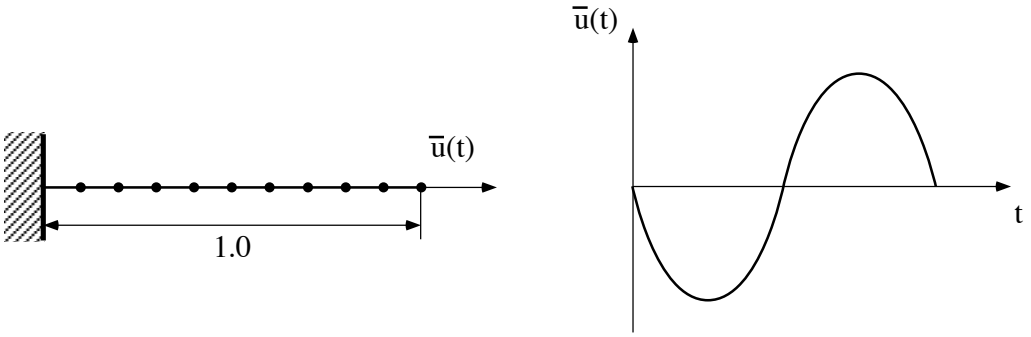

Figure 4.8: Discretized one-dimensional bar with the applied displacement schedule.

Linear viscoelasticity The analytical expression for stress is obtained by replacing the value of $E(t)$ and $\dot{E}(t)$ deduced from the schedule 4.17 in Eq. 3.29:

$$S(E) = \epsilon E + v\dot{E} = \epsilon \bar{E}_0 \sqrt{1 + tan^2(\varphi)} sin(\omega_s t + \varphi)$$

with

$$tan(\varphi) = \frac{v\omega_s}{\epsilon}$$

The damage and hardening function are indeterminate since flow of the internal

ϵ $[MPa]$	v $[MPa \cdot s]$	n	σ_- $[MPa]$	σ_+ $[MPa]$	ζ $[MPa \cdot s]$	m
1000	100	1	$+\infty$	$+\infty$	$-$	$-$

Table 4.2: Material constants used for linear viscoelasticity.

variable α is not allowed. The material constants used for this test are listed in Table 4.2 and the resulting stress-strain curve displayed in Fig. 4.9.

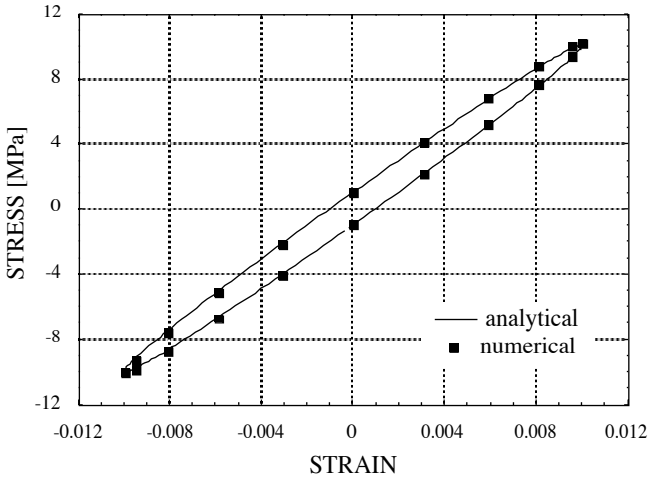

Figure 4.9: Numerical versus analytical result for linear viscoelasticity.

Elastoplasticity with linear hardening An incremental expression of S is derived from Eq. 3.50:

$$S(E) = \begin{cases} -\sigma_- - g & \text{if } E - E_0^p < -\frac{g(\alpha_0)+\sigma_-}{\epsilon} \\ f(\alpha_0)(E - E_0^p) & \text{if } -\frac{g(\alpha_0)+\sigma_-}{\epsilon} \leq E - E_0^p \leq \frac{g(\alpha_0)+\sigma_+}{\epsilon} \\ +\sigma_+ + g & \text{if } \frac{g(\alpha_0)+\sigma_+}{\epsilon} < E - E_0^p \end{cases}$$

where g is obtained by the projection algorithm.

ϵ $[MPa]$	v $[MPa \cdot s]$	n	σ_- $[MPa]$	σ_+ $[MPa]$	ζ $[MPa \cdot s]$	m
1000	–	–	6	3	–	–

Table 4.3: Material constants for elastoplasticity with hardening.

The material constants are given in Table 4.3, whereas the damage and hardening functions are chosen as:

$$\begin{aligned} f(\alpha) &\equiv 1 \\ g(\alpha) &= \gamma\alpha \qquad \gamma = 100[MPa] \end{aligned}$$

The resulting response of the material is shown in Fig. 4.10.

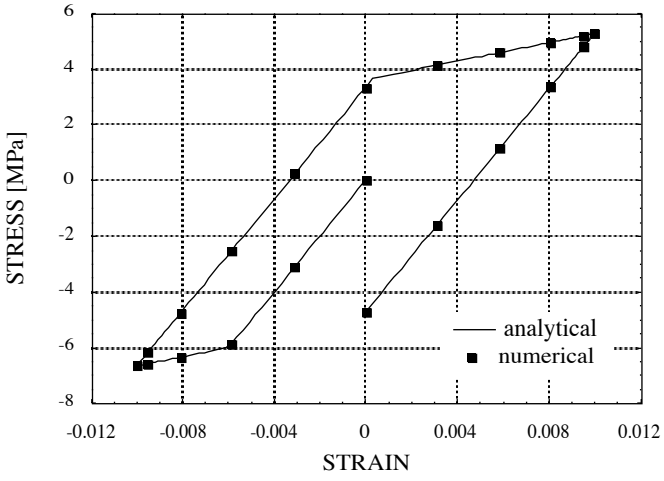

Figure 4.10: Numerical versus analytical result for elastoplasticity with hardening.

Pure damage with linear hardening The incremental expression of S is reduced to:

$$S(E) = \begin{cases} -\sigma_- - g & \text{if } E < -\frac{g(\alpha_0)+\sigma_-}{\epsilon f(\alpha_0)} \\ f(\alpha_0)E & \text{if } -\frac{g(\alpha_0)+\sigma_-}{\epsilon f(\alpha_0)} \leq E \leq \frac{g(\alpha_0)+\sigma_+}{\epsilon f(\alpha_0)} \\ +\sigma_+ + g & \text{if } \frac{g(\alpha_0)+\sigma_+}{\epsilon f(\alpha_0)} < E \end{cases}$$

where g is obtained by the projection algorithm.

ϵ $[MPa]$	v $[MPa \cdot s]$	n	σ_- $[MPa]$	σ_+ $[MPa]$	ζ $[MPa \cdot s]$	m
1000	–	–	6	3	–	–

Table 4.4: Material constants for elasticity with perfect damage.

The hardening function is chosen as:

$$g(\alpha) = \gamma\alpha \qquad \gamma = 100[MPa]$$

The material constants are shown in Table 4.4.

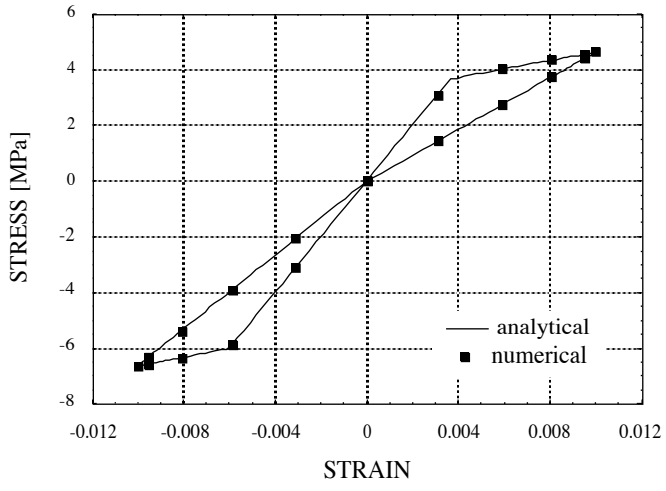

Figure 4.11: Numerical versus analytical result for elasticity with perfect damage.

As shown in Fig. 4.11 the model provides the expected damage behaviour.

Viscoplasticity without damage The schedule of the relaxation test is:

$$\begin{aligned} \bar{u}(t) &= \bar{u}_0 \\ \dot{\bar{u}}(t) &= 0 \end{aligned}$$

The analytical expression for the evolution of stress is obtained by solving the differential Eq. 3.56 for E^p and replacing the solution in 3.49:

$$S(t) = \sigma_+ + (\epsilon E_0 - \sigma_+) e^{-\frac{\epsilon}{\zeta} t}$$

The material constants used for this test are given in Table 4.5.

ϵ $[MPa]$	υ $[MPa \cdot s]$	n	σ_- $[MPa]$	σ_+ $[MPa]$	ζ $[MPa \cdot s]$	m
1000	–	–	6	3	400	1

Table 4.5: Material constants for viscoplasticity.

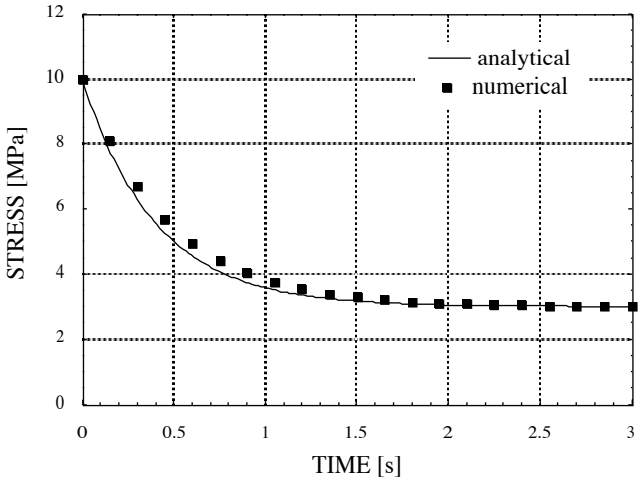

Figure 4.12: Numerical versus analytical result for viscoplasticity.

The damage and hardening functions are chosen as:

$$\begin{aligned} f(\alpha) &\equiv 1 \\ g(\alpha) &= \gamma\alpha \qquad \gamma = 100[MPa] \end{aligned}$$

By the means of 20 time steps, the algorithm provides already a reasonable approximation of the viscoplastic response (Fig. 4.12).

Example Using the sinewave displacement schedule, the response of the model was simulated for three combinations of the previous rheologic parts:

- Elasticity with rate-independent coupled plasticity and damage
- Elasticity with rate-dependent coupled plasticity and damage
- Viscoelasticity with rate-dependent coupled plasticity and damage

For each case, the material constants are summarized in Table 4.6 and the results shown in Fig. 4.13. In general, convergence of the global Newton method was reached after two steps.
The damage and hardening functions are chosen as:

$$\begin{aligned} f(\alpha) &= e^{-\frac{\alpha}{\alpha_f}} \qquad \alpha_f = 0.008 \\ g(\alpha) &= \gamma\alpha \qquad \gamma = 100[MPa] \end{aligned}$$

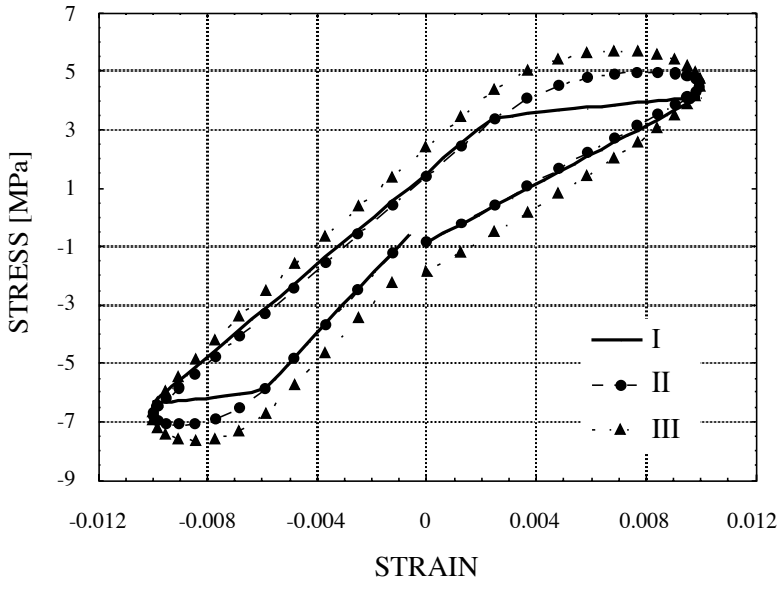

Figure 4.13: Numerical results for rate-independent (I) and rate-dependent (II-III) elastoplasticity with damage and hardening. Case II includes viscous flow of plasticity and damage while case III involves additionnally viscous elasticity.

	ϵ $[MPa]$	v $[MPa \cdot s]$	n	σ_- $[MPa]$	σ_+ $[MPa]$	ζ $[MPa \cdot s]$	m
I	1000	–	–	6	3	–	–
II	1000	–	–	6	3	400	1
III	1000	100	1	6	3	400	1

Table 4.6: Material constants for the examples of elastoplasticity with damage.

This example emphasizes the contributions of the time-dependent effects upon the rate-independent stress-strain curve of the simultaneous dissipation of plasticity and damage.

4.3 Three-dimensional model

In this subsection, the algorithm developed for the retained three-dimensional constitutive law for trabecular bone is described and a number of validation results presented.

4.3.1 Formulation

The three-dimensional model based on Section 3.3 is restricted to the rate-independent case and the algorithm is summarized as follows:
Assuming an initial state $\boldsymbol{E}_0$, $\boldsymbol{E}_0^p$, α_0, such that the associated conjugate variables:

$$\begin{aligned} \boldsymbol{S}_0 &= \overline{\mathbb{S}}(\boldsymbol{E}_0 - \boldsymbol{E}_0^p) + f(\alpha_0)\mathbb{S}'(\boldsymbol{E}_0 - \boldsymbol{E}_0^p) \\ S_0^\alpha &= -\frac{1}{2}f'(\alpha_0)(\boldsymbol{E}_0 - \boldsymbol{E}_0^p) : \mathbb{S}'(\boldsymbol{E}_0 - \boldsymbol{E}_0^p) - \tilde{\psi}'(\alpha_0) \end{aligned}$$

satisfy the yield criterion:

$$y(\boldsymbol{S}_0, S_0^\alpha) \leq 0$$

Given a new total strain $\boldsymbol{E}$, define a trial state $\boldsymbol{E}$, $\boldsymbol{E}_0^p$, α_0 and calculate the corresponding trial stresses:

$$\begin{aligned} \boldsymbol{S}_T &= \overline{\mathbb{S}}(\boldsymbol{E} - \boldsymbol{E}_0^p) + f(\alpha_0)\mathbb{S}'(\boldsymbol{E} - \boldsymbol{E}_0^p) \\ S_T^\alpha &= -\frac{1}{2}f'(\alpha_0)(\boldsymbol{E} - \boldsymbol{E}_0^p)\mathbb{S}'(\boldsymbol{E} - \boldsymbol{E}_0^p) - \tilde{\psi}'(\alpha_0) \end{aligned}$$

If the resulting yield function $y(\boldsymbol{S}_T,\, S_T^\alpha)$ verifies the criterion $y \leq 0$ then the final state is the trial state:

$$\begin{aligned} \{\boldsymbol{E}^p, \alpha\} &= \{\boldsymbol{E}_0^p, \alpha_0\} \\ \boldsymbol{S} &= \boldsymbol{S}_T \\ S^\alpha &= S_T^\alpha \end{aligned}$$

Remark 4.6 *In the rate-independent case:*

$$\boldsymbol{S} = \boldsymbol{S}^E = \boldsymbol{S}^{E^p}$$

The superscripts are thus abandoned to simplify the notations.

The continuum tangent operator is the elastic one:

$$\mathbb{S}^u = \nabla_E \boldsymbol{S}^E = \overline{\mathbb{S}} + f(\alpha_0)\mathbb{S}' \tag{4.19}$$

If the yield criterion is not satisfied, that is $y > 0$, the implicit projection involving a set of five equations is performed:

$$\begin{aligned} \boldsymbol{S} &= \overline{\mathbb{S}}(\boldsymbol{E} - \boldsymbol{E}^p) + f(\alpha)\mathbb{S}'(\boldsymbol{E} - \boldsymbol{E}^p) \\ S^\alpha &= -\frac{1}{2} f'(\boldsymbol{E} - \boldsymbol{E}^p) : (\alpha)\mathbb{S}'(\boldsymbol{E} - \boldsymbol{E}^p) - \tilde{\psi}'(\alpha) \\ \boldsymbol{E}^p - \boldsymbol{E}_0^p &= \lambda_\alpha \frac{\mathbb{E}'\boldsymbol{S}}{\sqrt{\boldsymbol{S} : \mathbb{E}'\boldsymbol{S}}} \equiv \lambda_\alpha \boldsymbol{N} \\ \alpha - \alpha_0 &= \lambda_\alpha \\ y(\boldsymbol{S}, S^\alpha) &= 0 \end{aligned}$$

Using appropriate substitutions, this set of equations can be reduced to:

$$\begin{aligned} \boldsymbol{Y}(\boldsymbol{S}, \lambda_\alpha) &= \overline{\mathbb{E}}(\boldsymbol{S} - \boldsymbol{S}_0) + \mathbb{E}'\left(\frac{\boldsymbol{S}}{f(\alpha_0 + \lambda_\alpha)} - \frac{\boldsymbol{S}_0}{f(\alpha_0)}\right) + \lambda_\alpha \boldsymbol{N} \\ y(\boldsymbol{S}, \lambda_\alpha) &= \sqrt{\boldsymbol{S} : \mathbb{E}'\boldsymbol{S}} - g(\alpha_0 + \lambda_\alpha) - y_\sigma = 0 \end{aligned}$$

where $\boldsymbol{S}$ and λ_α are the unknowns.
Linearization of these two coupled equations is given by:

$$\begin{aligned} \boldsymbol{Y}^{i+1}(\boldsymbol{S}^{i+1}, \lambda_\alpha^{i+1}) &= \boldsymbol{Y}^i + \nabla_S \boldsymbol{Y}^i(\boldsymbol{S}^{i+1} - \boldsymbol{S}^i) + \boldsymbol{Y}^i_{,\lambda_\alpha}(\lambda_\alpha^{i+1} - \lambda_\alpha^i) = 0 \\ y^{i+1}(\boldsymbol{S}^{i+1}, \lambda_\alpha^{i+1}) &= y^i + \nabla_S y^i : (\boldsymbol{S}^{i+1} - \boldsymbol{S}^i) + y^i_{,\lambda_\alpha}(\lambda_\alpha^{i+1} - \lambda_\alpha^i) = 0 \end{aligned}$$

The corresponding recurrence formulae are:

$$\begin{aligned}
\lambda_\alpha^{i+1} - \lambda_\alpha^i &= -\frac{\nabla_S y^i : (\nabla_S \boldsymbol{Y}^i)^{-1}}{\nabla_S y^i : (\nabla_S \boldsymbol{Y}^i)^{-1} \boldsymbol{Y}^i_{,\lambda_\alpha} - y^i_{,\lambda_\alpha}} \boldsymbol{Y}^i + \frac{1}{\nabla_S y^i : (\nabla_S \boldsymbol{Y}^i)^{-1} \boldsymbol{Y}^i_{,\lambda_\alpha} - y^i_{,\lambda_\alpha}} y^i \\
\boldsymbol{S}^{i+1} - \boldsymbol{S}^i &= -((\nabla_S \boldsymbol{Y}^i)^{-1} - \frac{(\nabla_S \boldsymbol{Y}^i)^{-1} (\boldsymbol{Y}^i_{,\lambda_\alpha} \otimes \nabla_S y^i)(\nabla_S \boldsymbol{Y}^i)^{-1}}{\nabla_S y^i : (\nabla_S \boldsymbol{Y}^i)^{-1} \boldsymbol{Y}^i_{,\lambda_\alpha} - y^i_{,\lambda_\alpha}}) \boldsymbol{Y}^i \\
&\quad - \frac{(\nabla_S \boldsymbol{Y}^i)^{-1} \boldsymbol{Y}^i_{,\lambda_\alpha}}{\nabla_S y^i : (\nabla_S \boldsymbol{Y}^i)^{-1} \boldsymbol{Y}^i_{,\lambda_\alpha} - y^i_{,\lambda_\alpha}}) \boldsymbol{Y}^i
\end{aligned}$$

where

$$\begin{aligned}
\nabla_S \boldsymbol{Y}^i &= \overline{\mathbb{E}} + \frac{\mathbb{E}'}{f(\alpha_0 + \lambda_\alpha^i)} + \lambda_\alpha^i \frac{\mathbb{E}'(\boldsymbol{S}^i : \mathbb{E}' \boldsymbol{S}^i) - \mathbb{E}' \boldsymbol{S}^i \otimes \mathbb{E}' \boldsymbol{S}^i}{(\boldsymbol{S}^i : \mathbb{E}' \boldsymbol{S}^i)^{\frac{3}{2}}} \\
\boldsymbol{Y}^i_{,\lambda_\alpha} &= (\frac{1}{\sqrt{\boldsymbol{S}^i : \mathbb{E}' \boldsymbol{S}^i}} - \frac{f'(\alpha_0 + \lambda_\alpha^i)}{f^2(\alpha_0 + \lambda_\alpha^i)}) \mathbb{E}' \boldsymbol{S}^i \\
\nabla_S y^i &= \frac{\mathbb{E}' \boldsymbol{S}^i}{\sqrt{\boldsymbol{S}^i : \mathbb{E}' \boldsymbol{S}^i}} \\
y^i_{,\lambda_\alpha} &= -g'(\alpha_0 + \lambda_\alpha^i)
\end{aligned}$$

The final internal variables are then given by:

$$\begin{aligned}
\boldsymbol{E}^p &= \boldsymbol{E}_0^p + \lambda_\alpha \boldsymbol{N} \\
\alpha &= \alpha_0 + \lambda_\alpha
\end{aligned}$$

The total material stress is also given by:

$$\boldsymbol{S} = \overline{\mathbb{S}}(\boldsymbol{E} - \boldsymbol{E}^p) + f(\alpha) \mathbb{S}'(\boldsymbol{E} - \boldsymbol{E}^p) \tag{4.20}$$

The consistency condition $\dot{y}(\boldsymbol{S}, S^\alpha) = 0$ provides the continuum tangent operator:

$$\mathbb{S}^u = \nabla_E \boldsymbol{S} = \mathbb{S} - \frac{\mathbb{S}(\mathbb{E}' \boldsymbol{S} \otimes \mathbb{E}' \boldsymbol{S}) \mathbb{S}}{\mathbb{E}' \boldsymbol{S} : \mathbb{S}\, \mathbb{E}' \boldsymbol{S} + c(\alpha) g'(\alpha) \sqrt{\boldsymbol{S} : \mathbb{E}' \boldsymbol{S}}} \tag{4.21}$$

where

$$c(\alpha) = \frac{f^2(\alpha)}{f^2(\alpha) - f'(\alpha)} \tag{4.22}$$

Remark 4.7 *Symmetry of the continuum tangent operator seems to be due to the existence of the pseudopotential* $\psi + \tau\phi$.

It has been shown by several authors that the notion of consistency between the tangent operator and the incremental algorithm is necessary to preserve the quadratic rate of asymptotic convergence of the Newton method [119]. This "consistent" tangent operator represents the linearization of the incremental implicit projection algorithm instead of that of the continuum rate law:

$$\begin{aligned} \mathbb{S}_a^u &= \nabla_{E^{i+1}} \boldsymbol{S}^{i+1} \\ &= \mathbb{S}_a^i - \frac{\mathbb{S}_a^i (\mathbb{E}' \boldsymbol{S}^i \otimes \mathbb{E}' \boldsymbol{S}^i) \mathbb{S}_a^i}{\mathbb{E}' \boldsymbol{S}^i : \mathbb{S}_a^i \mathbb{E}' \boldsymbol{S}^i + c^i g'(\alpha_0 + \lambda_\alpha^i) \sqrt{\boldsymbol{S}^i : \mathbb{E}' \boldsymbol{S}^i}} \end{aligned} \tag{4.23}$$

where

$$\mathbb{S}_a^i = (\nabla_S \boldsymbol{Y}^i)^{-1} \tag{4.24}$$

and

$$c^i = \frac{f^2(\alpha_0 + \lambda_\alpha^i)}{f^2(\alpha_0 + \lambda_\alpha^i) - f'(\alpha_0 + \lambda_\alpha^i)} \tag{4.25}$$

Remark 4.8 *The discrete consistent tangent operator degenerates into the continuum one when $\lambda_\alpha^i \to 0$, that is when the time step $\tau \to 0$.*

Remark 4.9 *The elastoplastic implicit projection algorithm developed by Rakotomanana et al. [110] is obtained from the present three-dimensional model when $f(\alpha) \equiv 1$ and $g(\alpha) \equiv 0$.*

4.3.2 Model for trabecular bone

The anisotropic three-dimensional model for trabecular bone has been simplified such that $\overline{\mathbb{S}} \equiv 0$ and $\mathbb{S}' \equiv \mathbb{S}$. The previous three-dimensional incremental algorithm can be rigorously applied by replacing $\mathbb{S}'$ and $\mathbb{E}'$ by $\mathbb{S}$, respectively $\mathbb{E}$. The implicit projection involves the following set of equations:

$$\begin{aligned} \boldsymbol{S} &= f(\alpha) \mathbb{S} (\boldsymbol{E} - \boldsymbol{E}^p) \\ S^\alpha &= -\frac{1}{2} f'(\alpha) (\boldsymbol{E} - \boldsymbol{E}^p) \mathbb{S} (\boldsymbol{E} - \boldsymbol{E}^p) - \tilde{\psi}'(\alpha) \\ \boldsymbol{E}^p - \boldsymbol{E}_0^p &= \lambda_\alpha \frac{\mathbb{E} \boldsymbol{S}}{\sqrt{\boldsymbol{S} : \mathbb{E} \boldsymbol{S}}} \equiv \lambda_\alpha \boldsymbol{N} \\ \alpha - \alpha_0 &= \lambda_\alpha \\ y(\boldsymbol{S}, S^\alpha) &= 0 \end{aligned}$$

In this case, the projection is radial:

$$\boldsymbol{S} = \frac{f(\alpha_0+\lambda_\alpha)\sqrt{\boldsymbol{S}:\mathbb{E}'\boldsymbol{S}}}{f(\alpha_0)\sqrt{\boldsymbol{S}:\mathbb{E}'\boldsymbol{S}}-\lambda_\alpha f(\alpha_0)f(\alpha_0+\lambda_\alpha)}\boldsymbol{S}_T$$

The coefficient λ_α is deduced from the condition:

$$y(\boldsymbol{S},\lambda_\alpha) = \sqrt{\boldsymbol{S}:\mathbb{E}'\boldsymbol{S}} - g(\alpha_0+\lambda_\alpha) - y_\sigma = 0$$

Replacing the expression of $\boldsymbol{S}$, the following equation is obtained:

$$F(\lambda_\alpha) = f(\alpha_0+\lambda_\alpha)(\sqrt{\boldsymbol{S}:\mathbb{E}'\boldsymbol{S}} + \lambda_\alpha f(\alpha_0) - f(\alpha_0)(g(\alpha_0+\lambda_\alpha)+y_\sigma) = 0$$

Linearization provides the recurrence formula:

$$\lambda_\alpha^{i+1} = \lambda_\alpha^i - \frac{F^i(\lambda_\alpha^i)}{F^i_{,\lambda_\alpha^i}}$$

where

$$F^i_{,\lambda_\alpha^i} = f'(\alpha_0+\lambda_\alpha^i)(\sqrt{\boldsymbol{S}^i:\mathbb{E}'\boldsymbol{S}^i} + \lambda_\alpha^i f(\alpha_0) + f(\alpha_0)(f(\alpha_0+\lambda_\alpha^i) - g(\alpha_0+\lambda_\alpha^i))$$

Since $\mathbb{S}\mathbb{E} = \mathbb{I}$, the continuum tangent operator reduces to:

$$\mathbb{S}^u = \nabla_E \boldsymbol{S} = \mathbb{S} - \frac{\mathbb{S}(\mathbb{E}\boldsymbol{S}\otimes\mathbb{E}\boldsymbol{S})\mathbb{S}}{\mathbb{E}\boldsymbol{S}:\boldsymbol{S} + c(\alpha)g'(\alpha)\sqrt{\boldsymbol{S}:\mathbb{E}\boldsymbol{S}}} \tag{4.26}$$

with

$$c(\alpha) = \frac{f^2(\alpha)}{f^2(\alpha)-f'(\alpha)} \tag{4.27}$$

Its discrete counterpart is:

$$\begin{aligned}\mathbb{S}^u_a &= \nabla_{E^{i+1}}\boldsymbol{S}^{i+1} \\ &= \mathbb{S}^i_a - \frac{\mathbb{S}^i_a(\mathbb{E}'\boldsymbol{S}^i\otimes\mathbb{E}\boldsymbol{S}^i)\mathbb{S}^i_a}{\mathbb{E}\boldsymbol{S}^i:\mathbb{S}^i_a\mathbb{E}\boldsymbol{S}^i + c^i g'(\alpha_0+\lambda_\alpha^i)\sqrt{\boldsymbol{S}^i:\mathbb{E}\boldsymbol{S}^i}}\end{aligned} \tag{4.28}$$

where

$$\mathbb{S}^i_a = \left(\frac{\mathbb{E}}{f(\alpha_0+\lambda_\alpha^i)} + \lambda_\alpha^i\frac{\mathbb{E}(\boldsymbol{S}^i:\mathbb{E}\boldsymbol{S}^i) - \mathbb{E}\boldsymbol{S}^i\otimes\mathbb{E}\boldsymbol{S}^i}{(\boldsymbol{S}^i:\mathbb{E}\boldsymbol{S}^i)^{\frac{3}{2}}}\right)^{-1} \tag{4.29}$$

and

$$c^i = \frac{f^2(\alpha_0+\lambda_\alpha^i)}{f^2(\alpha_0+\lambda_\alpha^i) - f'(\alpha_0+\lambda_\alpha^i)} \tag{4.30}$$

4.3.3 Validation

The three-dimensional model for trabecular bone has been coded in a FORTRAN subroutine E3BONE and integrated in the three-dimensional finite element software TACT, developped at the Laboratory of Applied Mechanics for contact mechanics applications. We divided its validation in two parts. In a first part, we performed one-dimensional experiments with a single finite element in order to check the programming of the model. In a second part, three boundary value problems were considered to investigate material inhomogeneity and check convergence of the implicit projection algorithm.

One-dimensional experiments

In this first validation part, we performed pure traction and pure shear experiments along the three orthogonal material orientations. Each test consisted in a single sine wave loading of one linear finite element.

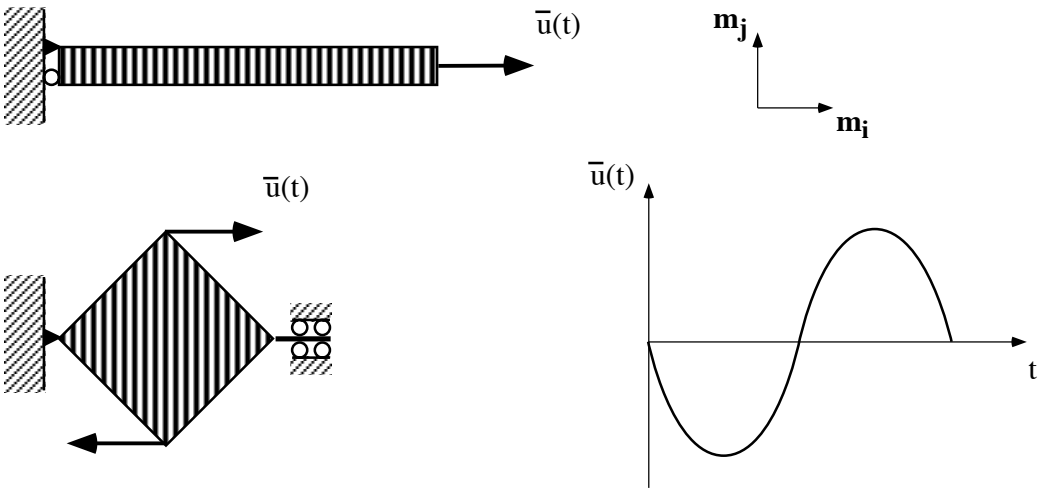

Figure 4.14: Traction and shear experiments for identification of orthotropic elasticity and elastoplasticity with damage.

The nine orthotropic elastic constants appear in the equation:

$$\boldsymbol{E} = \mathbb{E}\boldsymbol{S}$$

Using the map of the strain and stress spaces ($\mathcal{E}$ and $\mathcal{S}$) from $\mathcal{R}^3 \times \mathcal{R}^3$ onto $\mathcal{R}^6$:

$$\begin{pmatrix} E_{11} \\ E_{22} \\ E_{33} \\ \sqrt{2}E_{23} \\ \sqrt{2}E_{31} \\ \sqrt{2}E_{12} \end{pmatrix} = \begin{pmatrix} \frac{1}{\epsilon_1} & -\frac{\nu_{12}}{\epsilon_2} & -\frac{\nu_{13}}{\epsilon_3} & 0 & 0 & 0 \\ -\frac{\nu_{21}}{\epsilon_1} & \frac{1}{\epsilon_2} & -\frac{\nu_{23}}{\epsilon_3} & 0 & 0 & 0 \\ -\frac{\nu_{31}}{\epsilon_1} & -\frac{\nu_{32}}{\epsilon_2} & \frac{1}{\epsilon_3} & 0 & 0 & 0 \\ 0 & 0 & 0 & \frac{1}{2\mu_{23}} & 0 & 0 \\ 0 & 0 & 0 & 0 & \frac{1}{2\mu_{31}} & 0 \\ 0 & 0 & 0 & 0 & 0 & \frac{1}{2\mu_{12}} \end{pmatrix} \cdot \begin{pmatrix} S_{11} \\ S_{22} \\ S_{33} \\ \sqrt{2}S_{23} \\ \sqrt{2}S_{31} \\ \sqrt{2}S_{12} \end{pmatrix}$$

Remark 4.10 *The factor $\sqrt{2}$ is used in order to obtain equivalent scalar products in $\mathcal{R}^3 \times \mathcal{R}^3$ $(<:>)$ and $\mathcal{R}^6$ $(<\cdot>)$.*

Beneath the yield criterion, each traction experiment provides one elastic modulus and two Poisson ratios, while each shear experiment provides one shear modulus.

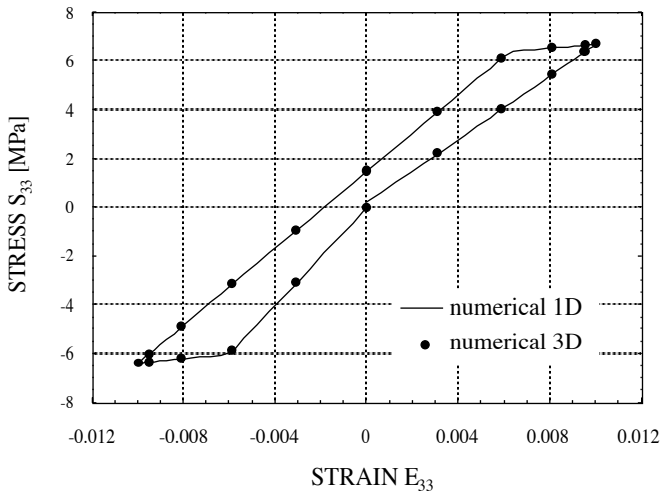

Figure 4.15: Numerical results for the traction experiment for both one-dimensional and three-dimensional algorithms.

The damage and hardening functions were chosen as:

$$\begin{aligned} f(\alpha) &= e^{-\frac{\alpha}{\alpha_f}} \qquad \alpha_f = 0.0756 \\ g(\alpha) &= \gamma\alpha \qquad \gamma = 0.2 \end{aligned}$$

For a traction experiment, the yield condition becomes:

$$\frac{|S_{ii}|}{\sqrt{\epsilon_i}} - g(\alpha) - y_\sigma = 0$$

The internal variable α is given by:

$$\alpha = \int_0^t \sqrt{\epsilon_i} |\dot{E}^p_{ii}| d\tau$$

The yield stress is provided by:

$$\sigma_{ii} = \sqrt{\epsilon_i} y_\sigma$$

In the shear experiment, the yield condition becomes:

$$\frac{|S_{ij}|}{\sqrt{\mu_{ij}}} - g(\alpha) - y_\sigma = 0$$

The internal variable α is given by:

$$\alpha = \int_0^t 2\sqrt{\mu_{ij}} |\dot{E}^p_{ij}| d\tau$$

The yield stress is provided by:

$$\sigma_{ij} = \sqrt{\mu_{ij}} y_\sigma$$

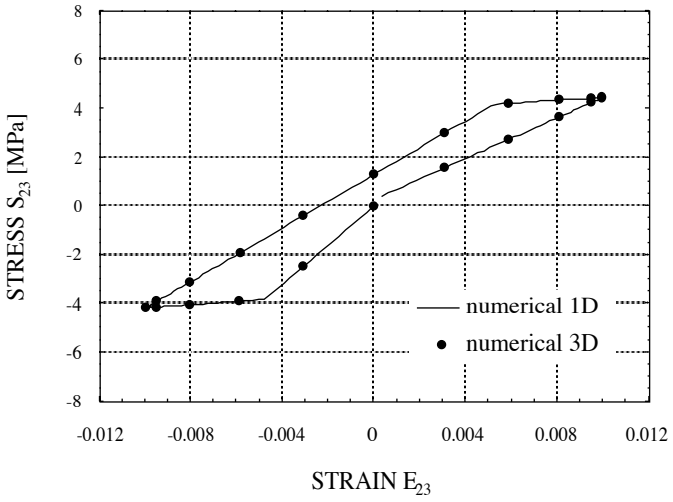

Figure 4.16: Numerical results for the shear experiment for both one-dimensional and three-dimensional algorithms.

The obtained one-dimensional stress-strain curves were compared with the appropriate one-dimensional models in the case where $\sigma_- = \sigma_+$. In order to verify correctness of the tangent matrix, similar experiments were performed with force instead of displacement schedules.

Boundary value problems

In this second validation part, we investigated the traction of a bar, the bending of a plate and the torsion of a cylinder with inhomogeneous material properties. For each problem, the numerical results of elasticity and elastoplasticity with damage were compared with the closed-form elastic solution for a single step loading.

Traction experiment In the traction experiment, the material properties were allowed to depend on the longitudinal axis of the bar (Fig. 4.17).

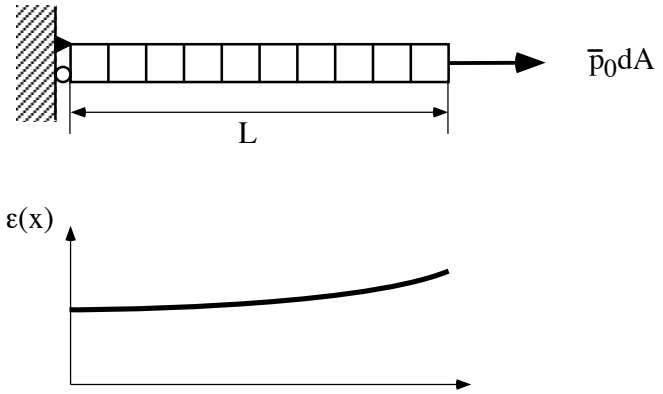

Figure 4.17: Finite element model for traction of an inhomogeneous bar.

The axial displacement of the free end of the bar due to an axial force per unit area $\bar{p}_0$ is given by:

$$u_x(x) = \bar{p}_0 \int_0^x \frac{1}{\epsilon(s)} ds$$

with

$$\epsilon(x) = \epsilon_c (0.9 + 0.1 \frac{x}{L})^2$$

The material constants are given in Table 4.7, whereas the damage and hardening functions were:

$$\begin{aligned} f(\alpha) &= e^{-\frac{\alpha}{\alpha_f}} \qquad \alpha_f = 1.054 \\ g(\alpha) &= g_{max}(1 - e^{-\frac{\alpha}{\alpha_g}}) \qquad g_{max} = 0.527 \qquad \alpha_g = 1.054 \end{aligned}$$

$Elements$	L $[mm]$	A $[mm^2]$	$\bar{p}_0$ $[MPa]$	ϵ_c $[MPa]$	ν_c	y_σ $[\sqrt{MPa}]$
10	1.0	0.01	0.1	1000	0.25	1.054

Table 4.7: Parameters and material constants of the traction simulation.

The results of the simulations are displayed in Fig. 4.18. Accuracy of the finite element model has proven to be excellent for traction, because of the use of an exact geometry and an exact analytical solution (Table 4.10). Flow of an irreversible deformation beyond the yield criterion increases significantly the deformation of the bar and emphasizes the nonlinear effect of material inhomogeneity.

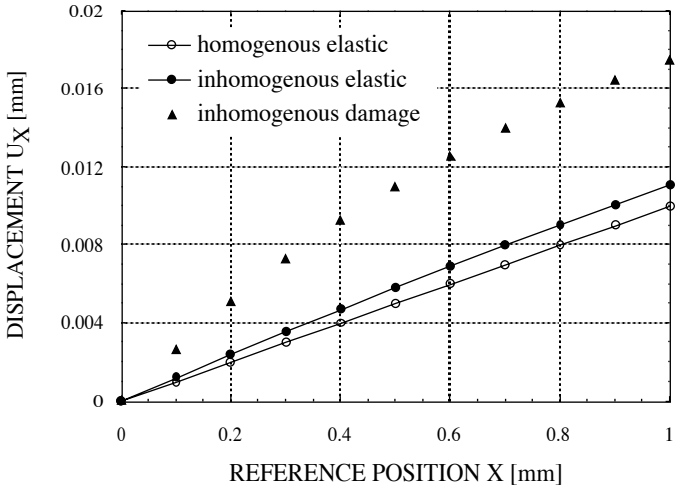

Figure 4.18: Numerical results for the traction experiments.

Bending experiment In the bending experiment, the material properties varied through the thickness of the plate (Fig. 4.19).
Deflection of the free end of a thin plate by an angular moment $\bar{M}$ is given by classical plate theory [127]:

$$u_z(x) = -\frac{1}{2}\frac{\bar{M}}{D_p}x^2$$

where D_p is the flexural rigidity of the plate:

$$D_p = \int_{-h}^{h} \frac{\epsilon(s)s^2}{1-\nu^2(s)}ds$$

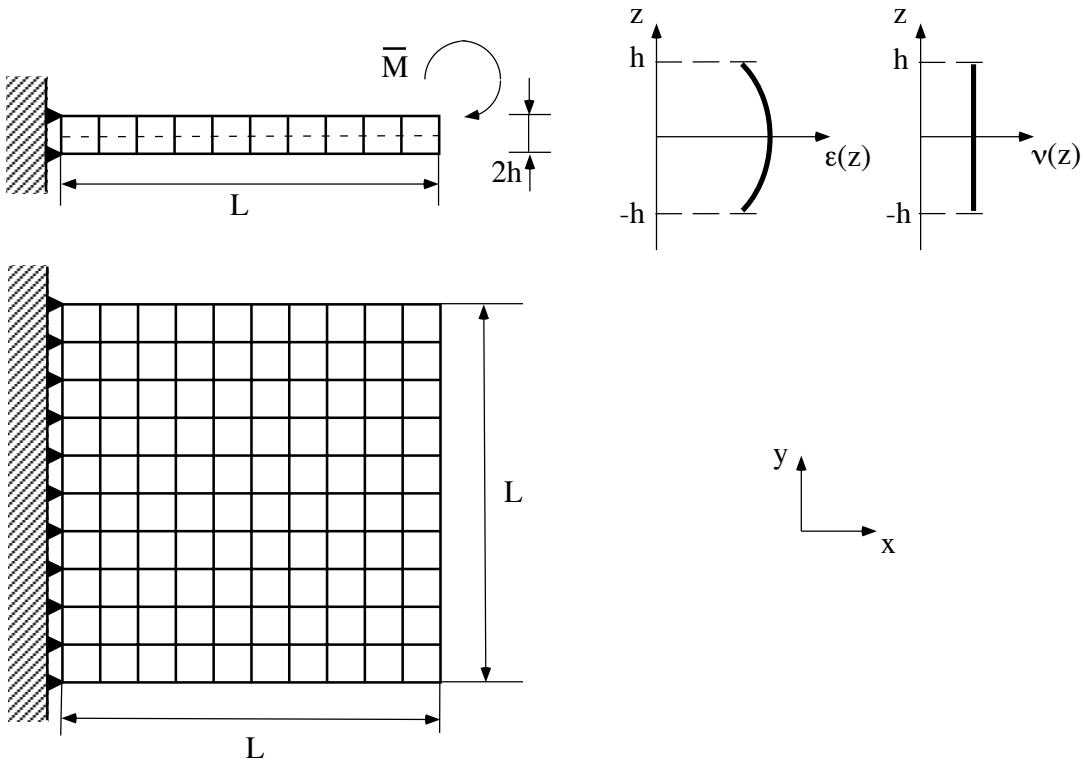

Figure 4.19: Finite element model for bending of an inhomogeneous plate.

Elements	L $[mm]$	h $[mm^2]$	$\bar{M}$ $[Nmm]$	ϵ_c $[MPa]$	ν_c	y_σ $[\sqrt{MPa}]$
400	40.0	2.0	2000	1000	0.25	1.054

Table 4.8: Parameters and material constants of the bending simulation.

We chose

$$\begin{aligned} \epsilon(z) &= \epsilon_c(1 - 0.1\frac{|z|}{h})^2 \\ \nu(z) &= \nu_c \end{aligned}$$

The material constants are shown in Table 4.8.

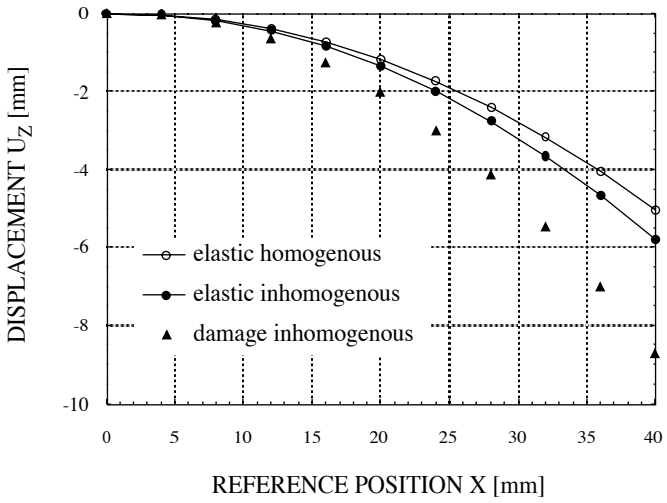

Figure 4.20: Numerical results for the bending experiments.

The damage and hardening functions were again chosen as:

$$\begin{aligned} f(\alpha) &= e^{-\frac{\alpha}{\alpha_f}} \qquad \alpha_f = 1.054 \\ g(\alpha) &= g_{max}(1 - e^{-\frac{\alpha}{\alpha_g}}) \qquad g_{max} = 0.527 \qquad \alpha_g = 1.054 \end{aligned}$$

A selective integration method was used in order to avoid the well-known problem of insufficient bending of the solid finite element encountered with the usual Gauss integration method. However, for the sake of comparison, we display the results obtained with the standard integration method (Fig. 4.20).
The overestimation of 2% encountered for the numerical results with respect to the analytical calculation is consistent with the approximation done in thin plate theory for the considered aspect ratio of the plate (Table 4.10). As expected, irreversible deformations concentrate on the upper and lower faces of the plate and increase the effect of bending (Fig. 4.20).

Torsion experiment In the torsion experiment, the material properties differed along the axis of the cylinder (Fig. 4.21).

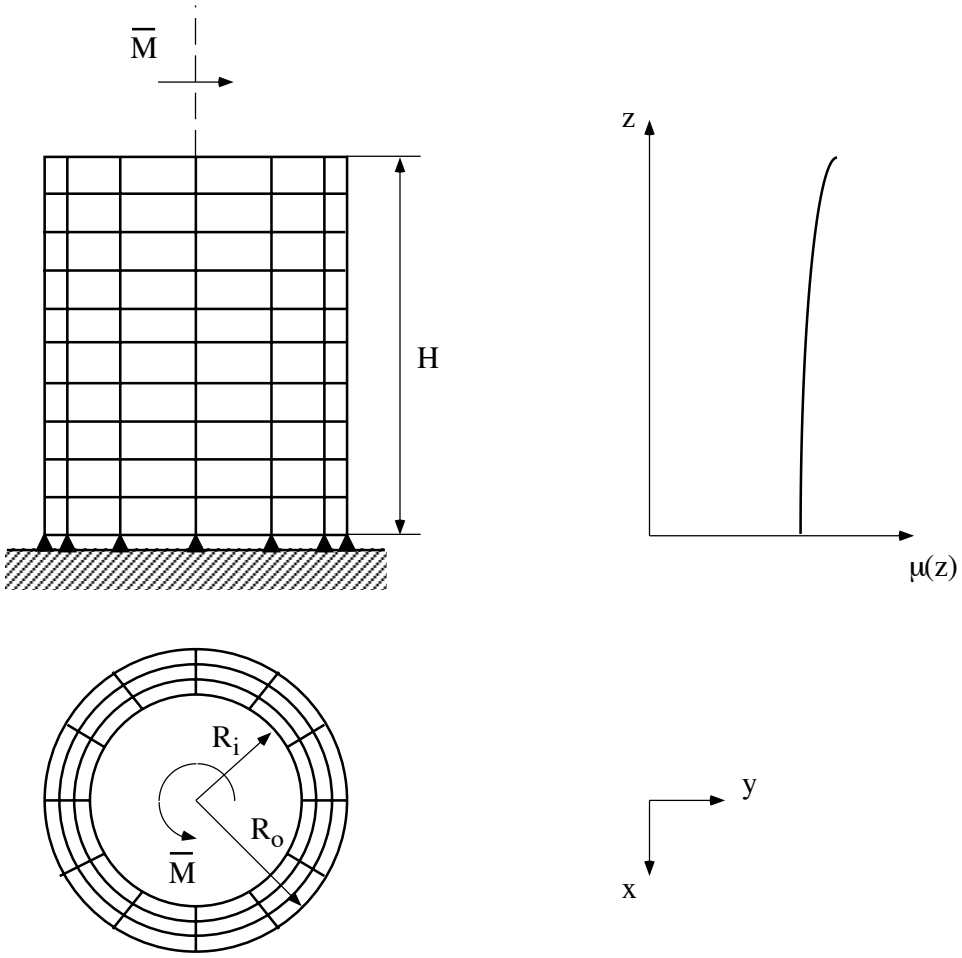

Figure 4.21: Finite element model for torsion of an inhomogeneous cylinder.

Angular displacement of the section of a thin hollow cylinder under the influence of an axial angular momentum $\bar{M}$ is determined by [106]:

$$\vartheta(z) = \frac{\bar{M}}{2\pi(R_o^4 - R_i^4)} \int_0^z \frac{1}{\mu(s)} ds$$

where R_o and R_i are the outer and the inner radius of the cylinder.
The shear coefficient is given by:

$$\mu(z) = \mu_c(0.9 + 0.1\frac{z}{H})^2$$

$Elements$	H $[mm]$	R_o $[mm]$	R_i $[mm]$	M $[Nmm]$	ϵ_c $[MPa]$	ν_c	y_σ $[\sqrt{MPa}]$
360	20.0	3.0	2.7	97.62	1000	0.25	1.054

Table 4.9: Parameters and material constants of the torsion simulation.

The damage and hardening functions were also chosen as:

$$f(\alpha) = e^{-\frac{\alpha}{\alpha_f}} \qquad \alpha_f = 1.054$$
$$g(\alpha) = g_{max}(1 - e^{-\frac{\alpha}{\alpha_g}}) \qquad g_{max} = 0.527 \qquad \alpha_g = 1.054$$

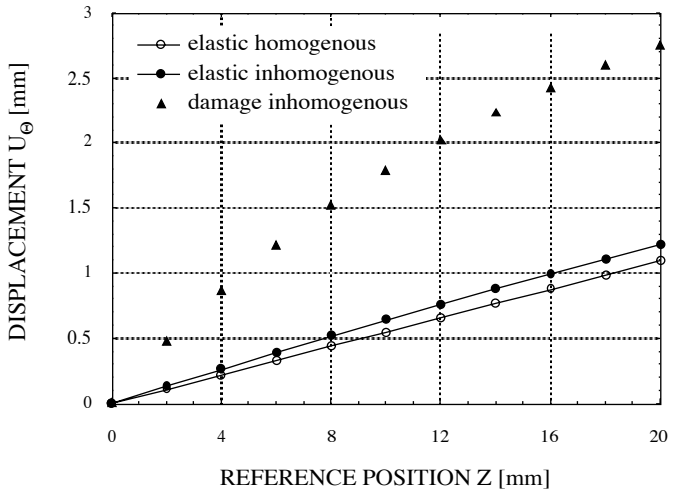

Figure 4.22: Numerical results for the torsion experiments.

In the torsion experiment, discretization of the cylinder induced a significant error in the area momentum of the section. We accounted for this problem by taking the average analytical solution for the internal and external ring associated with the polygonal section and obtained reasonable accuracy (Table 4.10). Localization of plastic deformations at the bottom of the cylinder increases significantly the global tangential displacements (Fig. 4.22).

In all experiments, convergence of the implicit projection algorithm was reached within a few steps and was quadratic in the neighborhood of the solution (Table 4.11). The three-dimensional numerical model has thus proven to behave properly

	value	analytical $[mm]$	numerical $[mm]$	error %
traction	$u(L)$	0.1111	0.1111	0.00
bending	$u_z(L)$	8.216	8.383	2.03
torsion	$u_\theta(H)$	0.3996	0.4076	2.00

Table 4.10: Comparison of analytical versus numerical results for the inhomogeneous elasticity problems.

and is ready for use in a large application as soon as the material constants have been identified.

step	traction	bending	torsion
1	$.200E+01$	$.200E+01$	$.200E+01$
2	$.400E+00$	$.503E+00$	$.553E+00$
3	$.112E+00$	$.196E+00$	$.229E+00$
4	$.107E-01$	$.156E-01$	$.560E-01$
5	$.122E-03$	$.191E-03$	$.405E-02$
6	$.201E-07$	$.278E-07$	$.275E-04$
7	–	–	$.155E-08$

Table 4.11: Convergence norms of the implicit projection algorithm for the three considered experiments.

Chapter 5

Identification of the constitutive laws

In this chapter, identification of both the one- and three-dimensional constitutive laws developed for trabecular bone is described through a number of pilot *in vitro* experiments we undertook on human and bovine specimens.

testing method	loading schedule	axis	Human cube	Bovine hexa	Bovine waisted hexa	Bovine waisted cyl
uniaxial	compression	x	127	–	4	–
		y	127	–	4	–
		z	121	–	5	–
	tension	z	–	–	3	–
	cycles	z	–	–	9	–
	creep	z	–	10	–	–
torsion	cycles	z	–	–	–	9

Table 5.1: Overview of the mechanical tests performed for identification of the constitutive laws.

As shown in Table 5.1, uniaxial and torsional mechanical tests were performed with different loading schedules and specimen geometry. The experiments on cu-

bic and hexahedral specimens involve artefacts associated with inhomogeneous boundary conditions and bring essentially qualitative insight, while the few experiments with waisted specimens provide also a quantitative evaluation of the quasistatic plastic and damage processes. Despite the known variability of trabecular bone properties and thus the necessity of large statistics, we privileged quality over quantity of the tests and intended to demonstrate the relevance of the developed models, to explore the appropriate tracks for future mechanical testing rather than producing definitive experimental data. We also take the opportunity to verify prediction of trabecular bone properties by non-invasive methods such as QCT and DEXA.

5.1 Three-dimensional orthotropic elasticity

This first set of experiments includes mechanical testing, stereological analysis and measurement of tissue properties for trabecular specimens extracted from the human proximal tibia. The resulting data are employed together with data from the literature for identification of the three-dimensional orthotropic elasticity model, in particular the constants ϵ_c,μ_c,ν_c,k and l.

5.1.1 Materials and methods

Six unembalmed human knees were obtained within $24h$ of autopsy from the Harvard Anatomic Gifts Program and frozen at $-20°C$. After *in situ* quantitative computed tomography (QCT), we sectioned defined regions of interest for the removal of trabecular specimens for mechanical testing, stereological analysis, and determination of apparent and ash densities.

Regions of interest Twenty-four regions of interest were defined in two sets of three planes parallel to the medial and lateral joint surfaces. This procedure accounted for the height difference between compartments, the sagittal retroversion of the tibial plateau and insured best alignment of the regions with respect to the principal direction of the trabecular structure. The locations of the planes

and regions of interest were calculated in proportion to the dimensions of each tibia. The slices containing the regions of interest were $6mm$ thick. After removal of soft tissue, the proximal tibias were carefully aligned in a plexiglas box and the regions calculated with the help of fine grain radiographs.

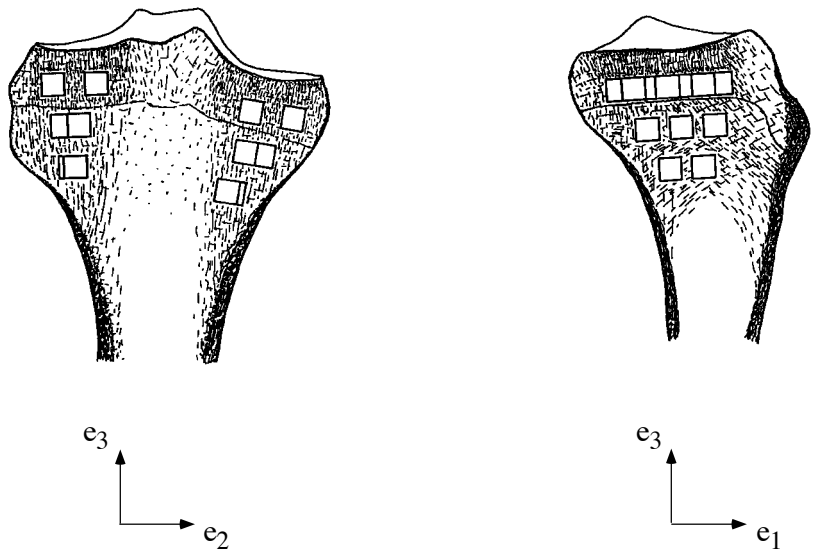

Figure 5.1: Orientation of the specimens in the coronal (left) and sagittal (right) sections of the proximal tibia.

Quantitative computed tomography The plexiglas box was then filled with physiological saline solution and a GE 9800 clinical scanner (General Electric, Milwaukee, WI, USA) was used together with a standard K_2HPO_4 calibration phantom for quantitative computed tomography (QCT). Precise alignment of the proximal tibia was obtained by the laser target of the scanner and the machined marks on the box. Six pairs of $3mm$ thick scans at $120KV$, $140mA$, $2s$, were performed to fit exactly the six slices containing the regions of interest. The scan field was $25cm$ and the image matrix 512×512 pixels. The resulting pixel size was approximately $0.5mm$. The regions of interest on the digital images were computed and the corresponding CT numbers averaged within each region. Using the calibration curve of the phantom, CT units were then transformed to equivalent bone mineral density units.

Specimen preparation After scanning, the proximal tibias were kept in the box and directly embedded with low expansion synthetic foam (Litecast, Isocast Systems, Clackamas, OR, USA). The foam block was then extracted from the box and stored at $-20°C$. The six slices were drawn on the frozen foam block and cut under water cooling on a circular saw with an aluminium oxide cut-off wheel (Buehler Ltd, Lake Bluff, IL, USA). The regions of interest were then drawn on each slice and all specimens extracted under water cooling on an Isomet saw with a diamond wafering blade (Buehler Ltd, Lake Bluff, IL, USA). The faces of the trabecular specimens were colored according to their anatomical orientation and frozen at $-20°C$.

Mechanical testing Compressive tests were performed using a 1331 Instron material testing system (Instron Corp, Canton, MA, USA), using either a $500N$ or a $2000N$ load cell (Sensotec, Columbus, OH, USA) and an axial strain gauge extensometer (Instron Corp, Canton, MA, USA). Calibration was repeated before each series of test.

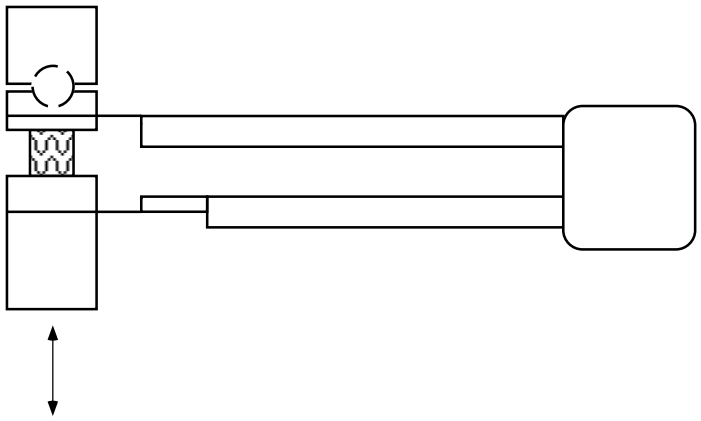

Figure 5.2: Axial compression of the cubic specimens and displacement measurement with an axial strain gauge extensometer.

Prior to testing, specimens were thawed at room temperature in physiological saline and their dimensions were measured with a micrometer. Each specimen was then placed between grease-coated loading platens and kept fully moist during the entire testing procedure. A preload of $10N$ was chosen to define zero strain.

The specimens were deformed to 0.625% strain and then an additional cyclic deformation of 0.125% amplitude was applied at a frequency of $0.5Hz$. The resulting deformation rate was $0.004s^{-1}$. After ten cycles of conditioning, data were collected at $1024Hz$ during one deformation cycle. The elastic modulus

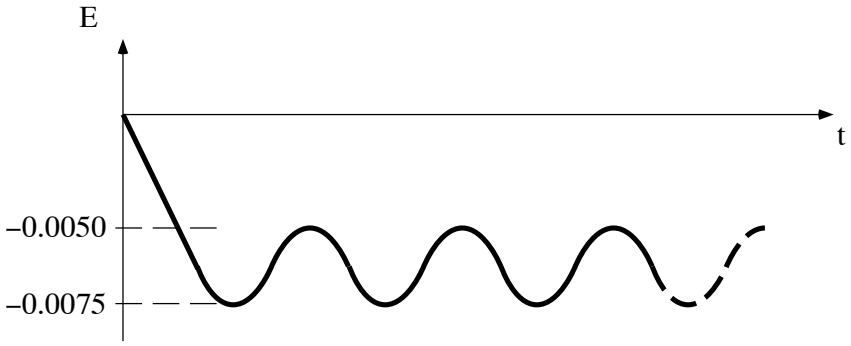

Figure 5.3: Schedule of the non-destructive mechanical testing.

was calculated by linear regression. Compressive testing was repeated for the six faces of each specimen and the elastic modulus of opposite directions averaged. All tests were performed at room temperature ($\sim 20°C$).

Quantitative stereology We used a computerized video digitizing system for analysis of planar trabecular images (Fig. 5.4).

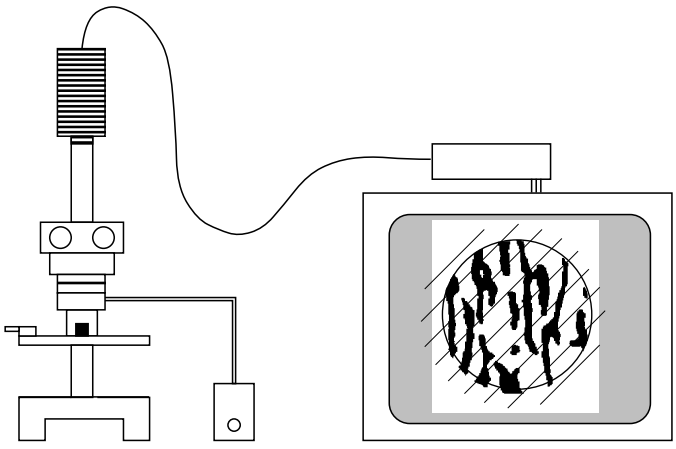

Figure 5.4: Quantitative stereolgy.

The six faces of the specimens were colored with permanent markers and packed with powdered sugar. The images of each face were captured by a video camera mounted to a low magnification reflected light microscope and digitized with an image processing system (Gould FD 5000, San Jose, CA, USA). Differentiation of bone and marrow phase was achieved by selecting a grey level threshold that minimized artifacts. The method of directed secants was applied to the six faces of each cubic specimen and a three dimensional positive definite tensor was fit to the results by a least squares method. The eigenvalues were then calculated as well as the usual three dimensional morphological parameters such as surface density, trabecular thickness, intertrabecular spacing and number of trabeculae per unit test line length.

Measurement of tissue properties All specimens were degreased in soapy water for $24h$ and immersed for $6min$ in an ultrasonic cleanser with 10% hypochloride bleach. Marrow was washed out under running water and the whole procedure repeated once. Specimens were next immersed in distilled water, vacuum degassed and weighed while suspended from an analytical balance to determine the submerged weight (Archimede's method). They were then centrifuged at $8000g$ for $20min$ in a piece of gauze to remove residual water and weighed to determine the hydrated weight. The apparent density of each specimen was calculated as the hydrated weight divided by the bulk volume. Volume of bone tissue was determined from the difference between hydrated and submerged weight. Structural density was calculated as the volume of bone tissue divided by the bulk volume of the specimen. Tissue density was obtained by dividing hydrated weight by bone tissue volume. For ash content determination, the specimens were first dehydrated for $24h$ in a convection oven at $75°C$ and then ashed in a muffle furnace at $600°C$ for $12h$. Finally, the residual ash of each specimen was weighed and apparent ash density calculated as the ash weight divided by the bulk volume and ash content as the ash weight divided by the bone tissue volume.

5.1.2 Results

Structural density of trabecular bone in the proximal tibia was highly inhomogeneous and ranged between 0.021 and 0.168, while tissue density averaged $2.030 g/cm^3$.

In situ QCT was strongly correlated with apparent ash density and thus with structural density:

$$\rho_{aa} = 0.80 \cdot QCT + 48.1 \qquad (n = 110, r^2 = .83, p < 0.0001)$$

$$\rho_s = 0.61 \cdot QCT + 0.038 \qquad (n = 110, r^2 = .81, p < 0.0001)$$

where ρ_{aa} and QCT are expressed in $[mg/cm^3]$.

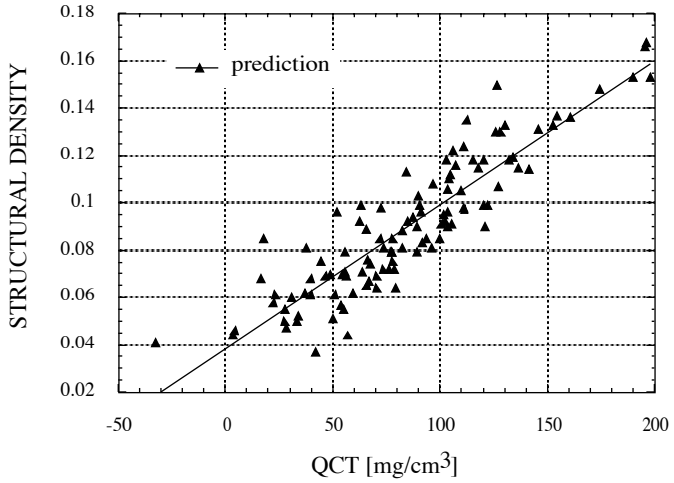

Figure 5.5: Prediction of structural density ρ_s by QCT.

Stereological analysis confirmed that the principal orientations of the trabecular structure corresponded approximately to the edges of the cubic specimens. The average angular deviations was lower than 6° in the coronal plane and lower than 17° in the axial and sagittal plane. The standard deviations reached 26° in the coronal plane and 41° in the axial and sagittal plane.

Maximum mean intercept length was primarily oriented along the axial direction 3 of the specimen, while minimum length was usually oriented along the sagittal axis 2 (Table 5.2). The mean intercept length ellipsoids were generally triaxial, i.e. with three different axis lengths. However, transverse isotropy was nearly holding. The extent of transverse isotropy, defined as the ratio of average transverse

	coronal 1	sagittal 2	axial 3
min	0.221	0.160	0.302
max	0.415	0.362	0.593
mean	**0.304**	**0.268**	**0.428**
sd	0.037	0.035	0.053

Table 5.2: Statistics of normalized mean intercept length.

(coronal and sagittal) versus longitudinal (axial) mean intercept length ($r_{ti} \simeq .67$) was poorly correlated with structural density ($n = 126, r^2 = .03, p < 0.1$).
As shown in Table 5.3, mechanical properties were even more heterogeneous as mean intercept lengths. However, transverse isotropy was still observed, with a much more pronounced degree than the morphologic one ($r_{ti} \simeq .14$).

	coronal 1	sagittal 2	axial 3
min	8	2	102
max	288	227	1726
mean	**90**	**67**	**545**
sd	61	48	342

Table 5.3: Statistics of the orthogonal elastic moduli in $[MPa]$.

As expected, power law relationships were obtained between elastic modulus and structural density in all directions:

$$\begin{aligned} \epsilon_1 &= 3558\rho_s^{1.6} \qquad (n = 127, r^2 = .50, p < 0.001) \\ \epsilon_2 &= 3873\rho_s^{1.8} \qquad (n = 121, r^2 = .40, p < 0.001) \\ \epsilon_3 &= 44134\rho_s^{1.9} \qquad (n = 127, r^2 = .83, p < 0.001) \end{aligned}$$

where ϵ_i are expressed in $[MPa]$. In all cases, the exponent of the power law was not significantly different from 2.0.

Identification Three coefficients of the three-dimensional orthotropic elasticity model are obtained with the relationship:

$$\epsilon_i = \epsilon_c m_i^{2k} \rho_s^{2l}$$

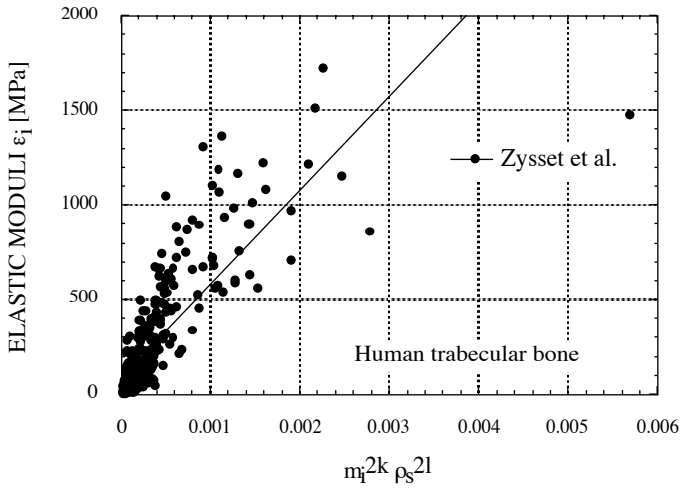

Figure 5.6: Orthotropic elastic moduli and the prediction of the constitutive law involving the normalized eigenvalues of the mean intercept length tensor as well as structural density.

Multilinear regression provided the following constants:

$$\begin{aligned} \epsilon_c &= 683512[MPa] \\ k &= 1.9 \\ l &= 0.9 \end{aligned}$$

with $n = 363, r^2 = .72, p < 0.001$.

5.1.3 Discussion

Quantitative computed tomography Our relationship between apparent ash density and QCT is in agreement with other investigations in the tibia, femur and spine, using the same QCT units and similar CT settings. For the spine, Glüer et al. [53] obtained the following relationship:

$$\rho_{aa} = 0.91 \cdot QCT + 25.2 \qquad (n = 62, r^2 = .85, p < 0.001)$$

The slope we obtained for the proximal tibia is within 12% of this result and our coefficient of determination is very similar ($r^2 = .83$). However, the intercept was substantially higher (91%) in our relationship, which may be explained by the different scanning geometry and bone material we used. Our experiments confirm the findings of Hvid et al. [72], who reported that QCT explains more than 80% of the variance of apparent density at the proximal tibia. The accuracy of this relationship is limited on one hand by the variability of bone tissue and bone marrow composition, and on the other hand, by the intrinsic artefacts of computed tomography, such as beam hardening [19]. Nevertheless, the fairly constant composition of trabecular bone allows to estimate directly structural density and thus a number of mechanical properties by QCT.

Tissue properties Average structural density in our proximal tibias correlated with age of the donors ($p < 0.0001$). The tissue density obtained in our proximal tibias is comparable or slightly greater than similar measurements performed in the vertebrae [2, 56, 101]. Our protocol, based on ultrasound cleaning with extremely low concentration of hypochloride acid, was efficient and might have raised the values of tissue density, when compared to those of other studies.

Quantitative stereology The moderate coefficient of determination between structural density determined by stereology and density measured by Archimede's method ($r^2 = .49$) emphasizes that accuracy of our stereological method was limited by inhomogeneity of the specimens and by the sensitivity of the measurements to the choice of grey level threshold during image processing. However, our stereological results for the proximal tibia are comparable with similar studies of the spine and the femur [121]. For all these anatomical locations, an increase in structural density is associated with a linear increase both in trabecular thickness and in the number of trabeculae along the axis 3. This represents a synergistic stiffening of the trabecular structure, which helps explaining the power law relationship between structural density and axial elastic modulus. The extent of anisotropy and structural density were independent, which justifies the choice that they remain uncoupled in our theoretical model.

Mechanical testing The relatively low elastic moduli obtained in this experiment coincide with the low structural densities and are mainly explained by the advanced age of the donors. Inhomogeneity of the mechanical properties in the proximal tibia is representative of those listed in Table 2.4 from other anatomical locations. However, the degree of anisotropy of the elastic properties obtained in this study contrasts with that obtained by another author with ultrasound measurements (Table 2.6). In fact, we suspect that substantial damage occured in the testing procedure due to excessive strain, as will be shown in the quasistatic experiments (Section 5.3). Since the axial direction was tested first, the elastic moduli in the two other directions were most probably underestimated. This fact helps explain the high coefficient k describing the influence of morphological anisotropy in our constitutive law as well as the lower correlations obtained for these measurements with structural density. Additional errors are due to misalignment of the specimens with the principal directions of the trabecular structure [130].

The power law relationships between elastic moduli and structural density correspond to the classical Eq. 2.11 and to the theoretical predictions for a cubic model of morphology type II mentioned in Table 2.7.

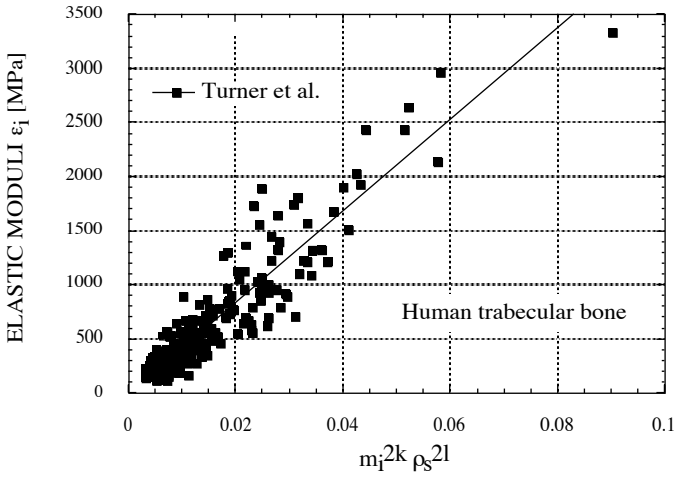

Figure 5.7: Orthotropic elastic moduli from Turner et al. [131] and prediction by our constitutive law.

Identification In order to check the validity of our model for all elastic constants, we performed multilinear regressions with data collected by Turner et al. [131] and Klever [79]. Since Klever did not collect morphological data, the mean intercept length eigenvalues were derived from the orthogonal Young's moduli by assuming $k = 1$.

The orthotropic elastic constants were fitted to:

$$\begin{aligned} \epsilon_i &= \epsilon_c m_i^{2k} \rho_s^{2l} \\ \mu_{ij} &= \mu_c m_i^k m_j^k \rho_s^{2l} \\ \nu_{ij} &= \nu_c \frac{m_j^k}{m_i^k} \end{aligned}$$

The results of this analysis are summarized in Table 5.4 and illustrated in Fig. 5.7 for the elastic moduli, Fig. 5.8 for the shear moduli and Fig. 5.9 for the Poisson ratios. They show a reasonable consistency between the exponents obtained for bone from the same species, excepted for the Poisson ratios. For the data from Turner et al., our coefficients of determination are comparable to those reported by these authors with the model of Cowin involving up to eight constants [131].

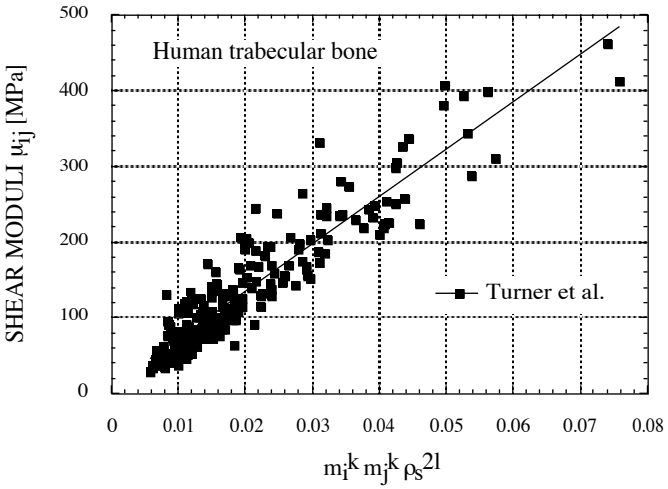

Figure 5.8: Orthotropic shear moduli from Turner et al. [131] and prediction by our constitutive law.

The dependence of the Poisson ratios with respect to structural density was found to be insignificant ($p = 0.18$), which coincides with the prediction of our model.

However, the rather approximate alignment of the specimens in the work of Klever may have reduced the measured anisotropy and thus underestimate the influence of the mean intercept length tensor on the Poisson ratios in terms of the constant k.

		Human tibia		Bovine femur
		Klever	Turner et al.	
ϵ_i	ϵ_c	–	39144	36498
	k	–	0.90	1.09
	l	–	0.56	0.89
	n	–	212	30
	r^2	–	.80	.82
μ_{ij}	μ_c	–	6608	11944
	k	–	1.40	1.37
	l	–	0.59	1.02
	n	–	212	33
	r^2	–	.84	.90
ν_{ij}	ν_c	0.32	–	–
	k	0.50	–	–
	l	ns	–	–
	n	108	–	–
	r^2	.75	–	–

Table 5.4: Identification of our constitutive law for orthotropic elasticity using data from other authors.

According to the theoretical model using a single structural tensor $\boldsymbol{M}$, material symmetry becomes isotropic when the eigenvalues m_i degenerate and thus:

$$\mu_c = \frac{\epsilon_c}{2(1+\nu_c)}$$

This equation is obviously not verified for human bone and would require that $\nu_c = 0.53$ in bovine bone, which is not only incompatible with the thermodynamic restrictions, but also not realistic from a physical point of view since $\nu_c = 0.5$

corresponds to an incompressible material. As checked with the model of Turner et al. and by inspection of the data we obtained in Section 5.3, this finding is an experimental fact and is not related to our specific model.

This contradiction shows that the type of mechanical symmetry encountered in the proximal tibia can not be described by a second order structural tensor $\boldsymbol{M}$ alone. To explain this fact, we suggest two hypotheses. Either, the harmonic analysis of experimental mean intercept length reveals terms of order higher than two, and description of material symmetry requires an additional tensor of rank four, or the anisotropy of the lamellar structure has an influence on the material symmetry due to the intermediary scale at which mechanical data are gathered.

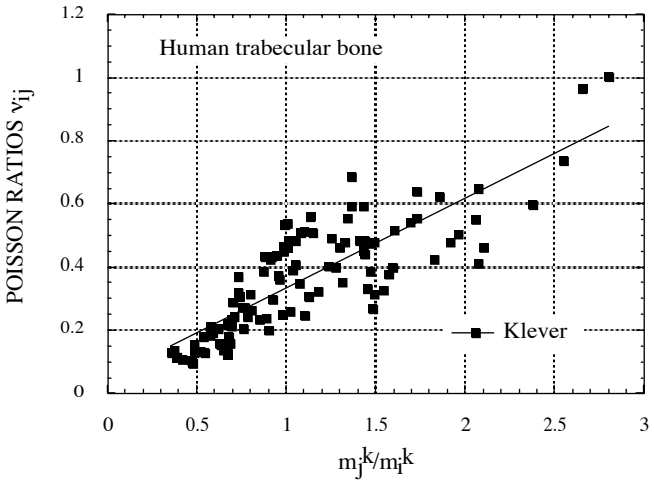

Figure 5.9: Orthotropic Poisson ratios from Klever [79] and prediction by our constitutive law.

To conclude, our orthotropic elasticity based on three constants and a second order approximation of mean intercept length proves to be a concise and efficient model that avoids the limitation encountered by the use of the tensor $\boldsymbol{M}$ as a single structural tensor. In particular, the expected development of non-invasive tools for *in vivo* assessment of mean intercept length may provide a promising role to the model in predicting of anisotropic mechanical properties [78].

5.2 One-dimensional compressive creep

This second set of experiments involves compressive creep testing of bovine trabecular bone. The collected data are used to identify the rate-dependent aspect of the irreversible process described by the one-dimensional model, in particular the material constants ζ and m.

5.2.1 Materials and methods

Trabecular bone hexahedron of $8 \times 8 \times 12mm$ were milled from fresh bovine proximal tibias along the normal direction to the joint surface and stored at $-20°C$. No longitudinal force and minimal lateral force was applied on the specimens during the milling procedure. Before testing, the specimens were thawed overnight at $-4°C$ and for two hours at room temperature.

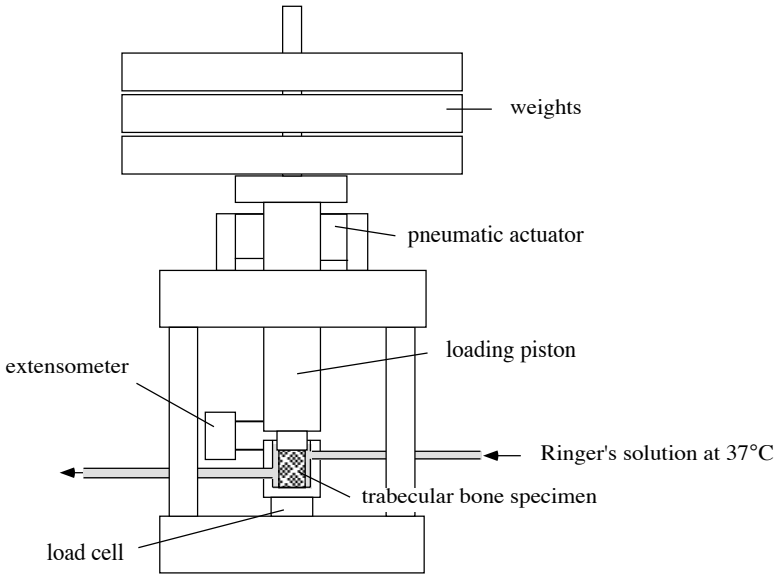

Figure 5.10: Specifically designed loading piston for creep testing of hydrated trabecular bone with temperature control.

In order to evaluate the appropriate creep load, each specimen was initially subjected to a single ramp compressive test on an Instron servohydraulic testing machine (Instron Corp, Canton, MA, USA) up to a maximum strain ranging from

0.012 to 0.02 (Fig. 5.11). The strain rate was $0.001s^{-1}$. The maximum applied stress and the elastic modulus were obtained from the stress-strain curves and normalized stress was calculated to account for the different structural density of the specimens.

Compressive creep testing was then conducted by the means of a custom-made loading piston, that released calibrated weights with a pneumatic actuator (Fig. 5.10).

The specimens were immersed and loaded in a stainless steel container filled with Ringer's solution kept at $37°C$, but no bacterial inhibitors were added. Displacements were measured between the loading piston and the container with an axial $12.5mm$ gauge length extensometer (Instron Corp, Canton, MA, USA), while data acquisition was triggered by a built-in $5000N$ load cell (Brüel & Kjær,Nærum, DK). Drift of the extensometer signal was tested overnight ($12h$) and found to be lower than $3\mu m$. Data acquisition was insured by an HP controller (Hewlett Packard Company, USA).

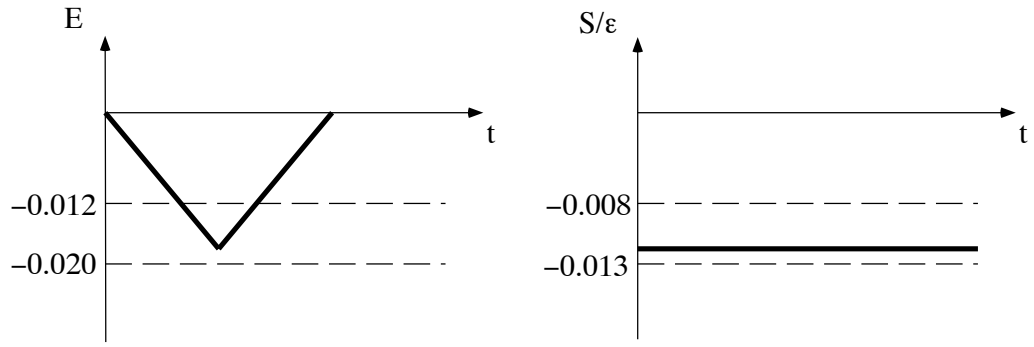

Figure 5.11: Single ramp compressive test and creep test schedules with a precalculated constant load.

5.2.2 Results

Ten specimens were successfully tested and analyzed. The maximum applied stresses ranged from -8.6 to $-30.4MPa$, while elastic moduli ranged from 816 to $2446MPa$. Like in other materials, the compressive creep behaviour of trabecular bone exhibited three successive stages (Fig. 5.12).

A primary stage where strain rate decreased progressively, a secondary stage where strain rate remained approximately constant and a tertiary stage where strain rate increased rapidly and lead to failure of the specimen by crushing.

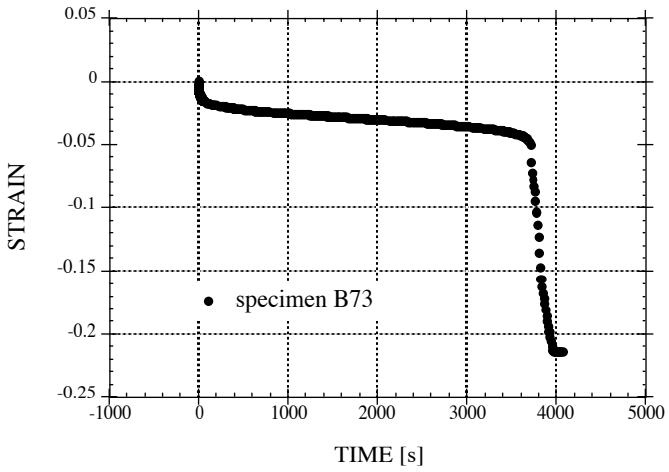

Figure 5.12: Experimental strain versus time curve for specimen B73, including the primary, secondary and tertiary creep stages.

For subsequent analysis, secondary stage strain rate was obtained by the tangent of the curve at the first inflexion point. In the tertiary stage, time to failure was defined by the second inflexion point of the curve and ranged from 72 to 577000s. Initial and final creep strains, given in Table 5.5, were defined by the value of the strain rate tangent at t=0 and at time to failure.

We noticed that the inflexion point of the secondary creep stage, and thus minimal strain rate, corresponds to the total strain defined by the extremum of the quasistatic stress-strain curve (Fig. 5.13).

Identification of the viscous material constants was then performed by the following nonlinear regression:

$$\dot{E}_{sec} = (1 + S\frac{f'(\alpha_{max})}{f^2(\alpha_{max})})(\frac{S - g_{max} - \sigma_-}{\zeta})^m$$

where the ratio f'/f^2 is a constant obtained from quasistatic damage experiments (Section 5.3). The index "max" refers to the extremum of the quasistatic curve and the index "sec" refers to secondary creep stage.

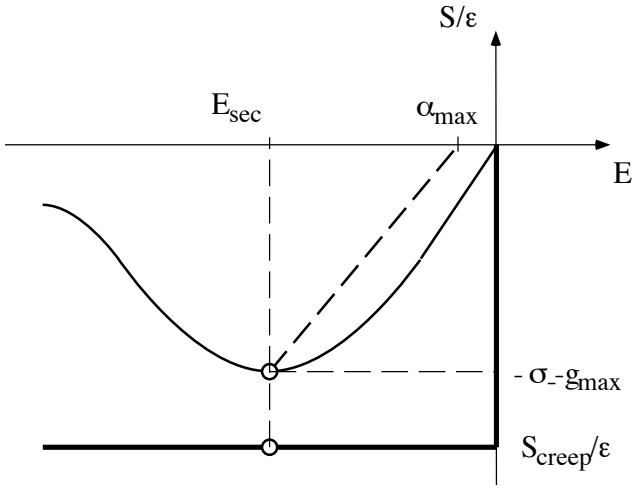

Figure 5.13: Correspondance between the extremum of the quasistatic stress-strain curve and the inflexion point of the secondary creep stage.

We obtained the coefficients:

$$\begin{aligned} \sigma_- + g_{max} &= 0.0082 \\ \zeta &= 0.34 \\ m &= 2 \end{aligned}$$

with $(n = 10, r^2 = .96)$. The corresponding theoretical curve is displayed in Fig. 5.14.

	initial	final	range
min	0.010	0.027	0.011
max	0.022	0.040	0.022
mean	**0.015**	**0.032**	**0.017**
sd	0.0045	0.0047	0.0031

Table 5.5: Statistics of the initial and final creep strains.

Time to failure can then be estimated from the ratio of final strain versus strain rate in the secondary stage:

$$T_f = \frac{E_f}{\dot{E}_{sec}}$$

Using the classical law of Norton, the secondary stage strain rate is approximated by:

$$\dot{E}_{sec} = 5.1 \cdot 10^{30} (\frac{S}{\epsilon})^{17.8}$$

In this case, time to failure becomes:

$$T_f = 6.3 \cdot 10^{-33} (\frac{S}{\epsilon})^{-17.8}$$

On a macroscopic level, failure often involved crushing of one or two ends of the specimen. In two cases, an oblique fracture was observed instead.

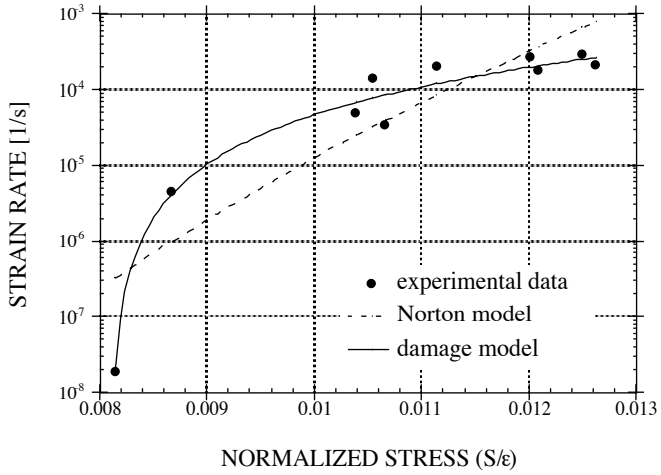

Figure 5.14: Identification of strain rate in the secondary creep stage and comparison with the phenomenological Norton model.

5.2.3 Discussion

The results of these creep tests give evidence of the viscous nature of the coupled plastic and damage process in trabecular bone.

The one-dimensional constitutive law predicts strain rate in the secondary stage and thus time to failure with a good accuracy (Fig. 5.14). Unlike the law of Norton, the model describes the three creep stages (Fig. 5.15) and predicts a normalized stress limit under which creep deformation stops and does not lead to failure.

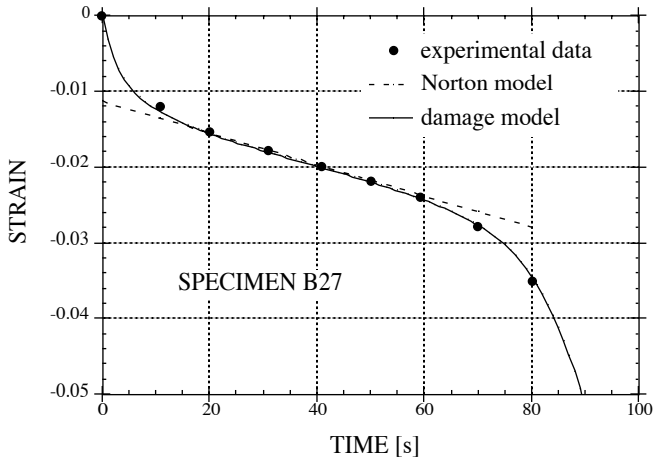

Figure 5.15: Experimental and numerical creep curve for specimen B27 and comparison with the Norton model.

Unfortunately, as emphasized in Chapter 2, artefacts due to inhomogeneous boundary conditions raise doubts about the quantitative evaluation of the creep process and thus about the identified coefficients. Most probably, the creep process exhibited a higher strain rate near the end of the specimens, which helps explain the occurence of failure in these regions.

In addition, the specimens might have degraded in the absence of bacterial inhibitors and the creep failure accelerate at the end of the experiments lasting several days.

Creep experiments were recently reported by Bowman et al. for bovine trabecular bone [13]. Their results for time to failure are substantially lower than ours (Fig. 5.16). We attribute this discrepancy to experimental differences in specimen size or aspect ratio, loading system, moisture conditions and temperature. As kwown from engineering materials, these parameters play a crucial role in creep behaviour.

It should also be noticed that bovine trabecular bone seems to exhibit a higher resistance to creep failure as human cortical bone (Fig. 5.16). In cortical bone, normalized stress for instantaneous failure is approximately .009, while in trabecular bone with the hexahedral geometry, the same definition provides a normalized stress of .015. Assessment of normalized stress rely on the measurement

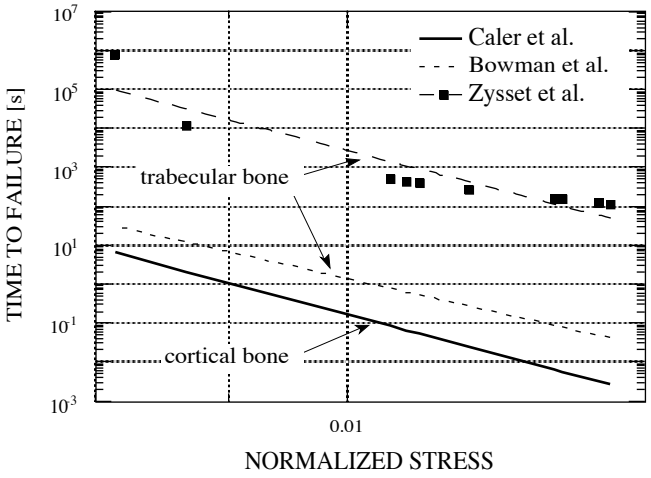

Figure 5.16: Comparison of creep results for cortical and trabecular bone.

of elastic modulus, which has been found, like strain, to be underestimated by approximately a factor 2 due to the inhomogeneous boundary effects. By taking this factor 2 into account, the time to failure would become lower for trabecular than for cortical bone, which turns out to be more compatible with the lower elastic and fatigue properties for trabecular than for cortical tissue reported by Choi et al. [26].

Consequently, estimation of *in vivo* creep for prediction of clinically observed spontaneous bone fractures should be done with extreme care. In addition, unconfined uniaxial experiments have a limited relevance for the multiaxial *in vivo* loading.

The real normalized stress level for trabecular bone remains thus to be measured without boundary artefacts and this will be further discussed in the next section.

Nevertheless, the observed viscosity of the plastic and damage process demonstrates the important ability of trabecular bone to sustain impact loading far beyond the quasistatic yield stress without undergoing substantial plastic strain and damage.

5.3 Three-dimensional quasistatic behaviour

The objective of this test category consists in measuring the material constants ϵ_c, μ_c for elasticity, y_σ for the yield surface as well as the damage and hardening functions $f(\alpha)$ and $g(\alpha)$ of bovine trabecular bone with minimal artefacts due to inhomogeneous boundary conditions.

5.3.1 Materials and methods

Fresh frozen bovine proximal tibias were cut in $50mm$ thick slices parallel to the joint surface with a band saw. From each slice, one or two blocks of trabecular bone ($\sim 50\times20\times20mm$) were extracted with their longitudinal axis perpendicular to the joint surface and stored at $-20°C$. Additional specimens were extracted with their longitudinal axis parallel to the joint surface along the coronal and sagittal directions. The frozen blocks were then milled down with a very sharp tool and low speed for one set into hexahedral specimens with dimensions $40 \times 16 \times 16mm$ and for the other set into cylindrical specimens with dimensions $40 \times 16mm$.

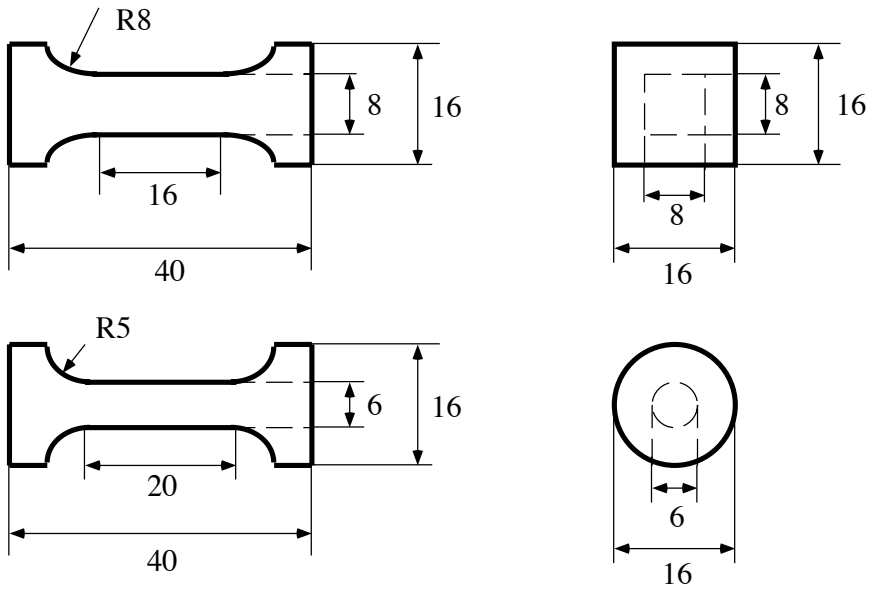

Figure 5.17: Waisted hexahedral and cylindrical trabecular bone specimens.

After visual inspection, the specimens including an epiphyseal line or any other artefact in the central region were eliminated. Cutting tools were specifically designed to mill waisted specimens as shown in Fig. 5.17. During the whole milling procedure, lateral constraints exerted by the holding device were minimized, while longitudinal constraints along the future testing direction of the specimens were avoided. The section of the specimens was measured with a caliper and the final size was obtained with an accuracy close to $0.2mm$. Two specimens were examined under the light microscope to insure that no major damage of the trabeculae occured during the milling process. Following the milling procedure, the specimens were stored again at $-20°C$. Prior to testing, each specimen was thawed overnight in a physiological saline solution at $-4°C$ and for two hours at room temperature ($\sim 20°C$).

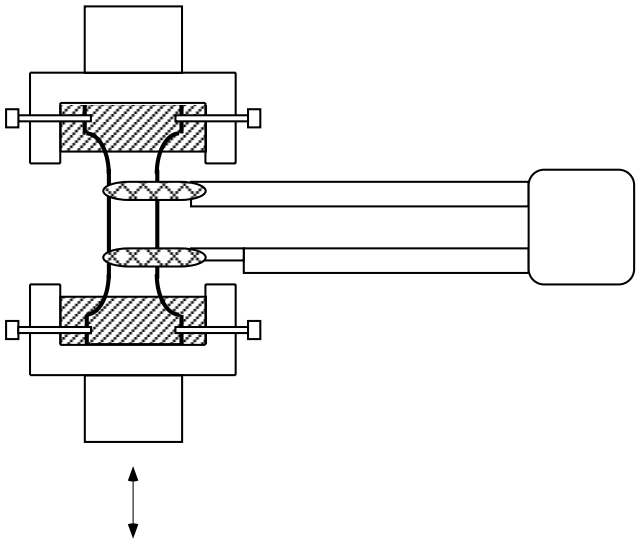

Figure 5.18: Special grips on which the specimen is positioned and cemented. The extensometer was attached with rubberbands.

Uniaxial tests Uniaxial tests were performed with a 1270 Instron servohydraulic material testing machine (Instron, High Wycombe, UK) equipped with a computer driven controller (Interlaken Tech Corp., Eden Prairie, MN, USA). The tests were done under displacement control using the feedback signal of an

Instron extensometer. Force was measured by an Instron load cell used in the $2000N$ range.

The specimens were positioned and cemented *in situ* with Suprastone ultrahard die stone (Kerr, Basel, CH) to custom made grips shown in Fig. 5.18 that were secured previously in the testing machine. A moist gauze prevented drying of the specimens during solidification of the cement ($\sim 15min$). The load appearing progressively from slight shrinking of the cement was compensated manually with appropriate displacement increments. A calibrated $12mm$ gauge length Instron extensometer was then directly attached on the specimens with rubberbands in order to minimize local damage. Finally, a regular stream of physiological saline at room temperature was established at the surface of the specimens with a closed-loop water pump.

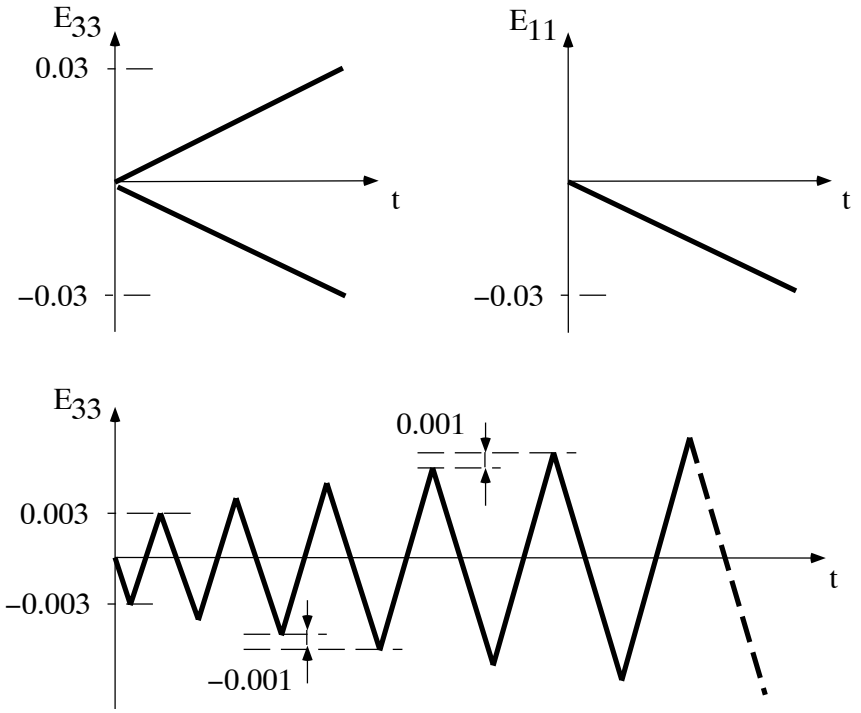

Figure 5.19: Uniaxial strain schedules applied to the hexahedral specimens.

Three different schedules, shown in Fig. 5.19, were used with the same strain rate of $0.001s^{-1}$. The first and the second schedules were single ramps in tension and compression, while the third schedule consisted of a saw like displacement function

with an increasing amplitude. The single ramp compressive tests were done with specimens oriented in the three orthogonal anatomical directions, whereas the other tests were restricted to specimens oriented along the axial direction. The tests were conducted up to macroscopic rupture and a photograph of the failed specimen was taken.

Torsion tests The torsion tests were performed on a Dynamic Analyser II rheometer (Rheometrics, NJ, USA) equipped with built-in angle and torque transducers. All commands and data acquisition were ensured by a computer driven controller. The cylindrical specimens were attached *in situ* at each end on an aluminium fixture plate with acrylic glue (Fig. 5.20).

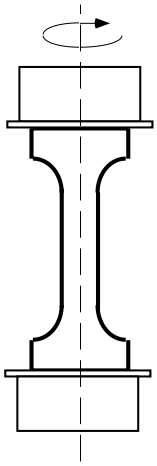

Figure 5.20: Configuration of the specimens in the torsion experiment.

The schedule displayed in Fig. 5.21 was applied with the same strain rate as in uniaxial tests: $0.001s^{-1}$. A moist gauze prevented drying of the specimens during the whole testing procedure performed at room temperature.
For the cylindrical specimens, failure was prevented by stoping the experiments after a substantial decrease in the maximum torque occured in successive cycles.

Data analysis and tissue properties For all mechanical tests, subsequent data analysis was performed with selfmade software which included data smoothing, extraction of strain and stress extremas, linear regression for calculation of

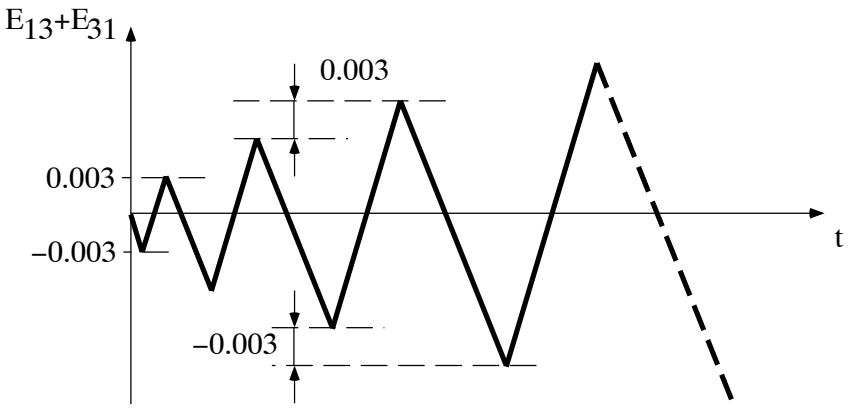

Figure 5.21: Shear strain schedule applied to the cylindrical specimens.

elastic moduli and integration for calculation of the elastic and dissipated energies.

After mechanical testing, the specimens were degreased in soap water for $24h$ and the interstitial marrow removed in an ultrasonic bath. The specimens were then allowed to dry at room temperature. In a further step, the bone mineral content of the specimens was measured by dual energy x-ray absorptiometry (DEXA) with a QDR-1000 scanner (Hologic Inc., Waltham, MA, USA). Each specimen was aligned on top of a plexiglas block with its longitudinal axis along the direction of the X-ray beam. A single scan was performed with the parameters summarized in Table 5.6 and the measured bone mineral content (BMD) recorded.

voltage $[KV]$	intensity $[mA]$	time $[s]$	frequency $[Hz]$	field $[mm]$	spacing $[mm]$	resolution $[mm]$
140	2.0	426	50	16×16	0.1	0.127

Table 5.6: Dual energy X-ray absorptiometry parameters used with the HOLOGIC QDR-1000 scanner.

A calibration curve was drawn for the DEXA scanner by the means of 18 reference specimens, for which ash weight was measured with an analytical balance after $24h$ ashing in a muffle furnace at $600°C$. Apparent ash density was calculated by assuming a tissue density of $1.93g/cm^3$.

5.3.2 Results

DEXA Bone mineral density (BMD) was found to be an excellent predictor of apparent ash density:

$$\rho_{aa} = 0.90 \cdot BMD - 0.038 \qquad (n = 18, r^2 = .99, p < 0.0001)$$

where ρ_{aa} and BMD are expressed in $[g/cm^3]$.

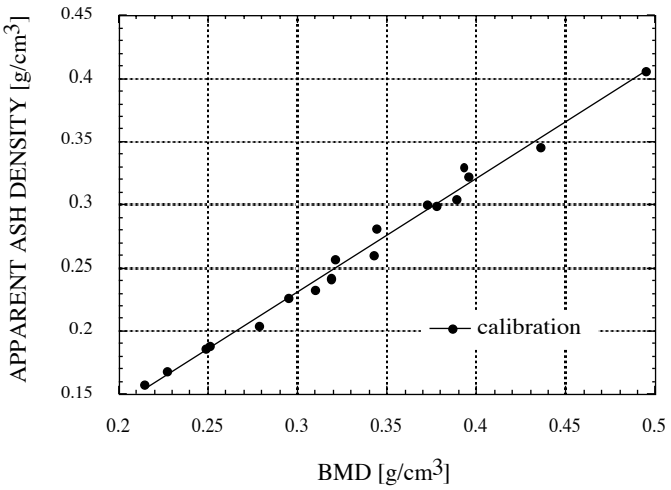

Figure 5.22: Calibration curve for bone mineral density.

Consequently, DEXA is a pragmatic and efficient tool for *in vitro* estimation of apparent ash density of trabecular bone specimens with known geometry. However, a separate calibration accounting for the scanning parameters and the specimen geometry is necessary to obtain the exact values.

Single ramp tests Due to minor differences, we assume material symmetry of the specimens to be transversely isotropic and merge the results from the coronal and the sagittal directions that become the transverse direction. The single ramp tests provided the stress-strain curves represented in Fig. 5.23 and were characterized by a linear part followed by a maxima in normalized stress at a specific strain.

In Table 5.7, elementary statistics reveal that maximal normalized stress is not significantly different in tension and compression ($p > 0.8$), but distinct along

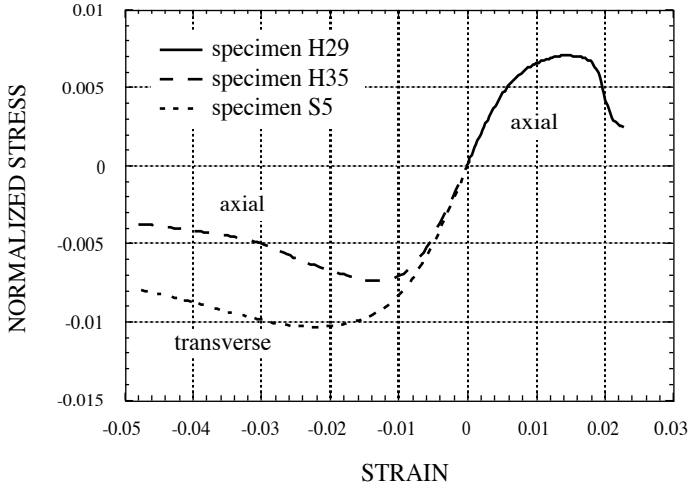

Figure 5.23: Single ramp tensile and compressive tests in the axial and transverse directions.

		tension	compression	
		axial	axial	transverse
	min	0.0068	0.0069	0.0092
max	max	0.0088	0.0082	0.0120
stress	**mean**	**0.0076**	**0.0077**	**0.0108**
	sd	0.0011	0.0005	0.0014

Table 5.7: Statistics of maximal normalized stress for single ramp tests.

		tension	compression	
		axial	axial	transverse
	min	0.0141	0.0105	0.0153
max	max	0.0156	0.0129	0.0333
strain	**mean**	**0.0150**	**0.0116**	**0.0241**
	sd	0.0007	0.0011	0.0063

Table 5.8: Statistics of strain associated with the maximal normalized stress for single ramp tests.

the two retained anatomical axes ($p < 0.002$). The associated strains listed in Table 5.8 were all significantly different ($p < 0.005$).

Cyclic tests Nine waisted hexahedral and nine cylindrical specimens were successfully tested with their respective cyclic schedules. The resulting stress-strain curves were similar but are presented separately in Fig. 5.24 and Fig. 5.25.

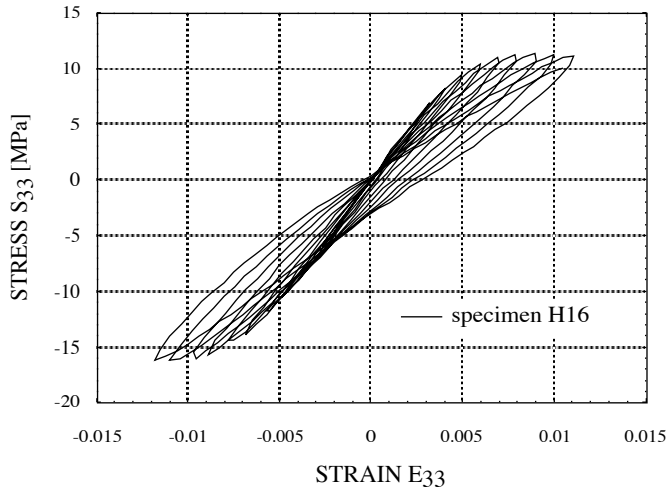

Figure 5.24: Stress-strain curve obtained by a cyclic uniaxial test.

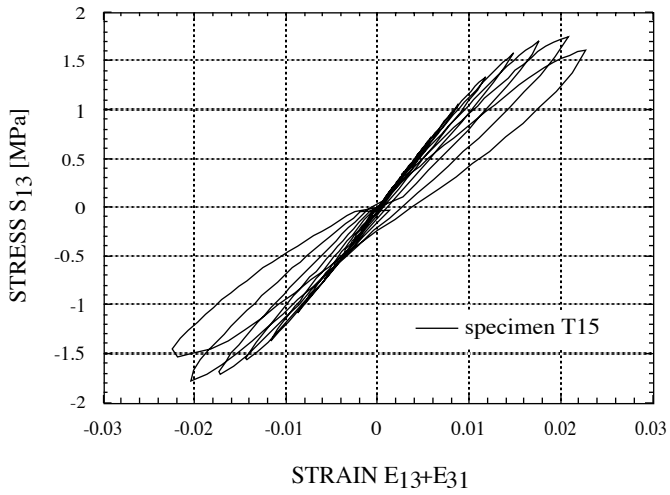

Figure 5.25: Stress-strain curve obtained by a cyclic torsion test.

In both uniaxial and torsion experiments, the first cycles appeared fairly elas-

tic, while the further cycles demonstrated progressively residual deformations as well as clear reductions in Young's modulus.

In the first cycle, variability in elastic constants reached 42%, while the difference between tensile and compressive Young's moduli averaged approximately 1% (Table 5.9).

	tension	compression	shear
min	986.3	1019.8	126.3
max	2875.7	2928.8	346.8
mean	**1704.7**	**1724.1**	**229.1**
sd	710.2	691.5	70.2

Table 5.9: Statistics of the elastic moduli in $[MPa]$ for tension, compression and shear obtained during the first loading cycle.

The experimental damage was defined by the ratios of the elastic moduli with respect to the elastic modulus of the first cycle. A clear relationship was obtained between damage and plastic deformation and thus the internal variable α (Fig. 5.26). The experimental hardening function was defined as the maximum normalized stress of each cycle and appeared also to be related with the damage variable α (Fig. 5.27).

	compression		tension		torsion	
	first	last	first	last	first	last
min	4.4	18.1	8.8	16.6	4.8	16.7
max	17.6	43.1	18.6	58.2	6.8	40.8
mean	**10.1**	**30.5**	**14.0**	**40.8**	**5.7**	**28.2**
sd	4.7	9.0	3.3	12.6	0.8	0.8

Table 5.10: Statistics of the relative dissipated energy (%) within the first and the last cycle preceeding failure.

The relative dissipated energy (with respect to the external work) within a cycle increased with α and reached up to 50% in the last cycle preceeding tensile failure (Table 5.10).

All hexahedral specimens failed in tension between the third and the tenth loading period. Fracture occured in three cases between the knives of the extensometer, in three cases close to the knives and in three cases away from the knives. However, a very similar stress-strain curve was obtained in all cases, except for the number of cycles before failure.

Identification With the choice $k = l = 1$ in Eq. 3.20 and 3.93-3.94, the relationships of the elastic and shear moduli with respect to structural density were the following:

$$\begin{aligned} \epsilon_3 &= 24'694 \cdot \rho_s^2[MPa] \qquad (n = 18, r^2 = .76) \\ \mu_{13} &= 5'904 \cdot \rho_s^2[MPa] \qquad (n = 9, r^2 = .83) \end{aligned}$$

The respective average maximum normalized stress along the axial and transverse directions provided the following eigenvalues of the structural tensor $\boldsymbol{M}$:

$$m_1 = m_2 = 0.294 \qquad m_3 = 0.412$$

Accordingly, the elastic constants become:

$$\begin{aligned} \epsilon_c &= 145'478[MPa] \\ \mu_c &= 48'742[MPa] \end{aligned}$$

To identify the damage function $f(\alpha)$, nonlinear regression of the data pooled from uniaxial and torsional cyclic experiments was done with an exponential function:

$$f(\alpha) = e^{-\frac{\alpha}{\alpha_f}} \tag{5.1}$$

We obtained:

$$\alpha_f = 3.13[\sqrt{MPa}] \qquad (n = 257, r^2 = .85)$$

The pooled data and the calculated nonlinear regression are shown in Fig. 5.26.

Remark 5.1 *This regression for $f(\alpha)$ was chosen to restrict identification to a single coefficient.*

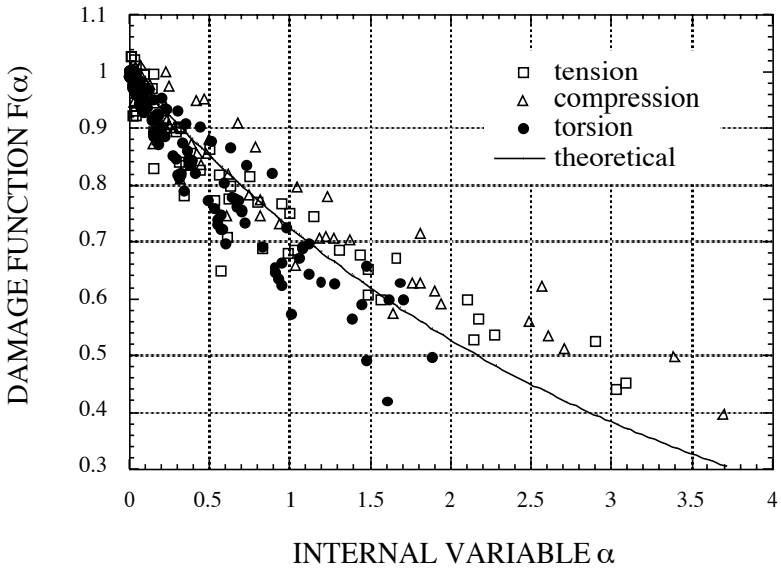

Figure 5.26: Experimental and theoretical damage function $f(\alpha)$.

The constant y_σ associated with the yield point is difficult to identify properly from the smooth hardening curves and we chose to define this limit as a reduction of 5% in elastic modulus.
The resulting values are given in Table 5.11.

	uniaxial		torsion
	tension	compression	shear
y_σ	0.60	0.72	0.69

Table 5.11: Values obtained for the yield point in $[\sqrt{MPa}]$ with the damage experiments.

The hardening curves obtained in tension, compression and shear were also somewhat different. Therefore, the normalized maximal stress amplitudes were first fitted separately with an exponential function:

$$g(\alpha) = g_{max}(1 - e^{-\frac{\alpha}{\alpha_g}})$$

The obtained coefficients are given in Table 5.12.

Remark 5.2 *This particular function $g(\alpha)$ was chosen in order to avoid softening of the constitutive law and the related numerical difficulties.*

	uniaxial		torsion
	tension	compression	shear
g_{max}	0.23	0.34	0.42
α_g	0.52	0.83	0.35
n	46	44	82
r^2	0.43	0.74	0.74

Table 5.12: Coefficients obtained for the identification of $g(\alpha)$ in $[\sqrt{MPa}]$ with the corresponding statistical parameters.

Finally, the pooled compressive, tensile and torsion data provides the following constants:

$$\begin{aligned} y_\sigma &= 0.68[\sqrt{MPa}] \\ g_{max} &= 0.33[\sqrt{MPa}] \\ \alpha_g &= 0.53[\sqrt{MPa}] \end{aligned}$$

with $n = 257, r^2 = .46$.

The pooled hardening data and the calculated regression are shown in Fig. 5.27.

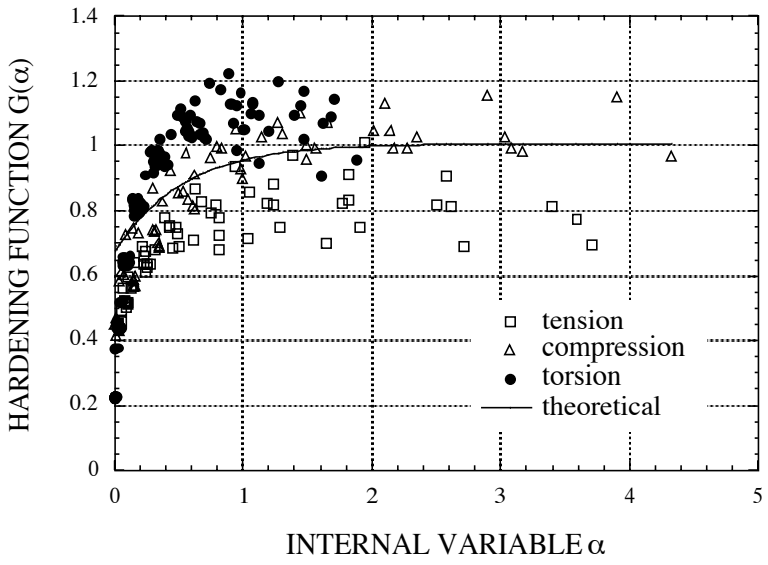

Figure 5.27: Experimental and theoretical hardening function $g(\alpha)$.

The final value for y_σ defines a yield criterion that is displayed in the normalized stress space together with the experimental data in Fig. 5.28.

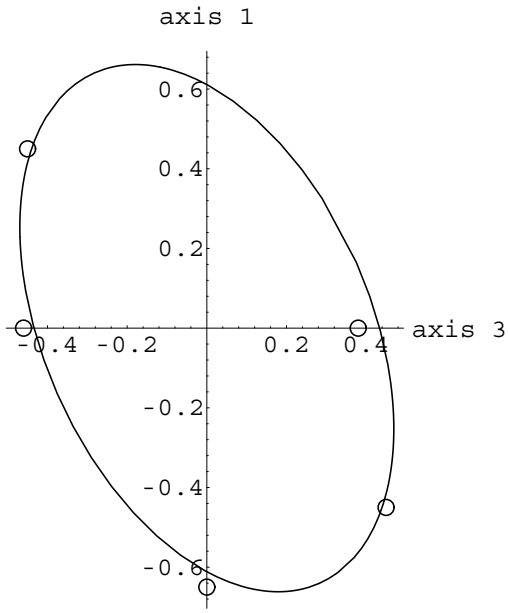

Figure 5.28: Experimental data and identified yield criterion in the normalized stress space (in %).

Remark 5.3 *The proposed theoretical yield criterion corresponds to the square root of strain energy density normalized with respect to structural density.*

5.3.3 Discussion

The results of these quasistatic experiments demonstrate and quantify for the first time the coupled mechanisms of plasticity and damage in trabecular bone. In addition, a coherent identification of the three-dimensional elastic constants and yield criterion has been performed for bovine trabecular bone without artefacts associated with inhomogeneous boundary conditions. Finally, dual energy X-ray absorptiometry has been found to be an excellent tool for *in vitro* assessment of apparent ash density. We intend to discuss now a number of more specific points.

Elasticity The negligible difference found between the elastic moduli in tension and in compression for tests performed on the same specimen suggests that symmetric elastic properties are most probably the rule for trabecular bone. The physical background of this result may lay in the symmetric bending and axial deformation mode of the trabecular structure cited in Table 2.7. The asymmetric elastic buckling mode may in fact not contribute to linear elasticity, but to the nonlinear transition zone preceeding yielding.

Plasticity and damage Single ramp tests confirm the qualitative description of the quasistatic stress-strain curve proposed in Chapter 2, but shows that trabecular bone exhibits a similar strength in tension and in compression. This finding cannot be checked on the cyclic experiments, which show that the maximum normalized stress was 20% lower in tension than in compression. Unfortunately, we started all uniaxial cyclic experiments on the compressive side and we can not evaluate the effect of kinematic hardening (Bauschinger effect) on this discrepancy.
The postyield behaviour of the specimens in uniaxial and torsion tests demonstrates that the irreversible processes of plastic strain and elastic damage are intrinsically coupled, which supports the basic hypothesis of our theoretical development. They also show that the hardening functions are somewhat different in uniaxial and torsion tests. This difference may be due to the non-homogeneous strain field of the torsion experiment or the reduced section of the cylindrical specimens when compared to the hexahedral ones. The yield stresses are found to be compatible with our three-dimensional continuum model as well as the criterion proposed by Gibson for biaxial loading of foams [52], but no statement can be drawn for the triaxial loading case. Note finally that the assumed homothetic evolution of the yield criterion is somewhat naive regarding the induced anisotropy of the damage phenomenon.

In agreement with our theoretical model, the maximum normalized stress and associated strain are higher along the direction of lower mean intercept lengths. This fact is best visualized on the yield criterion of Fig. 5.28 and is in doubtless contradiction with the isotropic stress criterion suggested by Stone at al. [122]

and with the hypothesis of Turner [131], who proposed an isotropic strain criterion. Discrimination of yield strain may be perturbed by insufficient alignment of the mechanical testing direction with the trabecular structure as well as the interference of boundary artefacts. Since yield strain is strongly related to the geometric properties of a material, we are not surprised to obtain significantly different yield strains along directions with different intertrabecular spacing or mean intercept lengths.

At the microscopic level, plasticity and damage may be associated with slipping of the bone lamellae along the cement lines [87] and progressive failure of the weakest trabeculae. From a rheological point of view, parallel damage of trabeculae will reduce the macroscopic elastic modulus, while series damage of trabeculae will induce a permanent strain. Using the parallel model, Krajcinovic modelled softening of the tensile stress-strain curve and progressive failure of cortical bone associated with a statistical distribution of strength in the bone lamellae [82]. By means of a finite element model, Guo demonstrated a similar statistical origin of material softening in the case of fatigue loading of trabecular bone [58]. The latter analysis helps also understanding of our quasistatic observations.

Softening of the stress-strain curve and macroscopic failure of the material correspond to localization of the damage process, which raises a number of difficult theoretical and numerical questions in continuum mechanics since even the basic notion of continuity may be lost. Important efforts are currently spent in the theoretical and numerical mechanics community to overcome a number of these difficulties, for instance by considering viscoplastic regularization or nonlocal dissipation [118]. Despite these efforts, strain localization draws the limits of the continuum approach chosen in the present work.

Variation of the fracture zone in uniaxial tests is due to trabecular bone inhomogeneity and indicates that waisting of the specimens was not sufficient to force the failure process in the middle. Fortunately, accumulation of damage and plastic strain was influenced neither by the failure level nor by the failure period. In fact, we suspect that this property holds in the hardening part of the stress-strain curve and breaks down in the softening part, when localization of damage occurs.

Artefacts The developed material testing technique avoids artefacts due to inhomogeneous boundary conditions in strain. A comparison with unwaisted hexahedral bovine specimens tested along the same anatomical direction with a similar single ramp schedule and identical strain rate suggests a 100% underestimation of the elastic modulus by the method including the boundary artefacts. Use of waisted specimens is mandatory for accurate identification of material constants. Ultrasonic measurements may represent a good alternative to these problems, but they are currently restricted to the identification of elasticity. In addition, verifications should also be done on this method to evaluate possible boundary effects.

As mentioned in Chapter 2, our testing method remains subjected to artefacts due to inhomogeneous distribution of stress in the section of the specimen. Fortunately, identification of the material constants in terms of normalized stress (i.e. strain) is not influenced by a correction of the applied stress, because the elastic modulus would undergo the same correction. However, the material constants given in physical units such as ϵ_c and μ_c may well be underestimated. Assuming a reduction of a half trabecular spacing in the linear dimensions of the weight-bearing section of the specimens, the correction would reach up to 25%.

Another potential source of inaccuracy is that local damage of the trabeculae might have occured under the knives of the extensometer. However, the lateral force exerted by the weight of the extensometer was close to $1N$, which is less than .3% of the maximal axial load applied on the weakest specimen.

Identification The normalized eigenvalues of the structural tensor $\boldsymbol{M}$ deduced in our tests from mechanical data correspond approximately to the anisotropy of our own stereological measurements in the human tibia and the measurements by Turner et al. in the bovine femur [129]. This finding suggests that human and bovine trabecular bone exhibit a similar anisotropy in regions subjected to high stress gradients.

The elastic constants provided in this work rely directly on the assumed bone tissue density and may obviously vary with the degree of mineralization of the tissue. However, in mature bovine bone the variability of bone tissue density

remains below a few percent [56].
The dimensionless elastic constant missing in the present approach can be estimated from the data of Klever [79]:

$$\nu_c = 0.32$$

Due to our different testing method, the elastic constants are substantially higher than those obtained in other studies. In particular, a statistical analysis including several previous studies suggests the following relationship for axial elastic modulus [112]:

$$\epsilon_3 = 70 + 2875 \cdot \rho_s^2 [MPa]$$

where we averaged the data from tensile and compressive tests. This average is almost one order of magnitude lower than ours.

The most striking fact is that extrapolation of our data to a structural density of 0.9, with the apparently standard anisotropy found in the proximal tibia, provides a reasonable approximation of all elastic constants of bovine cortical bone (Table 5.13).

	cortical bone	theoretical
	$[GPa]$	$[GPa]$
ϵ_1	10.7	10.2
ϵ_2	11.4	10.2
ϵ_3	20.7	20.0
μ_{13}	5.3	4.7
μ_{23}	5.6	4.7
μ_{12}	3.6	3.4
ν_{13}	0.18	0.23
ν_{23}	0.19	0.23
ν_{12}	0.46	0.45

Table 5.13: Elastic constants for bovine cortical bone obtained from averaged experimental data [32] and from prediction of our theoretical model.

Remark 5.4 *The value of* 0.9 *for structural density of cortical bone is an average choice made to account for the residual porosity associated with the vascular Havers and Vollkman canals as well as the lacunae of the cortical tissue [63].*

Therefore, our data rehabilitate the early hypothesis of Carter and Hayes [21] according to which cortical bone can be mechanically considered as dense trabecular bone. In particular, the correspondance of the respective anisotropies is added to the unified dependency of the elastic constants with respect to structural density.

Remark 5.5 *It should be emphasized that the material constants and functions provided in this section were identified with bovine trabecular bone. We expect human bone to exhibit a very similar behaviour, but the value of the respective constants and functions may be somewhat different and remain to be precisely identified.*

Numerical model In spite of the absence of viscosity, the three-dimensional numerical model fed with the identified material constants and functions provides a reasonable approximation of the nonlinear quasistatic response of trabecular bone subjected to the uniaxial cyclic schedule (Fig. 5.29).

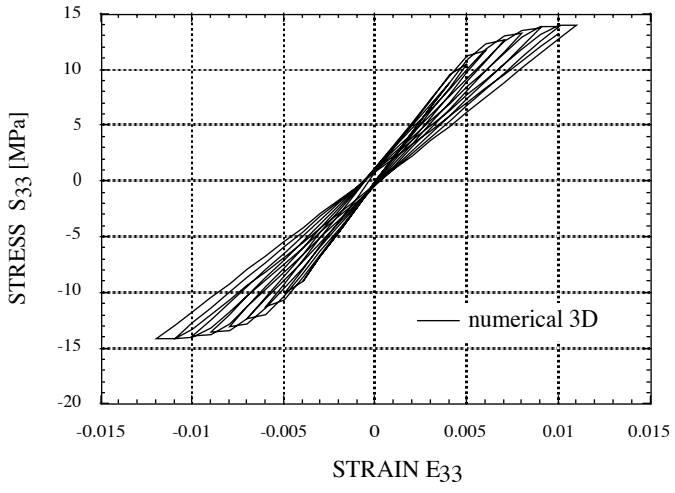

Figure 5.29: Numerical curve for the cyclic schedule applied to specimen H16 with the identified 3D material constants.

Chapter 6

Biomechanical application

In this chapter, the constitutive law developed for trabecular bone is used for the biomechanical evaluation of a cementless custom-made femoral total hip component using a 3D finite element model. Different measures of stress are calculated in the bone and micromotions are assessed at the bone-implant interface for the loading condition of stair climbing. The growth of damage is visualized and analysed in terms of bone stress for progressive loading.

6.1 Description of the model

The model is based on the clinical case of a 60 years old woman with a weight of $65kg$, who was subjected to total joint arthroplasty on the left hip using a cementless custom prosthesis (Symbios Inc., Yverdon, Switzerland).

6.1.1 Mesh

An automatic mesh generator of the proximal femur and the implanted prosthesis has been recently developed by Rubin et al. [114]. The bone geometry and structural density are obtained from quantitative computed tomography (QCT). Structural density is calculated using the equation:

$$\rho_s = 1.4315 \cdot 10^{-3} \cdot QCT - 0.08589$$

where QCT is expressed in CT units. A threshold procedure at $\rho_s = 0.7$ provided the periosteal (outer) and endosteal (inner) contours of cortical bone. The geometry of the prosthesis was obtained from the designer and inserted in a neutral varus-valgus position according to the usual pre-operative planning. As shown in Fig. 6.1, the mesh of the bone-implant system involves three sets of solid elements:

- cortical bone
- trabecular bone
- prosthesis

The number of solid elements of the respective sets are given in Table 6.1.

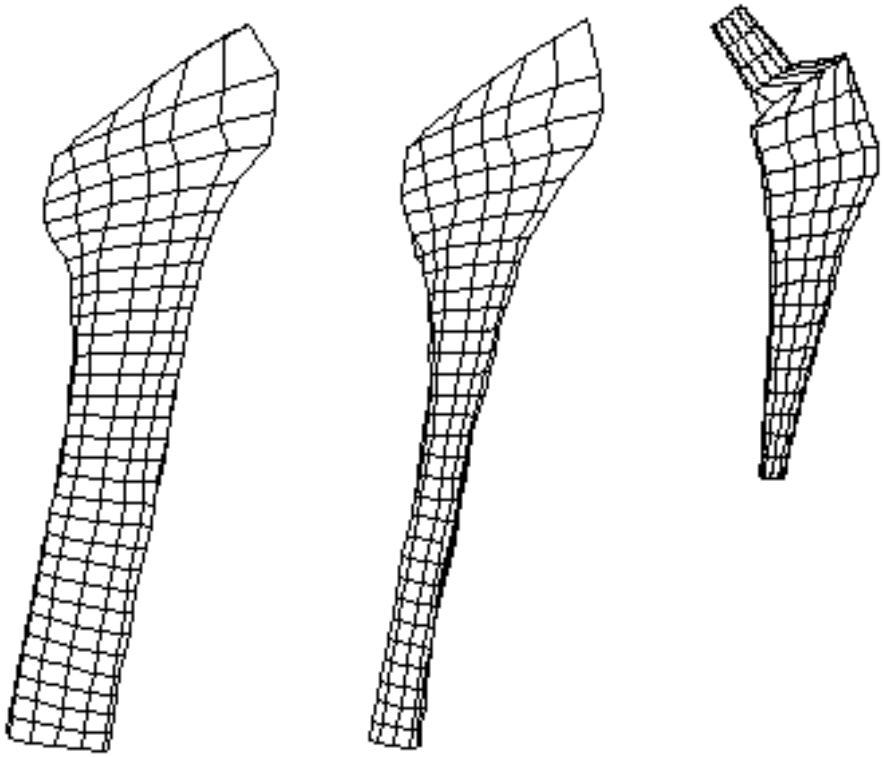

Figure 6.1: The respective meshs of the three sets involved in the bone-implant system.

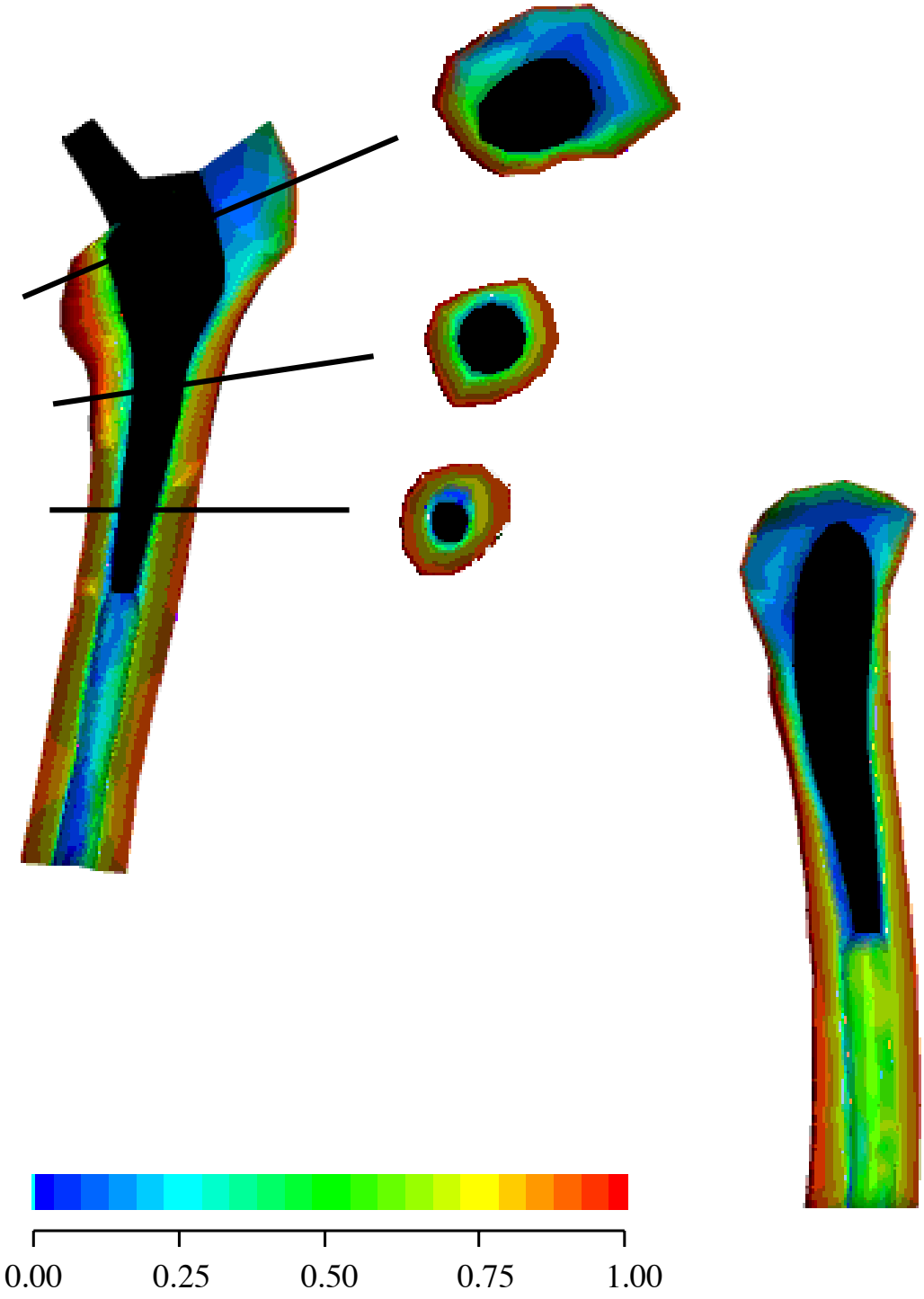

Figure 6.2: Structural density map of the bone material.

Remark 6.1 *In Chapter 5, the elastic properties of bovine cortical bone were found to correspond to an extrapolation of the properties of trabecular bone. In this application, we assume that the same finding holds for human bone.*

The assembled bone-implant system and the map of structural density for bone are displayed in Fig. 6.2.

	cortical	trabecular	prosthesis	total
elements	360	720	441	1521

Table 6.1: Number of solid elements of the respective sets of the mesh.

As shown in Fig. 6.3, the solid elements of the mesh are eight-node hexahedral linear elements.

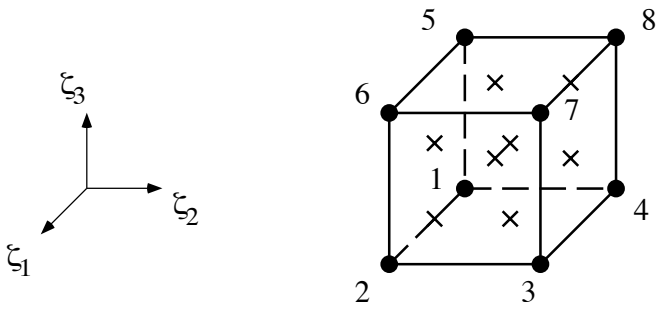

Figure 6.3: Eight-node hexahedral solid element with Gauss integration points.

In general, the geometric data of the mesh of an anisotropic material need to be completed by the privileged material orientations associated with the structural tensors. However, we choose a strategy whereby the mesh defines the privileged material orientations. The three orthogonal material directions are generated by the natural basis of the isoparametric element. In the real space, the associated directions correspond approximately to the orientations of the element if care is taken to avoid important distorsions. Due to the lack of detailed data about the curvilinear orthotropy of trabecular bone at the proximal femur, material symmetry of the model is assumed to be transversely isotropic and characterized by a single direction of anisotropy $\boldsymbol{m}_3$ following the medial curvature of the cortical shell (Fig. 6.4).

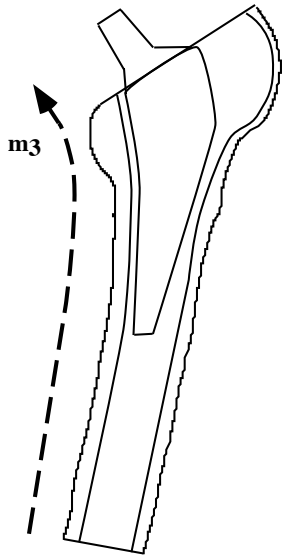

Figure 6.4: Direction of anisotropy chosen for the generation of the mesh.

In addition, the extent of anisotropy is supposed to be homogeneous:

$$m_1 = m_2 = 0.31 \qquad m_3 = 0.38$$

The mesh of the bone-implant system involves also three sets of 72 contact elements:

- proximal bone-implant interface
- middle bone-implant interface
- distal bone-implant interface

As shown in Fig. 6.5, the contact elements are seven-node striker-target elements, whereby node 3 is the Lagrange multiplier node. These node-on node small slip contact elements enable to model unilateral contact (Signorini conditions) in the normal direction to the interface and isotropic Coulomb's law of friction in the tangential plane of the interface.

6.1.2 Material properties

Cortical bone Cortical bone is assumed to be transverse isotropic and linearly elastic, which seems reasonable since yielding of the cortical shell would require

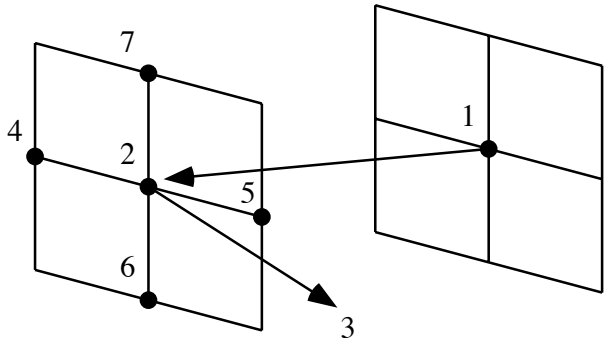

Figure 6.5: Seven-node contact element.

very high stresses that are incompatible with daily activities. The material coefficients chosen from the literature [32] are given in Table 6.2.

ϵ_1 $[MPa]$	ϵ_3 $[MPa]$	μ_{12} $[MPa]$	ν_{13}	ν_{12}
11′500	17′000	3′300	0.46	0.58

Table 6.2: Material coefficients of the cortical bone set.

Trabecular bone Trabecular bone is described by the three-dimensional constitutive law developed in Chapter 3. In Eq. 3.93 to 3.95 governing linear elasticity, the exponents k and l are assumed to be equal to 1. The dimensionless constants derived from experimental identification of bovine bone were assumed to be the best approximations of the properties of human trabecular bone. The constants in physical units ϵ_c and μ_c were adapted in order to provide the properties of human femoral cortical bone when structural density reached 0.9. The resulting coefficients are given in Table 6.3.

ϵ_c $[MPa]$	μ_c $[MPa]$	ν_c	y_σ $[\sqrt{MPa}]$	g_{max} $[\sqrt{MPa}]$	α_g $[\sqrt{MPa}]$	α_f $[\sqrt{MPa}]$
145′340	42′390	0.32	0.68	0.33	0.53	3.13

Table 6.3: Material coefficients of the trabecular bone set.

Prosthesis Total hip implants are made of titanium alloy, that we assume to be isotropic and linearly elastic.

ϵ $[MPa]$	ν
110′000	0.33

Table 6.4: Material coefficients of the prosthesis set.

Contact The numerical formulation of the contact law used in this model is essentially due to Curnier [36, 1]. For the three sets of the bone-implant interface, we assume the following coefficient of friction:

$$\mu_f = 0.6$$

This value is based on estimations from previous studies [117, 134].

6.1.3 Loading conditions

The loading conditions aim at simulating the forces and moments applied *in vivo* on the prosthetic head during daily activities such as walking or stair climbing. Such data has been provided in the original work of Davy et al. [42], who used a telemetrized hip prosthesis equipped with strain gages for measurement of transmitted forces and moments after total hip arthroplasty.

q_1 $[N]$	q_2 $[N]$	q_3 $[N]$	$\bar{M}_1$ $[Nmm]$	$\bar{M}_2$ $[Nmm]$	$\bar{M}_3$ $[Nmm]$
-348	-520	-1532	-1081	2355	-1048

Table 6.5: Loading conditions applied on the prosthetic neck during stair climbing.

In this work we consider exclusively the stance phase of the stair climbing loading case, that involves the highest forces among daily activities. Since our model does not include the prosthetic head, a set of forces and torques was applied at the top of the prosthetic neck after suitable transformation (Fig. 6.6). These forces and moments are expressed in the coordinates of the model in Table 6.5.

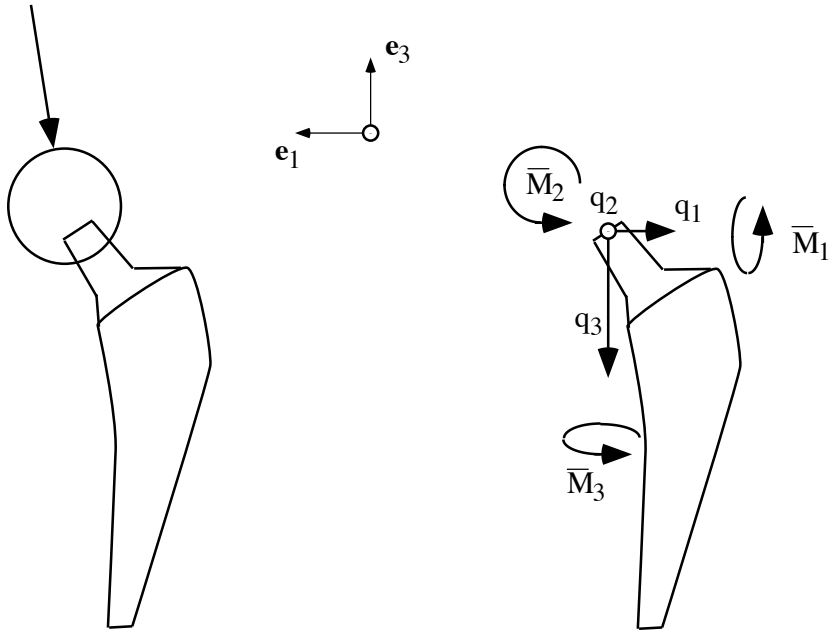

Figure 6.6: Loading conditions of the prosthetic neck adapted from the physiologic loading case.

The loading schedule consists in a simultaneous quasistatic ramp in force and torque as shown in Fig. 6.7.

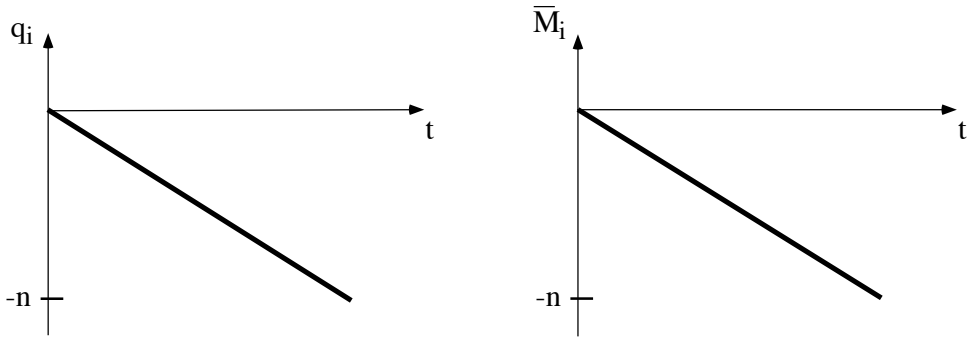

Figure 6.7: Single ramp quasistatic loading of the prosthetic neck. The force and torque are represented in terms of physiological loading (n=1).

6.2 Results

The results of the simulations are expressed in the following terms:

Prosthesis, cortical and trabecular bone elements

- Hydrostatic stress, $\frac{1}{3}Tr(\boldsymbol{S})$.
- Von Mises stress, $Tr(\boldsymbol{S}^2) - \frac{1}{3}Tr^2(\boldsymbol{S})$.

Cortical and trabecular bone elements

- Normal anisotropic stress invariant, $Tr(\boldsymbol{M}_3\boldsymbol{S})$. This stress invariant represents the normal stress along the privileged direction $\boldsymbol{m}_3$.
- Tangential anisotropic stress invariant, $\sqrt{Tr(\boldsymbol{M}_3\boldsymbol{S}^2) - Tr^2(\boldsymbol{M}_3\boldsymbol{S})}$. This stress invariant represents the shear stress acting in the plane normal to the privileged direction $\boldsymbol{m}_3$.

Trabecular bone elements

- Square root of the strain energy density (SED) normalized with respect to structural density, $\sqrt{\boldsymbol{S} : \boldsymbol{E}^e}/\rho_s$. This scalar is the first term of the yield criterion y.
- Damage function $f(\alpha)$.

Bone-implant contact elements

- Normal stress.
- Shear stress.
- Normal micromotions.
- Shear micromotions.

In the physiological loading case, the simulation required a single time step and 8 iterations. The runtime was approximately 30 minutes on a HP-9000/730 computer. At the bone-implant interface, maximum distractive micromotion reached $30\mu m$, while maximum slip micromotion reached $46\mu m$. Extrema of hydrostatic pressure in the bone-implant system are given in Table 6.6 and distribution of Von Mises stress is shown in Fig. 6.8.

	trabecular bone	cortical bone	prosthesis
min	-8.3	-32.0	-27.1
max	8.5	32.6	15.9

Table 6.6: Extrema of hydrostatic pressure in the bone-implant system ($[MPa]$).

Distribution of normal anisotropic stress invariant in the bone is represented in Fig. 6.9.

Additional simulations involving 4 and 7 times the physiological load were performed in order to demonstrate the growth of damage (Fig. 6.10 and 6.11). The simulations required up to 10 time steps including 6 to 8 iterations each. Runtime raised up to several hours.

Finally, the mechanical consequences of damage on the bone-implant system are illustrated by a comparison of the last loading case with the corresponding elastic case where trabecular bone is not allowed to yield. As expected, the simulation of the elastic case required a single time step.

	normal invariant $[MPa]$	tangential invariant $[MPa]$	strain energy density $[\sqrt{MPa}]$
$elastic$	147	37.6	7.16
$damaged$	66	20.5	1.01

Table 6.7: Comparison of stress extrema in trabecular bone for the elastic and the damaged case.

Maxima of the different stress measures in trabecular bone are given in Table 6.7. Distributions of shear stress at the interface are compared in Fig. 6.12.

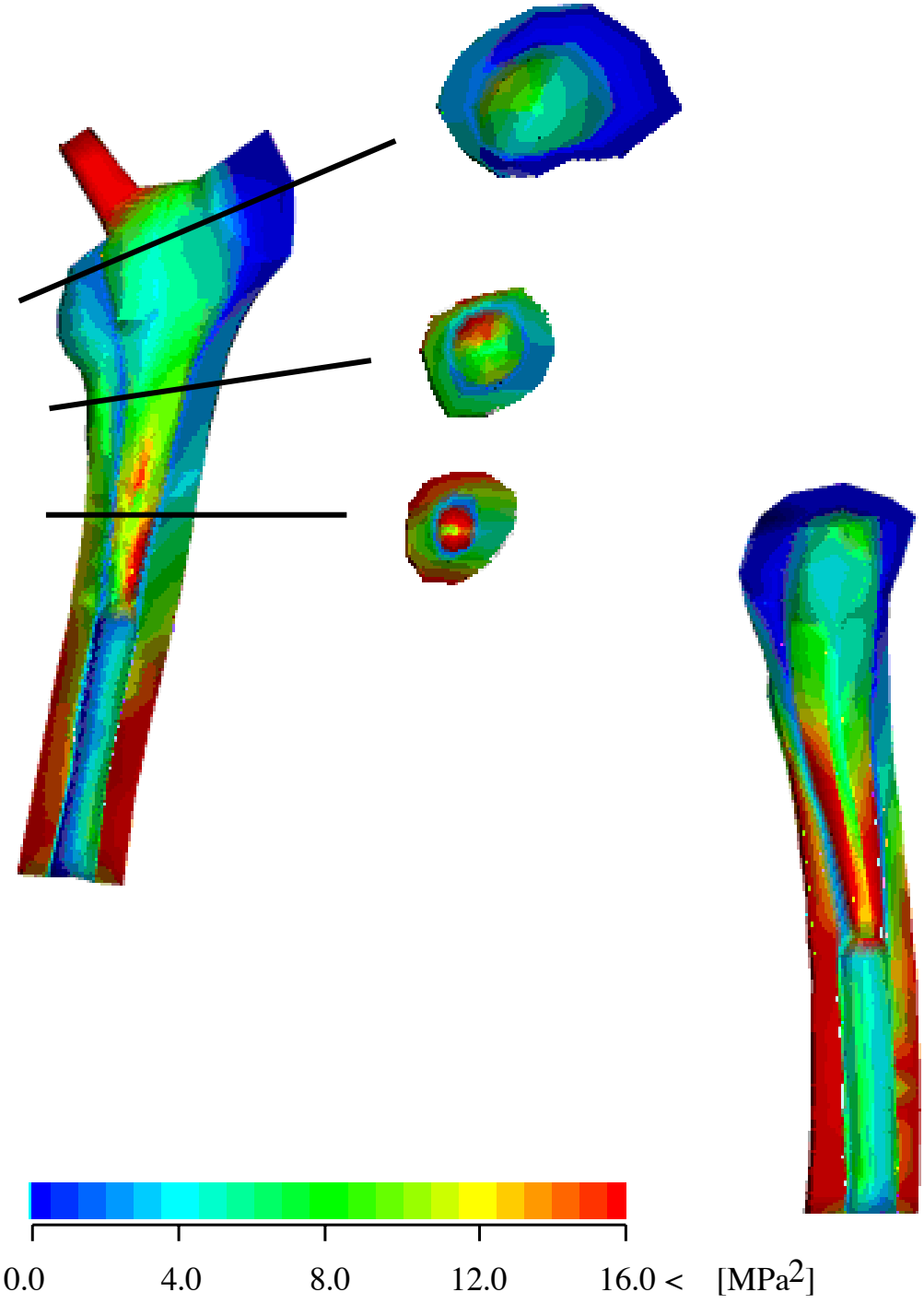

Figure 6.8: Von Mises stress in the bone-implant system.

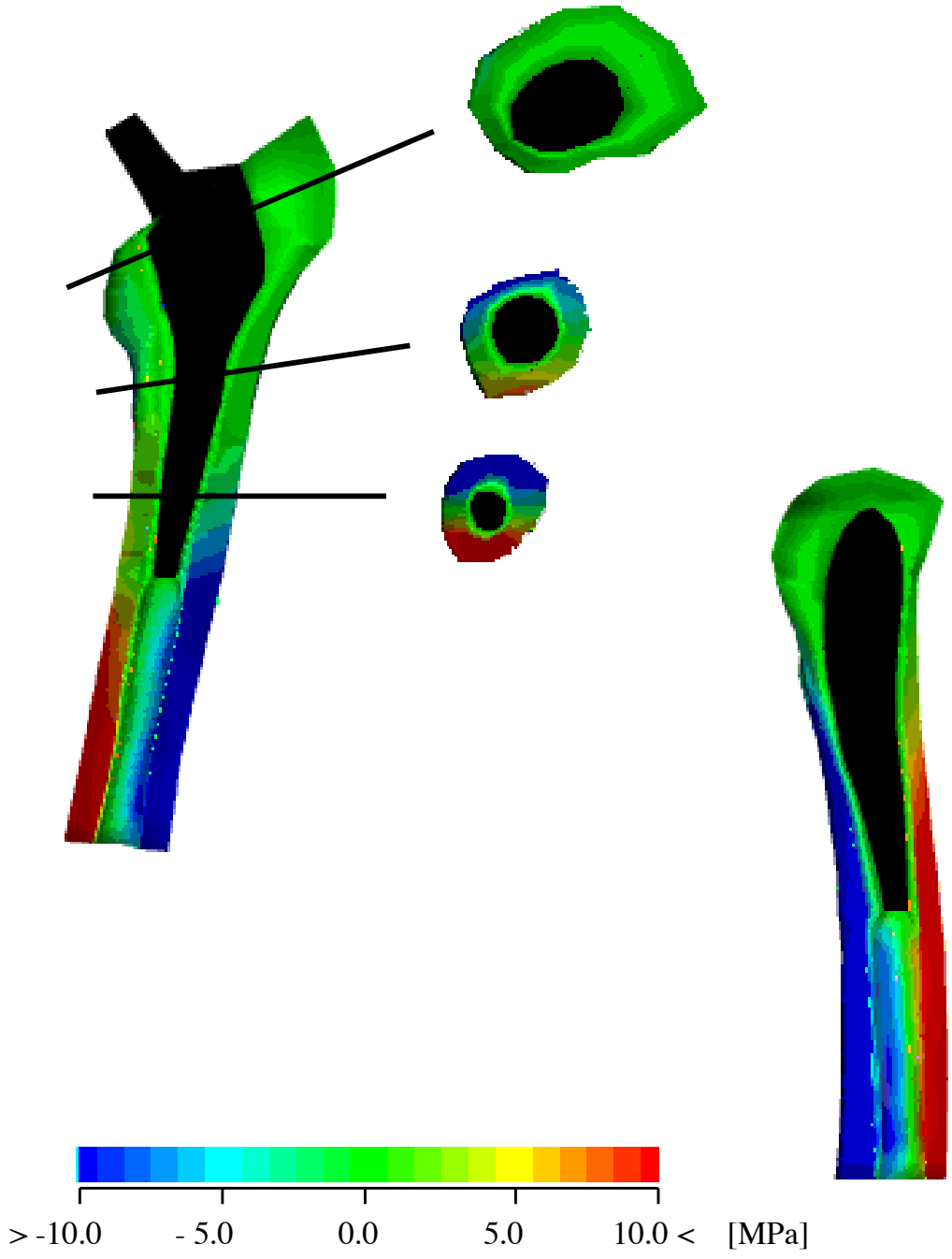

Figure 6.9: Normal anisotropic stress invariant in cortical and trabecular bone.

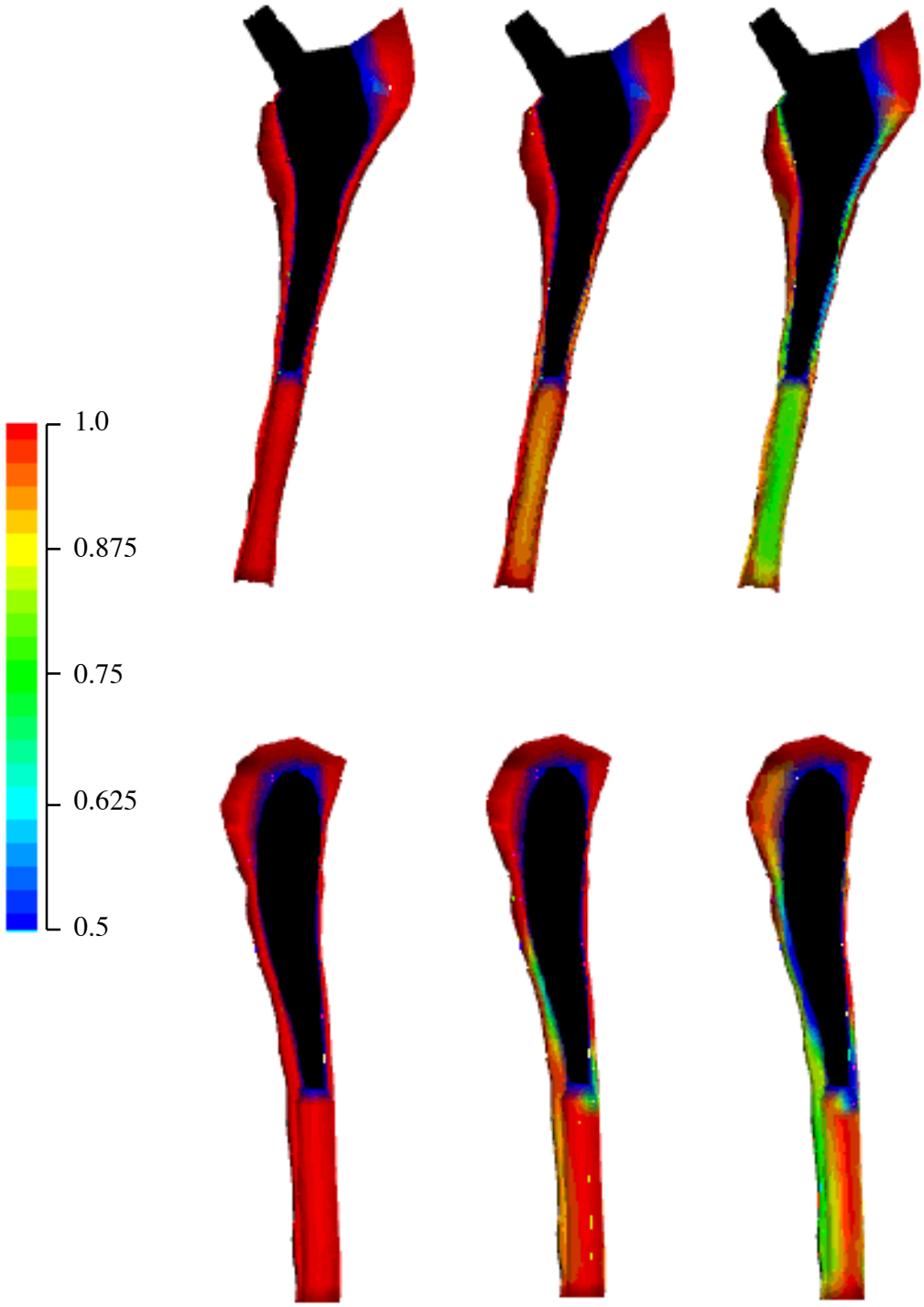

Figure 6.10: Damage function $f(\alpha)$ in trabecular bone for 1,4 & 7 times physiological loading.

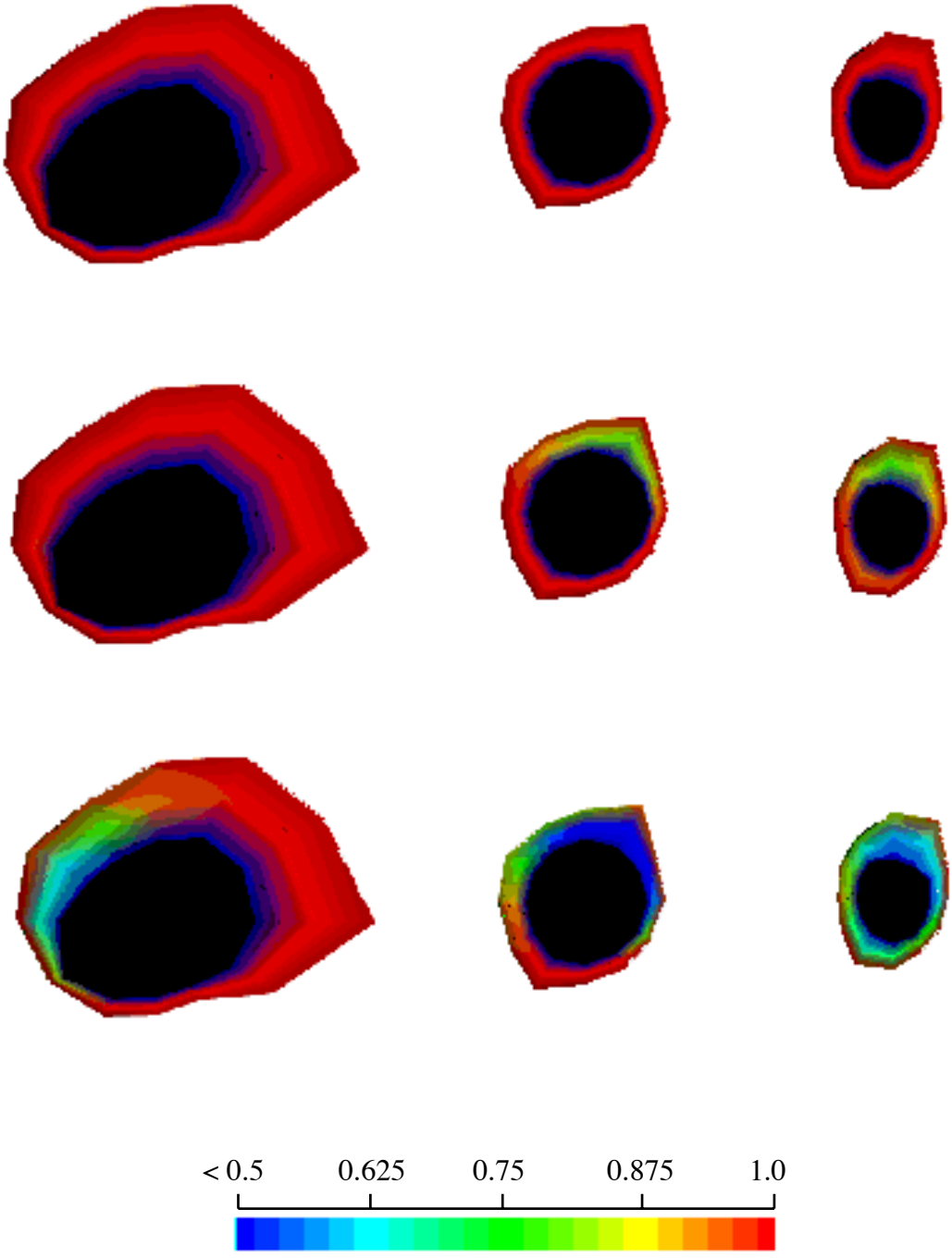

Figure 6.11: Damage function $f(\alpha)$ in trabecular bone for 1,4 & 7 times physiological loading.

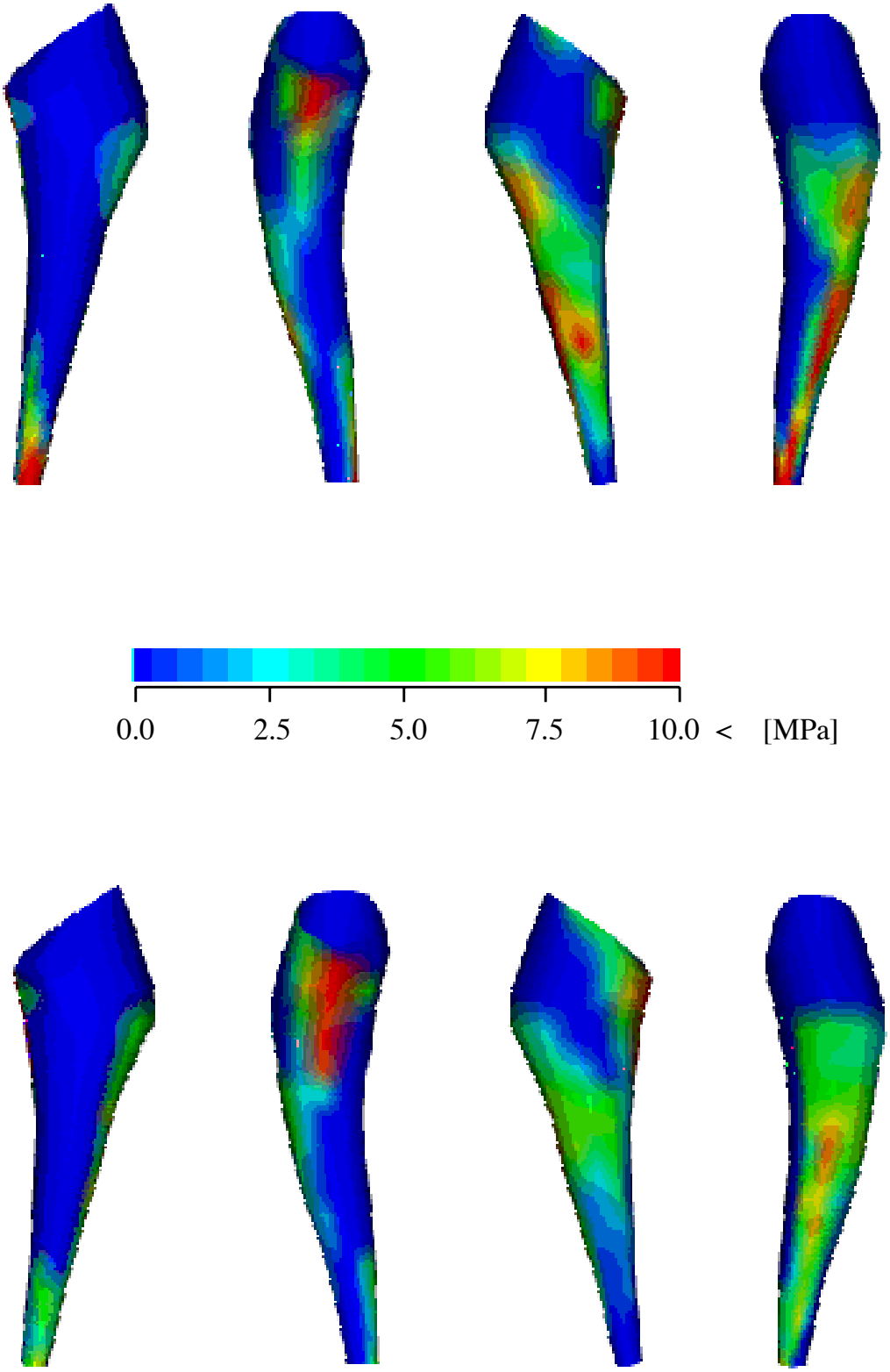

Figure 6.12: Comparison of tangential stress at the bone-implant interface in the elastic (top) and damaged (bottom) case under 7 times physiological loading.

6.3 Discussion

Important Von Mises stresses are found in the prosthetic neck and in the basis of the femoral shaft where load and displacement boundary conditions are imposed. In addition, an anterior and posterior band of high deviatoric stress appear at the tip of the prosthesis which suggests that substantial load is transfered at this level due to the increased antero-posterior force exerted on the joint during stair climbing. In fact, this region of load transfer corresponds to the thickening of the cortical shell in the sagittal plane.

Distribution of the normal anisotropic stress invariant emphasizes bending of cortical bone in both frontal and sagittal planes. Under physiological loading conditions, normal stress in cortical bone reaches approximately one third of the failure level mentioned in the literature [32]. The mechanical role of proximal trabecular bone seems to be reduced by resection of the femoral head and the resulting load by-passing effect of the stiff prosthesis with respect to trabecular bone. Accordingly, little stress is transfered in the proximal region of the femur.

Little damage occurs under physiological loading conditions which is consistent with the primary stability obtained after total hip arthroplasty with a custom implant. Under four times physiological loading, substantial damage appears in the load transfer regions at the posterior tip of the prosthesis and along the posterior part of the bending cortical shaft. Under seven times physiological loading, damage accumulates also in the postero-medial part of the proximal femur.

Damage of trabecular bone reduces the peak stresses and enlarge the contact zones at the bone-implant interface where load is transfered. Most interesting is the slight migration of these contact zones from the distal to the proximal part of the prosthesis. This phenomenon appears to be related to a slight irreversible sinking of the prosthesis in the femoral shaft. The occurence of damage involves thus an adaptation process, whereby the contact zones increase and the prosthesis migrates towards a site of higher stability.

In practice, seven times physiological loading may occur only exceptionnally during impacts. However, similar effects are expected for cyclic loading at lower amplitudes due to fatigue damage. In the long term, fatigue damage will enter

in competition with the bone remodelling response and determine whether the prosthesis remains stable or not.

Clinical relevance of the present model is somehow restricted by the absence of muscle forces that are exerted at different levels of the femoral shaft. Furthermore, a large number of loading cases should be considered in order to discuss the stress and micromotion patterns in depth.

Nevertheless, the present numerical model includes for the first time the essential features of the real quasistatic mechanical behaviour of trabecular bone, namely inhomogeneity, anisotropy and plasticity with damage. Inhomogeneity and anisotropy have proven to play major roles in the elastic behaviour of trabecular bone [110]. The importance of plasticity and damage appears as soon as the mechanical properties of trabecular bone become insufficient with respect to the applied stresses. Irreversible migration of orthopaedic implants is a clinical reality that has been found to be closely related with aseptic loosening. We expect accurate numerical models including nonlinear material behaviour to be innovative and efficient tools for implant design and optimization.

Chapter 7

Conclusion

The objective of this thesis consisted in developing a new constitutive law for trabecular bone with a specific attention towards irreversible phenomena.
An original theoretical model for the elastic, plastic and damaged behaviour is proposed in the framework of standard generalized materials. A free energy potential and a dissipation pseudopotential defined in terms of structural density and the second order mean intercept length tensor determine completely the mechanical response of trabecular bone and the evolution of plastic deformation and damage.

For anisotropic elasticity, the present model is an improved version of the original model conceived by Cowin [32]. A first important property of our model lies in the a priori satisfaction of the positive definiteness condition of the material elasticity tensor. A second property lies in the minimal number of material constants and the direct invertibility of the material elastic law. However, the main contribution of the model lies in its property to degenerate into cubic instead of isotropic symmetry when the eigenvalues of the mean intercept length tensor are identical and thus coincide with the experimental findings. Despite these improvements, there is no evidence that trabecular bone of any species or any part of the skeleton exhibits precisely the same elastic constants. The various types of morphology and degree of mineralization will have to be compared with the present model and eventually distinguished until a suitable generalization of our law, for instance with material tensors of higher order, has been achieved. The

material symmetry group of general orthotropy seems to offer a good compromise between accuracy and complexity for such a generalization.

For irreversible phenomena, our model represents the first attempt to characterize the simultaneous flow of plastic deformation and reduction in elastic properties of trabecular bone. The hypothesis of normal dissipation underlying the standard generalized material approach imposes a strong restriction in the choice of the yield criterion. However, the retained normalized strain energy density criterion provides a fair consistency with the experimental findings and may remain more realistic than foam models relying on uncoupled postyield mechanisms of an idealized cell until homogeneization theory allows to perform exact calculations. Improvement of our model will require examination of the norms corresponding to the invariant subspaces of the orthotropic elasticity tensor as well as a sophisticated experimental program for discrimination of their respective roles in the damage process. The strongest limitation of the model lies in the choice of a unique damage variable inducing isotropic reduction in elastic properties. This choice appears to be reasonable for a porous material in proportional loading, but may be less realistic for complex deformation paths, unless damage accumulation is effectively isotropic, as we were not able to verify. Description of the elasticity tensor by means of two damage orientation distribution functions represents an interesting approach to overcome this problem [66]. From a mathematical point of view, a further difficulty in damage mechanics emerges with the occurence of damage localization and is related to stability and bifurcation of the solution of the considered boundary value problem. The validity of our model is therefore restricted to the hardening part of the damage process preceeding localization and macroscopic failure of the material. It should be emphasized that the latter difficulties belong to the major open issues of continuum damage mechanics.

For rate-dependent behaviour, the one-dimensional formulation of viscous damage has proven satisfactory for the description of creep and generalization to the three-dimensional case should not present major difficulties. These rate-dependent aspects are essential for the understanding of impact problems where bone is subjected to high strain rates.

The account of damage in our model represents a preliminary step towards

formulation of the living aspect of bone tissue. While already a large number of theoretical and numerical recipes have been proposed to match experimental findings, the thermodynamical background of bone remodelling and its implications with respect to the general balance equations of mechanics have not been clarified. The nature of the mechanical stimulations and the physical forces responsible for their transduction to the bone cells inducing formation and resorption of the extracellular bone matrix remain unknown. Living tissue is an open system where mass, entropy and energy are stored and dissipated according to complex and interdependent biochemical processes. Modelling of such a system involves crucial choices in terms of thermodynamic variables and constitutive laws. For this purpose, the relationship between the mechanical loading conditions at the macroscopic level and the stimulation of the cellular activity at the microscopic level has to be clearly established. The respective roles of structural density and morphology need also to be understood in this interaction.

Nevertheless, there are a number of signs suggesting that bone remodelling is closely related to the process of bone damage [16, 25, 97, 108]. In this perspective, characterization of damage becomes necessary in the elaboration of an appropriate theoretical framework and the damage yield criterion may play a crucial role for the response of the living system as well. Indeed, bone formation and resorption lead to strengthening, respectively weakening, of the elastic properties which corresponds in the latter case to the context of damage. Bone formation is thus related to an inversion of the mechanism of damage and may involve reduction of entropy. Accordingly, the living aspect of bone tissue appears in the continuity of dissipative processes and constitutes a most challenging goal for future research in continuum mechanics and thermodynamics.

A numerical model for trabecular bone is integrated in the finite element code TACT and allows us to solve three-dimensional boundary value problems of bone or bone-implant structures. The numerical model consists in an extension of the classical implicit projection algorithm to the case of plasticity with damage and hardening. A large number of validation tests have proven the accuracy and convergence of both the one-dimensional and three-dimensional formulations. An important difficulty encountered with numerical applications in damage mechan-

ics lay in the loss of hyperbolicity of the incremental boundary value problem associated with material softening. In addition, the resulting strain localization exhibits a spurious mesh dependency [118]. Loss of hyperbolicity could be prevented by introducing a viscous component to the evolution of damage in the one-dimensional model. However, the time step needs to remain sufficiently small and the computing time may become prohibitive for applications in the three-dimensional case. Since no general solution such as the arc length method was available in our code to overcome these numerical and theoretical difficulties, material softening was avoided in the three-dimensional model.

Despite these limitations, our numerical model represents a good compromise between complexity and accuracy for simulation of the mechanical behaviour of trabecular bone at the continuum level.

A number of pilot *in vitro* identification experiments were performed to check the relevance of the proposed theoretical model and quantify the material constants.

For elasticity, data from the literature demonstrated the efficiency of our model in predicting the nine orthotropic constants with only three independent coefficients, structural density and the mean intercept length tensor. The elastic properties were found to be rigorously symmetrical in tension and compression. In addition, our data rehabilitate the early hypothesis that the elastic properties of cortical bone may be extrapolated from the properties of trabecular bone with the appropriate structural density (0.9).

Quasistatic experiments revealed the existence of plastic deformations and damage from strains as low as 0.004. The use of waisted specimens avoiding boundary artefacts lead to significantly higher elastic moduli and yield stresses than those found in the literature. A yield criterion has been identified for the first time for trabecular bone by means of uniaxial and torsion experiments. The criterion seems to be reasonably approximated by the strain energy density normalized with respect to structural density and contradicts previous hypotheses based on isotropic stress or strain functions. However, biaxial and triaxial mechanical tests will be necessary to set the definitive validity of the suggested criterion. The issue of yield stress symmetry in tension and compression remains

open and will require additional experiments in order to discriminate between isotropic and kinematic hardening.

The experimental finding according to which the elastic behaviour of cortical bone can be extrapolated from that of trabecular bone suggests that a similar relationship holds for plasticity and damage. Along this line, a 1D nonlinear constitutive law based on continuum damage mechanics was recently developped by Fondrk for cortical bone [45]. Using steady and transient creep experiments, he emphasized the dominating time-dependent aspects of the stress-strain curve at high stress regimes. Despite the different theoretical assumptions, our respective experimental contributions prove definitely the occurence of damage and residual strain in the postyield behaviour of both cortical and trabecular bone tissue.

The interpretation of elastic and damaged deformation at the microstructural level was not made in this work, but is currently attempted in a few laboratories. Plastic yielding and cracking of trabeculae are the most cited mechanisms for the understanding of damage. Mechanical testing at the bone tissue level revealed the importance of the lamellar organization as well as the distribution of lacunae in the obtained results [26]. Multiscale homogeneization techniques may allow in the future to estimate the elastic constants and the yield criterion from microstructural properties and calculate the stress and strain fields at the level of bone tissue [69].

Quantitative computed tomography and dual energy X-ray absorptiometry confirmed to be reliable methods for assessment of structural density of trabecular bone. Together with magnetic resonance imaging (MRI), these methods constitute promising tracks for the *in vivo* assessment of the anisotropic mechanical properties of both cortical and trabecular bone. On the one hand a map of morphological anisotropy could be established for the whole human skeleton and the corresponding interindividual variation assessed. In the case where this variation would remain small, the measurement of structural density by QCT for instance would then be sufficient for a first estimation of the orthotropic properties of any region of interest as far as no metabolic bone disease is involved. On the other hand, second order X-ray absorption and magnetic properties of bone tissue may allow in the future to assess the anisotropic morphology directly and

provide an even better prediction of the orthotropic mechanical properties.

A biomechanical evaluation of a femoral total hip component was performed in order to illustrate the potential of the developed model. Using different measures of stress, the characteristics of load transfer between the prosthesis and the inhomogenous, anisotropic bone were emphasized. Accumulation of damage in trabecular bone was visualized for increasing loading conditions and a stress adaptation phenomenon associated with distal migration of the prosthesis observed. Taking nonlinear material behaviour such as plasticity and damage into account, allows the model to address a much wider spectrum of clinical problems and may provide a valuable alternative to tedious experimental tests that raise numerous ethical and technical problems. In this respect, the developed numerical model exhibits a promising potential.
To conclude, we recall the significant contributions of this thesis:

- The development of a 1D rate-dependent and a 3D rate-independent constitutive law for trabecular bone including simultaneous flow of plastic deformation and damage in the framework of standard generalized materials. A simple orthotropic anisotropy based on a second order fabric tensor was derived for the 3D model.

- The extension of the implicit projection algorithm to the rate-independent and rate-dependent flow of plasticity and damage.

- The experimental demonstration of the plastic and damage behaviour of trabecular bone and the identification of the material constants associated with the 3D model with a method avoiding boundary artefacts.

We hope these contributions will be exploited in future investigation of skeletal failures or design of orthopaedic implants for the benefit of the patient.

List of symbols

Greek

α_c	finite difference stability coefficient
$\alpha(\boldsymbol{x}, t)$	plastic and damage internal variable
α_f	constant of the damage function $f(\alpha)$
α_g	constant of the hardening function $g(\alpha)$
α_{max}	value of α providing g_{max}
β_c	finite difference dissipation coefficient
γ	linear hardening coefficient
Γ	boundary of the present configuration
Γ_0	boundary of the reference configuration
Γ_0^p	part of Γ_0 subjected to a traction condition
Γ_0^u	part of Γ_0 subjected to a displacement condition
${}^e\Gamma$	boundary of ${}^e\Omega$
δ	representative trabecular length
δ_σ	yield strain
ϵ	Young's modulus
ϵ_-	Young's modulus in compression
ϵ_+	Young's modulus in tension
ϵ_i	Young's modulus along axis i
ϵ_c	normalized elastic material constant
$\hat{\epsilon}_c$	elastic material constant
$\varepsilon(\boldsymbol{x}, t)$	internal energy density
ζ	plasticity and damage viscosity coefficient

$\boldsymbol{\zeta}$	natural coordinates
ζ_m^n	natural coordinate m of the nth integration point
$\eta(\boldsymbol{x}, t)$	entropy
$\theta(\boldsymbol{x}, t)$	temperature
ϑ	angle of displacement
ι	kinematic hardening constant
κ	compressibility modulus
λ	Lamé elastic constant
λ_{ij}	orthotropic elastic constants
λ_c	normalized elastic material constant
$\hat{\lambda}_c$	elastic material constant
λ_c^*	normalized elastic material constant
$\hat{\lambda}_c^*$	elastic material constant
$\dot{\lambda}_L$	Lagrange multiplier
λ_α	unknown increment of α
μ	Lamé elastic shear modulus
μ_f	friction coefficient
μ_{ij}	orthotropic elastic shear modulus
μ_c	normalized elastic shear modulus
$\hat{\mu}_c$	elastic shear modulus
ν	Poisson's ratio
ν_{ij}	Poisson's ratio for strain along i versus j
ν_c	normalized elastic material constant
$\hat{\nu}_c$	elastic material constant
$\rho(\boldsymbol{x}, t)$	density
ρ_s	structural density
ρ_a	apparent density
ρ_{aa}	apparent ash density
σ	yield stress
$\hat{\sigma}$	normalized yield stress
σ_-	yield stress in compression

σ_+	yield stress in tension
σ_u	ultimate stress
σ_{c_i}	stress constant
Σ	constitutive function
τ	time step or constant
υ	viscoelasticity coefficient
φ	phase of a sinusoidal schedule
$\phi(\boldsymbol{x},t)$	dissipation pseudopotential
ϕ^*	Legendre-Fenchel transform of ϕ
$\hat{\phi}(\boldsymbol{x},t)$	normalized dissipation pseudopotential
$\Phi(\boldsymbol{x},t)$	dissipated power
$\xi_i(\boldsymbol{x},t)$	internal variables
$\boldsymbol{\xi}_i$	global internal variable vector
${}^e\boldsymbol{\xi}_i$	local internal variable vector
$\boldsymbol{\Xi}_i(\boldsymbol{x},t)$	objective internal variables
$\psi(\boldsymbol{x},t)$	free energy potential
$\tilde{\psi}(\alpha)$	hardening free energy potential
$\hat{\psi}(\boldsymbol{x},t)$	normalized free energy
ψ^*	Legendre transform of ψ
ω_s	pulsation of a sinusoidal schedule
ω_0	subset of the reference configuration
ω_m^n	weight associated with integration point ζ_m^n
Ω	present configuration
Ω_0	reference configuration
${}^e\Omega$	subset of Ω occupied by element e

Latin

a	discrete global acceleration vector
A	section of specimen or bar
A_b	relative area of the bone phase
$b^n(\boldsymbol{x})$	global basis function
${}^e b^k(\boldsymbol{x})$	local basis function
$\boldsymbol{b}(\boldsymbol{x},t)$	body force
b	body force vector
$\mathcal{B}$	solid body
B_A	boundary length per unit bone area
BMD	bone mineral density
$B(\boldsymbol{x})$	discrete global displacement matrix
${}^e B(\boldsymbol{x})$	discrete local displacement matrix
c	scalar constant
c_i	scalar constant or function
$c(\alpha)$	algorithmic function
$\boldsymbol{c}$	constant vector
$\boldsymbol{C}$	second order tensorial constant
$\mathbb{C}$	fourth order tensorial constant
C	mass matrix
D	classical damage variable
D_p	flexural rigidity
D	discrete damping matrix
$e(x)$	compliance jump at the interface
$\boldsymbol{e}_i$	canonical basis of $\mathcal{R}^3$
E	number of elements
$E(x,t)$	material strain
$E^e(x,t)$	elastic part of the material strain
$E^p(x,t)$	plastic part of the material strain
E_f	strain at failure

$\dot{E}_{sec}$	secondary creep strain rate
$\mathcal{E}$	material strain tensor space
$\bar{\mathcal{E}}$	first part of strain space decomposition
$\mathcal{E}'$	second part of strain space decomposition
$\boldsymbol{E}(\boldsymbol{x},t)$	Green-Lagrange material strain tensor
$\boldsymbol{E}^e(\boldsymbol{x},t)$	material elastic strain tensor
$\boldsymbol{E}^p(\boldsymbol{x},t)$	material plastic strain tensor
$\boldsymbol{\mathcal{E}}$	compliance tensor space
$\bar{\boldsymbol{\mathcal{E}}}$	first part of compliance tensor space direct sum
$\boldsymbol{\mathcal{E}}'$	second part of compliance tensor space direct sum
$\mathbb{E}$	compliance second order tensor
$\mathbb{E}_-$	compressive compliance tensor
$\mathbb{E}_+$	tensile compliance tensor
$\bar{\mathbb{E}}$	first part of compliance tensor decomposition
$\mathbb{E}'$	second part of compliance tensor decomposition
E	discrete stiffness matrix
$f(\alpha)$	damage function
$f(u,\dot{u},\xi_i)$	discrete internal force vector
F	iterative function
$\boldsymbol{F}_b(\boldsymbol{N})$	second order tensorial basis element
$\boldsymbol{F}(\boldsymbol{x},t)$	deformation gradient
$\mathbb{F}_b(\boldsymbol{N})$	fourth order tensorial basis element
g_c	constant for $g(\alpha)$
g_{max}	maximum value of $g(\alpha)$
$g(\alpha)$	hardening function
G	iterative function
$\mathcal{G}$	symmetry group
h	thickness of plate
$h(\alpha)$	damage hardening function
$h(\ddot{u})$	inertia force vector
H	height of cylinder

$\boldsymbol{H}(\boldsymbol{x},t)$	displacement gradient
$\mathcal{H}^i$	functional spaces
I_L	number of intersections
$I_{[...]}$	indicatrix function of a set
$\mathcal{I}$	identity symmetry operator
$\boldsymbol{I}$	identity second order tensor
${}^e\boldsymbol{I}$	local identity matrix
k	degree of homogeneity of m_i in ψ
K	number of nodes per element
$\boldsymbol{K}$	fabric tensor of rank two
l	degree of homogeneity of ρ_s in ψ
l_b	trabecular rod or plate length
L	length of specimen, bar or plate
L'	gauge length
$L_b(\boldsymbol{n})$	mean intercept length function
$\hat{L}_b(\boldsymbol{N})$	mean intercept length function
${}^e\boldsymbol{L}$	localization matrix
m	exponent of the viscoplastic law with damage
m_i	eigenvalues of $\boldsymbol{M}$
$\boldsymbol{m}_i$	eigenvectors of $\boldsymbol{M}$
$\bar{\boldsymbol{M}}$	applied angular momentum
$\mathcal{M}_i$	reflexion with respect to the plane orthogonal to $\boldsymbol{m}_i$
$\boldsymbol{M}(\boldsymbol{x})$	mean intercept length second order tensor
n	exponent of the viscoelastic constitutive law
$\boldsymbol{n}$	unit normal vector
N	number of nodes
N	sign of stress
N_T	sign of trial stress
N_f	number of cycles to failure
N_c	constant number of cycles
$\boldsymbol{N}$	unit normal dyad

$\boldsymbol{N}_E$	unit normal separating the strain half-spaces
$\boldsymbol{N}_S$	unit normal separating the stress half-spaces
$\mathcal{O}$	orthogonal second order tensor group
$\boldsymbol{p}(\boldsymbol{x},t)$	nominal stress vector
$\bar{\boldsymbol{p}}(\boldsymbol{x},t)$	prescribed nominal traction
$\boldsymbol{P}(\boldsymbol{x},t)$	Piola-Kirchhoff-1 nominal stress tensor
$\mathbb{P}^u$	rate-independent nominal tangent operator
$\mathbb{P}^{\dot{u}}$	rate-dependent nominal tangent operator
P_h^u	discrete nominal displacement tangent matrix
$P_h^{\dot{u}}$	discrete nominal velocity tangent matrix
${}^eP_h^u$	local discrete displacement tangent matrix
${}^eP_h^{\dot{u}}$	local discrete velocity tangent matrix
q	axial force
$\overline{\boldsymbol{q}}$	applied force
$\boldsymbol{q}(\boldsymbol{x},t)$	contact force
q	discrete contact force vector
QCT	mineral density of calibration phantom
r_{ti}	transverse isotropy ratio
$r(u)$	scalar iteration function
$r(u)$	discrete total force vector
$\tilde{r}(w,\dot{w},\ddot{w})$	linearization of $r(u)$
R_o	external radius of cylinder
R_i	internal radius of cylinder
$\boldsymbol{R}$	rotation tensor
$\mathcal{R}$	real numbers
$\mathcal{R}^-$	negative real numbers
$\mathcal{R}^+$	positive real numbers
$s(x)$	elasticity jump at the interface
S	material stress
$\hat{S}$	normalized material stress
$\tilde{S}$	effective stress

S_V	surface area per unit bone volume
S^i	approximation of $\frac{dr}{du}$ at u^i
$S^E(x,t)$	conjugate of E with respect to ψ
$S^{E^p}(x,t)$	conjugate of E^p with respect to ψ
S^α	conjugate of α with respect to ψ
$S^{\dot{E}}(x,t)$	conjugate of $\dot{E}$ with respect to ϕ
S_T^E	trial conjugate of E
$\mathcal{S}$	material stress space
$\bar{\mathcal{S}}$	first part of stress space decomposition
$\mathcal{S}'$	second part of stress space decomposition
$\boldsymbol{S}(\boldsymbol{x},t)$	Piola-Kirchhoff-2 material stress tensor
$\hat{\boldsymbol{S}}(\boldsymbol{x},t)$	normalized material stress tensor
$\boldsymbol{S}^E(\boldsymbol{x},t)$	conjugate of $\boldsymbol{E}$ with respect to ψ
$\boldsymbol{S}_T^E(\boldsymbol{x},t)$	trial conjugate of variable $\boldsymbol{E}$
$\boldsymbol{S}^{E^p}(\boldsymbol{x},t)$	conjugate of $\boldsymbol{E}^p$ with respect to ψ
$\boldsymbol{S}^{\dot{E}}(\boldsymbol{x},t)$	conjugate of $\dot{\boldsymbol{E}}$ with respect to ϕ
$\mathbb{S}$	elasticity second order tensor
$\mathbb{S}_-$	compressive elasticity tensor
$\mathbb{S}_+$	tensile elasticity tensor
$\mathbb{S}^u$	rate-independent material tangent operator
$\mathbb{S}_a^u$	algorithmic material tangent operator
$\mathbb{S}^{\dot{u}}$	rate-dependent material tangent operator
$\boldsymbol{\mathcal{S}}$	elasticity tensor space
$\bar{\boldsymbol{\mathcal{S}}}$	first part of elasticity tensor space direct sum
$\boldsymbol{\mathcal{S}}'$	second part of elasticity tensor space direct sum
$\bar{\mathbb{S}}$	first part of elasticity tensor decomposition
$\mathbb{S}'$	second part of elasticity tensor decomposition
t	time
t_b	trabecular rod or plate thickness
T	total time of simulation
T_f	time to failure

T_c	time constant
u	displacement
u_z	displacement along axis z
u_θ	tangential displacement along $\boldsymbol{e}_\theta$
$\boldsymbol{u}(\boldsymbol{x},t)$	displacement vector
$\boldsymbol{u}_h(\boldsymbol{x},t)$	displacement approximation
$\boldsymbol{u}^n(t)$	displacement of node n
${}^e\boldsymbol{u}_h(\boldsymbol{x},t)$	local displacement approximation
${}^e\boldsymbol{u}^k(t)$	displacement of node k of element e
$\bar{\boldsymbol{u}}(\boldsymbol{x},t)$	prescribed displacement
$u(t)$	discrete global displacement vector
${}^eu(t)$	discrete local displacement vector
v	discrete global velocity vector
V_b	relative volume of the bone phase
$\boldsymbol{w}(\boldsymbol{x},t)$	virtual displacement
$\boldsymbol{w}_h(\boldsymbol{x},t)$	virtual displacement approximation
$\boldsymbol{w}^n(t)$	virtual displacement of node n
${}^e\boldsymbol{w}_h(\boldsymbol{x},t)$	local virtual displacement approximation
${}^e\boldsymbol{w}^k(t)$	local virtual displacement of node k
$w(t)$	discrete virtual displacement vector
${}^ew(t)$	discrete local virtual displacement vector
W	width of specimen
$\boldsymbol{x}$	reference position vector
x	discrete global reference position vector
${}^ex$	local reference position vector
y	yield function
y_σ	yield value
$\boldsymbol{y}(\boldsymbol{x},t)$	present deformed position vector
$\tilde{\boldsymbol{y}}(\boldsymbol{x},t)$	deformed position including a change of reference frame
$\boldsymbol{Y}$	iterative function
z	viscous yield function

References

[1] P. Alart and A. Curnier. A mixed formulation for frictional contact problems prone to newton like solution methods. *Computer Methods in Applied Mechanics and Engineering*, 92:353–375, 1991.

[2] J.S. Arnold. Quantitation of mineralization of bone as an organ and tissue in osteoporosis. *Clinical Orthopaedics and Related Research*, 17:167–175, 1960.

[3] R.B. Ashman, S.C. Cowin, W.C.V. Buskirk, and J.C. Rice. A continuous wave technique for the measurement of the elastic properties of cortical bone. *Journal of Biomechanics*, 17:349–361, 1984.

[4] R.B. Ashman and J.Y. Rho. Elastic moduli of trabecular bone material. *Journal of Biomechanics*, 21:177, 1988.

[5] R.B. Ashman, J.Y. Rho, and C.H. Turner. Anatomical variation of orthotropic elastic moduli of the proximal human tibia. *Journal of Biomechanics*, 22:895–900, 1989.

[6] R.M. Aspden. The effect of boundary conditions on the results of mechanical tests. *Journal of Biomechanics*, 23:623, 1990.

[7] J.H. Bargren, C.A.L. Bassett, and A. Gjelsvik. Mechanical properties of hydrated cortical bone. *Journal of Biomechanics*, 7:239–245, 1974.

[8] G.S. Beaupré and W.C. Hayes. Finite element analysis of a three-dimensional open-celled model of trabecular bone. *Journal of Biomechanical Engineering*, 107:249–256, 1985.

[9] J.C. Behrens, P.S. Walker, and H. Shoji. Variations in strength and structure of cancellous bone at the knee. *Journal of Biomechanics*, 7:201–207, 1974.

[10] J.P. Boehler. *Introduction to the invariant formulation of anisotropic constitutive equations*, pages 3–65. Springer Verlag, 1987.

[11] W. Bonfield. Advances in the fracture mechanics of cortical bone. *Journal of Biomechanics*, 20:1071–1081, 1987.

[12] R.M. Bowen. *Introduction to continuum mechanics for engineers.* Plenum Press, New York, 1989.

[13] S.M. Bowman, T.M. Keaveny, and T.A. McMahon. Compressive creep behaviour of bovine trabecular bone. In *Proceedings 39th Annual Meeting ORS*, 1993.

[14] K. Brear, J.D. Currey, S. Raines, and K.J. Smith. Density and temperature effects on some mechanical properties of cancellous bone. *Engineering in Medicine*, 17:163–167, 1988.

[15] T.D. Brown and A.B. Ferguson. Mechanical property distributions in the cancellous bone of the human proximal femur. *Acta Orthopaedica Scandinavica*, 51:429–437, 1980.

[16] D.B. Burr and R.B. Martin. Calculating the probability that microcracks initiate resorption spaces. *Journal of Biomechanics*, 26:613–616, 1993.

[17] A.H. Burstein, J.D. Currey, V.H. Frankel, and D.T. Reilly. The ultimate properties of bone tissue: the effects of yielding. *Journal of Biomechanics*, 5:35–44, 1972.

[18] W.E. Caler and D.R. Carter. Bone creep-fatigue damage accumulation. *Journal of Biomechanics*, 22:625–635, 1989.

[19] C.E. Cann. Quantitative CT for determination of bone mineral density: A review. *Radiology*, 166:509–522, 1988.

[20] D.R. Carter and W.C. Hayes. Density and strain rate. *Science*, 194:1174–1176, 1976.

[21] D.R. Carter and W.C. Hayes. The compressive behaviour of bone as a two phase porous structure. *Journal of Bone and Joint Surgery*, 59:954–962, 1977.

[22] D.R. Carter, T.E. Orr, and D.P. Fyhrie. Relationship between loading history and femoral cancellous bone architecture. *Journal of Biomechanics*, 22:231–244, 1989.

[23] D.R. Carter, G.H. Schwab, and D.M. Spengler. Tensile fracture of cancellous bone. *Acta Orthopaedica Scandinavica*, 51:733–741, 1980.

[24] D.R. Carter and D.M. Spengler. Mechanical properties and composition of cortical bone. *Clinical Orthopaedics and Related Research*, 135:192–217, 1978.

[25] A. Chamay and P. Tschantz. Mechanical influences in bone remodeling. experimental research on Wolff's law. *Journal of Biomechanics*, 5:173–180, 1972.

[26] K. Choi and S.A. Goldstein. A comparison of the fatigue behaviour of human trabecular and cortical bone tissue. *Journal of Biomechanics*, 25:1371–1381, 1992.

[27] R.M. Christensen. Mechanics of low density materials. *Journal of Mechanics and Physics of Solids*, 34:563–578, 1986.

[28] M.J. Ciarelli, S.A. Goldstein, D. Dickie, J.L. Ku, M. Kapper, J. Stanley, M.J. Flynn, and L.S. Matthews. Experimental determination of the orthogonal mechanical properties, density and distribution of human trabecular bone from the major metaphyseal regions utilizing materials testing and computed tomography. In *Proceedings 32nd Annual Meeting ORS*, 1986.

[29] S.H. Cohn. *Non-invasive measurements of bone mass and their clinical application.* CRC Press Inc., Boca Raton, 1981.

[30] J.-P. Cordebois and F. Sidoroff. Endommagement anisotrope en élasticité et plasticité. *Journal de Mécanique Théorique et Appliquée*, No Special:45–60, 1982.

[31] S.C. Cowin. The relationship between the elasticity tensor and the fabric tensor. *Mechanics of materials*, 4:137–147, 1985.

[32] S.C. Cowin. *Bone Mechanics*. CRC Press, Boca Raton, 1989.

[33] S.C. Cowin and M.M. Mehrabadi. Identification of the elastic symmetry of bone and other materials. *Journal of Biomechanics*, 22:503–515, 1989.

[34] S.C. Cowin and C.H. Turner. On the relationship between the orthotropic Young's moduli and fabric. *Journal of Biomechanics*, 25:1493–1494, 1992.

[35] J.M. Crolet, B. Aoubiza, and A. Meunier. Compact bone: numerical simulation of mechanical characteristics. *Journal of Biomechanics*, 26:677–687, 1993.

[36] A. Curnier. A theory of friction. *International Journal of Solids and Structures*, 20:637–647, 1984.

[37] A. Curnier. *Méthodes numériques en mécanique des solides*. Presses polytechniques et universitaires romandes, Lausanne, 1993.

[38] A. Curnier, Q.-C. He, and P.K. Zysset. Conewise linear elastic materials. *Journal of Elasticity*, accepted, 1994.

[39] J. Currey. *The mechanical adaptations of bones*. Princeton University Press, Princeton, 1984.

[40] J.D. Currey. The mechanical properties of bone. *Clinical Orthopaedics and Related Research*, 73:210–231, 1970.

[41] M. Dalstra, R. Huiskes, A. Odgaard, and L.v. Erning. Mechanical and textural properties of pelvic trabecular bone. *Journal of Biomechanics*, 26:523–535, 1993.

[42] D.T. Davy, G.M. Kotzar, R.H. Brown, K.G. Heiple, V.M. Goldberg, J. Berilla, and A.H. Burstein. Telemetric force measurements across the hip after total arthroplasty. *Journal of Bone and Joint Surgery*, 70A:45–50, 1988.

[43] I. Ekeland and R. Temam. *Convex analysis and variational problems*. North-Holland, Amsterdam, 1976.

[44] M. Fondrk, E. Bahniuk, D.T. Davy, and C. Michaels. Some viscoplastic characteristics of bovine and human cortical bone. *Journal of Biomechanics*, 21:623–630, 1988.

[45] M. Fondrk. *An experimental and analytical investigation into the nonlinear constitutive equations of cortical bone.* Ph.D. thesis, Case Western Reserve University, 1989.

[46] Frost and Sullivan. Orthopaedic implants and allied products market outside de U.S. Technical report, Frost & Sullivan, 1989.

[47] J. Galante, W. Rostoker, and R.D. Ray. Physical properties of trabecular bone. *Calcified Tissue Research*, 5:236–246, 1970.

[48] H.K. Genant, J.E. Block, P. Steiger, C.C. Glüer, B. Ettinger, and S.T. Harris. Appropriate use of bone densitometry. *Radiology*, 170:817–822, 1989.

[49] P. Germain. *Cours de mécanique des milieux continus.* Masson, Paris, 1973.

[50] L.J. Gibson. The mechanical behaviour of cancellous bone. *Journal of Biomechanics*, 18:317–328, 1985.

[51] L.J. Gibson and M.F. Ashby. *Cellular solids.* Pergamon Press, Oxford, 1988.

[52] L.J. Gibson, M.F. Ashby, J. Zhang, and T.C. Triantafillou. Failure surfaces for cellular materials under multiaxial loads I.Modelling. *International Journal of Mechanical Science*, 31:635–663, 1989.

[53] C.C. Glüer and H.K. Genant. Impact of marrow fat on accuracy of quantitative CT. *Journal of Computed Assisted Tomography*, 13:1023–1035, 1989.

[54] S.A. Goldstein. The mechanical properties of trabecular bone: Dependence on anatomic location and function. *Journal of Biomechanics*, 20:1055–1061, 1987.

[55] S.A. Goldstein, D.L. Wilson, D.A. Sonstegard, and L.S. Matthews. The mechanical properties of human tibial trabecular bone as a function of metaphyseal location. *Journal of Biomechanics*, 16:965–969, 1983.

[56] J.K. Gong, J.S. Arnold, and H. Cohn. Composition of trabecular and cortical bone. *Anatomical Record*, 149:325–332, 1964.

[57] T. Gottesmann and Z. Hashin. Analysis of viscoelastic behaviour of bones on the basis of microstructure. *Journal of Biomechanics*, 13:89–96, 1980.

[58] X.E. Guo, L.J. Gibson, and T.A. McMahon. Fatigue of trabecular bone: avoiding end-crushing artifacts. In *Proceedings 39th Annual Meeting ORS*, 1993.

[59] M. Gurtin. *An introduction to continuum mechanics*. Academic Press, New York, 1981.

[60] T.P. Harrigan, M. Jasty, R.W. Mann, and W.H. Harris. Limitations of the continuum assumption in cancellous bone. *Journal of Biomechanics*, 21:269–275, 1988.

[61] T.P. Harrigan and R.W. Mann. Characterization of microstructural anisotropy in orthotropic materials using a second rank tensor. *Journal of Materials Science*, 19:761–767, 1984.

[62] W.C. Hayes and D.R. Carter. Postyield behaviour of subchondral trabecular bone. *Journal of Biomedical Materials Research*, 7:537–544, 1976.

[63] W.C. Hayes, S.J. Piazza, and P.K. Zysset. Biomechanics of fracture risk prediction of the hip and spine by quantitative computed tomography. *The Radiologic Clinics of North America*, 29:1–18, 1991.

[64] W.C. Hayes and B. Snyder. Toward a quantitative formulation of Wolff's law in trabecular bone, p. 43–68. In *Mechanical properties of bone*, S.C. Cowin, ASME, 1981.

[65] W.C. Hayes, L.W. Swenson, and D.R. Schurman. Axisymmetric finite element analysis of the lateral tibial plateau. *Journal of Biomechanics*, 11:21–23, 1978.

[66] Q.-C. He and A. Curnier. A more fundamental approach to damaged elastic stress-strain relations. *International Journal of Solids and Structures*, accepted, 1994.

[67] T.K. Hight and J.F. Brandeau. Mathematical modeling of the stress strain-strain rate behaviour using the ramberg-osgood equation. *Journal of Biomechanics*, 16:445–450, 1983.

[68] R. Hill. *The mathematical theory of plasticity.* Oxford University Press, Oxford, 1950.

[69] S.J. Hollister, D.P. Fyhrie, K.J. Jepsen, and S.A. Goldstein. Application of the homogenization theory to the study of trabecular bone mechanics. *Journal of Biomechanics*, 24:825–839, 1991.

[70] R. Huiskes. Biomechanics of artificial-joint fixation, p. 375. In *Orthopaedic Biomechanics*, V.C. Mow & W.C. Hayes, Raven Press, 1991.

[71] R. Huiskes and E.Y.S. Chao. A survey of finite element analysis in orthopaedic biomechanics: the first decade. *Journal of Biomechanics*, 16:385–409, 1983.

[72] I. Hvid, S.M. Bentzen, F. Linde, L. Mosekilde, and B. Pongsoipetch. X-ray quantitative computed tomography: The relations to physical properties of proximal tibial trabecular bone specimens. *Journal of Biomechanics*, 22:837–844, 1989.

[73] V. Kafka. On hydraulic strengthening of bones. *Journal of Biomechanics*, 26:761–762, 1993.

[74] S.J. Kaplan, W.C. Hayes, J.L. Stone, and G.S. Beaupré. Tensile strength of bovine trabecular bone. *Journal of Biomechanics*, 18:723–727, 1985.

[75] J.L. Katz. Hard tissue as a composite material I.Bounds on the elastic behaviour. *Journal of Biomechanics*, 7:455–473, 1971.

[76] T.M. Keaveny. Trabecular bone is linearly elastic up to yielding and yields by cracking. In *Proceedings 39th Annual Meeting ORS*, 1993.

[77] T.M. Keaveny, R.E. Borchers, L.J. Gibson, and W.C. Hayes. Trabecular bone modulus and strength can depend on specimen geometry. *Journal of Biomechanics*, 26:991–1000, 1993.

[78] J.H. Keyak, I.Y. Lee, S. Majumdar, H.B. Skinner, and H.K. Genant. Orthogonal mechanical properties of trabecular bone predicted by magnetic resonnance and computed tomography. In *Proceedings 39th Annual Meeting ORS*, 1993.

[79] F.J. Klever. *On the mechanics of failure of artificial knee joints.* Ph.D. thesis, University of Twente, 1984.

[80] R.J. Knops and L.E. Payne. *Uniqueness theorems in linear elasticity.* Springer-Verlag, Berlin, 1971.

[81] D. Krajcinovic. Damage mechanics. *Mechanics of materials*, 8:117–197, 1989.

[82] D. Krajcinovic, J. Trafimow, and D. Sumarac. Simple constitutive model for cortical bone. *Journal of Biomechanics*, 20:779–784, 1987.

[83] R.D. Krieg and D.B. Krieg. Accuracies of numerical solution methods for the elastic-perfectly plastic model. *Journal of Pressure and Vessel Technology*, 99:510–515, 1977.

[84] R.V. Krstić. *General histology of the mammal.* Springer, Berlin, 1985.

[85] R.V. Krstić. *Human microscopic anatomy.* Springer Verlag, Berlin, 1991.

[86] J.L. Ku, S.A. Goldstein, K.W. Choi, M. London, M.A. Herzig, and L.S. Matthews. The mechanical properties of single trabeculae. In *Proceedings 33rd Annual Meeting ORS*, 1987.

[87] R. Lakes and S. Saha. Cement line motion in bone. *Science*, 204:501–503, 1979.

[88] J. Lemaitre and J.L. Chaboche. *Mécanique des matériaux solides*. Bordas, Paris, 1988.

[89] F. Linde and I. Hvid. Stiffness behaviour of trabecular bone specimens. *Journal of Biomechanics*, 20:83–89, 1987.

[90] F. Linde, I. Hvid, and N.C. Jensen. Material properties of cancellous bone in repetitive axial loading. *Engineering in Medicine*, 14:173–177, 1985.

[91] F. Linde, I. Hvid, and F. Madsen. The effect of specimen geometry on the mechanical behaviour of trabecular bone specimens. *Journal of Biomechanics*, 25:359–368, 1992.

[92] F. Linde, I. Hvid, and B. Pongsoipetch. Energy absorptive properties of human trabecular bone specimens during axial compression. *Journal of Orthopaedic Research*, 7:432–439, 1989.

[93] F. Linde, P. Nørgaard, I. Hvid, A. Odgaard, and K. Søballe. Mechanical properties of trabecular bone. Dependency on strain rate. *Journal of Biomechanics*, 24:803–809, 1991.

[94] F. Linde, C.B. Gøthgen, I. Hvid, B. Pongsoipetch, and S. Bentzen. Mechanical properties of trabecular bone by a non-destructive testing approach. *Engineering in Medicine*, 17:23–29, 1988.

[95] J.C. Lotz, T.N. Gerhart, and W.C. Hayes. Mechanical properties of trabecular bone from the proximal femur: A quantitative CT study. *Journal of Computed Assisted Tomography*, 14:107–114, 1990.

[96] M. Martens, R.V. Audekercke, P. Delport, P.D. Meester, and J.C. Mulier. The mechanical characteristics of cancellous bone at the upper femoral region. *Journal of Biomechanics*, 16:971–983, 1983.

[97] R.B. Martin and D.B. Burr. A hypothetical mechanism for the stimulation of osteonal remodelling by fatigue damage. *Journal of Biomechanics*, 15:137–139, 1982.

[98] P.L. Mente and J.L. Lewis. Young's modulus of trabecular bone tissue. In *Proceedings 33rd Annual Meeting ORS*, 1987.

[99] W.A. Merz and R.K. Schenk. Quantitative structural analysis of human cancellous bone. *Acta Anatomica*, 75:54–66, 1970.

[100] G.H. Meyer. Die Architektur der Spongiosa. *Archiv fuer Anatomie, Physiologie und wissenschaftliche Medizin*, 34:615–628, 1867.

[101] K.H. Mueller, A. Trias, and R.D. Ray. Bone density and composition. *Journal of Bone and Joint Surgery*, 48-A:140–148, 1966.

[102] A. Odgaard, C.M. Pedersen, S.M. Bentzen, J. Jørgensen, and I. Hvid. Density changes at the proximal tibia after medial meniscectomy. *Journal of Orthopaedic Research*, 7:744–753, 1989.

[103] E.T. Oñat. Effective properties of elastic materials that contain penny shaped voids. *International Journal for Engineering and Science*, 22:1013–1021, 1984.

[104] C.E. Oxnard. Bones and bones, architecture and stress, fossils and osteoporosis. *Journal of Biomechanics*, 26:63–79, 1993.

[105] F. Pauwels. *Biomechanics of the locomotor apparatus.* Springer-Verlag, Berlin, 1980.

[106] S. Popov. *Introduction to mechanics of solids.* Prentice Hall, Englewood Cliffs, 1968.

[107] J.W. Pugh, R.M. Rose, and E.L. Radin. Elastic and viscoelastic properties of trabecular bone: Dependance on structure. *Journal of Biomechanics*, 6:475–485, 1973.

[108] J.W. Pugh, R.M. Rose, and E.L. Radin. A possible mechanism of Wolff's law: trabecular microfractures. *Archives Internationales de Physiologie et de Biochimie*, 81:27–40, 1973.

[109] J.W. Pugh, R.M. Rose, and E.L. Radin. A structural model for the mechanical behaviour of trabecular bone. *Journal of Biomechanics*, 6:657–670, 1973.

[110] R.L. Rakotomanana, A. Curnier, and P.F. Leyvraz. An objective anisotropic elastic plastic model and algorithm applicable to bone mechanics. *European Journal of Mechanics*, 10:327–342, 1991.

[111] D.T. Reilly, A.H. Burstein, and V.H. Frankel. The elastic modulus for bone. *Journal of Biomechanics*, 7:271–275, 1974.

[112] J.C. Rice, S.C. Cowin, and J.A. Bowman. On the dependence of the elasticity and strength of cancellous bone on apparent density. *Journal of Biomechanics*, 21:155–168, 1988.

[113] H. Roesler. The history of some fundamental concepts in bone biomechanics. *Journal of Biomechanics*, 20:1025–1034, 1987.

[114] P.J. Rubin, R.L. Rakotomanana, P.F. Leyvraz, P.K. Zysset, A. Curnier, and J.H. Heegaard. Frictional interface micromotions and anisotropic stress distribution in a femoral total hip component. *Journal of Biomechanics*, 26:725–739, 1993.

[115] S.D. Ryan and J.L. Williams. Tensile testing of rodlike trabeculae excised from bovine femoral bone. *Journal of Biomechanics*, 22:351–355, 1989.

[116] C.M. Schoenfeld, E.P. Lautenschlager, and P.R. Meyer. Mechanical properties of human cancellous bone in the femoral head. *Medical and Biological Engineering*, 12:313–317, 1974.

[117] A. Shirazi-Adl, M. Dammak, A. Forcione, and G. Paiement. Friction measurements at the bone-implant interface: application to the analysis of cementless prostheses. In *Proceedings 38th Annual Meeting ORS*, 1992.

[118] J.C. Simo. Strain softening and dissipation: A unification of approaches, p. 440–461. In *Cracking and damage*, J. Mazars & Z.P. Bazant, Elsevier Applied Science, 1989.

[119] J.C. Simo and R.L. Taylor. Consistent tangent operators for rate-independent elastoplasticity. *Computer methods in applied engineering*, 48:101–118, 1985.

[120] I. Singh. The architecture of cancellous bone. *Journal of Anatomy*, 127:305–310, 1978.

[121] B.D. Snyder and W.C. Hayes. Multiaxial structure-property relations in trabecular bone, pages 31–59. In *Biomechanics of Diarthrodial Joints*, V.C. Mow, A. Ratcliffe & S.L.-Y. Woo, Springer Verlag, 1990.

[122] J.L. Stone, G.S. Beaupré, and W.C. Hayes. Multiaxial strength characteristics of trabecular bone. *Journal of Biomechanics*, 16:743–752, 1983.

[123] S. Struhl, S.A. Goldstein, D.L. Dickie, M.J. Flynn, and L.S. Matthews. The distribution of mechanical properties of trabecular bone within vertebral bodies and iliac crests: Correlation with computed tomography density. In *Proceedings 33rd Annual Meeting ORS*, 1987.

[124] S. Sutcliffe. Spectral decomposition of the elasticity tensor. *Journal of Applied Mechanics*, 59:762–773, 1992.

[125] H. Takechi. Trabecular architecture of the knee joint. *Acta Orthopaedica Scandinavica*, 48:673, 1977.

[126] D.W. Thompson. *On growth and form: A new edition.* Cambridge University Press, Cambridge, 1942.

[127] S. Timoshenko and S. Woinowsky-Krieger. *Theory of plates and shells.* McGraw-Hill, New-York, 1959.

[128] P.R. Townsend and R.M. Rose. Buckling studies of single human trabeculae. *Journal of Biomechanics*, 8:199–201, 1975.

[129] C. Turner. On Wolff's law of trabecular architecture. *Journal of Biomechanics*, 25:1–9, 1992.

[130] C.H. Turner and S.C. Cowin. Errors induced by off-axis measurement of the elastic properties of bone. *Journal of Biomechanical Engineering*, 110:213–215, 1988.

[131] C.H. Turner, S.C. Cowin, J.Y. Rho, R.B. Ashman, and J.C. Rice. The fabric dependance of the orthotropic elastic constants of cancellous bone. *Journal of Biomechanics*, 23:549–561, 1990.

[132] J.K. Weaver and J. Chalmers. Cancellous bone: It's strength and changes with aging and an evaluation of some methods for measuring its mineral content. *Journal of Bone and Joint Surgery*, 48-A:289–299, 1966.

[133] E.R. Weibel. *Stereological methods: Theoretical foundations.* Academic Press, London, 1980.

[134] K. Weimann and C. Kaddick. Comparative evaluation of the initial stability and the interface stresses of cementless tibial components of TKR. In *Proceedings 6th Meeting ESB*, 1988.

[135] H. Weinans, R. Huiskes, and H.J. Grootenboer. The behavior of adaptive bone-remodeling simulation models. *Journal of Biomechanics*, 25:1425–1441, 1992.

[136] W.J. Whitehouse. The quantitative morphology of anisotropic trabecular bone. *Journal of Microscopy*, 101:153–168, 1974.

[137] J.L. Williams and J.L. Lewis. Properties and an anisotropic model of cancellous bone from the proximal tibial epiphysis. *Journal of Biomechanical Engineering*, 104:50–56, 1982.

[138] J. Wolff. *Das Gesetz der Transformation der Knochen.* A. Hirchwild, Berlin, 1892.

[139] L.H. Yahia, G. Drouin, and P. Duval. A methodology for mechanical measurements of technical constant of trabecular bone. *Engineering in Medicine*, 17:169–173, 1988.

[140] H. Zilch, A. Rohlmann, G. Bergmann, and R. Kolbel. Material properties of femoral cancellous bone in axial loading Part II: Time dependent properties. *Archives of Orthopaedic and Traumatic Surgery*, 97:257–262, 1980.

[141] P.K. Zysset, M. Sonny, and W.C. Hayes. Morphology-mechanical property relations in trabecular bone of the osteoarthritic proximal tibia. *Journal of Arthroplasty*, 9:203-216, 1994.

Curriculum Vitæ

Philippe Kurt Zysset

Personnel

Adresse:	Chemin de la Maison-Jean, 44
	CH-1801 Le Mont-Pèlerin
Naissance:	le 22 octobre 1963 à Genève
Origine:	Troinex, Genève
Etat civil:	Marié

Formation

1978-1982	Maturité , type C
	Collège de Candolle, Genève
1982-1987	Diplôme d'ingénieur physicien EPFL
	Ecole Polytechnique Fédérale de Lausanne

Activités

1988-1989	Protek AG, Bern
	Département de recherche et développement
	Ingénieur de développement
1989-1990	Harvard Medical School, Boston, USA
	Orthopaedic Biomechanics Laboratory
	Collaborateur scientifique
1990-1994	Ecole Polytechnique Fédérale de Lausanne
	Laboratoire de Mécanique Appliquée
	Doctorant

Publications

- Hayes W.C., Piazza J.P. & Zysset P.K.
  "Biomechanics of fracture risk prediction of the hip and spine by quantitative computed tomography"
  The Radiologic Clinics of North America, 29,1-18, 1991

- Michel M.C., Zysset P.K. & Hayes W.C.
  "Fatigue behaviour of trabecular bone"
  37th Orthopaedic Research Society, Anaheim, 1991

- Rubin P.J., Rakotomanana R.L., Leyvraz P.F., Zysset P.K.
  Curnier A. & Heegaard J.H.
  "Frictional interface micromotions and anisotropic stress distribution in a femoral total hip component"
  Journal of Biomechanics, 26, 725-739, 1993

- Curnier A., He Q.-C. & Zysset P.K.
  "Conewise linear elastic materials"
  Journal of Elasticity, accepted, 1994

- Zysset P.K., Sonny M. & Hayes W.C.
  "Morphology-mechanical property relations in trabecular bone of the osteoarthritic proximal tibia"
  Journal of Arthroplasty, 9, 203-216, 1994

- Zysset P.K., Angst M.P., Michel M.C. & Curnier A.
  "Compressive creep behaviour of bovine trabecular bone "
  3rd Conference of the EORS, Paris, 1993